Compact Fiber-Optic Diffuse Reflection Probes for Medical Diagnostics

Theodore Paul Moffitt
B.S., Physics, Western Washington University (1997)
M.S., Electrical and Computer Engineering, Oregon Graduate Institute
of Science and Technology (2000)

A dissertation submitted to the faculty of the
OGI School of Science & Engineering
at Oregon Health & Science University
in partial fulfillment of the
requirements for the degree
Doctor of Philosophy
in
Electrical and Computer Engineering

July 2007

The dissertation "Compact Fiber-Optic Diffuse Reflection Probes for Medical Diagnostics" by Theodore Paul Moffitt has been examined and approved by the following Examination Committee:

Scott A. Prahl
Assistant Professor
Thesis Research Advisor

Steven L. Jacques
Professor

Sean J. Kirkpatrick
Associate Professor

James W. Whittaker
Associate Professor

Acknowledgements

I would like to express thanks to the following people in their many capacities in which they have helped me to achieve the accomplishment of this thesis. First and foremost, I would like to thank my research advisor, Dr. Scott Prahl, who encouraged, supported and mentored my development in scientific research. Next, I express my gratitude to Dr. Steve Jacques, who among many other things showed me that working hard and playing hard can be one and the same task. I give my thanks to Dr. Sean Kirkpatrick who taught me the value of speckle and shared the joys of mechanical testing. I thank Dr. Jim Whittaker for teaching me the many modes of spectroscopy. I am most grateful for the opportunity to work with these four individuals who make up my advisory committee. In addition, I express my gratitude to Dr. Ken Gregory who supported my graduate studies not only financially, but also in creating a unique multidisciplinary environment at OMLC which fostered my growth. I thank Dr. Jim Kratochvil for the opprotunity to work with him in the OH&SU Dental School and to Sean who brought Jim's intriguing problem to my attention. To Dr. Theresa Goodell, I give thanks for nursing me through the world of statistics.

I give thanks to all the people with whom I have had the pleasure and pain of insightful discussions. I thank Dr. Jessica Ramella-Roman, Dr. Paulo Bargo and Dr. John Viator who shared my early years. I am also thankful to other various students Dr. Dan Gareau, Kirstin Engelking, Dr. Yin-chu Chen, Jon Adams, Yongji Fu, Ravi, Patrick Roman, Deb Baker, Abe Janis, and Laurel Jones. I am thankful to Lisa Buckley for her encouragement. I must thank all the wonderful people who have come and gone through OMLC; for they have been a very supportive and wonderful group to work with. I also thank Rob Kalke, the original OMLC groupie for sharing great discussions over beer. And a hearty thanks goes to Tim Thomas, who not only provided complete SEM support, but also opened a

door towards employment.

Finally, I would like to thank my family who allowed me to grow to be what I am today. My parents, Chuck Moffitt and Cathy Kornmeyer taught me the value of an education and I am very thankful to all they have given me. I thank my brother John, who inspired me to always achieve more in life. I give thanks to my in-laws who supported and believed in my success. Last but not least, I am eternally grateful to my wife, Supriya, who did all the little things, in addition to encouragement and support while prodding me to the finish-line with this thesis.

Contents

List of Tables

List of Figures

Abstract

Fiber optics can facilitate a non-invasive means of tissue biopsy through optical inspection in small volumes to differentiate between normal and diseased tissue. Optical fibers provide a non-complex means to deliver and collect reflected light allowing for the determination of the absorption and scattering properties. These optical properties correlate with the chemical and structural state of the tissue. The arrangement of the emission and collection fibers dictates the volume of tissue that is optically sampled. Fiber-optic probes that sample the smallest possible volume by emitting and collecting their own backscattered light are investigated.

Two complimentary studies are presented that are necessary to provide the tools to evaluate the behavior of fiber-optic probes. First, a method to fabricate optically stable phantoms is investigated. The optical properties of the phantoms are defined at two wavelengths. Linear relations are given for the concentration of dyes and TiO_2 scattering agent that predict the absorption and scattering properties of the finished phantoms with less than 4% error. The phantoms are demonstrated to be stable over a period exceeding one year. Second, a combined inverse adding-doubling and Monte Carlo model is presented to evaluate the optical properties of the phantoms using integrating sphere measurements. The combined IAD/MC model is demonstrated to accurately determine optical properties of homogenous optically turbid samples with a reasonable precision using multiple sample thicknesses and sample port sizes for both single and double sphere experiments. The scattering is predicted with 1% error and absorption error is 2–4%. The nomenclature for integrating sphere measurements is simplified and rationalized using the concept of sphere gain to express the results. Explicit directions for determining sphere parameters were shown. Formulas were given that work for diffuse incidence or collimated incidence or any combination thereof.

A new kind of fiber optic probe, a sized-fiber reflectometry device is presented and investigated. Experimental studies are performed using phantoms with known absorption and scattering properties. A Monte Carlo model is developed to simulate the device

behavior to evaluate effects due to absorption scattering, scattering anisotropy, and optical sampling volume. The model is validated by comparison to experimental results. Both experiments and Monte Carlo simulations of the sized-fiber device indicate that 50% of the signal arises from roughly 1.2 and 1.9 reduced mean free paths for the 200 and 600 μm fibers respectively and that in general larger fibers sample deeper optically. Specular reflectance is shown to act as a noise source comparable in magnitude to the diffuse reflection signal for perpendicularly polished fibers and can be rejected with bevel-tipped fibers. The measurement variability decreases 6 fold to 4.5% on *in vivo* skin with a 200 micron fiber with the beveled-tip fiber and to 2.2% for a 1000 micron fiber with the beveled-tip fiber. The absorption and scattering sensitivity is presented for a bevel- tipped sized fiber device using a Monte Carlo generated grid to invert optical properties from the measured diffuse reflectance. The scattering coefficient could be predicted with an error of $1.5 \pm 0.2\%$ over the entire range of absorption and scattering properties. A second two-fiber probe design is investigated that uses two identical diameter fibers with only a single source fiber and both fibers collecting reflected light. The inversion of absorption and the reduced scattering is investigated using a heuristically determined closed form relationship from device simulations. The scattering coefficient could be predicted with a mean error of $\pm 4.3\%$. Typical error for absorption coefficient determination is shown to be between 50-100% for absorption less than $2\,\mathrm{cm}^{-1}$. The poor resolution of absorption is related to the mean optical path for collected light which typically is less than 2 mm for tissue.

A clinical study is presented using a dual 400 micron fiber probe to distinguish oral pigmented lesions caused by either melanin or dental amalgam. Two methods of discrimination were investigated. The first method used the spectral features of melanin in the 640–720 nm wavelength band. The pigmented lesions containing melanin exhibited a higher change in reflectance with respect to wavelength over this band in comparison to amalgam tattoos or non-pigmented sites. The sensitivity and specificity for identifying melanotic lesions from amalgam tattoo was 98% and 92% respectively. The second method of discriminating amalgam tattoo, melanin pigment and non-pigmented sites uses discriminant function analysis on uniformly spaced wavelength bands of reflectance to

simulate spectrally filtered reflected light. The sensitivity and specificity was 94% and 100% respectively for classifying melanin pigmented sites.

Chapter 1

Introduction

The purpose for this body of work is to develop a non-invasive and highly-localized method of performing a biopsy optically with fiber-optics. In order to achieve this goal, two parallel studies are presented that are necessary to characterize the fiber optic devices. First, a method for fabricating optically stable phantoms that mimic tissue with engineered optical properties is presented. Second, a technique that uses the integrating spheres in conjunction with inverse adding doubling for determining optical properties of the tissue-phantoms or any other homogeneous material in a slab geometry is presented for use as a gold standard method of establishing optical properties. An overview of the sized-fiber device from its original conception [1] is given in conjunction with basic performance. Corrections in the fiber design compensate for specular reflectance noise in single fiber measurements and increase sensitivity relating to absorption. Finally, a clinical study using the fiber device is presented showing the ability to distinguish pigmented oral lesions.

1.1 Fiber optic devices

The optical fiber provides a highly adaptable and low-cost means to interrogate tissue *in situ* using optical spectroscopy. The flexible nature of optical fibers provides a robust and convenient means to deliver and collect light. The versatility of fiber optic probes allows a consistent optical interface between the tissue and the instrumentation in numerous configurations. Fiber-probes have been developed using direct perpendicular contact with the tissue [2,3], offset from the tissue [3], and in side-firing (i.e. side-viewing) configurations [4, 5]. In addition to topical probe designs, the compact dimensions and

rigid structure of optical-fibers allows for insertion of fiber-probes through narrow tubular channels in devices such as endoscopes and catheters or through needles to penetrate into tissue structures for minimally invasive applications [5]. Finally, the optical sampling volume in tissue may be controlled by the selection of spacing between the emission and collection fibers. A goal of this work is to elucidate the design implications where the same fiber is used for both light delivery and collection giving the smallest possible optical sampling volume.

Due to the adaptability of fiber optics, they are widely employed in application of a variety of spectroscopic techniques. Optical biopsy (tissue diagnosis by optical spectroscopy) has been extensively studied over the last 15 years [3,6,7]. Several recent studies employed fiber optic devices to assess differences in optical properties derived from diffuse reflectance spectroscopy to discriminate normal and abnormal tissue in the esophagus [8,9], oral cavity [10], kidney [11], ovaries [12], colon [13], breast [14] and skin [15]. Diffuse reflectance spectroscopy has three modes of application: steady-state reflectance [16,17], time-resolved reflectance [18–20], and frequency modulated reflectance [21–23]. Other spectroscopic modalities include polarized reflectance [24–26], fluorescence spectroscopy [27, 28], and Raman spectroscopy (inelastic light scattering) [29, 30]. Though generally not used spectroscopically, imaging fiber bundles are commonly used in medicine (e.g., endoscopy or laparoscopy).

Though many modes are possible, I will limit the discussion here to diffuse reflectance spectroscopy, the mode used in this work. For each of the temporal methods of diffuse reflectance, the absorption and scattering properties of diseased and healthy tissue must be differentiated for diagnosis. Time-resolved measurements provide a robust determination of scattering properties given by time of delay between the input and collection of light and the fraction of light collected relates to the absorption [18, 31]. In the time domain, laser sources provide pulse lengths of less than 100 ps that provide adequate temporal resolution. Two options have been employed for detectors, streak cameras [32] and time correlated single photon counting [19]. The major drawback of time-domain measurements is the high cost of the light sources and detectors.

Frequency domain measurements contain the same information as time-domain measurements. In the frequency domain, the phase delay in the reflected pulse and amplitude reduction (modulation) are related to the scattering and absorption properties [21,33]. At frequencies below 300Mhz, the cost of instrumentation is considerably less expensive than time-domain techniques. Just as with time-domain systems, the sensitivity of frequency domain measurements increase with increasing source-detector separation; the phase shift increases with distance and the modulation falls below unity. The optimal source-detector separation is in the range of 1-2 cm [34]. Shorter source detector separation requires an increase in the frequency in order to resolve phase shifts in the collected light relative to the source, increasing the cost of instrumentation. When a single fiber is used for both emission and collection, the cost benefit of the frequency domain measurements versus time domain measurements is nullified at the frequencies necessary to resolve a phase shift.

Steady-state measurements convey less information than the time and frequency domain measurements since the measured attenuation contains no temporal information. The determination of scattering and absorption properties using steady-state measurements has historically relied upon spatially resolved reflectance measurements. Data is fitted into an analytical expression based upon diffusion theory [17, 20, 35–37]. Like frequency domain, the spatial distribution of measurements is optimal for source-detector separations greater than 1 cm. In the last decade, work has begun to determine optical properties from steady-state diffuse reflectance probes with source-detector fiber separations less than 1 cm with the drive to minimize the optical sampling volume.

Though many studies exist using spatially resolved diffuse reflectance, far less work exists that investigates diffuse reflectance probes with emission and collection fiber separations where the assumptions of diffusion theory no longer hold. In one of the first studies, Mourant et al. show that measurements made with separations between emission and collection fibers less than one mean free path-length are more sensitive to scatterer size (spheres) than at larger separations [38]. This is followed by a study showing the existence of a fiber separation that was nearly independent of scattering properties for optical properties in the range for tissues [39] which occurs with small fiber separation

distance. In the following year, the first description of a fiber device is proposed that used a single fiber both emission and collection of light for reflectance [1] and fluorescence [27]. Bevilacqua et al. present a fiber probe design to optically characterize a few cubic millimeters of tissue using spatially resolved measurements with source detector separation in the range of 0.3-1.4 mm in conjunction with a Monte Carlo model of light transport to extract optical properties. Two other significant fiber probe designs using small fiber separations have either several fibers [40] or two fibers [41, 42] and use *a priori* chromophore absorption spectra to establish relative chromophore content and the scattering properties within a small tissue volume.

1.2 Tissue optics

The optical characteristics of tissues are generally described by three parameters: the absorption coefficient (μ_a), scattering coefficient (μ_s), the scattering anisotropy (g). The refractive index (n) is a fourth parameter that does not characterize tissues since it is essentially a constant value [43].

The absorption coefficient describes the exponential decrease in irradiance I of a collimated beam of light through a homogenous medium over the distance d by

$$I = I_0 e^{-\mu_a d}$$

where the incident irradiance is given by I_0. The Beer-Lambert law defines this relationship, but also states that the absorption coefficient is proportional to chromophore concentration C,

$$\mu_a = C\sigma_a$$

where σ_a is the absorption cross-section.

The scattering mean free path between describes the average distance that a packet of photons will travel between scattering events. The scattering mean free path is the reciprocal to the scattering coefficient ($1/\mu_s$), the parameter of characterization. Ballistic light (unscattered) is described by

$$I = I_0 e^{-\mu_s d}$$

for a collimated source in a non-absorbing medium. Both the scattering and absorption coefficients have units of inverse distance (e. g., cm^{-1} or mm^{-1}). Scattering is also described by another parameter, the anisotropy, g that is the mean cosine of the scattering angle

$$g = \int_0^{2\pi} \cos\theta f(\cos\theta)\, d\cos\theta$$

where $f(\theta)$ is the scattering phase distribution function. The scattering anisotropy at $g = 0$ is isotropically scattered and at $g = 1$ light is completely forward scattered. In the visible and NIR spectrum, tissue has been shown to be strongly forward scattering with anisotropy in the range of $0.69 \leq g \leq 0.99$ [44]. Often, the scattering anisotropy is combined with the scattering coefficient defined as the reduced scattering coefficient marked with a prime

$$\mu_s' = (1 - g)\mu_s$$

that describes the effective reduced mean free path (mfp') between scattering events as if scattering is isotropic. Macroscopically, similar light distributions are obtained with the reduced scattering approximation in comparison to models that distinguish the anisotropy from the scattering coefficient, but the reduced mean free path has no real physical meaning.

An optical biopsy characterizes the optical properties of the tissue to determine the chemical or structural content of the volume of tissue being measured. The absorption coefficient is a composite of absorption by many individual chromophores. The major endogenous absorbers in the visible spectrum in tissue are oxy and deoxygenated hemoglobin, myoglobin, melanin, and bilirubin. In the NIR spectral region water and fat also significantly contribute to absorption [45]. The "therapeutic window" is considered to be between 600–1000 nm where absorption is low and optical penetration can be centimeters [46]. Below 600 nm, optical penetration is limited to a few millimeters before absorption by hemoglobin [47]. Much work has been done to quantify exogenous chromophores such as photodynamic agents to measure *in vivo* drug concentrations [48–50]. Information regarding the structural composition of tissue is imparted by the size, shape and concentration of the scattering particles. The average effective scatterer size can be determined

by the wavelength dependence of the scattering coefficient [51] or by single fiber reflectance measurements [52]. Spatially resolved reflectance can establish collagen fiber orientation by a two-fold change in the scattering coefficient with directional orientation of the fiber probe [53].

Complete optical characterization of tissue is rarely performed with a single device as a minimum of four measurements are necessitated to determine parameters. The refractive index is generally ignored as it has been shown to be relatively constant for many tissues with a value between 1.38-1.41 [43]. Microscopic variations of the refractive index account for scattering but a value of 1.40 is used for the average macroscopic refractive index of tissue throughout this thesis unless otherwise noted. To reduce the independent measures needed further, the reduced scattering coefficient is determined rather than separating the scattering anisotropy from the scattering coefficient. In total two parameters are determined, the absorption and reduced scattering coefficient from two independent measures of diffuse reflectance.

The main goal in this thesis is to develop an optical fiber probe to perform diagnostics based on the light absorption and scattering properties in the smallest possible volume of tissue. By focusing on a compact probe design, the range of minimally-invasive applications increase due to the ease that the device may be employed such as device insertion through a needle. Furthermore, it is desired that the optically sampled volume is kept smaller than the dimension of the features in the tissue of interest (e. g., lesions). The contents of this thesis is organized as follows.

In chapter 2, I describe a method for the preparation of a polyurethane phantom to simulate the optical properties of biological tissues at two wavelengths in the visible and near infrared spectral range. Molecular absorbers with relatively narrow absorption bands (FWHM 32 and 76 nm for Epolight 6084 and 4148 respectively) provide independent absorption at 690 nm for absorption up to $5\,\mathrm{cm}^{-1}$ and 830 nm for absorption up to $3\,\mathrm{cm}^{-1}$. Absorption by both dyes is linear in these respective regions and is consistent in polyurethane both before and after curing. The dyes are stable over long durations with no more than 4% change. The absorption of visible light by polyurethane decreases with time and is stable in less than one year with a drop of $0.03 \pm 0.003\,\mathrm{cm}^{-1}$ from 500–830 nm.

The scattering properties arise from the addition of TiO_2 particles to the polyurethane. These properties at 690 and 830 nm are related to the weight per volume. The variation in absorption and scattering properties for large batch fabrication (12 samples) is demonstrated to be ±3%. The optical properties of the phantoms did not significantly change over a period of more than one year which makes them suitable for use as a reference standard.

Chapter 3 describes a combined inverse adding-doubling and Monte Carlo model to extract the optical properties from measurements made using integrating spheres. Models used to extract optical properties of a sample from total diffuse reflection and transmission measurements made with integrating spheres overlook two effects that occur when integrating spheres are used. The first effect is that the sphere itself alters the measurements. Second is the effect of light that leaks out through the edges of the sample. An expression for the light collected for both single and double-integrating sphere experiments is derived. Correcting for the integrating sphere influence requires knowledge of the sphere wall reflectance; methods for measuring this are given. These equations may be used with any one-dimensional light transport model including Monte Carlo models. I present a theoretical framework for single and double integrating sphere measurements. These equations are the basis for a combined inverse adding-doubling and Monte Carlo model to invert optical properties from integrating sphere measurements. The method is tested for accuracy and precision using multiple sample thicknesses, multiple sample port dimensions for both single and double sphere arrangements. The standard deviation of optical properties for measurements with two sample thicknesses and 4 sample port sizes is 7% for absorption and 4% for scattering with double-sphere experiment. For single-sphere results the 6 sample ports sizes were measured for one sample giving a standard deviation of 5% for absorption and 2% for scattering. Absorption is shown to be resolvable down to $0.005\,\mathrm{mm}^{-1}$ with sample thickness of 10 mm. The absorption and reduced scattering coefficients are measured for a suspension of titanium dioxide in water over the wavelengths 400–1700 nm.

In chapter 4, the sized-fiber probe is introduced. Sized-fiber spectroscopy describes a device and method for measuring absorption and reduced scattering of tissue using

optical fibers with different diameters. The device used in this paper consists of two fibers with diameters of 200 and 600 μm. Each fiber emits and collects its own backscattered light. Backscattered light measurements for solutions with absorption coefficients of 0.1–2.0 cm^{-1} and reduced scattering coefficients of 5–50 cm^{-1} demonstrate that the device is most sensitive for the highest scattering materials. Monte Carlo simulations suggest the device is insensitive to the fiber illumination distribution and that the light returning to the fiber is nearly uniform over all directions. Finally, experiments and Monte Carlo simulations of the sized-fiber device indicate that 50% of the signal arises from roughly 1.2 and 1.9 reduced mean free paths for the 200 and 600 μm fibers respectively.

Chapter 5 considers the effects of specular reflections when a single fiber is employed to emit and collect light from an optically diffusing medium such as biological tissues. The light collected by the fiber consists of two components: diffusely scattered light from within the tissue and specularly reflected light from the surface. Only the diffuse reflection contains the desired information regarding the optical absorption and scattering properties of the tissue, but the specular component is comparable in magnitude to the diffuse reflection with visible light. The refractive index mismatch between the fiber and tissue account for a portion of the specular reflection. However, imperfect contact of the fiber with the surface of tissue creates additional boundaries and thus additional specular reflections. Experiments performed with a 200 micron diameter fiber and a 632.8 nm He-Ne source characterize the collection of specular reflections through the same fiber using water as a coupling medium. The collection efficiency measured for a fiber in imperfect contact shows the sensitivity of fiber angular tilt with the surface on a glass substrate (specular reflection only) and an epoxy resin tissue phantom (specular and diffuse reflection components). Next, the collection efficiency is measured for a separation between the fiber and the samples for perpendicular illumination to the surface, 14 degrees, and 25 degrees from the normal. Imperfect contact is demonstrated to vary the amount of specular reflection collected using a single fiber where changes in angle greater than 4 degrees or a separation between the fiber and the surface in excess of 400 micron caused a minimum of 7 percent reduction of the collected specular reflection.

In chapter 6, two dual fiber probe designs are tested for the purpose of determining the

absorption and reduced scattering properties of highly turbid media using bevel-tipped fibers. The first device is a sized-fiber probe with 200 and 1000 microns diameter fibers. Optical properties are determined using a Monte Carlo grid of diffuse reflectance for absorption coefficients between 0.1–5.0 cm^{-1}, scattering between 100–1000 cm^{-1} and the anisotropy constant at 0.9. The expected error for predicting scattering is less than 2% using linear interpolation between points on the grid. The error for predicted absorption is greater than 50% for absorptions less than 1 cm^{-1} due to the small mean optical path-length for collected light. A second probe is shown using dual 400 micron diameter fibers with one emitting fiber and both fibers collecting reflected light. Only minor difference exists in performance between the probes. The single emitting fiber fiber probe has more compact physical dimensions and a slightly longer optical sampling path-length (a 25-30% increase) relative to the sized-fiber probe. The Monte Carlo calculated mean optical path-length is 2.5 mm or less for the single emitter fiber probe. Relations are presented between the collected light and the absorption and scattering based on Monte Carlo calculations. However, the inversion of optical properties using linear interpolation of optical properties from a Monte Carlo generated grid demonstrated better performance than the empirically derived relations for the single emitting fiber probe, despite its greater mean sampling optical path-length. The optical properties of a polyurethane phantom are measured with the single emitting fiber probe and differ by a factor of 2 with the results measured using an integrating sphere.

Chapter 7 presents a clinical application of the dual 400 micron fiber probe to differentiate specific oral pigmented lesions in a pilot study as a non-invasive screening device. Pigmented oral lesions are biopsied to rule out the possibility of oral melanoma, a rare condition with poor prognosis. Pigmented oral lesions caused by implantation of dental amalgam (amalgam tattoo) or by natural racial melanin pigmentation are measured in thirty subjects. Two methods of discrimination are presented. In the first method, the content of melanin is related to the spectral slope in the 640–720 nm wavelength band and a threshold is used to differentiate pigments. The receiver operator characteristic (ROC) curve for various threshold values is reported independently for each optical fiber measurement. A sensitivity of 98% was obtained with a specificity of 92% with a slope

threshold of -0.0017 for the collection fiber to identify melanin sites. The second method of analysis used the reflectance spectra obtained in the clinic to simulate data collected using either spectral filters or LED sources centered at 11 wavelengths from 450-700 nm. Separation of three groups: amalgam tattoo, melanin pigment and non-pigmented sites is performed using discriminant function analysis. The discriminant functions are created using two-thirds of the measurements to determine the classification functions and the remaining third of the measurements to evaluate the correct determination of the groups by the these functions. 94% of melanin pigmented lesion were correctly classified with 6% (one measurement) falsely attributed as amalgam. 53% of melanin sites were correctly classified with the remaining classified falsely as non-pigmented sites. 90% of non-pigmented sites were correctly classified as non-pigmented with all false attributions being classified as amalgam tattoo.

Chapter 2

Preparation and Characterization of Polyurethane Optical Phantoms

2.1 Introduction

Phantoms that simulate the optical characteristics of tissues are commonly used to mimic light distributions in living tissue. Tissue phantoms are often designed and utilized for three purposes: to simulate light distributions with a geometry of physical tissue [54], for the calibration of optical devices [13, 55], and for recording a reference measurement with an optical measurement device [56]. For all three uses, the absorption and scattering properties of the created tissue phantom is the primary design factor. Optical tissue phantoms are necessary to calibrate any optical measurements on real tissues to establish quantitative information [13]. Optical device calibration requires using several phantoms with the optical properties that span the typical range of the tissue to be simulated. Furthermore, phantoms that are optically stable are also suitable for use as a reference measurement taken in conjunction with measurements on living tissues.

Several types of phantoms to mimic the optics of human tissue have been described in the literature including homogenized milk [57], non-dairy creamer [58], wax [59], and a blood and yeast suspension [60]. Suspensions of oils/fats in an aqueous solution such as Intralipid [61] and a water soluble dye (India ink [62]) appear to be the most commonly

This chapter was originally published under the title, "Preparation and characterization of polyurethane optical phantoms" by T. P. Moffitt, Y. Chen and S. A. Prahl in *Journal of Biomedical Optics*, Vol. 11(4), 041103, 2006.

used phantom materials. Difficulties arise in creating inhomogeneities using liquid phantoms such as layered structure. A desire for solid phantoms led to the development of suspensions of Intralipid and India ink in agar [63], agarose [64] and polyacrylamide [65] that could be cut and shaped to provide inhomogeneities in the phantoms. The inclusion of inhomogeneities limited the selection of dyes used to waterproof inks to prevent diffusion of dyes between regions [63]. However, these phantoms mostly suffer from relatively short useable lifetimes which are usually limited to no more than two months.

More robust phantoms made of rubbers or plastics have been described that give long-term optical stability and greater shaping flexibility. Phantoms compositions of silicone [54, 66], polyester [67, 68], polyurethane [69], and epoxy resin [70] have been described. There may be no great advantage of one material over another. For example, silicone more closely matches the mechanical properties of tissue and may be cast into arbitrary shapes, whereas epoxy, polyurethane, and polyesters are easier to machine after casting. Typically, the selection of a material is determined by the choice of absorbers and their stability in that medium.

The choice of scattering agents in solids is usually limited to aluminum oxide (Al_2O_3) [54, 66], titanium dioxide [67], and silicon dioxide [68, 70], polyester [54], polystyrene, or latex microspheres. Mie theory can be used to predict the scattering properties of microspheres with knowledge of the relative refractive index, size distribution and number density. Unfortunately, microspheres tend to be much more expensive than aluminum oxide or titanium dioxide particles. One primary difference between aluminum oxide and titanium dioxide particles may be the maximum attainable value for g (the cosine for the mean angle of scattering) which describes the scattering anisotropy; Firbank and Deply found that TiO_2 is limited to $g = 0.7$ whereas Al_2O_3 can reach $g = 0.97$ in polyester resin [67]. Arridge et al. [71] has shown that any arbitrary scattering angle distribution can be theoretically matched using an appropriate distribution of particle sizes.

Our goal was to make durable stable optical phantoms with predefined optical properties at two wavelengths, 690 and 830 nm that are commonly used for oximetry [72, 73]. To our knowledge, previous phantom designs have been developed for a single wavelength or for use with a single broadband absorbing dye that determines the absorption spectrum. I

wanted to use component materials that would be photostable. Moreover, the dyes needed to have absorption spectra with minimal overlap. Two problems during initial material selection experiments were encountered . First, dyes that absorb strongly at 830 nm also exhibited comparable absorption at 690 nm and second, dyes that bleached during the curing process of the binding medium. The dyes selected for our phantoms determined the bulk material used to suspend the dyes and scatterers.

A method is needed to determine the scattering characteristics of the phantoms. Inverse adding-doubling (IAD) was used to find the scattering and absorption of a slab of turbid material using total reflection and total transmission measurements. This method is applicable to homogeneous turbid slabs with any optical thickness, albedo, or phase function. The slab may have a different index of refraction from its surroundings and may or may not be bounded by glass. The optical properties are obtained by iterating an adding-doubling solution of the radiative transport equation until the calculated values of the reflection and transmission match the measured ones. Alternatively, spatially [4,17,37] and/or temporally [23,74,75] resolved measurements of diffuse light distributions can also be used to quantitatively determine absorption and reduced scattering coefficients.

A method for fabricating solid optical tissue phantoms that are castable and photostable is presented. These optical phantoms are designed to be suitable reference standards at two distinct wavelengths and whose optical properties have been carefully measured. The final materials were verified by making several optical phantoms with differing quantities of dye and scattering particles. Phantoms made without added scatterers were made to verify the stability of the dyes' absorption properties before and after the curing process and over a duration of 14 months.

2.2 Materials and Methods

2.2.1 Component material selection

The optical phantoms consist of three components: the polyurethane, the absorbing chromophores, and the scattering agent. Selection of the three primary components were driven by our choice of absorbing dyes.

A phthalocyanine dye (Epolight 6084, Epolin Inc., Newark, NJ) was used as the absorber at 690 nm. The absorption at 830 nm was achieved using a palladium dye (Epolight 4148). The dye manufacturer listed these dyes for use in optical filters and laser goggle applications and suggested polyurethane as a casting material. I verified that both dyes lost their absorption during the curing process in epoxy resin (Marine grade epoxy resin, Side A 314 resin and Side B 109 hardener, Tap Plastics, Inc., Dublin CA). Both dyes exhibit narrow absorption bands (FWHM 32 and 76 nm for Epolight 6084 and 4148 respectively) that allow nearly independent absorption at the wavelengths 690 nm by Epolight 6084 and 830 nm by Epolight 4148 when cured in polyurethane (Figure 2.1). Titanium dioxide (Ti-Pure R-900, Dupont Chemicals, Wilmington, DE) was assumed to behave as a pure scatterer with negligible absorption between 650 and 850 nm. Finally, a two part polyurethane system (WC-781 A/B, BJB Enterprises Inc., Tustin, CA) that had a 30 minute pot life was used to suspend the titanium dioxide and absorbing dyes. This polyurethane is a clear rigid casting resin that was designed to be tintable and pigmentable. This polyurethane was formed by mixing part "A" with part "B" in a ratio of 100/85 by weight (100/88 by volume). The pot life for the polyurethane was a convenient duration because it allowed sufficient time to mix and de-gas but still cured quickly enough that no apparent settling of the scatterers took place. The viscosity of the mixed polyurethane was 650 cps. The demolding time was 24 hours. Optical measurements could be made at 24 hours. However, complete curing of the polyurethane required 5-7 days at room temperature or 16 hours at 71–82 degrees C.

2.2.2 Initial studies

Absorber characterization

The absorption coefficients as a function of dye concentration were measured in cured polyurethane (WC-781 A/B, BJB Enterprises Inc., Tustin, CA). Stock solutions of the two powdered dyes were prepared in xylene with concentrations of 6.64 mg/mL of Epolight 6084 and 1.56 mg/mL of Epolight 4148. Stock solutions of the dyes were pipetted and mixed in 5 quantities of 15, 25, 35, 40, and 45 μl of Epolight 6084 stock into 10 ml of polyurethane part A and 5 quantities ranging 50 to 250 μl in 50 μl increments of Epolight

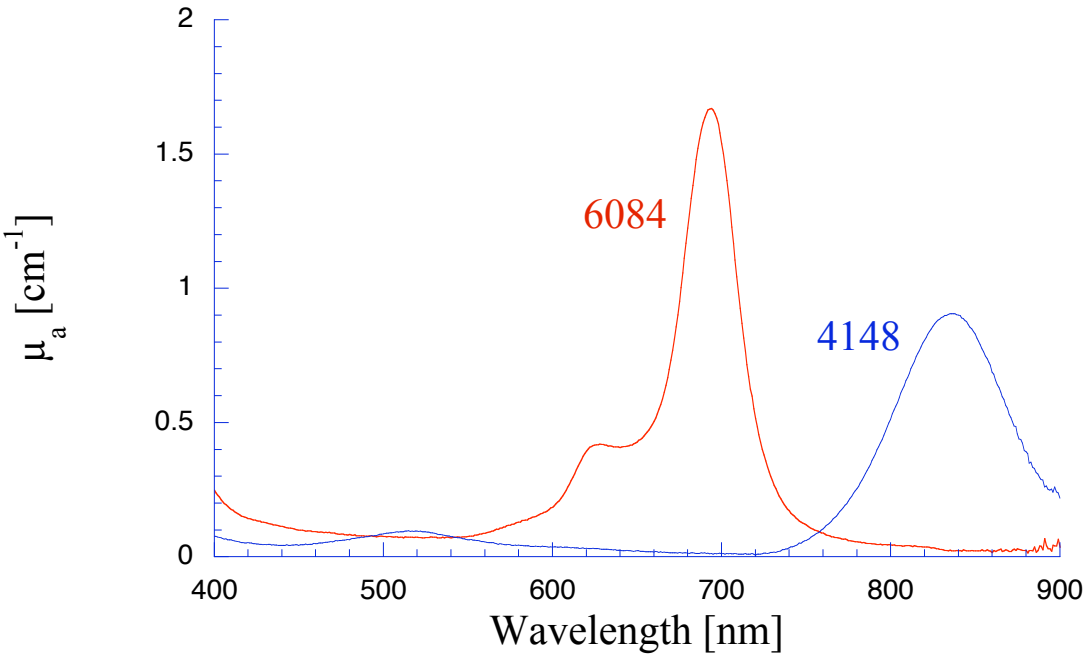

Figure 2.1: The absorption coefficient spectra of 10 μg/mL Epolight 6084 in polyurethane and 17 μg/mL Epolight 4148 in polyurethane.

4148 stock into 8.8 ml of polyurethane part B. The absorbance of each concentration of Epolight 6084 in part A was measured using a dual beam Cary 100 Bio Spectrophotometer (Varian Scientific Instruments Inc., Walnut Creek, CA) with a cuvette of polyurethane part A in the path of the reference beam. Likewise, the absorbance of Epolight 4148 for each concentration was measured with a cuvette of polyurethane part B in the reference beam path. Then the two parts of the polyurethane were randomly combined with the concentration of dye in part A randomly assigned to each concentration of dye in part B. The samples are thoroughly mixed together and poured into 1 cm cuvettes. Degassing of the mixtures was performed by placing the samples into a desiccator/vacuum chamber (Nalgene 5311 desiccator, Nalge Nunc International, Rochester, NY) that was connected to a vacuum pump (Speedivac 2, Edwards High Vacuum Int., England) capable of reducing the pressure to less than 1 mbar. After full curing, the absorbance of the cuvettes was measured on the Cary spectrometer. These measurements used polyurethane without added absorbers cured in an identical cuvette in the reference beam path.

A difference of absorbance measurements with the Cary spectrophotometer were used to determine the absorption coefficient of polyurethane. Two samples of polyurethane were cast without any added absorbers, one as a thin slab and another as a tall cylinder. After 48 hours of curing, the samples were removed from their respective molds. The surfaces of each sample was hand polished starting with 9 micron grit aluminum oxide sandpaper (AngstromLap, Fiberoptic Center, Inc., New Bedford, MA) and finishing with 0.3 micron grit paper to create an optically smooth surface. The final thickness of the slab and cylinder of polyurethane were respectively 0.41 and 3.44 cm. The difference between the two samples relative to air (i.e. nothing in the reference beam path) produced a lower noise signal than when the thin slab was placed in the reference arm of the spectrometer and the cylinder in the sample arm.

Titanium dioxide scattering

A stock solution of titanium dioxide consisted of 20.0 grams of titanium dioxide suspended in 60 mL ethanol. Before dilution into the polyurethane, the titanium dioxide stock solution was shaken by hand then sonicated for at least five minutes to ensure

complete suspension of TiO_2 particles. To test the scattering coefficients of different concentrations of titanium dioxide in polyurethane, different amounts of TiO_2 stock solution were added into polyurethane in two separate batches. The first batch had two samples with a TiO_2 concentrations of 2.5 and 5 mg/ml; I added 3.84 μg/ml of Epolight 6084 dye and 3.11 μg/ml of Epolight 4148 dye for final absorption coefficients, $\mu_a^{690} = 0.74\,\mathrm{cm}^{-1}$ and $\mu_a^{830} = 0.19\,\mathrm{cm}^{-1}$ to both samples. For the second batch consisting of two samples with TiO_2 concentrations of 0.5 and 1 mg/ml, I added 7.69 μg/ml of Epolight 6084 dye and 1.56 μg/ml of Epolight 4148 dye for final absorption coefficients, $\mu_a^{690} = 1.17\,\mathrm{cm}^{-1}$ and $\mu_a^{830} = 0.11\,\mathrm{cm}^{-1}$ to each sample. From each sample in both batches, a small portion of the final mixture was poured into a weighing boat, degassed for about 8 minutes. This provided a thin disk used for the inverse adding-doubling method. The inverse adding-doubling (IAD) method (described in a later section) was used to characterize the scattering coefficient for each of the above samples.

Scanning electron microscopy was used to evaluate the size distribution of the TiO_2 particles. Three samples were prepared by diluting the stock solution of TiO_2 with additional ethanol. A 5 μl drop of the diluted stock was pipetted onto a clean microscope cover slip and allowed to evaporate leaving a film of TiO_2 particles. The horizontal width of 112 randomly selected particles was measured from 5 separate SEM images using ImageJ software. The scale bar was used to establish the width of a pixel within each image.

2.2.3 Phantom design

Our two wavelength phantoms had four variables to specify (μ_{a,λ_1}, μ_{a,λ_2}, μ'_{s,λ_1}, and μ'_{s,λ_2}) but only three free parameters since the reduced scattering coefficients at the two wavelengths are related by the use of a single scattering agent. In other words, the optical properties at the first wavelength could be selected but, the reduced scattering at the second wavelength has a constant proportional relationship to the reduced scattering at first wavelength with respect to scatterer concentration. To compensate, the desired optical properties were condensed into three parameters μ_{a,λ_1}, μ_{a,λ_2}, and the reduced

albedo at the second wavelength (a'_{λ_2}). The reduced albedo was defined by

$$a'_{\lambda_2} = \frac{\mu'_{s,\lambda_2}}{\mu_{a,\lambda_2} + \mu'_{s,\lambda_2}}$$

The desired absorption and reduced scattering properties at the second wavelength (830 nm) would be modified by the following method which kept the reduced albedo constant for λ_2. A flow chart of this process was diagrammed in figure 2.2. The wavelength dependence of the reduced scattering coefficient for our TiO_2 particles was determined using IAD and fit by the equation $\mu'_s = (5.2\,\mathrm{cm}^{-1})(\frac{\lambda}{1000\,\mathrm{nm}})^{-0.8}$. The effective reduced scattering coefficient at 830 nm was calculated given the desired reduced scattering coefficient at 690 nm. The modified absorption coefficient was calculated using the desired reduced albedo and the dependent reduced scattering coefficient at 830 nm.

2.2.4 Fabrication method of tissue phantoms

The optical properties of the tissue phantoms were chosen to represent a range of different optical properties at the 690 and 830 nm wavelengths. The absorption coefficient at these two wavelengths would be varied to correspond to physiologic relevant values for the sum total of contributions by a fractions of water, oxygenated and deoxyhemoglobin and a wavelength constant background absorption. For all the phantoms, the scattering coefficient would be held constant. However, the wavelength dependence of the scattering from TiO_2 differs from tissue in that the ratio of scattering coefficients at 690 nm to 830 nm for TiO_2 does not equal the target ratio for tissue. To account for this effect, the target absorption coefficients at 830 nm were adjusted as described in the previous section. Finally, a single set of optical properties was used to make twenty identical phantoms.

The sequence for phantoms preparation was as follows using the stock solutions of dye and TiO_2 described above. Cylindrically-shaped phantoms 7 cm in diameter and about 5 cm in height were cast. This corresponded to ~200 mL polyurethane by mixing 113.4 g of part A and 97 g of part B. In addition, an extra 5.3 g of part A and 4.5 g of part B was prepared for making thin slab for optical property characterization. The proportions of each part of polyurethane was determined by weight and the addition of either dye or TiO_2 were neglected since their contribution was less than 1 part in 200 for all phantoms.

Absorbers were added to the polyurethane in part A while the scatterers were mixed to part B. Since the scattering of all phantoms were to be identical, 11 ml of TiO_2 stock was mixed into 2628 g of part B polyurethane which was sufficient quantity for all phantoms.

Part A of the polyurethane (118.8 g) was weighed out for a single phantom into a polyethylene container. Stock of Epolight 4148, the near-infrared dye was first pipetted into part A and stirred in with a glass rod until visibly homogenous. This dye had a pale violet tint when mixed into the polyurethane but was not noticeable after the addition of the Epolight 6084 stock which produces a strong turquoise blue tint. When both dyes are homogeneously stirred into part A, about 2 ml was placed in a cuvette for an absorbance measurement on the Cary Spectrometer using a cuvette of part A polyurethane without dye in the reference arm to verify proper absorption attenuation.

At this point, 5.3 g of the part A with dye was set aside in a plastic weigh boat dish. The remaining portion of polyurethane part A with dye was weighed again to calculate the appropriate quantity of the part B with TiO_2 to be added by weight. While on the scale, part B was poured into part A. The final amount of Part B was added drop by drop using a wooden tongue depressor. The large flat area of the tongue depressor allowed drops to be controlled so that weight of any drops could be controlled with precision of about 0.03 g. The polyurethane is thoroughly mixed using a tongue depressor to scrape the container sides/bottom and stir for about 2 minutes. Most of the mixture was then poured into 16 oz. HDPE molds (16 oz specimen containers, Fisher Scientific International, Inc., Fair Lawn, NJ). The remaining material was poured into two plastic weighing-boats to cast thin disks of differing thickness and about 6 cm in diameter. The set aside 5.3 g of polyurethane part A and dye was treated identical as above, except it had 4.5 g of transparent part B added to it. Also these samples were mixed then poured into 1 cm pathlength cuvettes for casting.

It was necessary to remove entrapped bubbles in the polyurethane introduced by the mixing of components together. Up to five phantoms or weigh boat slabs could be degassed at a time. This restricted us to mixing no more than two sets of optical properties together at a single time since for each set, a phantom and two slabs were made. The second second set was mixed while the first set was degassing. Degassing was done by placing the samples

in a desiccator/vacuum chamber (Nalgene 5311 desiccator, Nalge Nunc International, Rochester, NY). The chamber was connected to a vacuum pump (Speedivac 2, Edwards High Vacuum Int., England) capable of reducing the pressure to less than 1 mbar. Samples were degassed for about 8 minutes at which time bubbles stopped forming.

After degassing, the phantoms were set onto a level surface and covered. The phantoms were solid after 24 hours and could be removed from the mold. However at 24 hours, the polyurethane is relatively soft, such that fingerprints can be embedded on the surface with moderate pressure. In general, a period of 48 hours passed before removing the samples from the casting mold. The phantoms in the specimen container molds were removed by flexing the walls of the container and then pushing on the bottom while holding the phantom upside down. The samples cast in weigh boats were removed by peeling the weigh boat which tore away from the polyurethane.

The phantoms were finished by leveling the top surface of the polyurethane block. A lathe was used to mill the meniscus lip from the top of each phantom until the shiny surface was completely removed. Then each phantom was sanded by hand in two steps: rough finishing with 200 grit wet sandpaper and fine finishing with 600 grit wet sandpaper. In each sanding step, the paper was wet with water and placed on a glass surface while the polyurethane block was sanded in a circular motion. Elimination of visible surface scratches were used as a completion condition.

2.2.5 Testing of phantom optical properties

Absorption of each phantom was measured using the Cary spectrometer 48 hours after casting. The clear samples cured in cuvettes for each phantom were measured referenced to cured polyurethane without dyes in a cuvette. Four absorbance measurements of each sample were recorded. Additional measurements of the same cuvette samples were recorded 13 and 14 months later to establish long term stability.

Inverse Adding-Doubling (IAD) was used to find the scattering and absorption of a slab of turbid material using total reflection and total transmission measurements. Two measurements on each of the two thin slabs for each phantom were made. Total diffuse

reflection measurements were made using an 203.2 mm diameter integrating sphere (IS-080-SF, Labsphere, Inc., North Sutton, NH) with a 12.7 mm diameter detector port and a 31.75 mm diameter sample port with a baffle between ports. Light was guided to the phantom disk through a 400 micron diameter optical fiber (0.22 numerical aperture) placed about 4 mm above the sample centered with the port hole. A 4 mm diameter steel tube coated with multiple coats of flat white paint was used to sleave the fiber through a 6.35 mm top port down to the phantom disk. An Oriel mercury lamp was used for the source and a 600 micron diameter (0.38 numerical aperture) delivered light from the integrating sphere to a scanning grating detector system of a Fluorolog-3 spectrofluorometer (Instruments S.A., Inc., Edison, NJ). Signals above 850 nm were often poor as a consequence of lower power from the lamp at longer wavelengths and lesser efficiency of the photomultiplier tube above 800 nm. The detector fiber was connected to the integrating sphere using an SMA connector surrounded by white shielding in the 12.7 mm port. Measurements were referenced to a 99% Spectralon reflectance standard (Labsphere, Inc., North Sutton, NH) and a dark measurement where the sample port was open and the fiber illuminating black felt on the optical table 254 mm below the port. Four measurements were made on each disk; two measurements on each side. The phantom disks were placed flush with the sample port. Figure 2.3 shows the sphere measurements for total reflection and figure 2.4 shows the reference sphere calibration measurements.

Total diffuse transmission measurements were made with another identical integrating sphere. In this set-up only two ports were open, the 25.4 mm diameter sample port and 12.7 mm diameter detector port with a baffle between ports. For this arrangement, the phantom disk was placed on the top port and light was collected with the same detector 600 micron diameter fiber described previously. Light was delivered to the phantom disk with the 400 micron fiber. The end of the fiber was positioned just above the phantom disk ($<$ 1 mm) centered with the port hole. Again, four measurements were recorded on each disk; two measurements on each side. Measurements were referenced to 100% with the fiber illuminating the open port hole and a dark measurement with an open port but the fiber removed from the sample porthole. Figure 2.5 shows the sphere arrangement for total diffuse transmission measurements.

Two other values were needed to calculate the scattering properties. The thickness of each phantom disk was measured using a depth gage (ID-C112EB, Mitutoyo Corp. Japan). The refractive index of the cured polyurethane was measured at 670 nm using an Abbé refractometer as 1.468. A negligible change in the refractive index over the spectral range of 500 to 900 nm was assumed.

The total diffuse reflectance and transmittance measurements in terms of percentage at all wavelengths were input into the IAD program. The total diffuse reflection was calculated using

$$r_{sample} = \frac{P_{sample} - P_0}{P_{std} - P_0}$$

The total diffuse transmission was calculated using

$$t_{sample} = \frac{P'_{sample} - P'_0}{P'_{std} - P'_0}$$

The batch variability was measured on twelve out of twenty phantoms from a single batch to establish the variability in our fabrication method. A thin slab was cut and sanded flat from twelve of the phantoms. The thickness of each slab was measured with a depth gage. Total diffuse reflection and transmission measurements were recorded for each of the twelve slabs along with reference measurements as previously described. Inverse adding-doubling was used to determine the absorption and reduced scattering coefficient for each slab over the wavelength range of 650–850 nm.

2.3 Results and Discussion

2.3.1 Absorption characterization

Both dyes exhibit stable absorption properties in polyurethane after a period of 14 months from casting. The visible/NIR spectrum for the absorption coefficient of Epolight 6084 and 4148 is shown in figure 2.1. The absorption coefficient at 690 nm relates only to the concentration of Epolight 6084 (C_{6084}) by the relation

$$\mu_a^{690} = a_1 C_{6084} + \mu_{a0}^{690} \tag{2.1}$$

where $a_1 = 0.16\,\mathrm{cm}^{-1}\mathrm{mL}/\mu\mathrm{g}$ and $\mu_{a0}^{690} = 0.019\,\mathrm{cm}^{-1}$ is the absorption coefficient for polyurethane at 690 nm after 13 months when the Epolight 4148 is present at a concentration

less than 21 μg/mL. Likewise, when Epolight 6084 is less than 16 μg/mL, the absorption coefficient at 830 nm depends solely on the concentration of Epolight 4148 (C_{4148}) by the linear relation

$$\mu_a^{830} = a_2 C_{4148} + \mu_{a0}^{830} \tag{2.2}$$

where $a_2 = 0.065\,\mathrm{cm}^{-1}\mathrm{mL}/\mu\mathrm{g}$ and $\mu_{a0}^{830} = 0.013\,\mathrm{cm}^{-1}$ is the absorption coefficient for polyurethane at 830 nm after 13 months. The linear relations for the absorption coefficient are applicable for Epolight 6084 up to a concentration of at least 32 μg/mL and for Epolight 4148 up to 45 μg/mL. A comparison of the absorption from each dye in solution in one part of the polyurethane and then after casting is shown in figure 2.6 for Epolight 6084 and figure 2.7 for Epolight 4148. The absorption spectrum of both dyes was unaffected by curing.

The tissue phantoms are limited by a minimum intrinsic absorption coefficient that is due to the absorption the of the binding medium. The absorption coefficient of polyurethane at a time point one week after casting is greater than after 13 months from casting as shown in figure 2.8. The change of absorption at these time points is $0.03 \pm 0.003\,\mathrm{cm}^{-1}$ over the wavelength range of 500–835 nm. The polyurethane absorption is stable between 13 and 14 month time points, but it is not known how gradual or when exactly the drop in absorption occurred between the one week and 13 month time points. The polyurethane exhibited less absorption than two other resins (an epoxy resin and a polymer resin) which showed significant absorption occurring below 500 nm thus giving each a yellow tint as shown in figure 2.8.

2.3.2 Scatterer characterization

The scattering coefficients were determined from diffuse reflection and transmission measurements. A typical spectra is shown in figure 2.9. This illustrates the wavelength separation in the absorption of the two dyes in the reflected and transmitted light. The reduced scattering coefficient as a function of wavelength (figure 2.10) was obtained using inverse adding-doubling using the total diffuse reflection and transmission measurements shown in figure 2.9. For comparison, the absorption coefficient obtained from a spectrometer measurement of a sample without titanium dioxide is also shown in figure 2.10

with the absorption coefficient calculated by IAD. The reduced scattering coefficient, μ_s' relates to the scattering coefficient (μ_s) and the cosine of the mean angle of scattering (g) from the incident direction of light by the equation $\mu_s' = (1-g)\mu_s$. The reduced scattering coefficient is an equivalent optical parameter that is one over the mean free path between scattering events when the scattering phase function is isotropic. Since, two measurements are recorded, only absorption and the reduced scattering coefficient can be determined. The anisotropy and the scattering coefficient, μ_s were not determinable separately with another measurement of ballistic photons. Our slabs (ranging from 2–7 mm) were sufficiently thick that all transmitted light was completely diffuse.

The derived scattering properties for the titanium dioxide follow the relations

$$\mu_{s,690}' = a_3 C \tag{2.3}$$

$$\mu_{s,830}' = a_4 C \tag{2.4}$$

where $a_3 = 8.0\,\mathrm{cm}^{-1}$ mL/mg, $a_4 = 6.6\,\mathrm{cm}^{-1}$ mL/mg and C is the concentration of the titanium dioxide. The different slopes correspond to the altered scattering efficiencies of the titanium dioxide particles at 690 and 830 nm. The size distribution of the titanium dioxide particles is shown in figure 2.11 having a mean of 340± 90 nm. By approximating the particles as spheres, Mie theory was used to predict the scattering anisotropy for the average particle size. Three-fourths of all particles were between 250 and 400 nm in diameter. An average of the g-value calculated in 10 nm increments across the range 250 and 400 nm in particle diameter is $g = 0.51$ at the 690 nm wavelength and $g = 0.52$ at the 830 nm wavelength.

2.3.3 Phantom optical properties

A set of ten optical phantoms were made with differing levels of absorption but with the same scattering properties. The variation among the ten phantoms in the scattering coefficient at 690 and 830 nm is shown in figure 2.12. The measured absorption coefficients at 690 and 830 nm of the ten samples are shown relative to the predicted absorption from equations 1 and 2 in figure 2.13. The difference between predicted and the measured

absorption coefficients for the ten phantoms was plus or minus 3 percent at 690 nm and 6 percent at 830 nm.

The reproducibility of a phantom with a single set of absorption and scattering properties is shown in figures 2.14 for twelve phantoms made from a single batch. Both absorption and scattering varied by plus or minus 3% between 600 and 800 nm. Between 500 and 600 nm, the percentage absorption variation increases but the absolute error remains constant. At wavelengths longer than 800 nm, the error increased (as previously stated) due to lamp power and decreased detector efficiency. Since both the Epolight 6084 and 4148 were mixed together in one part of the polyurethane and titanium dioxide to the other part before combining the two parts, the actual percentage variation in absorption at 830 nm should be comparable to that at 690 nm. Since all twenty phantoms come from a single large batch where all the dye was added to Part A of the polyurethane and the TiO_2 was added to part B for all twenty samples, then the variation in the samples can only come from 2 sources: weighing errors for the combination to the two parts of polyurethane or inhomogeneities in our large solutions of components. The largest weighing error was less than 2% for all phantoms including the ten with different absorption properties.

To minimize error due to inhomogeneities, the part of the polyurethane with TiO_2 was regularly stirred to prevent settling of the scatterers before mixing with the part with the added absorbers. However after combining the two parts of the polyurethane together, the phantom cannot be stirred once the degassing step begins. Samples were held under vacuum at a minimum of eight minutes but may be degassed for 10-12 minutes. Though the pot life of the polyurethane was a half-hour, by 30 to 45 minutes the polyurethane was still liquid but warming and noticeably beginning to gel. It is doubtful that full degassing of phantoms can be performed with a pot-life less than half an hour since gelling of the polyurethane will inhibit gas from escaping. It took about 5 hours to make all twenty phantoms with two people working. The timeliest part of the process was degassing due to a space limitation of only being able to place 4 or 5 phantoms in a vacuum chamber.

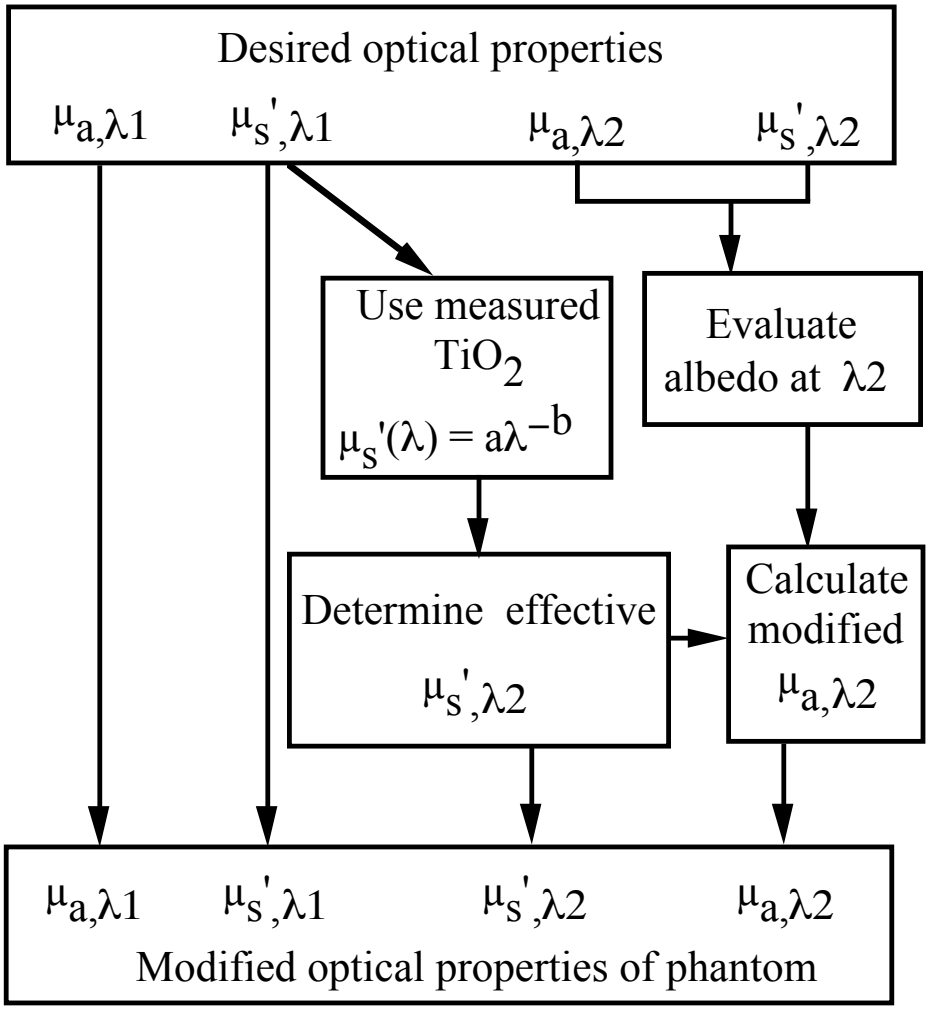

Figure 2.2: Process for maintaining the four desired optical properties with only three independent variables. The reduced scattering of the first wavelength establishes the reduced scattering at the second wavelength. A new absorption coefficient is calculated at the second wavelength that holds the desired reduced albedo at the second wavelength constant relative to the new optical properties.

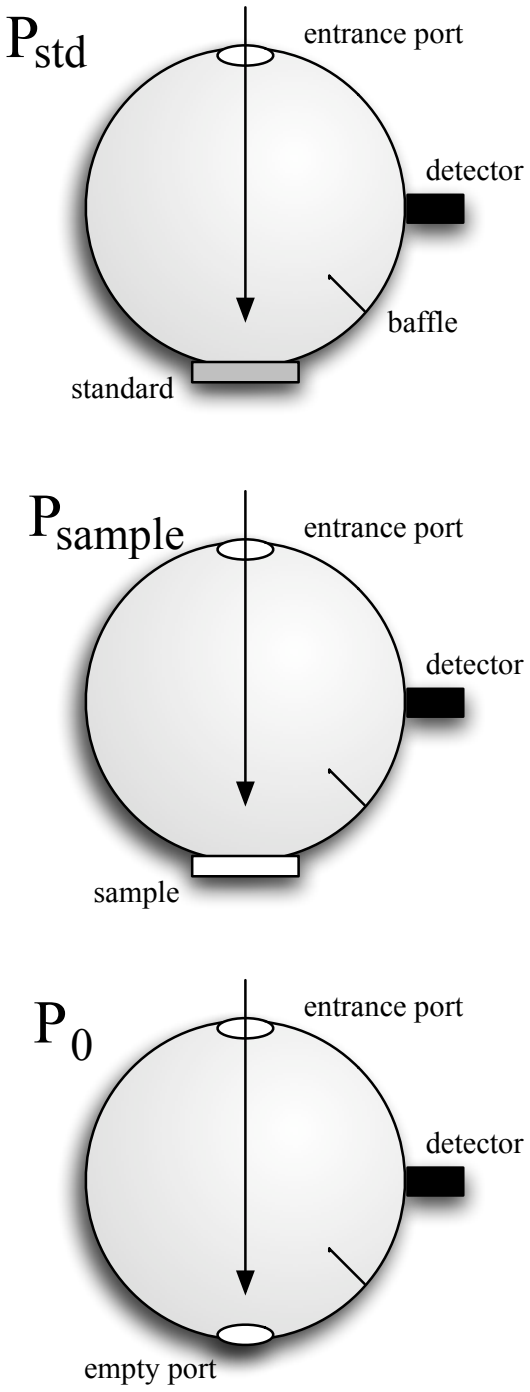

Figure 2.3: Diagrams of various integrating sphere reflectance measurements that are needed.

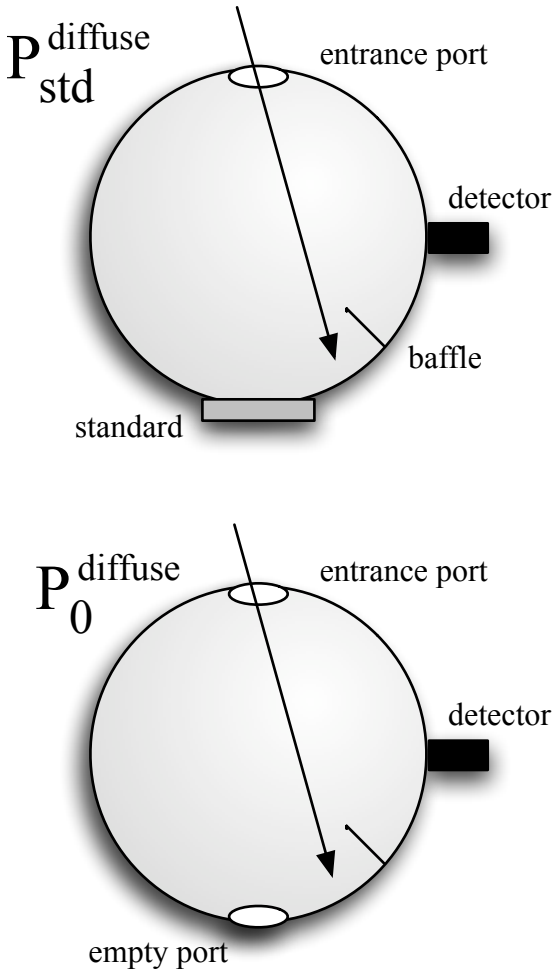

Figure 2.4: Diagrams of various measurements needed to determine the fraction of diffuse illumination f and the sphere parameter γ.

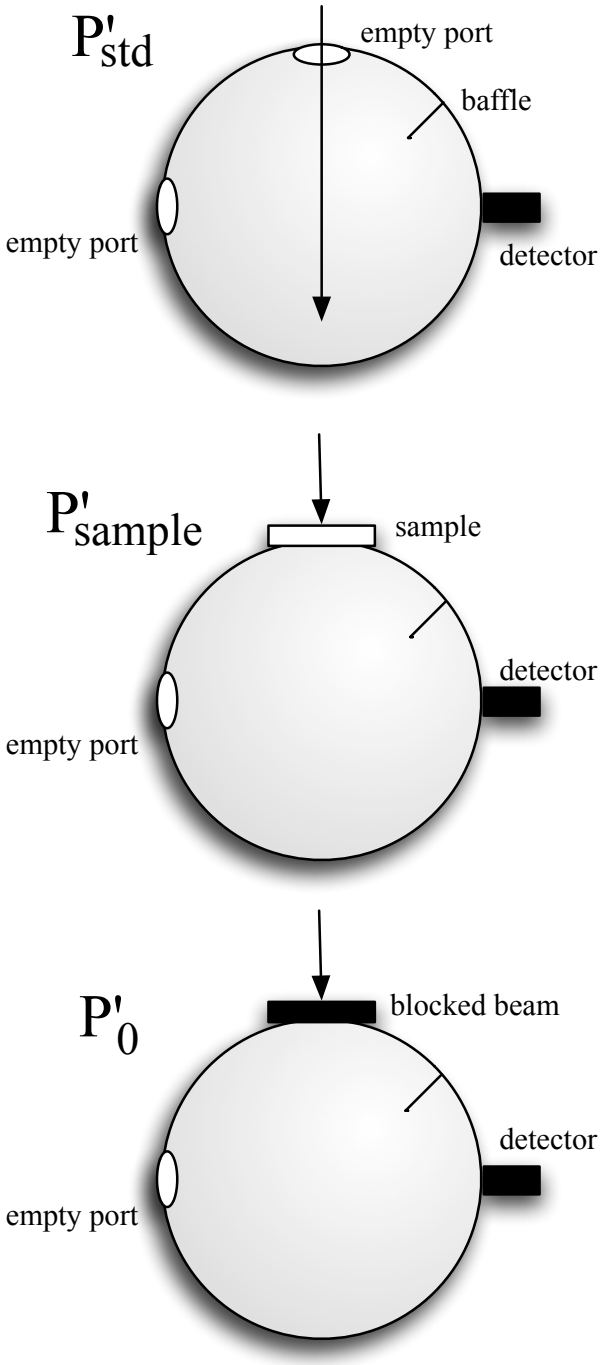

Figure 2.5: Diagrams of various integrating sphere transmission measurements that are needed. The empty port on the bottom of the spheres should be identical to the size of the entrance port in the sphere reflection measurements.

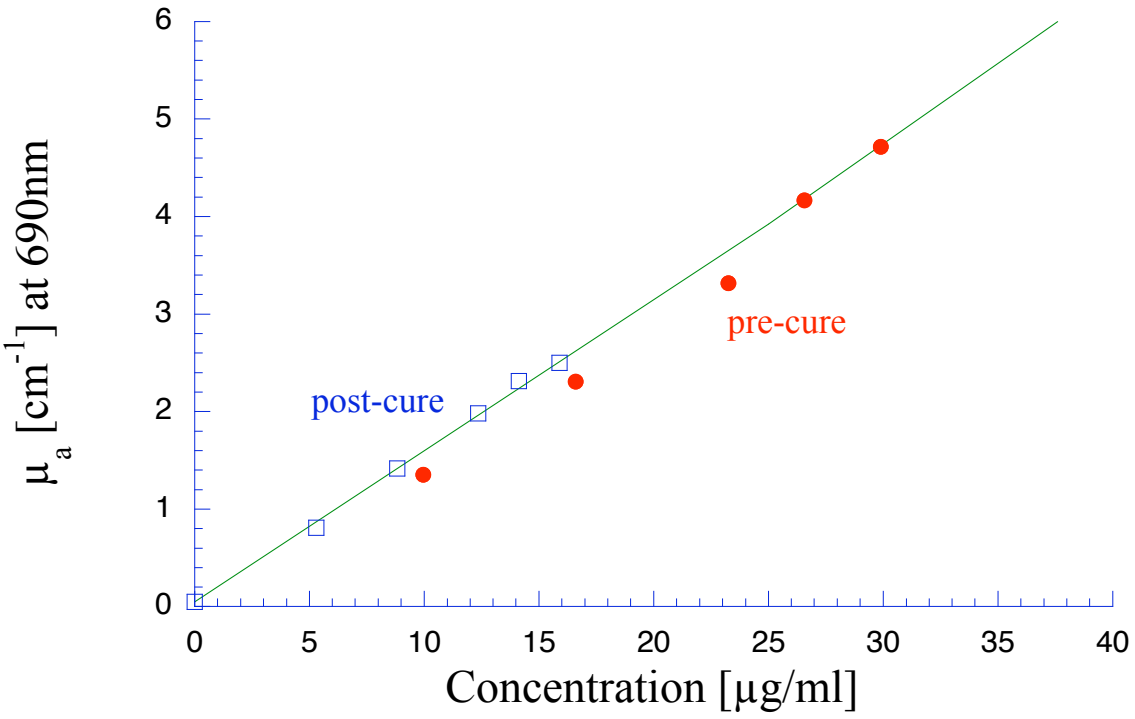

Figure 2.6: The absorption coefficient at 690 nm as a function of dye concentration of Epolight 6084 in part A of the polyurethane (circles) and after curing in polyurethane (squares). The fitting line is $\mu_a^{690} = a_1 C_{6084} + \mu_{a0}^{690}$, where $a_1 = 0.16\,\mathrm{cm}^{-1}\mathrm{mL}/\mu\mathrm{g}$ and $\mu_{a0}^{690} = 0.046\,\mathrm{cm}^{-1}$ is the absorption coefficient of polyurethane at 690 nm one week after casting.

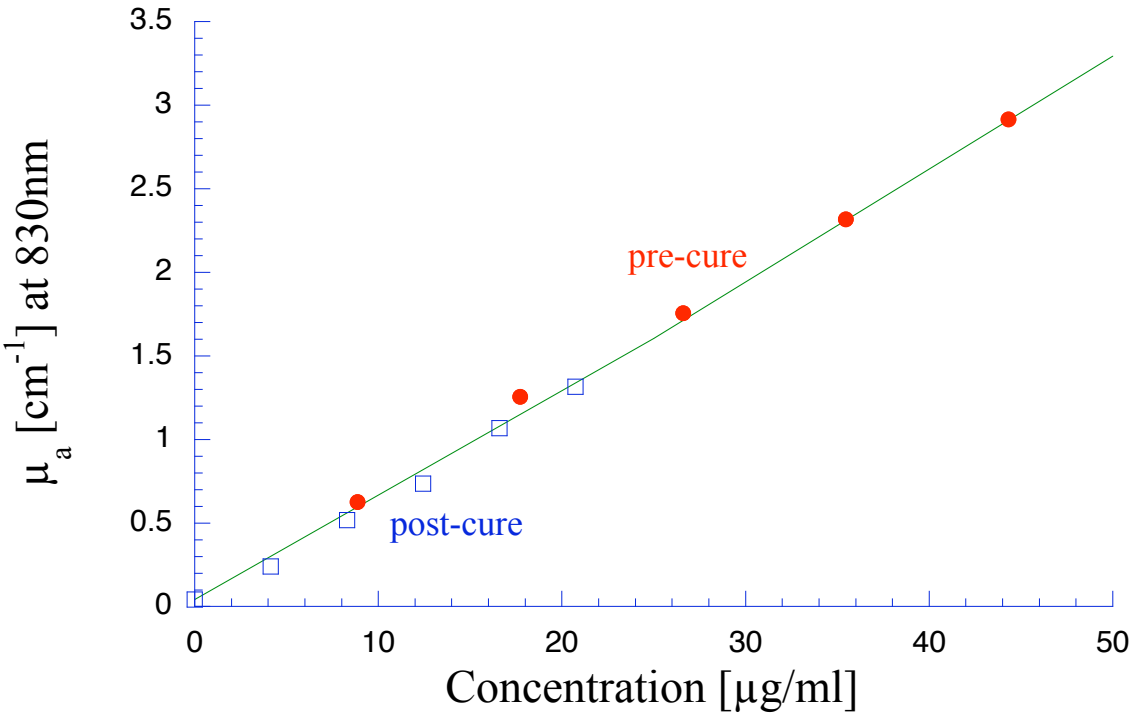

Figure 2.7: The absorption coefficient at 830 nm as a function of dye concentration of Epolight 4148 in part B of the polyurethane (circles) and after curing in polyurethane (squares). The fitting line is $\mu_a^{830} = a_1 C_{4148} + \mu_{a0}^{830}$, where $a_2 = 0.065\,\mathrm{cm}^{-1}\mathrm{mL}/\mu\mathrm{g}$ and $\mu_{a0}^{830} = 0.042\,\mathrm{cm}^{-1}$ is the absorption coefficient of polyurethane at 830 nm one week after casting.

.

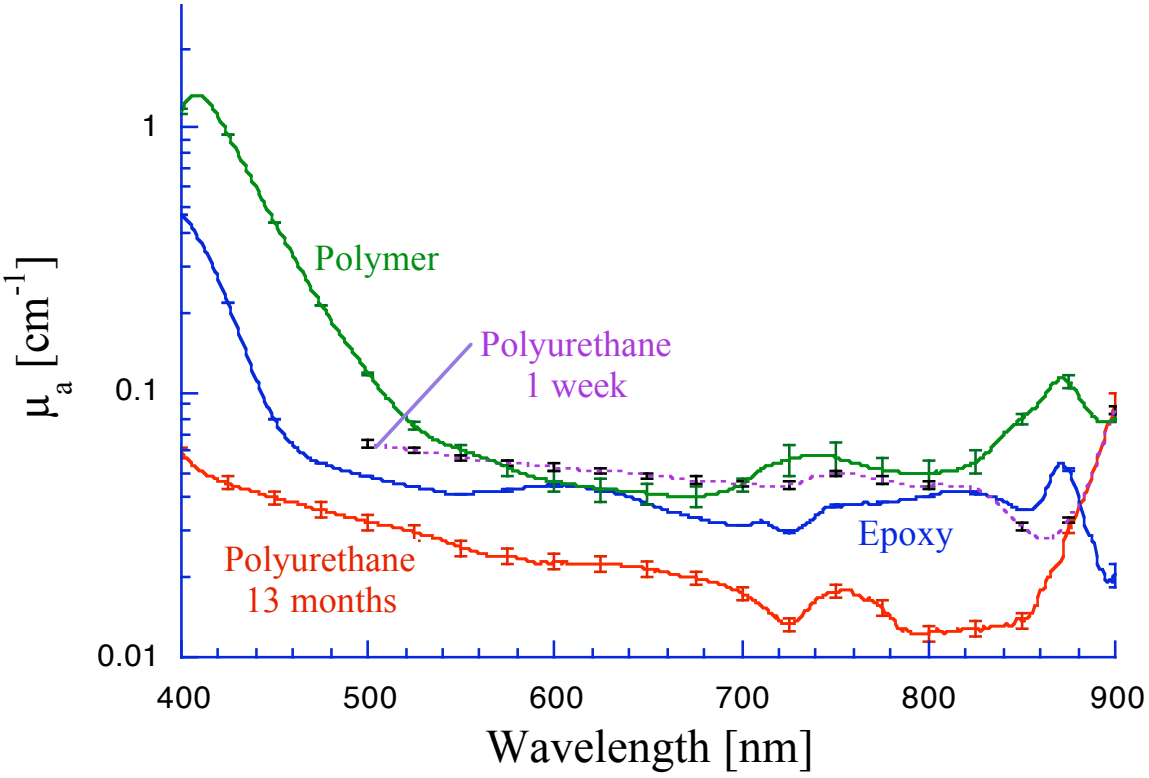

Figure 2.8: The absorption coefficient spectra of an epoxy resin, a polymer resin, and the polyurethane 13 months after being cast in addition to the polyurethane 1 week after casting.

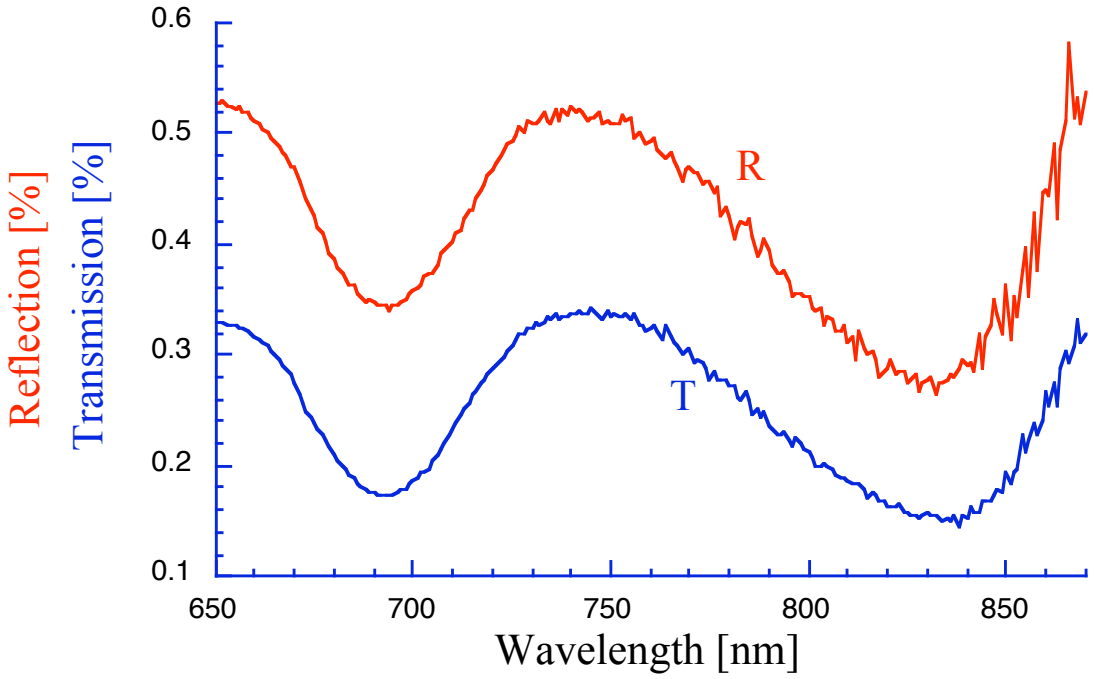

Figure 2.9: Typical reflectance and transmission measurements used to derive optical properties using the inverse adding-doubling method.

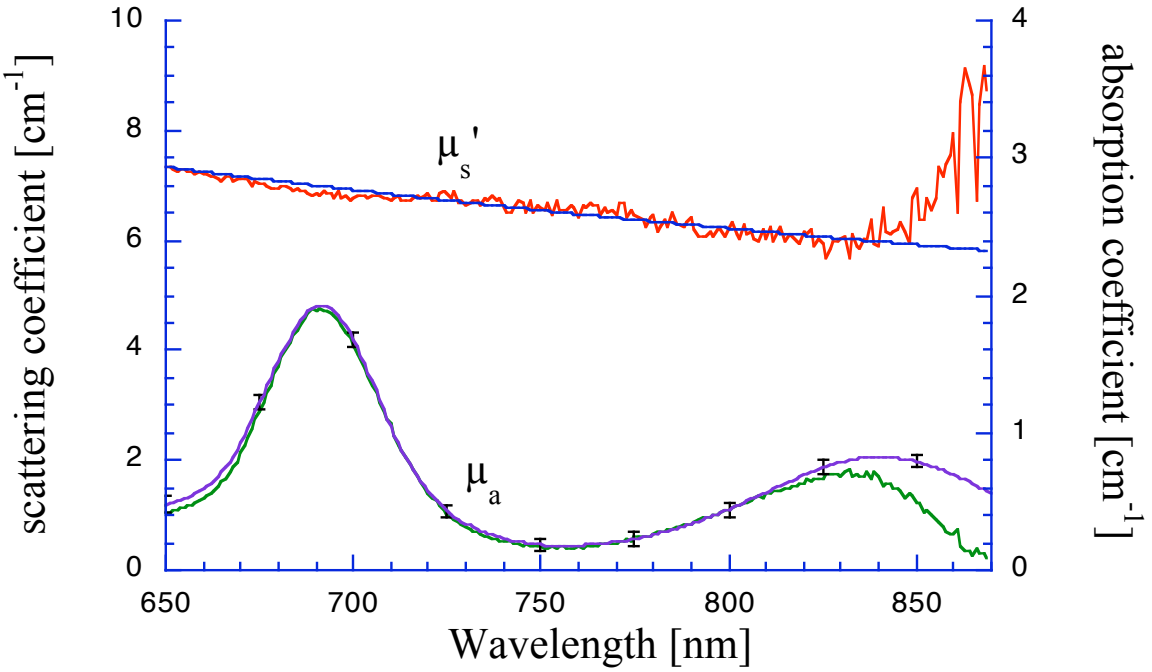

Figure 2.10: The reduced scattering and absorption coefficients spectra for the reflection and transmission data in figure 2.9 is shown in comparison to the spectrometer measurement of absorption for the same phantom made without added scatterer. The error bars are the standard deviation of three spectrometer measurements through the clear phantom. Above 830 nm, the sensitivity of the detector drops precipitously causing error in the resultant optical properties. The reduced scattering is fit by the relation $\mu_s' = (5.2\,\mathrm{cm}^{-1})(\frac{\lambda}{1000\,\mathrm{nm}})^{-0.8}$.

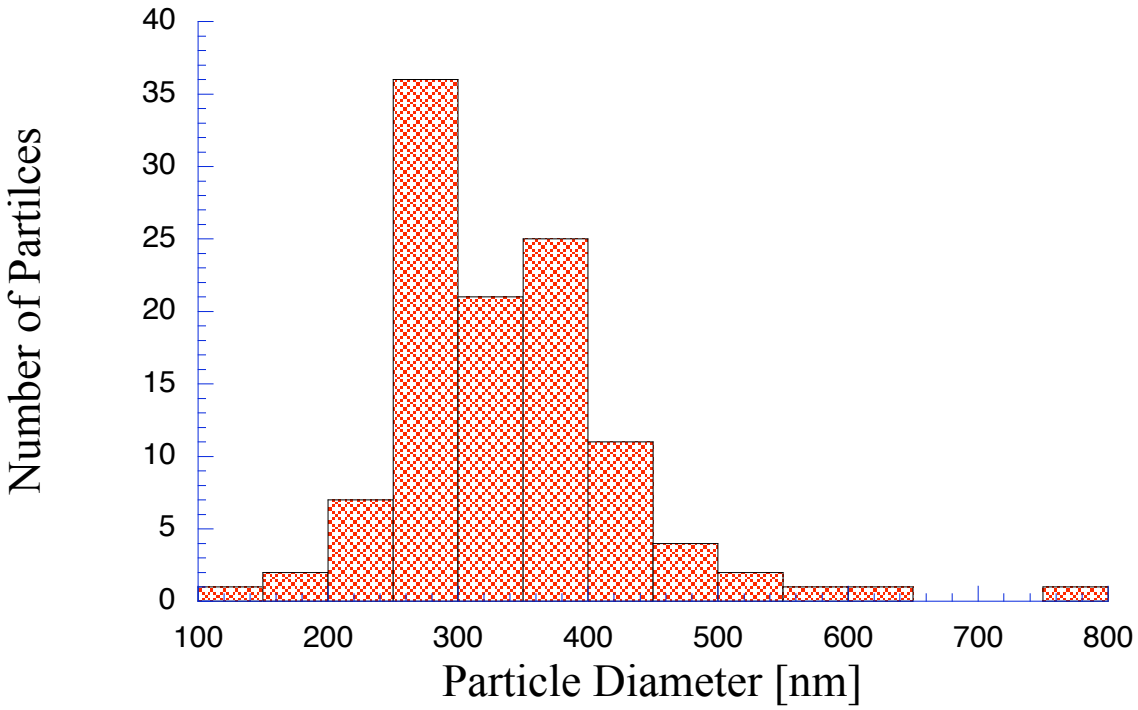

Figure 2.11: The size distribution of diameters of 112 titanium dioxide particles has a mean of 340± 90 nm.

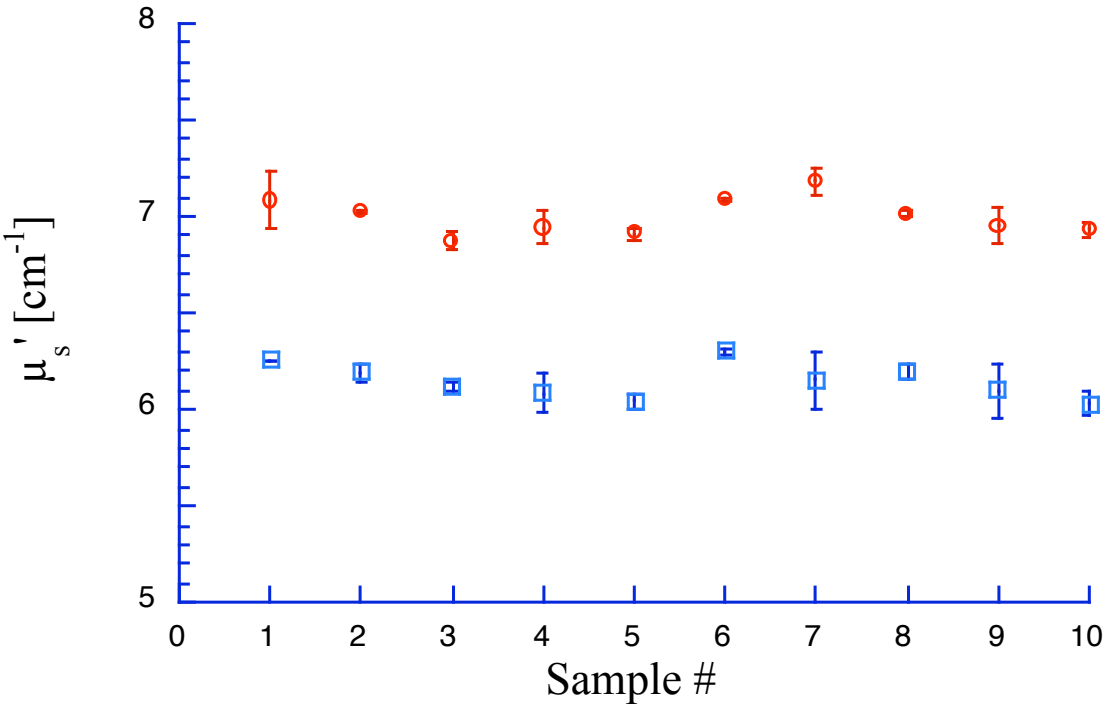

Figure 2.12: The variation in reduced scattering coefficient for ten different phantoms at 690 nm (circles) and 830 nm(squares) measured by the IAD method. All samples were designed to have the same reduced scattering properties. The error bars are the standard deviation of four sets or reflection and transmission measurements for each sample.

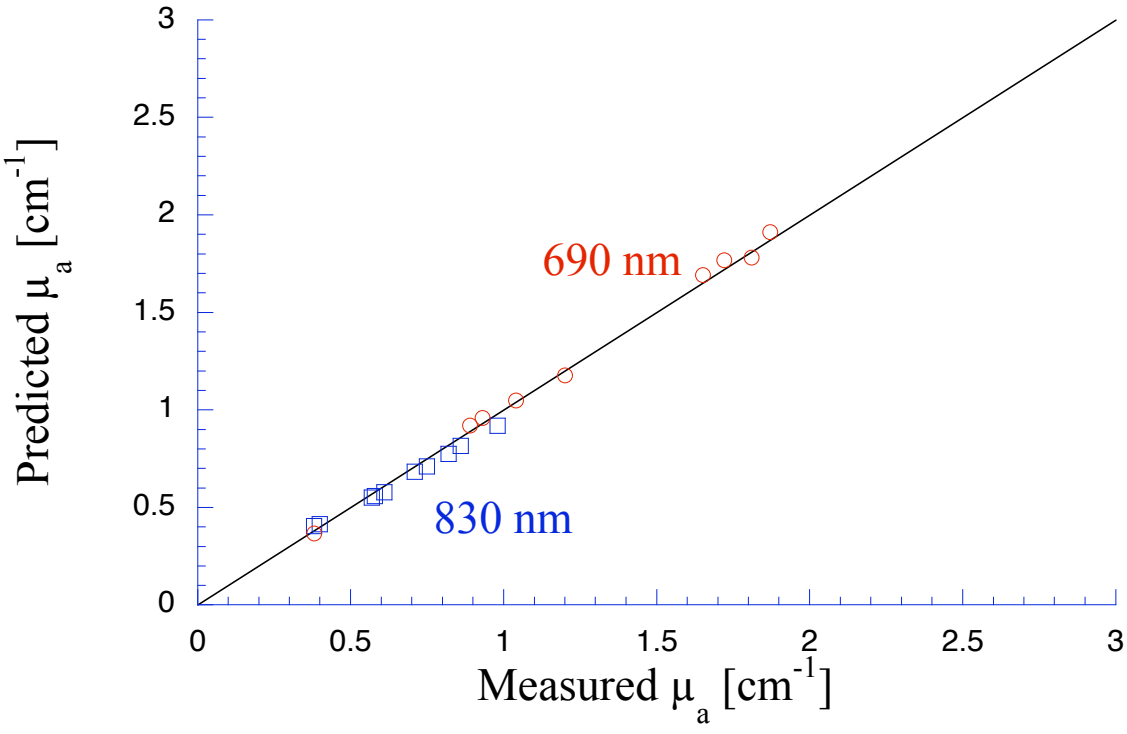

Figure 2.13: The predicted absorption coefficient using equations 1 and 2 are shown relative the spectrometer measured absorption coefficient for the ten different phantoms.

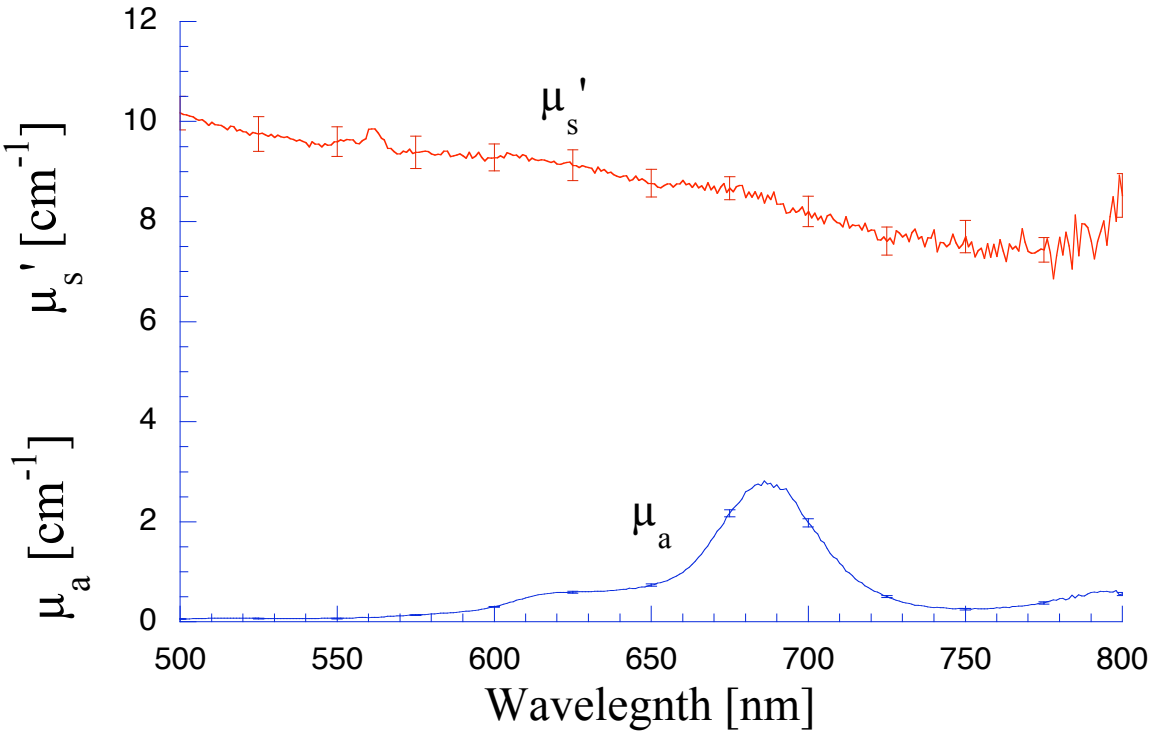

Figure 2.14: The absorption and reduced scattering coefficient spectra for twelve of the 20 identical phantoms. The error bars show the standard deviation for each optical property among the twelve phantoms and are approximately ± 3% between 600 and 800 nm.

2.4 Conclusions

I presented a method to fabricate tissue phantoms that simulate the optical properties of living tissue at the 690 and 830 nm wavelengths. The optical properties of the phantoms has been consistent in a period of 14 months from the date of casting. The two molecular dyes provided independent absorption between our chosen wavelengths for absorption coefficients up to 5 and 3 cm^{-1} at 690 and 830 nm respectively. These dyes exhibited stable absorption through the curing process of polyurethane. In addition, the high molecular extinction coefficient of each dye allowed us to keep the addition of dye stock to less than 0.1 percent of the volume of the polyurethane. The polyurethane itself was the only component that changed optical properties after casting. The absorption due to the polyurethane decreased approximately by a factor of 2 over the visible spectrum. This change is assumed to occur gradually though I don't have evidence to support this belief. Though polyurethane slowly changes absorption properties, the effect is to make the material more colorless which help to make any added dyes the more dominant absorber.

Polyurethane as a phantom material was easy to work with and handle. The material becomes solid by 24 hours after mixing but is not fully cured. I found that the polyurethane could not be machined for at least 48 hours. Even sanding of the material before 48 hours is futile because ripples would form on the surface. This polyurethane may be cast into any shape but the material of the mold determines how easy it is to extract the polyurethane after curing. Polyethylene containers readily released after curing. Attempts to cast the polyurethane between glass slides proved more problematic. Spray on mold release (Ease Release 400, Mann Formulated products, Easton, PN) allowed the polyurethane to release from glass but the thin film of mold release caused surface roughness to the polyurethane making it like frosted glass. Polycarbonate molds behaved more like glass in terms of demolding. The mold release allowed polyvinylchloride (pvc) pipe to act as a mold too, but only the polyethylene worked well without the mold release.

Degassing of the polyurethane was a necessary though time-consuming step in the phantom preparation. Significant bubble formation occurs during each mixing step. For our phantoms at least three mixing steps occurred for each phantom, since two dyes and

the two components of polyurethane were combined. Bubbles that were not removed provide many inhomogeneities, and may act as large scatterers. Removal of the bubbles allowed for consistency in the finished product that otherwise would not be obtainable.

Four linear relationships (eqs. 1–4) that describe the the absorption coefficient as a function of dye concentration and the reduced scattering coefficient as a function to the titanium dioxide concentration were determined. These relationships predicted the measured absorbing and scattering properties with less than 4% error. The optical properties of the phantoms have shown to be stable over a period of 14 months making the phantoms suitable for use as reference standards.

Chapter 3

A Combined Inverse Adding-doubling and Monte Carlo Model with Experimental Correction Factors for Optical Property Determination using Single and Double Integrating Sphere Measurements

3.1 Introduction

Numerous instances have been presented using the integrating sphere as a tool to measure the total diffuse reflection and transmission of optically turbid and homogeneous materials, including several biological tissues [76–81] since it was first described by Ulbricht [82] in 1900. Using a light propagation model, the integrating sphere measurements may be used to calculate the absorption and scattering properties for a sample with a slab geometry. The inverse adding-doubling (IAD) algorithm is a fast and accurate method to solve for the absorption and scattering coefficients of *in vitro* tissues or other optically turbid materials from measurements of the total diffuse reflectance and transmittance [83]. Monte Carlo (MC) models of light transport have been used with integrating sphere measurements to determine optical properties [76–79, 84–86]. Like the inverse adding-doubling method, an optimization routine finds the absorption and scattering coefficients by iteratively calculating the reflectance and transmittance. The IAD and MC models

employed often overlook important effects that occur when integrating spheres are used to measure the reflection and transmission Many MC models ignore the fact that the sphere itself alters the measurements. The IAD model ignores the light that escapes through the edges of the sample.

The effect of the integrating sphere on the measured reflectance has been documented extensively [87–94]. An experimental method to account for the sphere's perturbation of the measurements was attempted by Pickering [95]. Unfortunately, inconsistencies in the experimental and theoretical parameters make this method difficult to use. Pickering also gave the first description of a method using two spheres for simultaneous measurement of both the reflectance and transmittance [94]. This was novel in that the dynamic processes caused by external stimuli such as heating [96,97] and dehydration [98] could be monitored. However, double sphere measurements are made when single sphere measurements would suffice, often due to the convenience of simultaneous measurements of reflectance and transmittance [99–101].

Light lost through the edges of the sample is a common source of experimental error [83]. A discussion of the consequences for light loss errors is given by Pickering, where the effect leads to an over-estimation of absorption by the sample [95]. The light loss (which may be as high as 30%) is a function of the sample dimensions, the sample port size, the illuminating beam diameter, and the optical properties of the sample [102]. Lost light must be corrected for each of these variables making it impractical to pre-calculate. Therefore, a three dimensional model such as a freely adaptable MC model is commonly used for inverting optical properties and calculating light loss.

The purpose of this work is to improve the accuracy of integrating sphere measurements. A mathematical model of integrating sphere measurements for both single sphere and double-sphere arrangements is presented. This derivation is consistent with prior integrating sphere theory work [87, 88, 92, 94]. A clear and simple characterization of the effect of the integrating spheres upon measurements is given as a single function for gain. Practical correction factors for single and double integrating sphere arrangements are presented. These factors are included into a combined IAD and MC model to calculate optical properties from sphere measurements. I demonstrate the robustness of the model

to produce consistent results for an optically stable polyurethane phantom under a wide range of experimental sphere conditions (eg. multiple sample thicknesses and sample port sizes). I measure the optical properties of a water suspension of titanium dioxide particles over the wavelength range of 400-1700 nm. This demonstrates the ability to resolve absorption for more than three orders of magnitude. An analysis of potential errors in sphere measurements shows that experimental error is comparable to optical property error with appropriately matched experiments and an inversion model. Finally, a set of guidelines for obtaining the best results using integrating spheres is given.

3.2 Theory

Quite a few variables are required to describe the light within an integrating sphere. There are variables describing areas within the sphere: the inside area of the sphere A, the area of the sample port A_s, the detector port A_d, the entrance port A_e, and the area of the sphere wall A_w. For simplicity, these are normalized to $a_s = A_s/A$, $a_d = A_d/A$, $a_e = A_e/A$, and $a_w = 1 - a_s - a_e - a_d$ so that they describe the fractional area of each region in the sphere. The average reflection of the sphere wall, the detector, and the sample under diffuse illumination are denoted r_w, r_d, and r_s respectively. The reflection of the sample by direct or collimated illumination is given by r_s^{direct}. The term r_{std} is used for the sample reflection of a reference standard. The transmission of the sample for direct or collimated illumination is denoted t_s^{direct}, while the transmission of the sample with diffuse illumination is t_s. The illumination light power is P. The power incident upon a region of the sphere is denoted by a subscript with the regions being the sphere wall P_w, the sample P_s, and the detector P_d.

3.2.1 Single integrating sphere

This section describes the interaction of reflected (or transmitted) light with a single integrating sphere. The greatest advantage of the integrating sphere is that it collects nearly all the light reflected by (or transmitted through) a sample. A significant fraction of this light is collected and redirected back to the detector. The exact amount depends on

geometric sphere factors and the reflectivity of the sphere walls and sample. The concept of the sphere gain to describe the increase in the irradiance on the detector due to the reflective sphere walls is introduced. Unfortunately, the sphere gain is not an experimental constant, but instead depends on the reflectance of the sample r_s.

Single Sphere Gain

Assume that a sphere is illuminated with diffuse light having a power P and that this light reaches all parts of the sphere — specifically, light from this source is not blocked by a baffle. Subsequent reflections however are restricted by a baffle located between the sample and detector ports. Multiple reflections in the sphere will increase the power falling on non-white areas in the sphere (e.g., the sample, detector, and entrance). To find the total light falling on each area of the sphere, the total power is summed for each successive incidence (followed by a reflection). A superscript denotes the number of times light is incident upon each surface within the sphere and pertains only to the contribution of power for that incidence. The first incidence for the diffuse light is

$$P_w^{(1)} = a_w P, \qquad P_s^{(1)} = a_s P, \qquad P_d^{(1)} = a_d P$$

The second incidence on the wall is

$$P_w^{(2)} = a_w r_w P_w^{(1)} + (1 - a_e) r_d P_d^{(1)} + (1 - a_e) r_s P_s^{(1)}$$

The light from the detector and sample is multiplied by $(1-a_e)$ and not by a_w because the light from the detector (and sample) is not allowed to hit either the detector or sample. The light that hits the walls on the kth incidence has the same form as above

$$P_w^{(k)} = a_w r_w P_w^{(k-1)} + (1 - a_e) r_d P_d^{(k-1)} + (1 - a_e) r_s P_s^{(k-1)}$$

Since the light falling on the sample and detector can only arrive from the wall due to a baffle,

$$P_s^{(k)} = a_s r_w P_w^{(k-1)} \qquad \text{and} \qquad P_d^{(k)} = a_d r_w P_w^{(k-1)},$$

Therefore, the incident light on the wall for the kth incidence becomes

$$P_w^{(k)} = a_w r_w P_w^{(k-1)} + (1 - a_e) r_w (a_d r_d + a_s r_s) P_w^{(k-2)}$$

The total power falling the detector is

$$P_d = a_d P + \sum_{k=2}^{\infty} a_d r_w P_w^{(k-1)} = a_d P + a_d r_w \frac{a_w + (1-a_e)(a_d r_d + a_s r_s)}{1 - a_w r_w - (1-a_e) r_w (a_d r_d + a_s r_s)} P$$

This result is in agreement with other investigators [88, 92, 94].

The gain $G(r_s)$ is defined as the irradiance on the detector relative to a black sphere as

$$G(r_s) \equiv \frac{P_d / A_d}{P / A}$$

where A_d and A are respectively the area of the detector port and the entire area of the sphere. The gain is

$$G(r_s) = 1 + \frac{r_w}{a_w} \cdot \frac{a_w + (1-a_e)(a_d r_d + a_s r_s)}{1 - a_w r_w - (1-a_e) r_w (a_d r_d + a_s r_s)} \tag{3.1}$$

The gain for a detector in a transmission sphere is similar [94], except that primed parameters are used to designate the use of a potential second sphere. For a black sphere the gain $G(0) = 1$, which is easily verified by setting $r_w = 0$, $r_s = 0$, and $r_d = 0$. Conversely, when the sphere walls are perfectly white, the irradiance at the entrance port, the sample port, and the detector port must increase so that the total power leaving via these ports is equal to the incident diffuse power P.

Single Sphere Measurements

The power falling on the detector in a single reflectance sphere will be

$$P_d = a_d \cdot (\textit{initial uniform diffuse light}) \cdot G(r_s)$$

In a typical measurement, the initial diffuse light in the reflection sphere will arise from (1) incident light that hits the sphere wall before the sample and (2) incident light that hits the sample first. Since the fraction of light that first hits the wall is defined as f, the first reflection is $r_w f P$. However this is not uniformly diffuse (since it cannot hit either the sample or the detector because of the presence of a baffle) so the light must strike the walls one more time before becoming uniform. This means that the first portion is given by $f r_w^2 (1 - a_e) P$.

The light reflected by the sample is $(1-f)r_s^{direct}P$. Since baffles ensure that the light cannot reach the detector from the sample, the light must bounce off the sphere walls to become a uniform diffuse source. The contribution will then be $(1-f)r_s^{direct}(1-a_e)r_wP$. The measured reflection will be

$$R(r_s^{direct}, r_s) = a_d(1-a_e)r_w[(1-f)r_s^{direct} + fr_w]P \cdot G(r_s) \tag{3.2}$$

Similarly the power falling on the detector measuring transmitted light is

$$T(r_s^{direct}, r_s) = a'_d t_s^{direct} r'_w (1-a'_e) P \cdot G'(r_s). \tag{3.3}$$

These expressions for R and T also work for entirely diffuse illumination where the incident light initially strikes the sphere wall in which case $f = 1$. However, this is generally undesirable because of the small difference between $R(r_{std}, r_{std})$ and $R(0,0)$.

To remove the source power(P) dependence, I define the sample reflectance M_R as

$$M_R = r_{std} \cdot \frac{R(r_s^{direct}, r_s) - R(0,0)}{R(r_{std}, r_{std}) - R(0,0)}. \tag{3.4}$$

M_R is the ratio of the difference in power measured between a sample and an open sample port to the difference in power measured between a reflection standard and an open sample port, where the experimental setups for $R(r_s^{direct}, r_s)$, $R(0,0)$, and $R(r_{std}, r_{std})$ are specified in figure 3.2. Subtraction of a dark signal measurement provides two significant benefits over normalization by a ratio $R(r_s^{direct}, r_s)/R(r_{std}, r_{std})$. First, error is reduced especially for low reflection samples caused by a DC offset in the signal due to dark current in the detector. Second, the measurement $R(0,0)$ is largely a measure of the fraction of light that is initially incident upon the sphere wall f, especially when white light sources are employed. By subtracting $R(0,0)$, the effect of f may be accounted for without a direct method of determining its value. Similarly, the measured transmittance is defined as

$$M_T = t_{std} \cdot \frac{T(t_s^{direct}, r_s) - T_{dark}}{T(0,0) - T_{dark}} \tag{3.5}$$

where the experimental setups for $T(t_s^{direct}, r_s)$, $T(0,0)$, and T_{dark} are shown in figure 3.3.

Additionally, reflectance and transmittance values determined using dark subtraction have a range between 0 and 1, as opposed to a constant lower limit greater than zero that

depends upon the experimental apparatus. The measured reflectance with a sphere and the true reflectance are exact at values of zero and r_{std} and are relative at intermediate values as shown in figure 3.4.

3.2.2 Double spheres

When two integrating spheres are used (fig. 3.5), all light must be absorbed by the sample, the sphere walls, the detector, or lost through the entrance port just as for single sphere measurements. However, the power of light falling on the detector differs from single sphere measurements because light may repeatedly pass back and forth through the sample between the two spheres. Thus, the gain becomes more complicated and now depends on both the reflectance and transmittance of the sample. In the following derivation, the subscript 1 refers to the reflection sphere and the subscript 2 to the transmission sphere and arrows are used to denote the direction of the source to the destination sphere.

Two sphere gains

The double-sphere gain may be derived from the single-sphere gain by considering the light passing through the sample between spheres as a new source that sums ad infinitum. Here a superscript denotes the number of times light passes through the sample between spheres and pertains only to the contribution of power for that number of passes. If P is uniform diffuse light in the first (reflection) sphere, then the light falling on the detector (assuming that no light has passed back and forth through the sample) is

$$P_{1\to1}^{(0)}(r_s, t_s) = a_d G(r_s) P$$

The attenuation factor $X_{1\to2}$ for light crossing from the first (reflection) sphere to the second (transmission) is

$$X_{1\to2} = a_s t_s (1 - a'_e) r'_w$$

For light crossing the other direction, the attenuation factor is

$$X_{2\to1} = a'_s t_s (1 - a_e) r_w$$

It follows that the light reaching the detector in the first sphere, after the light has crossed back and forth through the sample k times is

$$P_{1\to1}^{(k)}(r_s,t_s) = a_d G(r_s) P \cdot \left[G'(r_s) X_{1\to2} X_{2\to1} G(r_s)\right]^k$$

The total light on the detector of the first sphere for diffuse illumination originating in the first sphere is

$$P_{1\to1}(r_s,t_s) = \frac{a_d G(r_s) P}{1 - G'(r_s) X_{1\to2} X_{2\to1} G(r_s)}$$

The corresponding gain is defined as

$$G_{1\to1}(r_s,t_s) \equiv \frac{P_{1\to1}(r_s,t_s)/A_d}{P/A} = \frac{G(r_s)}{1 - a_s a_s' r_w r_w' (1-a_e)(1-a_e') G(r_s) G'(r_s) t_s^2}$$

The gain for light on a detector in the second sphere for diffuse light P arising in the first sphere is identical except for an extra factor of $X_{1\to2} G'(r_s)$. Thus

$$G_{1\to2}(r_s,t_s) = a_s(1-a_e') r_w' t_s G'(r_s) G_{1\to1}(r_s,t_s)$$

Similarly, when the light starts in the second sphere, the gain for light on the detector in the second sphere $G_{2\to2}$ is found by switching all primed variables to unprimed. Thus $G_{2\to2}(r_s,t_s)$ is

$$G_{2\to2}(r_s,t_s) = \frac{G'(r_s)}{1 - a_s a_s' r_w r_w' (1-a_e)(1-a_e') G(r_s) G'(r_s) t_s^2}$$

and

$$G_{2\to1}(r_s,t_s) = a_s' t_s (1-a_e) r_w G(r_s) G_{2\to2}(r_s,t_s)$$

Double integrating sphere measurements

The expressions for direct illumination of a sample between two integrating spheres follow from the above formulas for diffuse illumination. In this case, the light on the detector in the reflection (first) sphere arises from three sources: the fraction of light directly reflected off the sphere wall $f r_w^2 (1-a_e) P$, the fraction of light reflected by the sample $(1-f) r_s^{direct} r_w^2 (1-a_e) P$, and the light transmitted through the sample $(1-$

$f)t_s^{direct} r'_w (1 - a'_e) P,$

$$\begin{aligned} R_2(r_s^{direct}, r_s, t_s^{direct}, t_s) &= G_{1\to1}(r_s, t_s) \cdot a_d(1 - a_e) r_w^2 f P \\ &+ G_{1\to1}(r_s, t_s) \cdot a_d(1 - a_e) r_w (1 - f) r_s^{direct} P \\ &+ G_{2\to1}(r_s, t_s) \cdot a_d(1 - a'_e) r'_w (1 - f) t_s^{direct} P \end{aligned}$$

which simplifies to

$$\begin{aligned} R_2(r_s^{direct}, r_s, t_s^{direct}, t_s) &= a_d(1 - a_e) r_w P G_{1\to1}(r_s, t_s) \\ &\times \left[(1 - f) r_s^{direct} + f r_w + (1 - f) a'_s r'_w (1 - a'_e) t_s^{direct} t_s G'(r_s) \right] \end{aligned}$$

For the power on the detector in the transmission (second) sphere one has the same three sources. After a bit of algebra,

$$\begin{aligned} T_2(r_s^{direct}, r_s, t_s^{direct}, t_s) &= a'_d(1 - a'_e) r'_w P G_{2\to2}(r_s, t_s) \\ &\times \left[(1 - f) t_s^{direct} + (1 - a_e) r_w a_s t_s (f r_w + (1 - f) r_s^{direct}) G(r_s) \right] \end{aligned}$$

Double-sphere normalization differs slightly from the single-sphere method. The experimental arrangement for the spheres in double-sphere measurements is shown in figure 3.5. The normalized reflectance is then

$$M_R = r_{std} \cdot \frac{R_2(r_s^{direct}, r_s, t_s^{direct}, t_s) - R_2(0,0,0,0)}{R_2(r_{std}, r_{std}, 0, 0) - R_2(0,0,0,0)} \tag{3.6}$$

and transmission by

$$M_T = \frac{T_2(r_s^{direct}, r_s, t_s^{direct}, t_s) - T_2(0,0,0,0)}{T_2(0,0,1,1) - T_2(0,0,0,0)}. \tag{3.7}$$

3.2.3 Sphere parameters

Two experimental parameters are needed to fully evaluate equations 3.2–3.7. These are the fraction of diffuse illumination (f) and average sphere wall reflectance (r_w). Fortunately as is shown later, it is not necessary to measure f as long as it is less than 40%. If needed, f is

$$f = R(0,0)/R_0^{diffuse}$$

as shown in figures 3.2 and 3.6.

The average reflectance of the sphere wall needs to be measured to minimize error. It may also be determined with two measurements. Both measurements use diffuse illumination, but one has an open sample port ($R_0^{diffuse}$) and the other a reflectance standard in the sample port ($R_{std}^{diffuse}$). To make the light diffuse, all the light is directly incident on the sphere wall behind the baffle in relation to the detector port. The ratio of the light when no sample is present to that when a reflectance standard may be represented as

$$\frac{R_0^{diffuse}}{R_{std}^{diffuse}} = \frac{1 - a_w r_w - (1 - a_e) r_w (a_d r_d + a_s r_{std})}{1 - a_w r_w - (1 - a_e) r_w a_d r_d}.$$

A solution for the wall reflectance is then

$$r_w = \frac{1 - \frac{R_0^{diffuse}}{R_{std}^{diffuse}}}{\left(1 - \frac{R_0^{diffuse}}{R_{std}^{diffuse}}\right)(a_w + a_d r_d (1 - a_e)) + a_s (1 - a_e) r_{std}}. \tag{3.8}$$

The reciprocal of the wall reflectance gives a cleaner relationship,

$$\frac{1}{r_w} = a_w + a_d r_d (1 - a_e) + a_s (1 - a_e) r_{std} \frac{R_{std}^{diffuse}}{R_{std}^{diffuse} - R_0^{diffuse}}. \tag{3.9}$$

Equation 3.8 is consistent with other investigators method for determining the wall reflectance [92, 93] and illustrates the difficulty in making accurate measurements of the sphere wall reflectance. The two diffuse reflectances $R_{std}^{diffuse}$ and $R_0^{diffuse}$ will only differ by the amount of diffuse light leaking from the sphere when the port is empty. Consequently, the difference will be small and any errors in the measurements will be magnified when the division is done.

It is possible to gain insight into the relation between measurements and r_w by making a few assumptions. For example, the relative detector area a_d and the entrance port area a_e are usually negligible and can be ignored. The equation for r_w can be expanded in terms of a_s

$$r_w = 1 - a_s \frac{R_0^{diffuse} - (1 - r_{std}) R_{std}^{diffuse}}{R_{std}^{diffuse} - R_0^{diffuse}} + O(a_s^2). \tag{3.10}$$

Since r_{std} is often close to one, the second term in the numerator is small which leads to

$$r_w \approx 1 - a_s \frac{R_0^{diffuse}}{R_{std}^{diffuse} - R_0^{diffuse}} \qquad \text{if} \qquad r_{std} = 0 \tag{3.11}$$

Ultimately, only two calibration measurements (per integrating sphere) $R_{std}^{diffuse}$ and $R_0^{diffuse}$ are necessary to perform sphere corrections. There are six other constants to be calculated: the fractional area of the sphere wall a_w, the fractional area of the sample port a_s, the fractional area of the detector a_d, the fractional area of the entrance port a_e, the reflectance of the detector r_d; and the reflectance of the standard r_{std}. These parameters in combination with the five additional measurements form a complete set of data necessary to determine optical properties using an integrating sphere, two reflection measurements $R(r_s^{direct}, r_s)$ and $R(r_{std}, r_{std})$ and three transmission measurements $T(r_s^{direct}, r_s)$, T_{dark}, and $T(0, 0)$.

3.3 Materials and Methods

The aim is to provide two methods using integrating spheres to indirectly determine the optical properties of a material and show that the process is accurate and consistent under a wide variety of experimental conditions.

3.3.1 Test samples

To show that our experimental method is robust, a sample is required that is simple, stable and whose absorption properties are known by independent means from the method presented here. The majority of experiments used a solid polyurethane phantom. An advantage of the solid phantom was that it could be placed over the port of the integrating sphere without a special holder or glass covers. Construction of the polyurethane phantom was shown previously and demonstrated to be optically stable [103]. Two slabs roughly 60 mm in diameter of the same batch were produced with thicknesses of 4.93 ± 0.01 and 6.67 ± 0.01 mm. Additionally, a sample was made from the same batch cast in a 10 mm pathlength cuvette without added scatterer (TiO_2 particles) for independent absorption coefficient determination using an absorbance spectrometer (Cary 100 Bio Spectrophotometer, Varian Scientific Instruments Inc., Walnut Creek, CA). The refractive index of the polyurethane (1.468) was measured using an Abbé refractometer at visible wavelengths.

A second sample was included that provided a greater range of absorption over the visible and near-infrared spectrum. A solution of titanium dioxide particles (Ti-pure R-900, Dupont Chemicals, Wilmington, DE) suspended in ultra-filtered water was prepared at a concentration of 0.63 mg/ml. The TiO_2 particles are the same as in the solid phantoms and were shown to have a mean diameter of 340 ± 90 nm using SEM imaging [103] . The particle suspension was sonicated for an hour to prevent settling and then pipetted into holders and measured within the next hour. During that time, notable settling did not occur. Two sample holders were used with optical pathlengths of 0.15 mm and 11.3 mm. Water was assumed to be the dominant absorber especially at infrared wavelengths.

3.3.2 Integrating sphere measurements

Single sphere experiments were performed as diagrammed in figures 3.2 and 3.3. A 203.2 mm diameter integrating sphere (IS-080-SF, Labsphere, Inc., North Sutton, NH) with a Spectraflect coating was used for all measurements. The sphere has three 50.8 mm ports and a 12.7 mm port adjacent to a baffle. The ports are spaced equally along the equator of the sphere. The port opposite the 12.7 mm detector port was capped to close the port. The detector port had a custom fabricated cap with an SMA optical fiber connector that reduced the detector port to a 3.2 mm diameter. This custom cap was coated on the interior surface with barium sulfate (white reflectance coating #6080, Eastman Kodak, Rochester, NY). A 1 mm diameter fiber (PWF1000T, CeramOptec Industries, East Longmeadow, MA) guided light from the detector port to one of two scanning grating detectors in a spectrofluorometer (Fluorolog-3, Instruments S. A.,Inc., Edison, NJ); a photo-multiplier tube (PMT) detector for visible wavelengths to NIR (400–850 nm) and a liquid nitrogen cooled germanium detector for the wavelength range of 800–1700 nm.

Slightly different integrating sphere arrangements were used for the two types of samples. For the polyurethane phantom, a 1 mm optical fiber was used to deliver light to the sample from a tungsten lamp, (Fiber-lite, Dolan-jenner Industries, Boxborough, MA). The optical fiber was sleeved through a steel tube (4 mm diameter) holding the fiber face centered with the sample port at 10 mm from the sample giving a 4 mm diameter spot

size. The steel tube was coated with multiple layers of flat white paint. The fiber extended beyond the steel tube about 5 mm. The entrance port was 6.35 mm in diameter for reflection (fig. 3.2) measurements but closed for transmission (fig. 3.3). The 6.67 mm thick phantom was measured with multiple sample port diameters: 6.35, 12.7, 19.1, 25.4, 31.8, 44.5, and 50.8 mm for single-sphere experiments. Only the 25.4 mm sample port was used to measure the 4.93 mm thick phantom in a single sphere experiment.

However, additional measurements were recorded with a 25.4 mm sample port from 400–1000 nm using a silicon diode array grating spectrometer detector (SD2000, Ocean Optics inc., Dunedin, FL) for both of the solid phantom thicknesses. Due to the limited dynamic range of the silicon detector, full spectrum results could not be obtained from a single set of measurements. And so, multiple reflectance and transmittance were stitched together (400–500 nm, 500–600 nm, 700–800 nm and 800–1000 nm) such that the measurement of the reference standard was at least 50% detector saturation limit (but not saturated) in each spectral section. Neutral density filters were used to attenuate the light source and the integration time was set to 0.5, 0.7 or 1.0 s to meet that criteria. To further reduce noise, three acquisitions were averaged during collection.

Measurements of the titanium particle suspension used a single-sphere arrangement. For the light source, a tungsten lamp (6333, Oriel Instruments, Stratford, CT) had an image of the filament focused in the plane of the sample port with a spot size of 10 mm for the largest dimension. For reflection measurements, an entrance port cap reduced the port diameter to 19.1 mm and the sample port diameter was the maximum possible 50.8 mm. Transmission measurements were made with a sample port of 50.8 mm in diameter. The entrance port cap (19.1 mm) from the reflection measurements was placed opposite to the detector, keeping the fractional sphere wall area, a_w constant for both reflection and transmission measurements.

Double sphere experiments were performed as diagrammed in figure 3.5 using two identical spheres, the same as described for the single sphere experiments. Measurements were made for four sample port sizes (19.7, 31.8, 44.5, and 50.8 mm) for each of the polyurethane phantom sample thicknesses (4.93 and 6.67 mm). The two spheres were mounted to

an optical rail to allow for the sandwiching of the sample between spheres. Only the transmission sphere was moved to keep the reflection sphere fixed with respect the illumination fiber (4 mm beam-diameter on the sample). The PMT detector of the spectrofluorometer was used as described above for the single-sphere using a 1 mm collection fiber. Reflection and transmission were recorded by serially alternating the connection of the detector collection fiber between spheres without otherwise changing the sphere arrangement.

For all experiments, the reference was a 50.8 mm diameter 99% Spectralon reflection standard (Labsphere, Inc., North Sutton, NH) for reflection or an open port as the reference in transmission. The optical properties were determined from the measured reflectance (eqn. 3.4 for single-sphere experiments or eqn. 3.6 for double-spheres) and transmittance (eqn. 3.5 for single-sphere experiments or eqn. 3.7 for double-spheres) using an IAD program [83].

3.3.3 Measuring the Sphere Parameters

Though values of the sphere wall reflectivity usually accompany vendor supplied integrating spheres, the reflectivity may change over time as dust settles on the sphere surface over time. The experimental determination of the average sphere wall reflectance follows section 2.3. The measurements of $R_{std}^{diffuse}$ and $R_0^{diffuse}$ were used to determine the sphere wall reflectance r_w (eqn. 3.8) as shown in figure 3.6. The integrating sphere was rotated with respect to the collimated lamp beam so that light was directly incident upon the sphere wall between the sample port and the baffle. The fractional area of the sphere wall a_w, the sample port a_s and the detector port a_d was calculated using a disc geometry for the ports rather than the area of a spherical cap. Goebel showed that flat surfaces within an integrating sphere reduce the overall efficiency of the sphere introducing an error equivalent the the difference in area between a spherical cap and a disc of the same radius [92]. Finally, I assumed a detector reflectance, r_d of 0.05 to account for the reflectance by the fiber in addition to the steel SMA connector which made up 90% of the area of the detector port.

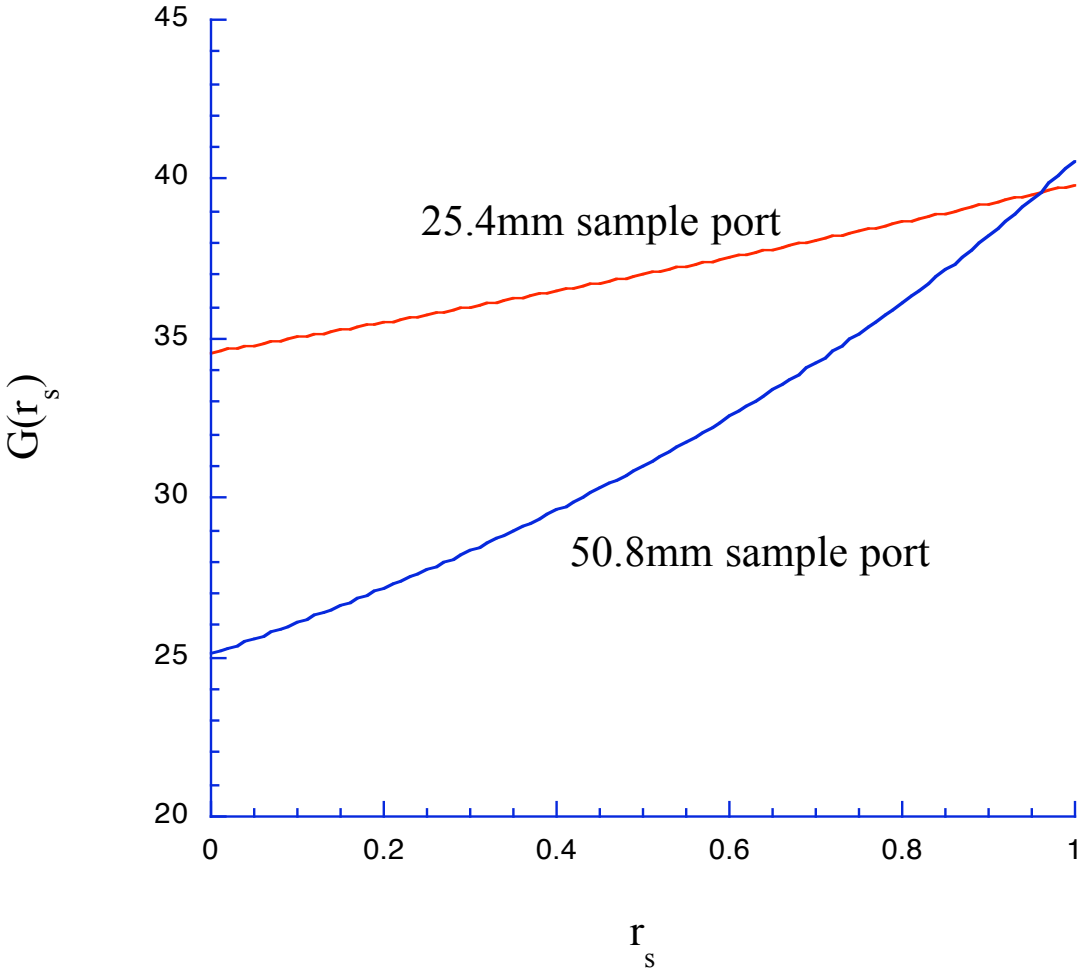

Figure 3.1: The gain (relative to a black sphere) for a 203 mm (8 in.) integrating sphere. The wall reflectivity is assumed to be 0.975 and the detector reflectivity to be zero. In both curves, the entrance port (6.35 mm) and detector port areas (3.18 mm) are identical. The increase in the gain as the sample reflection increases is the primary reason that sphere corrections are needed.

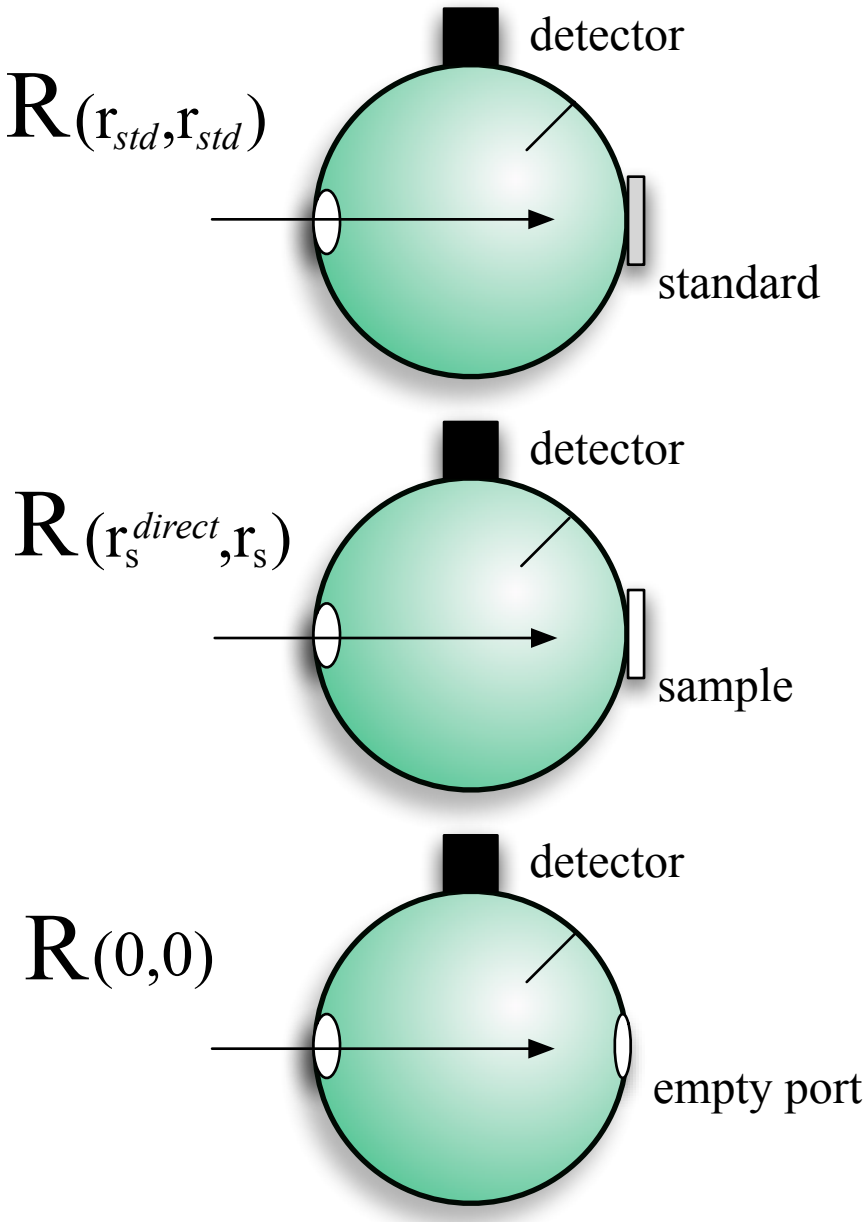

Figure 3.2: Diagrams of various integrating sphere reflectance measurements needed to make a reflectance measurement (eqn. 3.4) using a single sphere set-up.

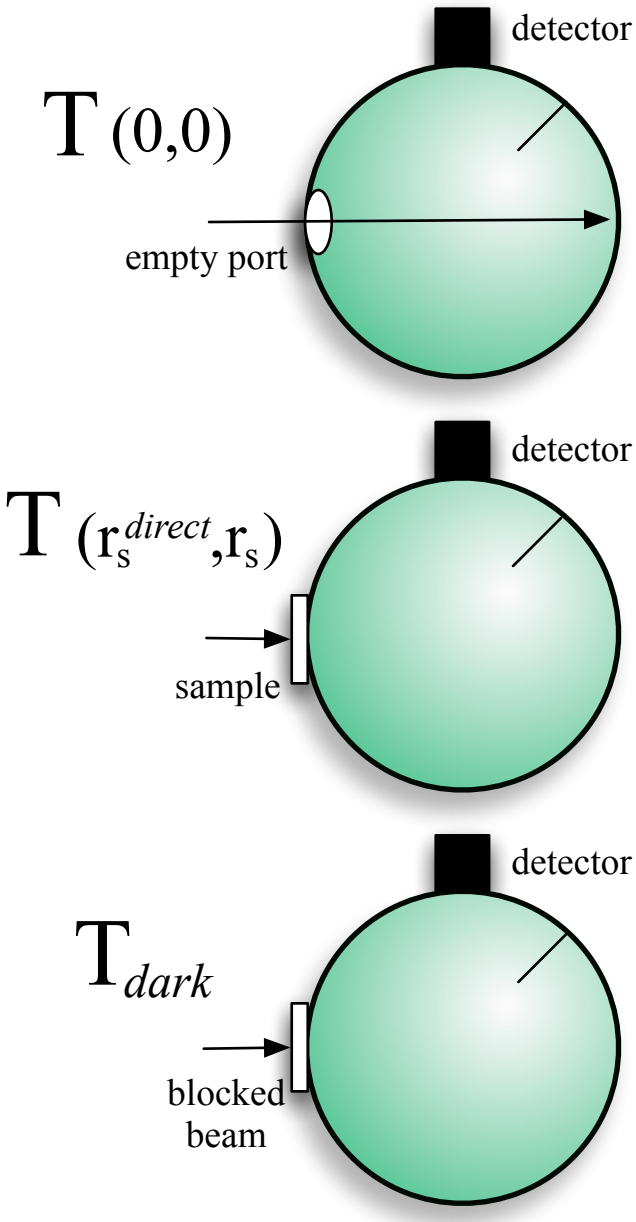

Figure 3.3: Diagrams of various integrating sphere transmission measurements needed to make a transmittance measurement (eqn. 3.5) using a single sphere set-up.

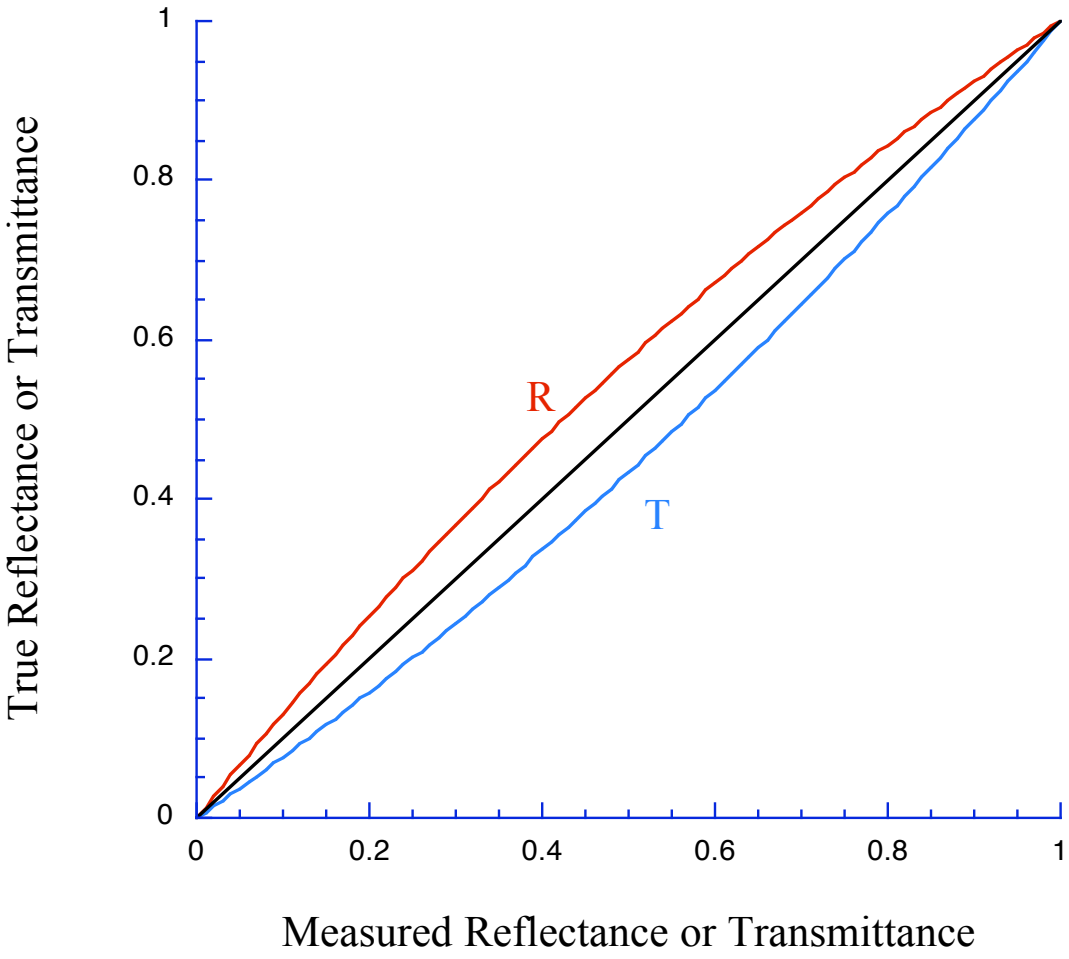

Figure 3.4: The difference between measured and true sample reflectance and transmittance are shown in comparison to unity slope. The relationship is determined by combining eq. 3.2 with eq. 3.4 to describe reflectance and transmittance by combinging eq. 3.3 with eq. 3.5 for a 203.2 mm diameter sphere with a wall reflectivity of 0.975, a 50.8 mm diameter sample port, a 6.35 mm diameter entrance port, and a 3.18 mm diameter detector port.

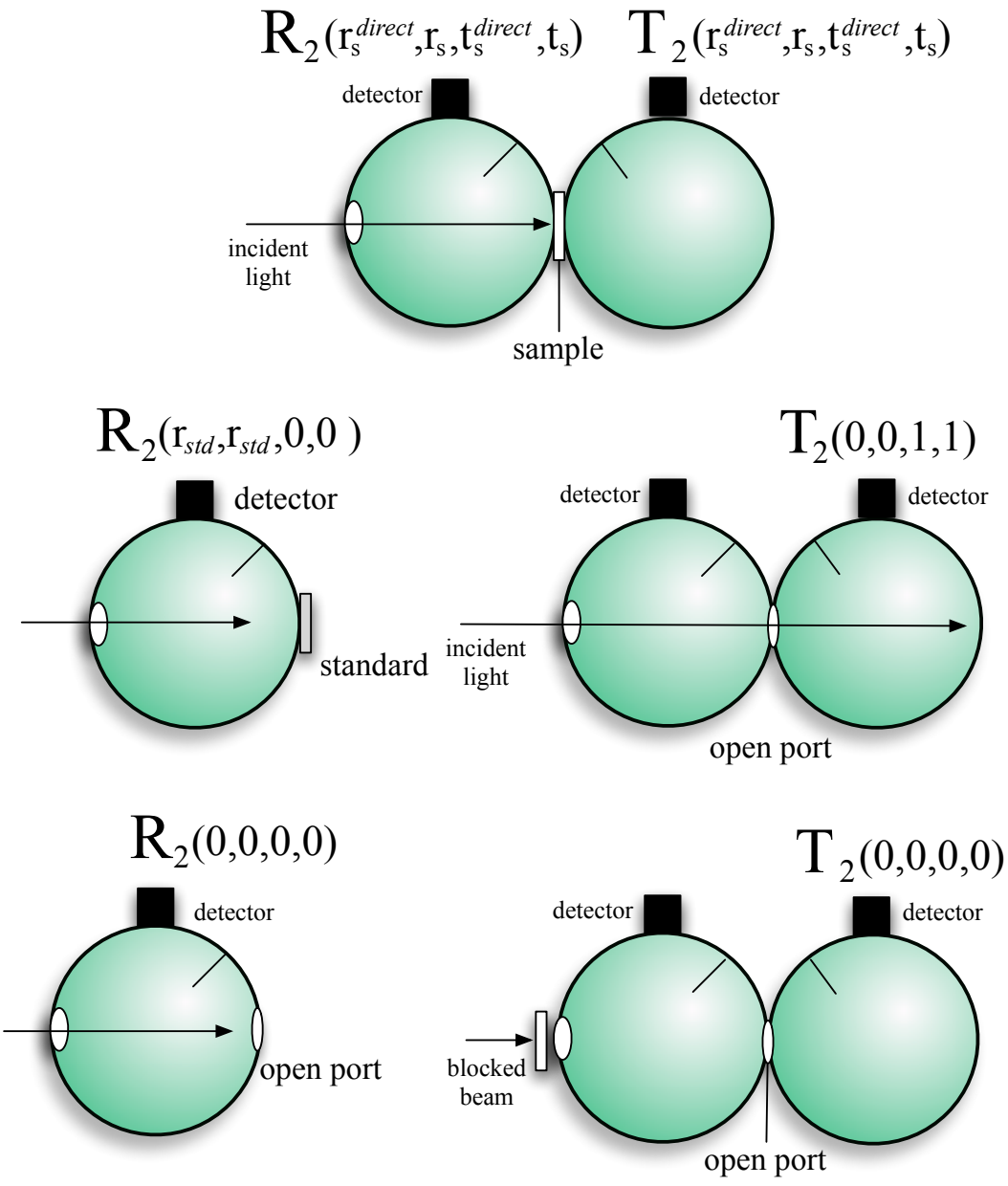

Figure 3.5: Diagram of a double-integrating sphere experiments needed for the simultaneous measurement of reflectance (eqn. 3.6) and transmittance (eqn. 3.7).

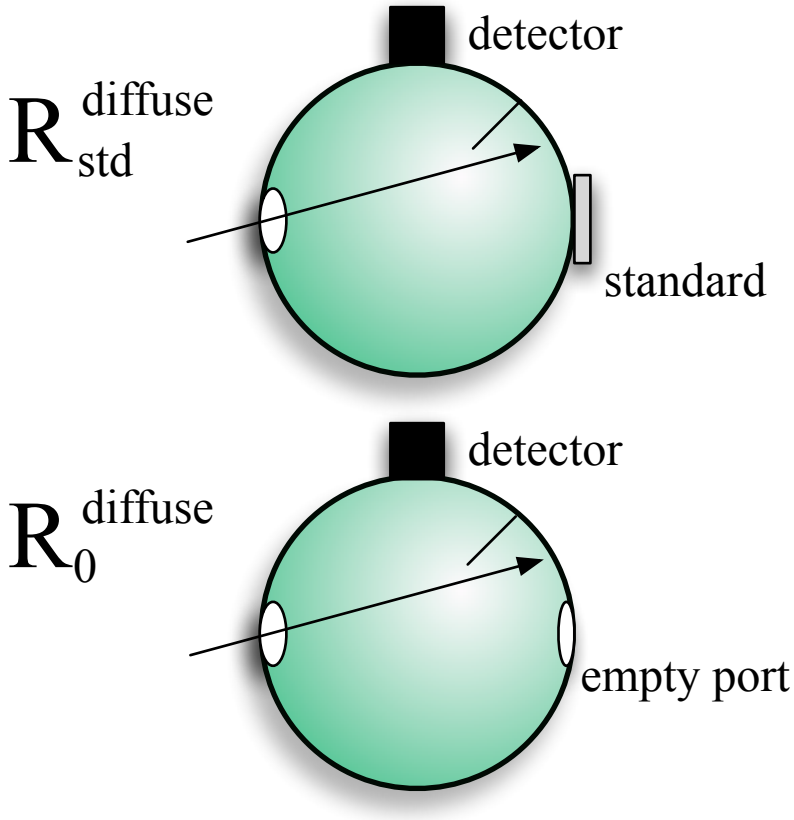

Figure 3.6: Diagrams of various integrating sphere measurements needed to determine the fraction of diffuse illumination f and the average sphere wall reflectance.

3.3.4 Optical property inversion

A new IAD program was made that follows the experimental method described in the above single and double sphere experiments and follows the mathematical model of the Theory section. Monte Carlo (MC) simulations of light transport were included in the IAD program to evaluate the fraction of light lost out of the edges of the sample. The measured reflectance and transmittance were input to the program along with experiment specific values. These values included the sample thickness, the refractive index of the sample and any cover slides, the number of spheres used, the port diameters for each sphere, the reflectivity of the detector and the sphere wall for each sphere and the value of the reference reflection and transmission.

A flow chart of the program logic is shown in figure 3.7. The program initializes by calculating a course grid for measured reflectance and transmittance values with preset absorption (μ_a) and scattering coefficients (μ_s) and anisotropy (g) (when collimated transmission is input) with the adding-doubling algorithm. The light lost through the sample edges is initialized to zero. The adding-doubling algorithm then loops to calculate the diffuse and direct reflectance and transmittance for a set of optical coefficients (μ_a, μ_s and g), subtracts the light lost proportionally for the diffuse and direct fractions, and calculates the total reflectance and transmittance. The process is repeated changing the optical coefficients until the calculated values equal the measured values. When they match, a MC simulation is performed to calculate the fraction of lost light. The adding-doubling loop is repeated to find new optical coefficients with the light loss correction. The MC simulations are repeated until both the change in the predicted absorption and scattering coefficients is less than 0.1%.

3.3.5 Error analysis

Integrating sphere measurements are generally performed to determine the optical absorption and scattering properties of a sample. Since the optical properties are the desired result, the percent change of the inverted optical properties are calculated from independent perturbations to three input measurements (M_R, M_T and r_w). For our data

set, the reflectance and transmittance of the 6.67 mm thick polyurethane phantom is used with a single sphere arrangement and a 25.4 mm diameter sample port. The analysis was divided into two areas, the model corrections of the measurements and experimental measurements errors.

There were two types of corrections made with our model of the sphere measurements. The first type was sphere corrections that accounted for the corresponding differences between the measured values of reflectance and transmission and the true reflectance r_s^{direct} and transmission t_s^{direct}. Second, light loss corrections were made using a Monte Carlo simulation to calculate the light lost through the sample edges. The light loss was separated into two categories, direct loss and diffuse loss which are shown respectively in figure 3.8. The optical properties using sphere and light loss corrections were determined using IAD. Next, the percent change to the absorption and reduced scattering coefficients with no corrections, sphere corrections alone, and light loss corrections alone was calculated using the relation

$$\%\ change = \frac{\mu_{a,s}^{limited\ \ corrections} - \mu_{a,s}^{sphere\ \ and\ \ MC\ \ corrections}}{\mu_{a,s}^{sphere\ \ and\ \ MC\ \ corrections}}$$

The sphere corrections accounted for the corresponding differences between the measured values of reflectance and transmission and the true reflectance r_s^{direct} and transmission t_s^{direct}.

Experimental error was produced by a perturbation of the data set to run with IAD to determine the percent change of the output optical properties. I ran the same set of data through the IAD program making independent 1% reductions (a multiplicative factor of 0.99) to the reflectance, transmittance, and the sphere wall reflectance. The percent change in optical properties was calculated by the equation

$$\%\ change = \frac{\mu_{a,s}^{normal} - \mu_{a,s}^{perturbed}}{\mu_{a,s}^{normal}}$$

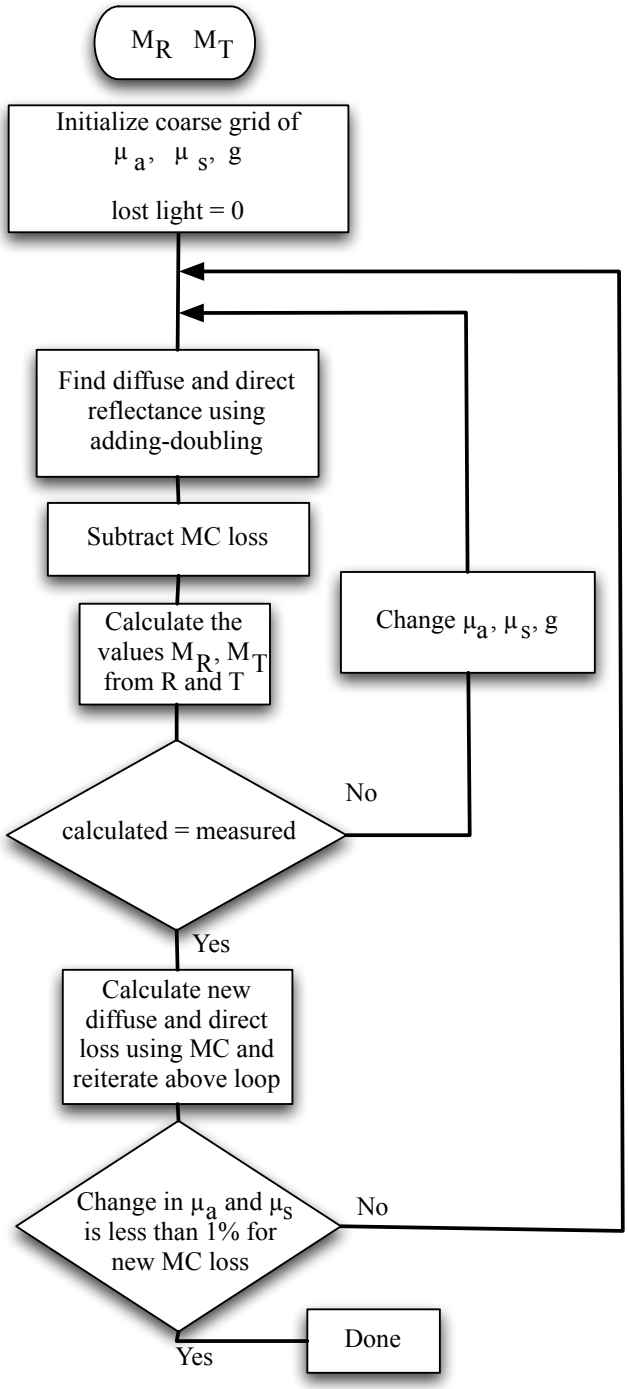

Figure 3.7: The logic flow of inverse adding-doubling program with a Monte Carlo model for calculation of light lost through the sample edges.

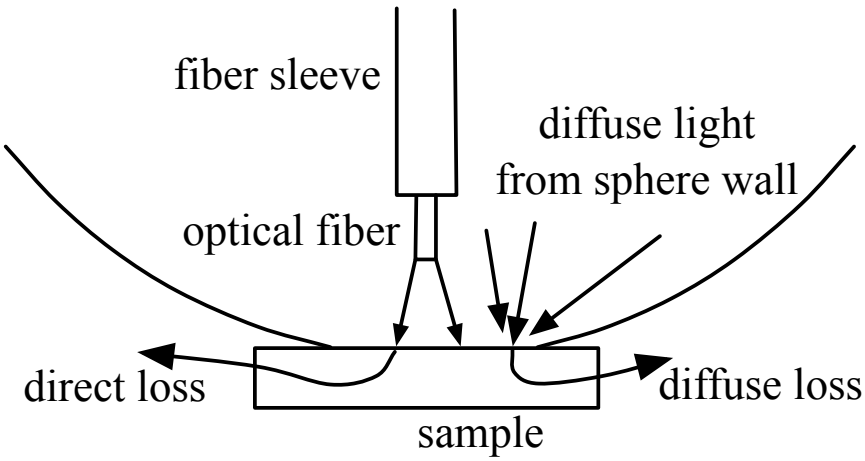

Figure 3.8: Light incident upon the sample from the initial irradiating beam that scatters out the side of the sample so that it neither enters the reflectance sphere or a transmission sphere and leads to larger value than the true absorption of the sample. This error is referred to as direct light loss. Light reflected by the sample back into the integrating sphere becomes diffuse in nature after reflecting off the sphere wall. Diffuse light incident upon the sample has a greater likely-hood of scattering out the side of the sample. Light lost in this manner is referred to as diffuse light loss.

3.4 Results

3.4.1 Optical properties

The mean absorption and reduced scattering coefficients of the polyurethane phantom are shown in figure 3.9 for seven different single sphere experiments and eight different double sphere experiments. The variation among measured optical properties made with differing sample port sizes exceeded the variation in measurements for a single experimental set-up. The standard deviation for the single sphere arrangements is 4% for absorption and 3% for scattering. The double sphere arrangements have a standard deviation of the mean of 6.5% for absorption and 4% for scattering. The measured absorption of the non-scattering sample differed by as much as 13% from the sphere measurements. Fixed numbers of iterations of the Monte Carlo simulations were performed on a single sample to evaluate for absorption convergence for multiple corrections for light lost through the sample edges. The result for absorption is shown in figure 3.10. A comparison of the optical properties is shown figure 3.11 using different detectors over a greater spectral range. Figure 3.12 shows the calculated optical properties for a 0.63 mg/ml titanium dioxide particle suspension in water in a 11.3 mm thick sample holder. The fraction of transmitted light drops below the noise level of the detector above 1350 nm due to absorption by water. The calculated absorption of the 0.15 mm thick sample holder is also shown for wavelengths ranging 1350–1700 nm.

3.4.2 Error analysis

A single data set of total diffuse reflection and transmission measurements are used for the error analysis with the polyurethane phantom. The optical property coefficients for absorption and scattering differ from the mean optical properties shown in figure 3.9 by less than 2%. The change in the optical properties calculated without corrections, with light loss only and sphere corrections only relative to optical properties with both light loss and sphere corrections are shown in figure 3.13. The effect of a 1% decrease to the sphere wall reflectance upon the IAD determined optical coefficients is shown in figure 3.14(bottom). The effect of a change in the fraction of initial diffuse light (f)(data

not shown) is spectrally flat for both absorption and scattering. This partial derivative is at least three orders of magnitude smaller than the sphere wall reflectance, the total diffuse reflection, or total diffuse transmission. The change in optical properties for a perturbation of a 1% decrease to the reflectance and transmittance are respectively shown in figures 3.14 top and middle.

3.5 Discussion

I demonstrate in figure 3.9 that our method of calculating absorption and the reduced scattering coefficient gives consistent results regardless of the experimental conditions. The optical properties determined using a single sphere is indistinguishable from two sphere experiments. The maximum deviation for any single experiment is 8% from the mean for the reduced scattering coefficient. The over-prediction of small absorption coefficients had been widely discussed as a concern with IAD [80, 81, 95] and integrating sphere measurements in general [84–86]. Monte Carlo simulations were shown to increase the lower resolution of absorption down to $0.05\,\mathrm{mm}^{-1}$ with loss corrections [85]. In figure 3.11, the absorption coefficient is in good agreement with the spectrometer absorbance measurement down to $0.01\,\mathrm{mm}^{-1}$ for samples roughly 5 and 7 mm thick. The titanium particle suspension in water follows the absorption spectrum of water down to $0.006\,\mathrm{mm}^{-1}$ with a sample thickness of about 11 mm.

A suspension of TiO_2 particles in water was chosen expecting that water would be the dominant absorber which is well characterized [104]. In the visible to near infrared wavelengths water absorption spans several orders of magnitude. Our results showed (fig. 3.12) that water absorption is dominant in the NIR. However in the visible portion of the spectrum, our measurement of absorption deviates dramatically from water absorption alone. Cabrera et al. [105] measured the absorption coefficient for rutile TiO_2 and water suspensions for five manufacturers' particles over the wavelengths 275- 405 nm. They show that properties vary significantly between manufacturers. Our measured absorption between 390-405 nm is within a factor of two of Cabrera et al. To our knowledge, no studies have shown absorption properties in the visible spectrum of titanium dioxide particles which

may be quite different than the properties of films. Therefore, I believe that absorption between 400-800 nm is dominated by the TiO_2 particles rather than water. Additional studies are needed to validate this result.

The combined IAD and MC model to determine optical properties utilizes the advantage of both techniques. IAD is a one dimensional model and therefore gives a fast and accurate method of calculating optical properties. The MC model is three dimensional and so it accounts for effects of light lost out the sample's edges which can not be accounted for with IAD alone. Since the MC model is used in a limited role, fewer photon bundles are needed to solve the light loss problem alone than are needed to solve both the inversion and light loss problems. The iterative use of the MC model to calculate the light loss hides the statistical error of MC models. It also removes the guess work in deciding the number of MC corrections needed to reach a stable set of optical properties. The drawback to the iterative approach is that a minimum of two MC simulations must be performed for each data point even when only a single iteration is sufficient to meet the tolerance for stability.

3.5.1 Sources of error

The error is separated into two classes, model errors and experimental errors. The model presented for both single and double sphere experiments is specific to the experimental method. Total reflectance and transmittance measurements using integrating spheres need to account for the effect the sphere has upon the measurement. The problem is that the measured reflectance and transmittance are not linearly related to the sample reflectivity and transmissivity as shown in figure 3.4. Inexact correction for this problem is referred to as a sphere correction error. I also refer to improper correction for light lost through the sample edges as a modeling error which is solved for with a MC model. Figure 3.13 shows the percent change in optical properties with either one or both model corrections not performed. Without either of the model corrections the absorption is over-predicted by 10–160% whereas the reduced scattering coefficient is under-predicted by 3–4%. Adding sphere corrections reduces the scattering error to 1%. MC simulations correct most of the error in the predicted absorption, but sphere corrections still account

for 2–4% error. In all cases, the magnitude of the error for the predicted absorption decreases with higher absorption.

Experimental error in which one of the measured values (e.g. reflectance, transmittance and sphere wall reflectivity) is imprecisely determined is shown in figure 3.14. The magnitude of the error for the predicted optical properties is generally equal to the error in the measurement. At low absorption, the error in the predicted absorption does increase to about 2% for a 1% perturbation in the reflectance and transmittance. The difference between modeling error and experimental error is stark. It implies that the greatest error occurs when the experimental method does not match the method assumed by the inversion model. When the inversion program accurately models the experiment, the uncertainties in the predicted optical properties will be approximately equal to the experimental uncertainties.

3.5.2 The inversion model

Since accurate determination of optical properties relies upon the model matching the experimental method, the implicit assumptions of combined IAD and MC inversion model are discussed in detail. Four assumptions are made. 1. The integrating sphere measurements are performed using the substitution method (defined below). 2. The reflectance and transmittance are normalized with a dark measurement subtraction. 3. The specular reflection from the sample is collected in the reflectance measurement. 4. There is a baffle inside the sphere blocking direct reflections between the sample and detector ports.

Two modes of integrating sphere experiments are referred to as substitution and comparison methods [88, 92]. The substitution method implies that the integrating sphere has a single sample port. The sample is substituted by the reflectance standard in a subsequent measurement to normalize the reflectance and transmittance. An alternative method used by investigators [79] is to make comparison measurements using two samples ports. With comparison measurements, the sample is placed in one sample port while the standard is placed in the other identical size sample port. Light is incident upon the sample for the sample measurement and then made incident upon the standard for the reference measurement. Since both the sample and the reference are present on both

measurements, the sphere gain is identical on both measurements. The advantage of the comparison method is that the reflectance and transmittance equal the sample reflectivity and transmissivity, but only when no light is initially incident upon the sphere wall.

I considered two experimental parameters in the IAD model, the fraction of light directly incident upon the sphere wall f and the sphere gain $G(r_s)$. Subtraction of a dark-signal measurement from both the sample and reference measurements (eqs. 3.4, 3.5, 3.6, and 3.7) nearly eliminates the effect of f. Subtraction of a dark signal containing the light initially incident upon the sphere wall removes the large background signal of diffuse light from light directly incident on the sphere wall. Dark measurement subtraction also removes any DC offset due to dark current in the detector. The greatest difference between optical properties determined with IAD that includes corrections for f versus without correction is $0.003\,\mathrm{mm}^{-1}$ for the reduced scattering and $0.001\,\mathrm{mm}^{-1}$ for absorption measurements on the polyurethane phantom (single-sphere data from (fig. 3.9) for the 6.35, 12.7, 19.05 and 25.4 mm sample ports and a 4 mm beam diameter. In these data sets, f varies from 0.07–0.15. There are two cases where corrections for f are substantial (1-5% error): when more than half of the light is initially incident upon the sphere wall or when the sample reflectance is close to zero. Both cases are the result of a poorly designed experiment and are best avoided. Therefore, I believe that it is unnecessary to make a measurement of f to accurately determine optical properties using the presented method of signal normalization.

Our model assumes that specularly reflected light is collected inside the integrating sphere. Some integrating spheres are designed to trap the reflected specular light [79]. A light trap acts as an additional port with zero reflectivity. Whether or not specular collection is collected makes little difference, provided the inversion model is consistent with the experiments.

The foundation of the presented IAD/MC inversion model is based on eqs. 3.2 and 3.3 for single sphere experiments and eqs. 3.6 and 3.6 for double sphere experiments. The lone restriction for these equations is that a baffle is present between the sample and the detector blocking direct reflections between the ports. These equations are consistent with

previous integrating sphere models [88, 92, 94]. The complexity in the equations is contained by the sphere gain for substitution mode experiments. The gain terms quantify the effect of multiple reflections caused by the presence of the sphere relating to the efficiency of light incident on the detector port. The gain term for single sphere experiments is functionally related to the sample reflectance. However, double sphere gain also depends on the transmission of the sample because it also includes the cross-talk of light traveling between the spheres through the sample. It is possible to create an inversion model for any method of signal normalization based on the equations 3.2, 3.3, 3.6, and 3.6, as they are universal in describing an individual measurement recorded with an integrating sphere with a baffle.

3.5.3 Best practices

There are many ways that integrating spheres may be employed to measure reflectance and transmittance. Therefore, I address the variables involved with spheres to elucidate how to obtain the best results. To begin, I consider the difference between single or double sphere measurements. The use of two spheres allows for the simultaneous measurement of reflectance and transmittance which is necessary for monitoring dynamic processes. However, the use of two spheres is more involved than a single sphere arrangement . For example with two spheres, the sample ports must be aligned and the sample held between the ports without gaps for light to escape. Single sphere arrangements are more versatile in that either comparison mode or substitution mode can be made whereas only the latter mode can be performed using two spheres. Substitution mode is better suited for measurements using white light sources which inevitably produce some light that is initially incident upon the sphere wall. Comparison measurements have the advantage that no sphere corrections are necessary only if absolutely all light is initially incident upon the sample (or standard). Therefore, the comparison mode is best suited for sources which are easily collimated such as lasers.

The effect of the sphere upon measurements in substitution mode is related to the choice of the reflection and transmission reference. The magnitude of the correction for transmittance is nearly equal to the correction reflectance, but never greater than the

correction for reflectance when a 99% reflectance standard is used as the reference. It should also be noted that in reflectance, the smaller the difference between the reflectance of the standard and the sample, the smaller the correction is for the sphere. Therefore when a sample is expected to have low reflectivity, the extrapolation between the true and measured values for a comparable reflectance standard would be much less than for a 99% standard. Thus, the likelihood for error due to the sphere corrections would be reduced for inexact values of the sphere parameters (e.g. sphere wall reflectance).

Without light loss corrections, the choice of a sample port size is restricted by the ratio of beam diameter to the sample port [95, 106]. The physical dimensions of the sample, the integrating sphere port, the optical properties of the sample, and the size of the incident beam all contribute to the amount of light lost out through the side of the sample. For a fixed port diameter, the light loss is smaller for thinner samples, samples with higher absorption and scattering coefficients, and for smaller diameter illumination beams. The amount of light escaping the sample edges decreases with larger diameter sample ports for both direct and diffuse illumination. The combined IAD/MC inversion model gives consistent absorption results regardless of port size. The advantage of using larger ports is that generally fewer MC simulations will be performed in calculating light loss before convergence thereby reducing the calculation time. In comparing sample port sizes with the polyurethane phantom (6.67 mm thick), a 25.4 mm port needed an average of 2.4 iterations. The 19.05 mm sample port averages 3.4 iterations, the 12.7 mm port averages 5.8 iterations and the 6.35 mm sample port averages 13.5 iterations. Each iteration adds about 4 minutes per 100 data points. However, the sample should not be smaller in dimension than the port. An under-filled sample port can be accounted for by increasing the area of the entrance port by the same area by which the sample does not cover the port. This practice is difficult to quantify and is likely to increase error in the predicted absorption.

Erroneous determination of optical properties occurs when information is lacking in the reflectance and transmittance. When the transmission measurement has a value of zero, it becomes impossible to obtain both the absorption and reduced scattering for the sample. In this case, only the ratio of absorption to scattering (or rather the reduced albedo,

$\frac{\mu_s'}{\mu_s'+\mu_a}$) is uniquely determinable. Less obvious is the limited information when the sum of the reflectance and transmittance is close to one. The sum of absorption, reflection and transmission must equal the incident power. When the absorption is small, the accuracy is limited by the precision of both the reflectance and transmittance measurements. An example of this condition occurs in the visible region (450–550 nm) of figure 3.11. In that region, the measured absorption coefficient is 0.001–0.004 mm^{-1} greater than the polyurethane matrix absorption alone [103]. The limit of absorption resolution is 0.001 mm^{-1} for samples on the order of 10 mm thick for a reduced scattering of 0.9 mm^{-1}.

The use of an optical fiber to illuminate the sample alters the effect of the entrance port. In addition, the use of a sleeve [5] to direct and hold the optical fiber near the sample in a reflection measurement deserves discussion. The effect of a sleeve is to close a portion of the area of the entrance port and translate that area to a position inside the sphere. It is assumed that the sleeve is coated so that it has the same reflectance as the sphere wall or is inside the sphere when measuring the average sphere wall reflectance. The sleeve then behaves as a baffle inside the sphere. To verify that the sleeve had minimal impact, I measured diffuse light inside a 200 mm diameter sphere with and without a sleeve inserted approximately 170 mm (data not shown). The two measurements were indistinguishable.

The combined IAD/MC model may also be used to evaluate the scattering anisotropy (average cosine of the scattering angle) with a third measurement of the fraction of unscattered transmission. A port may be open opposite the sample in a transmission measurement to let the unscattered light pass to a detector far from the sphere [96,99,101]. Though double spheres arrangements are necessary to measure dynamic processes, an experimental error is introduced in the transmittance [107]. Roos shows that a fraction of highly forward scatttered light also escapes along with the unscattered transmission through the port. Additional measurements can be made to estimate the fraction escaped [107]. However, a measurement of the unscattered transmission is simple to measure independently without the integrating sphere. A good unscattered transmission measurement requires that a sample be optically thin, preferably having an optical thickness $\tau < 5$ ($\tau = (\mu_a + \mu_s)d$ where d is the sample thickness) [95]. High albedo samples often will need large optical thickness to resolve small absorption coefficients relative to the scattering coefficient

which is contrary to the unscattered transmission preference. Separate independent measurements of the unscattered transmission prevent conflict by using two sample thickness which are appropriate for each measurement. The unscattered transmission should then be included in the integrating sphere transmittance.

Sample handling

Biological tissue samples provide a unique challenge to measure optically. The method of handling of a sample may cause dramatic differences in the optical properties. Tissue dehydration effects the refractive index of the tissue [108], its scattering characteristics [109], and even absorption [110]. Sandwiching a tissue between glass or quartz plates limits the rate at which a tissue dehydrates and provides support and well defined boundary conditions for soft tissues and fluids. Additionally saline may be sandwiched with the tissue to clamp the hydration level of the tissue. Compression of tissue can lead to an increase in scattering and absorption due to a reduction in tissue volume increasing chromophore and scatterer concentrations [111] The inverse adding-doubling algorithm calculates the Fresnel reflections of incident light from the sample [83]. A flat surface to the sample simplifies the accounting for Fresnel reflections whereas a rough sample will specularly reflect light in all directions in the integrating sphere.

3.6 Conclusions

The combined IAD/MC model was demonstrated to accurately determine optical properties of homogenous optically turbid samples with a reasonable precision using multiple sample thicknesses and sample port sizes. Inversion of optical properties from integrating sphere measurements requires a theoretically compatible inversion model and experimental methods otherwise gross error occurs. With substitution method sphere measurements, the inversion model must correct for the sphere gain which increases the measured reflectance and decreases transmittance. A 3D model such as Monte Carlo is essential to correct for light lost through sample edges which improves the resolution and accuracy of samples with small absorption coefficients. With these two corrections, experimental

error becomes comparable in magnitude to the error in the predicted optical properties for the presented IAD/MC model.

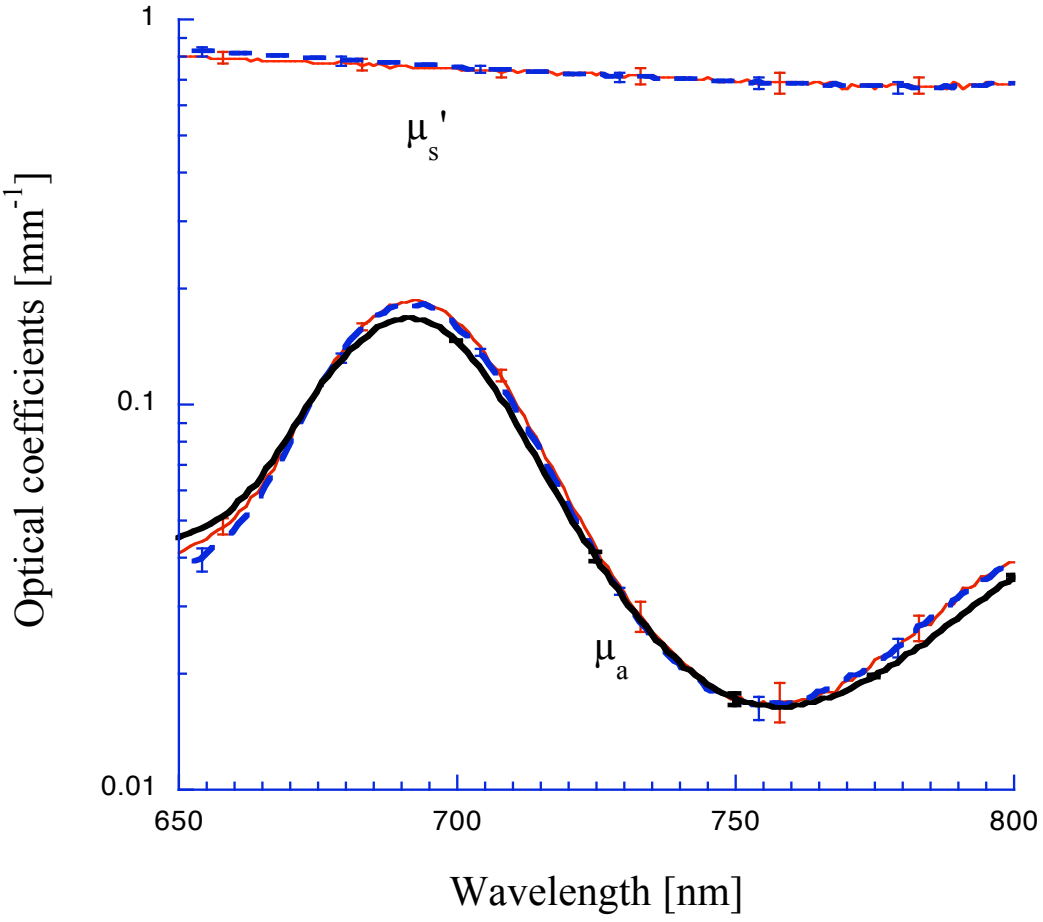

Figure 3.9: The calculated mean absorption and reduced scattering coefficient for a 6.67 mm thick polyurethane phantom measured with sample port sizes of 6.35, 12.7, 19.05, 25.4, 31.75, 44.45 and 50.8 mm in diameter for a single-sphere measurements is shown (solid thin line). Error bars indicate the standard deviation. The calculated mean absorption and reduced scattering coefficient for a 4.9 and 6.7 mm thick identical polyurethane phantoms measured with sample port sizes of 19.05, 31.75, 44.45 and 50.8 mm in diameter for a double-sphere measurements is shown as the dashed line. The illumination beam was 4 mm in diameter on the sample in all measurements. The bold line is the absorption coefficient determined by the spectrometer for a phantom without scatterer.

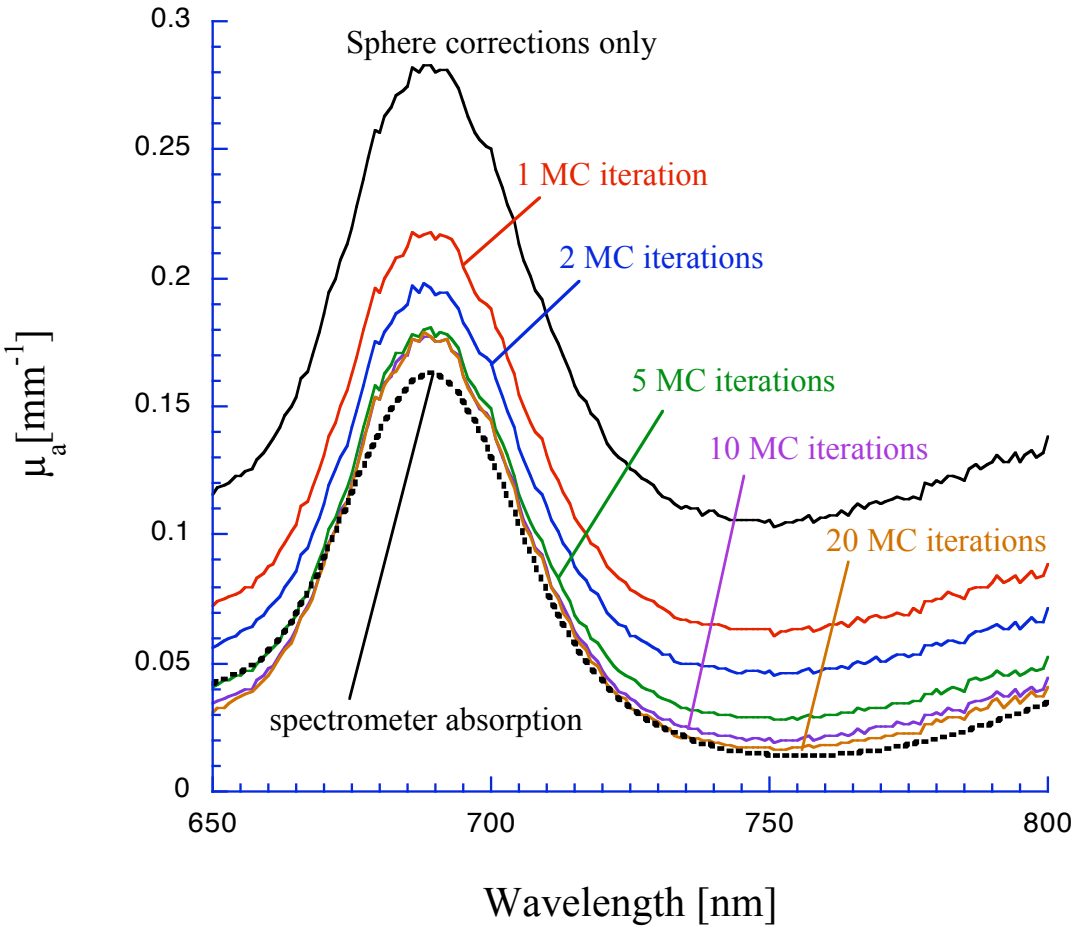

Figure 3.10: The calculated absorption coefficient for a 6.67 mm thick polyurethane phantom measured with a 6.35 mm diameter sample port and 4 mm illumination beam. The dashed curve is the absorption coefficient measured for a phantom without added scatterer. After 5 iterations of a Monte Carlo simulation to correct for light lost through the sample edge, the absorption was over-predicted at coefficients less than 0.1 mm^{-1}, but by less than a factor of 2.

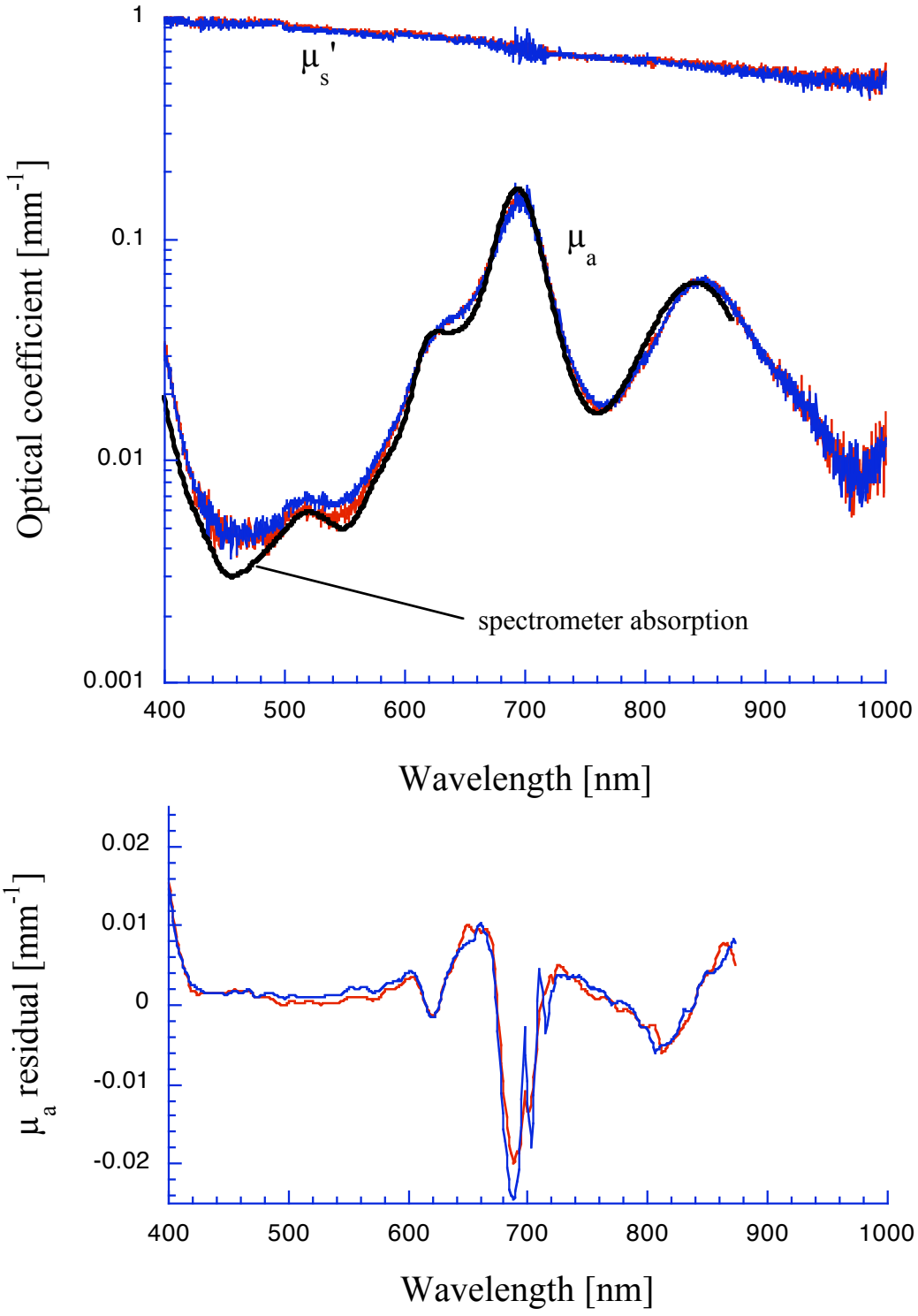

Figure 3.11: The absorption and reduced scattering coefficient for two thicknesses (4.93 and 6.67 mm) of a polyurethane phantom. The intrinsic absorption of the polyurethane at 450 nm is 0.004 $mm^{-}1$ [103]. For comparison, the absorption coefficient measured for a phantom without added scatterer is shown as a bold line.

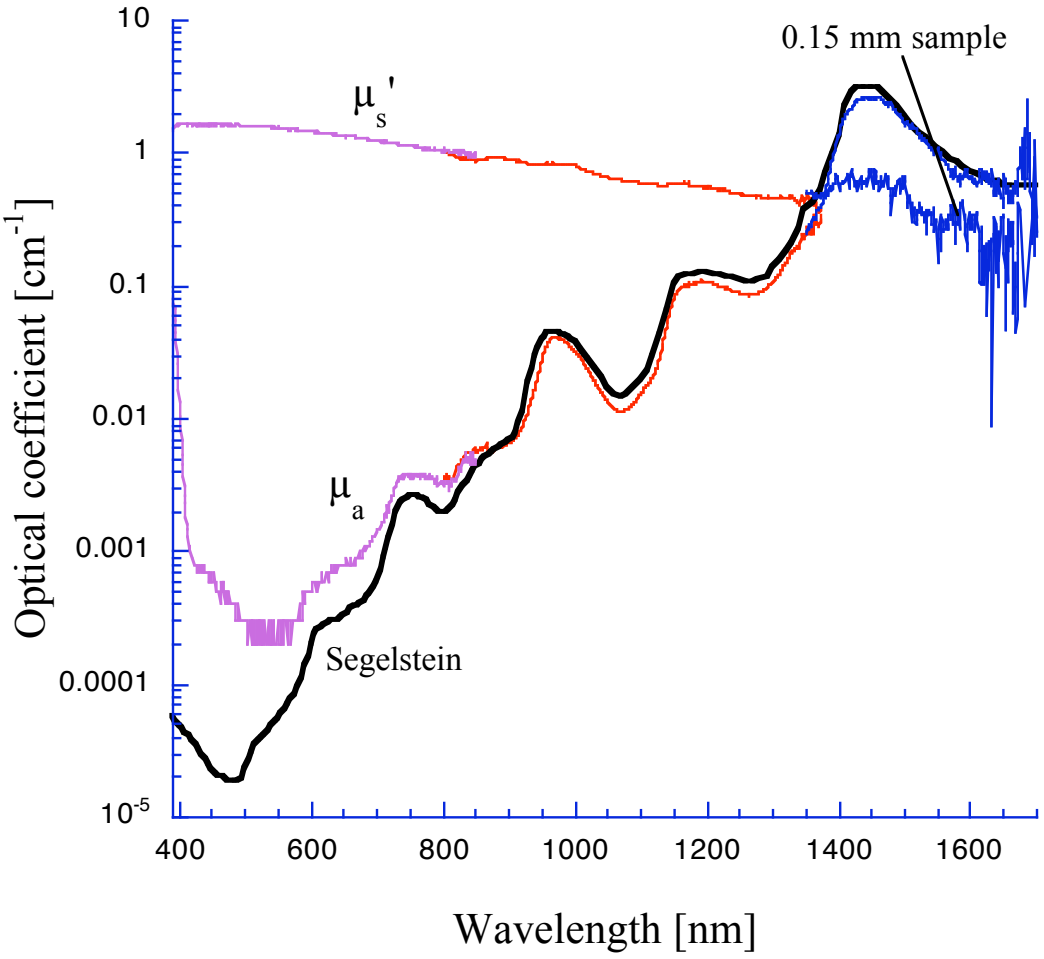

Figure 3.12: The reduced scattering and absorption coefficients determined with the inverse adding-doubling algorithm for single sphere experiments. The absorption coefficient for the 0.15 mm sample is shown from 1350–1700 nm. For comparison, the absorption coefficient of water compiled by Segelstein [104] is shown.

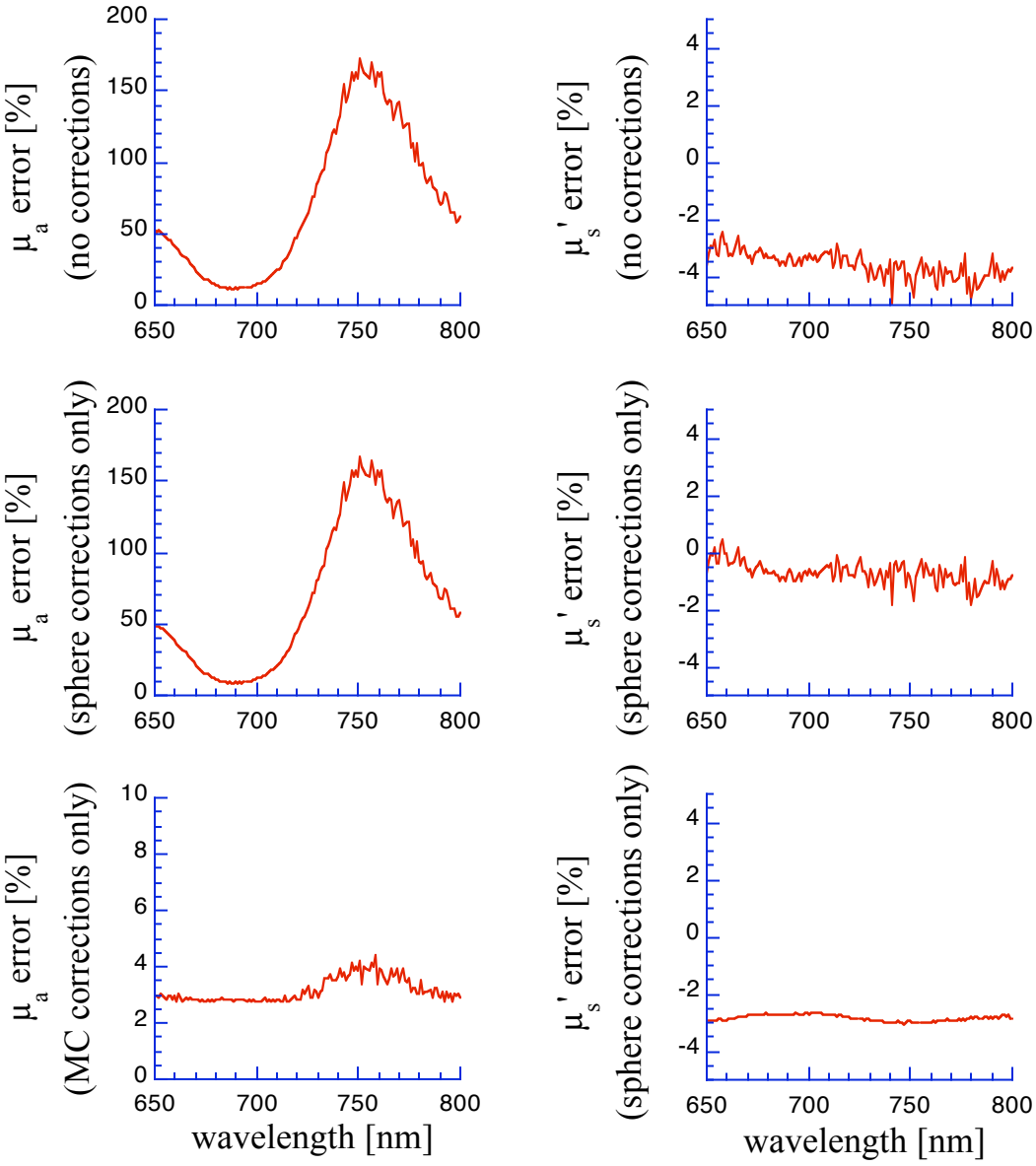

Figure 3.13: The percent change for the absorption coefficient and reduced scattering coefficient for no corrections (top), for sphere corrections only (middle), and for lost light corrections (bottom). Sphere corrections account for the non-linear relationship between the reflectance (transmittance) and the sample reflectivity (transmissivity). Lost light is predicted using Monte Carlo simulations of the sphere experiment.

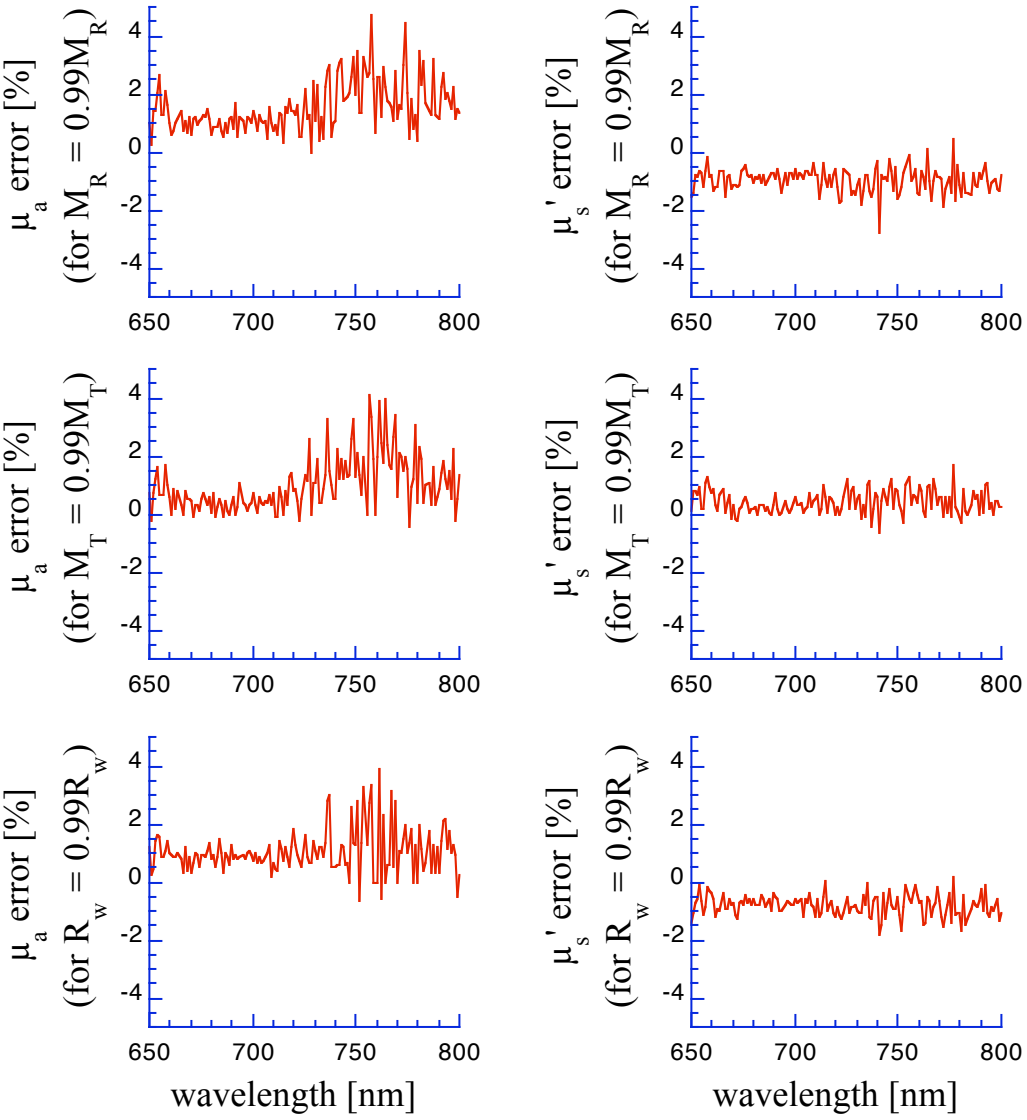

Figure 3.14: The percent change for the absorption coefficient and reduced scattering coefficient for a 1% underestimate of the reflectance (top), transmittance (middle), and the sphere wall reflectivity (bottom). The perturbations shown correspond to single sphere experiments using a 25.4 mm diameter sample port with the 6.67 mm thick polyurethane phantom.

Chapter 4

Sized-Fiber Reflectometry for Measuring Local Optical Properties

4.1 Introduction

Determining the optical scattering and absorption properties of tissue for diagnostic and therapeutic applications is of interest in medicine. For example, the dosimetry of photodynamic therapy is greatly dependent upon the scattering and absorption properties [48,112] for both light delivery and measurement of drug concentrations. Optical properties have been used to estimate exogenous [113, 114] and endogenous [115] chromophore concentrations. Moreover, light scattering and absorption can provide information about both chromophore content and structure, which might be used to distinguish normal and malignant tissues as well as chemical state information [116, 117] (e.g. oxy- versus deoxy-hemoglobin). In this regard, an optical biopsy can be performed using optical information of hemoglobin and water content differences in normal and malignant tissue [23, 74].

Several techniques and algorithms have been developed to measure the optical properties. Spatially [16, 37, 39] and temporally [22, 31, 118] resolved measurements have been proposed to extract the optical properties using light distributions based on diffusion theory [17, 119] and/or Monte Carlo simulations [120]. A wide variety of algorithms have been explored to extract optical properties including neural network [121] and multiple polynomial regression methods [122]. However, most reflectance techniques rely on light

distribution information over a large area ($>1\,\mathrm{cm}^2$) or have separate illumination and collection fibers with a separation distance on the order of 1 cm.

Much work has been compiled on devices with separate source and detector fibers. Two studies show that the mean photon penetration depth increases as the square root of the separation between source and detector fibers either spatially [123] or temporally [124]. Source-detector fiber devices sample relatively large volumes, because of the separation between the fibers. Though effort has been made to minimize the sampling volume using small source-detector separations [125], little work has been done on photon penetration depths when the source fiber is also used to collect backscattered photons [1]. Since large sampling volumes are less likely to be homogenous, we developed a device that acquires information from small volumes of tissue ($< 1\,\mathrm{mm}^3$) by using the same fiber for both source and detector to minimize the sampling volume.

We propose a compact dual-fiber device to make simple and rapid measurements of the absorption and reduced scattering properties of tissue. Each fiber illuminates and collects light independently of the other fiber. The device is based on the fact, that in general, tissues with different scattering and absorption properties will scatter different numbers of photons back into a fiber. If only a single fiber is used, two samples with different optical properties could backscatter the same number of photons. This paper proposes a device containing a second, different size fiber to make a second measurement. This second fiber collects information from a different effective volume of the sample than the first fiber.

In this study, we present experiments on an Intralipid tissue model and Monte Carlo simulations to elucidate the details of light emission and collection with a single fiber. As a first step, we conduct single wavelength experiments at 632.8 nm with a device using 200 and 600 μm fibers to assess the feasibility of extracting optical properties for these fiber sizes. We have adapted the sized-fiber system for use with white light (500–800 nm) to measure the wavelength dependent absorption and reduced scattering coefficients (herein referred to as μ_a and $\mu_s' = (1-g)\mu_s$, respectively). Experimental results are presented for an array of Intralipid solutions of known absorption, 0.1–2.0 cm^{-1}, and reduced scattering, 5.2–52 cm^{-1}. Monte Carlo simulations of a 200 and 600 μm fiber device are presented for comparison. Also presented are experiments and Monte Carlo simulations of the

penetration depth of photons collected by two fiber sizes, 200 and 600 μm in diameter. Finally, Monte Carlo simulations are used to determine the effect numerical aperture of a fiber and the influence of mode filling of the fiber on reflectance measurements.

4.2 Materials and Methods

4.2.1 Sized-Fiber Device

The sized-fiber device uses a pair of bifurcated fibers to separate the illumination light from the backscattered light. The first of these is made by end-coupling two 300 μm diameter fibers onto the face of a 600 μm diameter fiber with SMA connectors. The second bifurcated fiber consists of two 100 μm diameter fibers end-coupled to a 200 μm fiber also using SMA connectors. One each of the 100 and 300 μm fibers have He-Ne laser light (632.8 nm) focused onto their face. The remaining 100 and 300 μm fibers are coupled to UDT silicon photodiodes. The ends of the 200 and 600 μm fibers are epoxied (120387, Dymax Corp., Torrington, CT) together by UV curing and then polished (Fig. 4.2). All fibers are fused silica glass/glass from Polymicro Technologies LLC, Phoenix, AZ. The manufacturer cites a numerical aperture of 0.22 which corresponds to a maximum exit angle of 12.7 degrees in air. We measured 13 ± 1 degrees for both emission and transmission with the 200 and 600 μm fibers for the maximum acceptance angle. The maximum half-angle for acceptance, θ depends on the numerical aperture of the fiber, NA $= n \sin\theta$, where n is the index of refraction of the surrounding medium. This corresponds to an angle of 9.5 degrees for our fibers in water. The distal ends of the 200 and 600 μm fibers are sleeved through one meter of polycarbonate tubing (6.2 mm O.D., 4.7 mm I.D.) to inhibit tight bending of the fibers. The 100 and 300 μm fibers outside the polycarbonate tubing are kept fixed throughout the experiments so that losses through the fiber cladding remain relatively constant from measurement to measurement in those sections of fiber. Two choppers (MC 1000, Thorlabs Inc., Newton, NJ) operating at 690 Hz and 700 Hz eliminate cross-talk between fibers. The reflectance signal from each fiber is detected by a lock-in amplifier (LIA 100, Thorlabs Inc., Newton, NJ). The fibers are rinsed in a water bath then washed with ethyl alcohol between measurements. Washing the fibers is critical

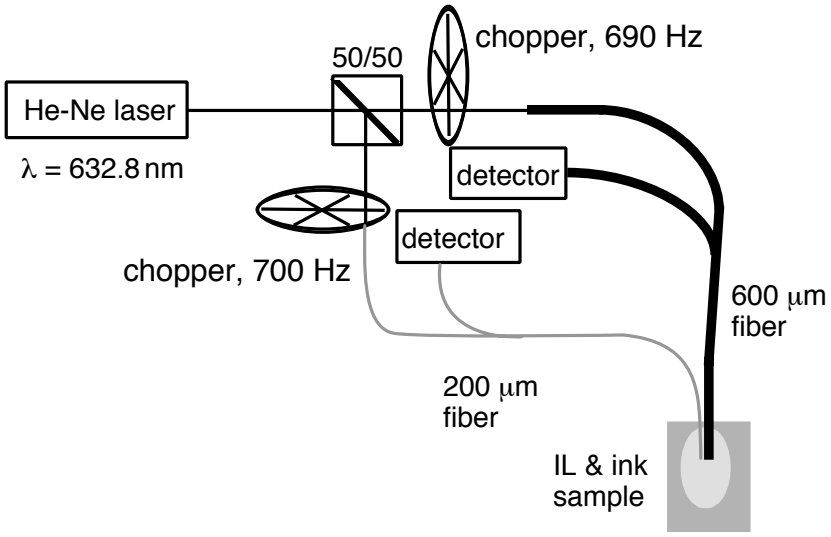

Figure 4.1: This is a diagram of the sized-fiber device. A pair of bifurcated fibers emit and collect light simultaneously by chopping at two distinct frequencies exceeding 690 Hz. The fibers are submerged at least 1 cm into the Intralipid to eliminate boundary effects.

for reproducibility with the Intralipid tissue model which can leave an oily residue on the fiber that affects later measurements.

The sized-fiber device also works with white light reflectometry [126]. A tungsten-halogen white lamp (LS-1, Ocean Optics,Inc., Dunedin, FL) couples to the source fibers via the SMA connectors. The collection fibers are coupled into a spectrometer (s2000, Ocean Optics,Inc., Dunedin, FL). The spectrum is processed in near real-time using LabView (National Instruments, Austin, TX). A baffle must be inserted so that only one fiber emits and collects at a time, since cross-talk will not be rejected with this method.

All data points are normalized by using Fresnel reflection from the fiber face in air and water. The voltage returned from the photodiode is converted by

$$\text{Reflectance} = \frac{(V_{sample} - V_{water})}{(V_{air} - V_{water})} * (3.46\% - 0.19\%) + 0.19\%$$

where 3.46% is the Fresnel reflectance for the fiber core/air junction and 0.19% is the Fresnel reflectance for the fiber core/water junction at normal incidence. Measurements of the air and water Fresnel reflectance are taken periodically throughout the experiments

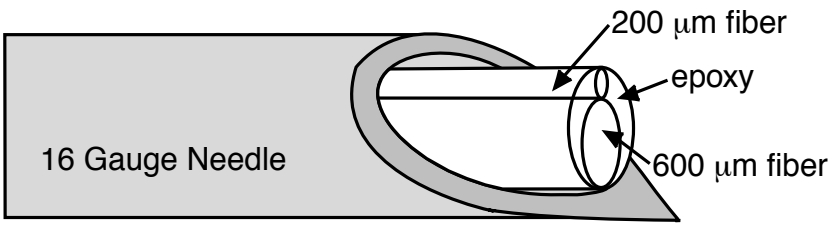

Figure 4.2: The 200 and 600 μm fibers are joined with a medical grade epoxy so that they may be simultaneously inserted through a needle for measurement of tissues. The two fibers can easily fit through a 16 gauge needle. When measuring tissues, water is placed at the tip of the fiber to reduce the index mismatch between the fiber cores and the tissue.

to correct for any variations in laser power.

4.2.2 Tissue Model

For tissue phantoms with known absorption and reduced scattering properties, an array of Intralipid (Liposyn II, Abbott Laboratories, North Chicago, IL) and India ink mixtures with optical properties in the range of tissues were constructed. Five dilutions of the Intralipid are made from a single bottle of Intralipid making concentrations of 1, 2, 4, 9 and 10% (10% lipid indicates 10 g of lipid per 100 ml of suspension) to be used as stock solutions. Also five stock solutions of India ink (No. 4415, Higgins, Lewisburg, TN) and deionized/distilled water are made with absorption of 0.2, 0.4, 1.0, 2.0, and 4.0 cm^{-1} at 632 nm as measured using a spectrophotometer (HP 8452A). The absorption of light at 632 nm by Intralipid [61] is less than 0.01 cm^{-1} at the highest concentration and thus is negligible in comparison to absorption by the India ink. The phantoms are made by mixing one part of each Intralipid concentration to one part of each ink solution for a total of 25 samples. The resultant solutions have all possible combinations of Intralipid concentrations of 0.5, 1, 2, 4.5, and 5% corresponding to reduced scattering coefficients of 5.2, 10.4, 20.8, 46.8, and 52.0 cm^{-1} and absorption coefficients of 0.1, 0.2, 0.5, 1.0, and 2.0 cm^{-1} at 632 nm. The optical properties are determined by $R(r)$ measurements [17] and cross-checked using total diffuse reflectance measurements using an integrating sphere [95] in conjunction with inverse adding-doubling [127]. We measured a reduced scattering

coefficients of $104\,\mathrm{cm}^{-1}$, which is between those of and Flock et. al [61] and van Staveren et. al. [128] who measured of 65 and $130\,\mathrm{cm}^{-1}$ respectively for 10% Intralipid.

4.2.3 Chicken Breast Experiment

Chicken breast, purchased from the supermarket, was measured using the sized-fiber device inside a 16 gauge needle. The needle was filled with water before inserting the optical fibers to aid the coupling of light between the fibers and the tissue. The needle was inserted into the muscle along the muscle grain in three locations. The needle was withdrawn and inserted so that the needle tip was in the same three locations but oriented perpendicular to the muscle grain for the second set of measurements. All the measurements were performed within 5 minutes to minimize changes in the optical properties due to dehydration of the tissue. Additionally, paper towels saturated with phosphate buffered saline covered the chicken between measurements.

4.2.4 Planar Absorber Effect on Signal Experiment

To measure the effect of an absorbing boundary on the signal detection, the Thorlabs lock-in amplifiers were replaced by SR830 lock-in amplifiers (Stanford Research Systems, Sunyvale, CA) for their phase adjustment capability and improved signal to noise ratio. Optically thick India ink mixed in acrylamide was used for an absorbing plane. The 1 cm thick acrylamide was set in the bottom of a 50 ml beaker. The Intralipid phantom described above with an absorption coefficient of $0.5\,\mathrm{cm}^{-1}$ and reduced scattering coefficient of $20.8\,\mathrm{cm}^{-1}$ covered the black acrylamide layer. The fibers were brought into contact with the gelatin before the Intralipid was added to obtain a zero position. The fibers were backed away from the surface for a distance of 1 cm. Measurements were then recorded for the 200 and $600\,\mu$m fiber simultaneously in 0.1 mm increments until the fibers were submerged into the gelatin. At this point the signal was constant and equal to the Fresnel reflection of the fiber in water. Measurements of the reflectance in air and water were also recorded for calibration.

4.2.5 Monte Carlo Simulations

A Monte Carlo program was adapted to simulate the light collected by a fiber irradiating an infinite homogeneous scattering and absorbing medium; the fiber face was the only boundary included into the simulations, thus neglecting the sides of the fiber (e.g. the fiber jacket, etc.). Experimental results confirm the validity of the computer simulations (Fig. 4.3). Also, the photon penetration depth was tracked to give insight as to the volume being sampled for each size fiber. Additional simulations were performed to examine the effect of photon launching angle and the effect of varying the numerical aperture.

The geometry of the Monte Carlo simulation is set up as follows. Let the z-axis be parallel with that of the fiber so that the face of the fiber is in the $z = 0$ plane. Photons are launched with equal probability over the entire face of the fiber. The direction by which photons are launched is specified by the direction cosines (ν_x, ν_y, ν_z). The angle $\nu_z = \cos\theta_z$ is given a Gaussian distribution that depends on the acceptance angle of the fiber while the other direction cosines are uniformly distributed. The angular distribution chosen approximates the emission from the fibers but due to under-filled modes, the experimentally measured distribution is not a true Gaussian but only deviates by 12%. The distribution of angles that the photon might take is given by the function

$$p(\theta_z)d\theta_z = \frac{1}{\sqrt{2\pi}} \exp\left(-\frac{\theta_z^2}{2\theta_a^2}\right) d\theta_z$$

where θ_a is the acceptance angle for the fiber. Moreover, the angles were limited such that $\theta_z \leq \theta_a$.

The primary statistic collected by the Monte Carlo program was the fraction of light backscattered into the fiber. Photons which were collected must pass back through the fiber face. Only photons that had an angle less than or equal to the maximum acceptance angle for the fiber were counted into the diffuse reflectance. The maximum acceptance angle for the fiber was input into the program for the fiber in air, then converted using Snell's law for the index of refraction for the incident medium. Photons incident on the fiber face but outside the cone of acceptance were attributed to light lost through the cladding. The acceptance angle was corrected for the index of refraction change of the medium. The index of refraction for the core of the fiber was assumed to be 1.457 as

given by the manufacturer's specifications; 1.333 was used for the index of the medium. A returning photon's weight was attenuated due to an index mismatch for both launching and collection using the Fresnel reflection for normal incidence introducing an error $\approx 0.02\%$. The anisotropy was chosen to be 0.83 in accordance to Flock *et. al.* [61]. In a single simulation, a minimum of 20,000 photons were launched ten times for each simulation to accumulate statistical error of the mean. Specular reflectance due to the index mismatch at the fiber face while launching was added to the diffuse reflectance to get the total reflectance.

In the depth profiling absorbing plane simulations, 400,000 photons were launched. A perfect absorbing planar boundary was added parallel to the x-y plane. The collected diffuse reflectance was related to the fiber-plane separation distance, simulating the experiment in section 2.4. Additional simulations were performed with the absorption held fixed at $0.5\,\mathrm{cm}^{-1}$ while the scattering was varied ($\mu_s' = 8.5$–$34\,\mathrm{cm}^{-1}$) and with the reduced scattering fixed at $21\,\mathrm{cm}^{-1}$ while absorption was varied ($\mu_a = 0.05$–$2.0\,\mathrm{cm}^{-1}$). In the Monte Carlo code, the photon weight became zero when it crossed into the absorbing plane. The location of the boundary, determined by a z-position was varied for each set of optical properties.

Finally, the maximum angles for launching and collection were varied independently. The maximum angle (measured from the normal of the fiber face) for the launching photons was varied independent of the collection angle, to simulate under-filling of fiber modes. The maximum launch angle was stepped in two degree increments while the collection angle was held fixed at 12 degrees for the fiber in air. Next, the maximum launch angle was held fixed while the maximum acceptance angle of the fiber was varied to evaluate the sensitivity with respect to numerical aperture. The acceptance angles chosen were concentrated around 13 degrees for the fiber in air (for a NA ≈ 0.2) and then extended to include very small and large NA fibers (0.02–0.65). For all simulations the optical properties were held constant with $\mu_s = 61.18\,\mathrm{cm}^{-1}$, $\mu_a = 0.5\,\mathrm{cm}^{-1}$, and g = 0.83.

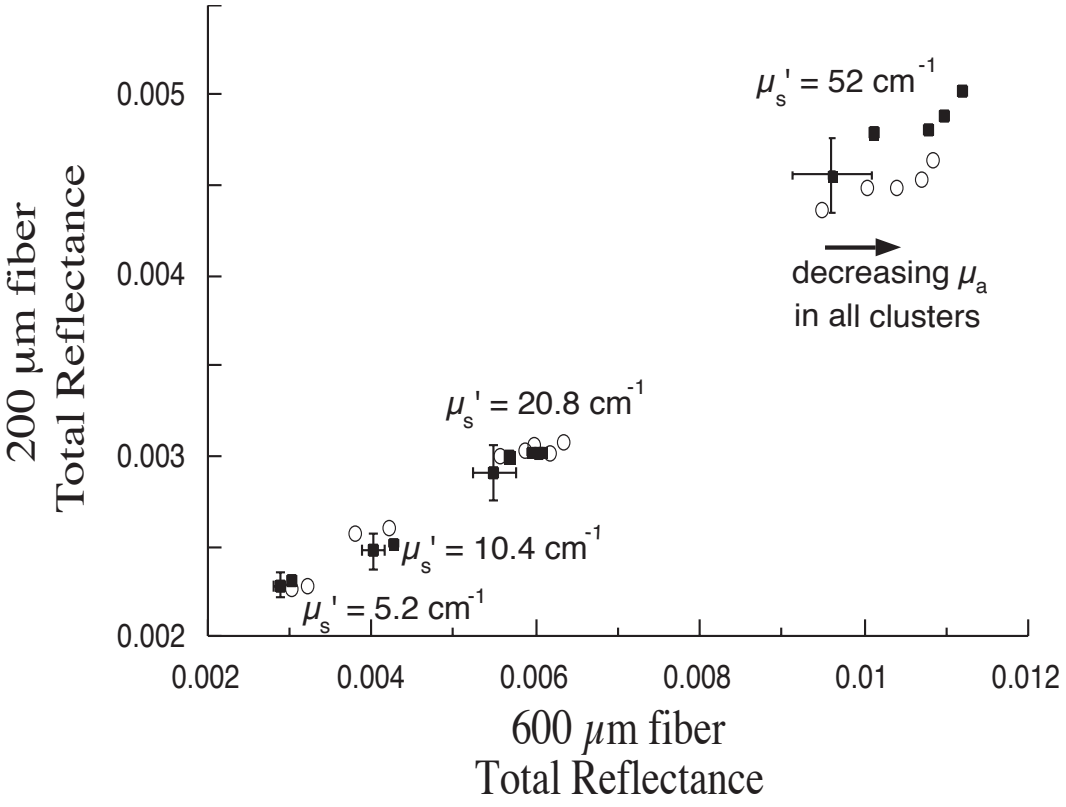

Figure 4.3: The optical properties can be determined from a mapping of the reflectance for each fiber. The open circles are the experimental measurements of each sample. The solid squares are the Monte Carlo simulation results. For samples with $\mu_s' = 5.2$ and $10.4\,\mathrm{cm}^{-1}$, Monte Carlo results are only shown for $\mu_a = 0.1$ and $2.0\,\mathrm{cm}^{-1}$ for clarity.

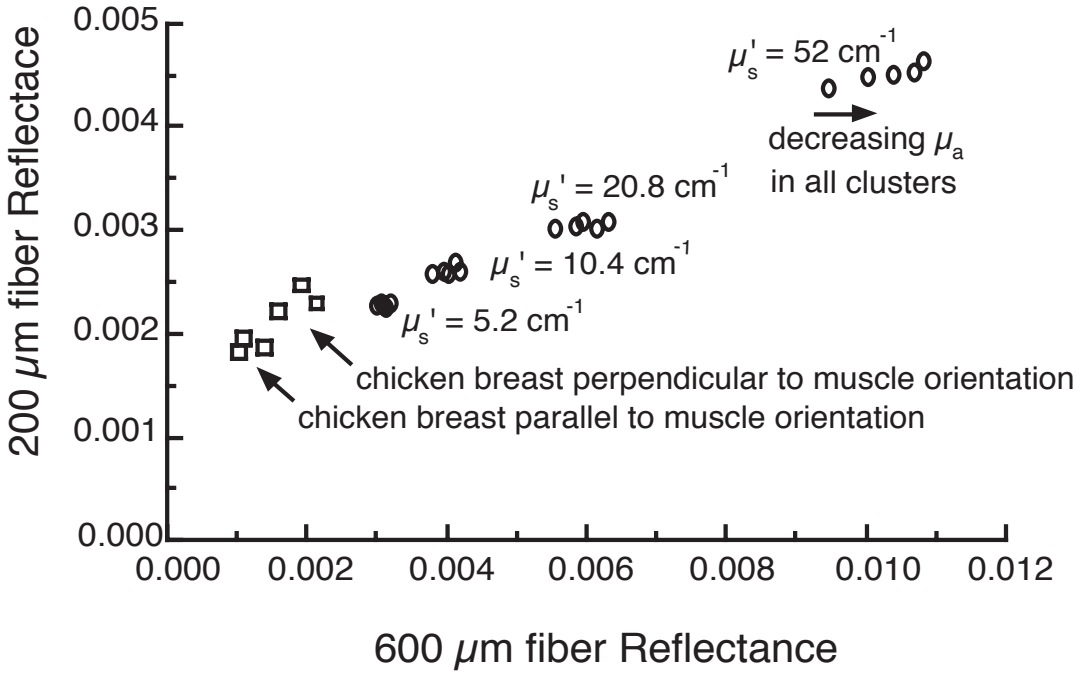

Figure 4.4: Measurements of the twenty Intralipid mixtures and repeated measurements of chicken muscle with two distinct fiber orientations relative to the muscle grain. Each cluster is a constant Intralipid concentration with five different absorption coefficients which decrease from left to right.

4.3 Results

4.3.1 Tissue Model

Fig. 4.3 shows measurements of the Intralipid array as well as the results of the Monte Carlo simulations. The experimental variation in measurement was smaller than that returned by the simulations. Typical experimental variation are shown in Fig. 4.5.

Fig. 4.4 also shows twenty measurements of the samples (the 4.5% Intralipid are omitted for clarity) along with *in vitro* chicken breast. All concentrations of ink are shown at each Intralipid concentration. Each cluster represents solutions with the same scattering coefficient. Within each cluster, the higher absorbing solution has a lower reflection with respect to the 600 μm fiber reflectance. Marijnissen [129] *et. al.* reported a scattering coefficient for chicken muscle ($\mu_s' = 3.3\,\mathrm{cm}^{-1}$ and $\mu_a = 0.17\,\mathrm{cm}^{-1}$) which agrees with the

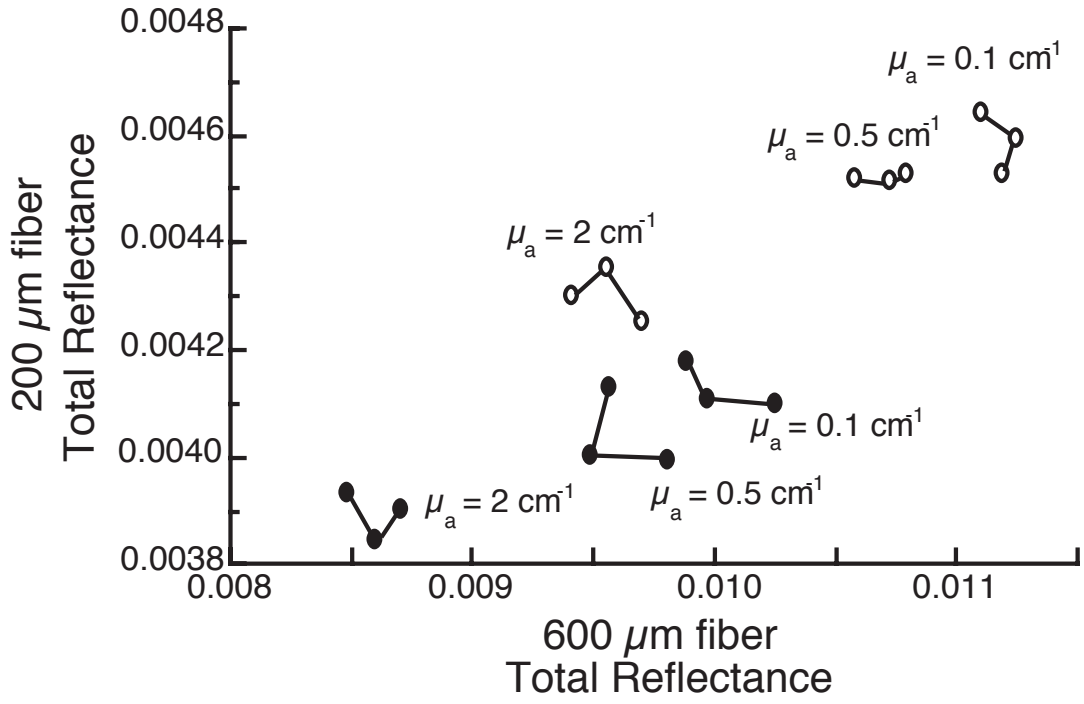

Figure 4.5: Independence of sized-fiber measurements for two scattering samples with three different absorption coefficients. The filled and unfilled circles correspond to $\mu_s' = 47$ and $52\,\mathrm{cm}^{-1}$ respectively. Each joined cluster of three points represents three measurements on a single sample.

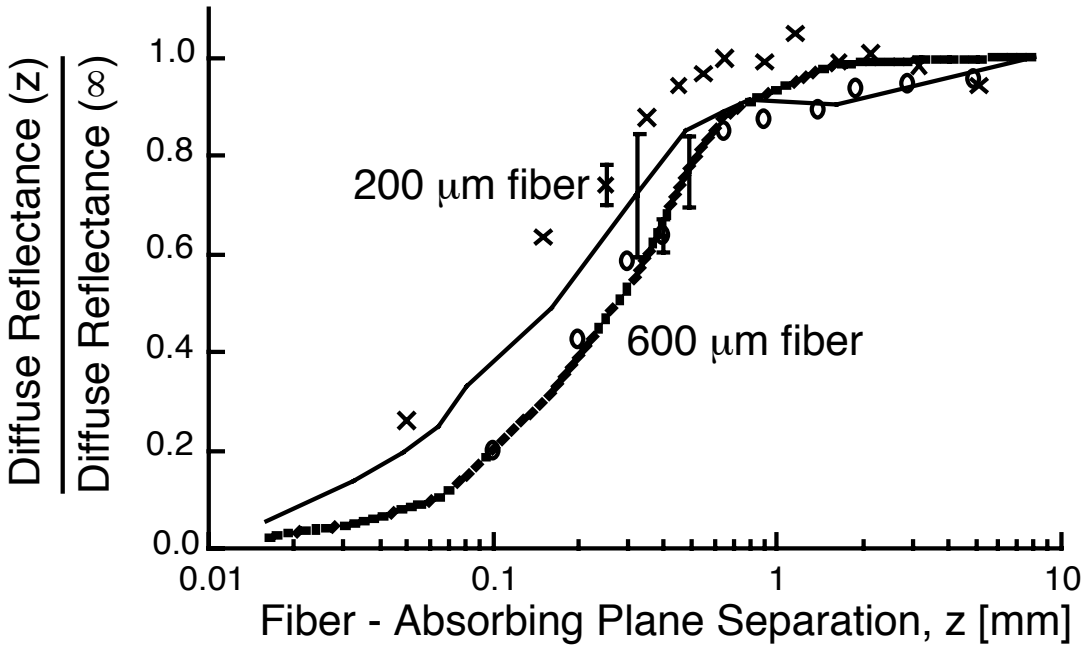

Figure 4.6: The signal attenuation for 200 and 600 μm fibers is shown as the fibers approach an absorbing plane of India ink in acrylamide gelatin. The signal is normalized to the diffuse reflectance measured in the intralipid solution far from boundaries ($\mu_s' = 10.4\,\mathrm{cm}^{-1}$, $\mu_a = 0.5\,\mathrm{cm}^{-1}$, g = 0.83). The curves represent Monte Carlo simulations of the experiment with standard errors of the mean and the points are the experimental data.

data presented here, but the absorption coefficient of chicken is unresolvable with the sized-fiber device for such a low scattering coefficient. Fig. 4.5 shows a comparison of the 5% Intralipid samples with absorption coefficients of 0.1, 0.5, and $2.0\,\mathrm{cm}^{-1}$ with 4.5% Intralipid solutions with the same absorption coefficients. A slight decrease of scattering ($\Delta\mu_s' = 5.2\,\mathrm{cm}^{-1}$) in one sample relative to another is distinguishable by a drop in the 200 μm fiber reflectance. A drop in the reflectance also occurs as the absorption increases but the effect is more pronounced with the 600 μm fiber reflectance measurement.

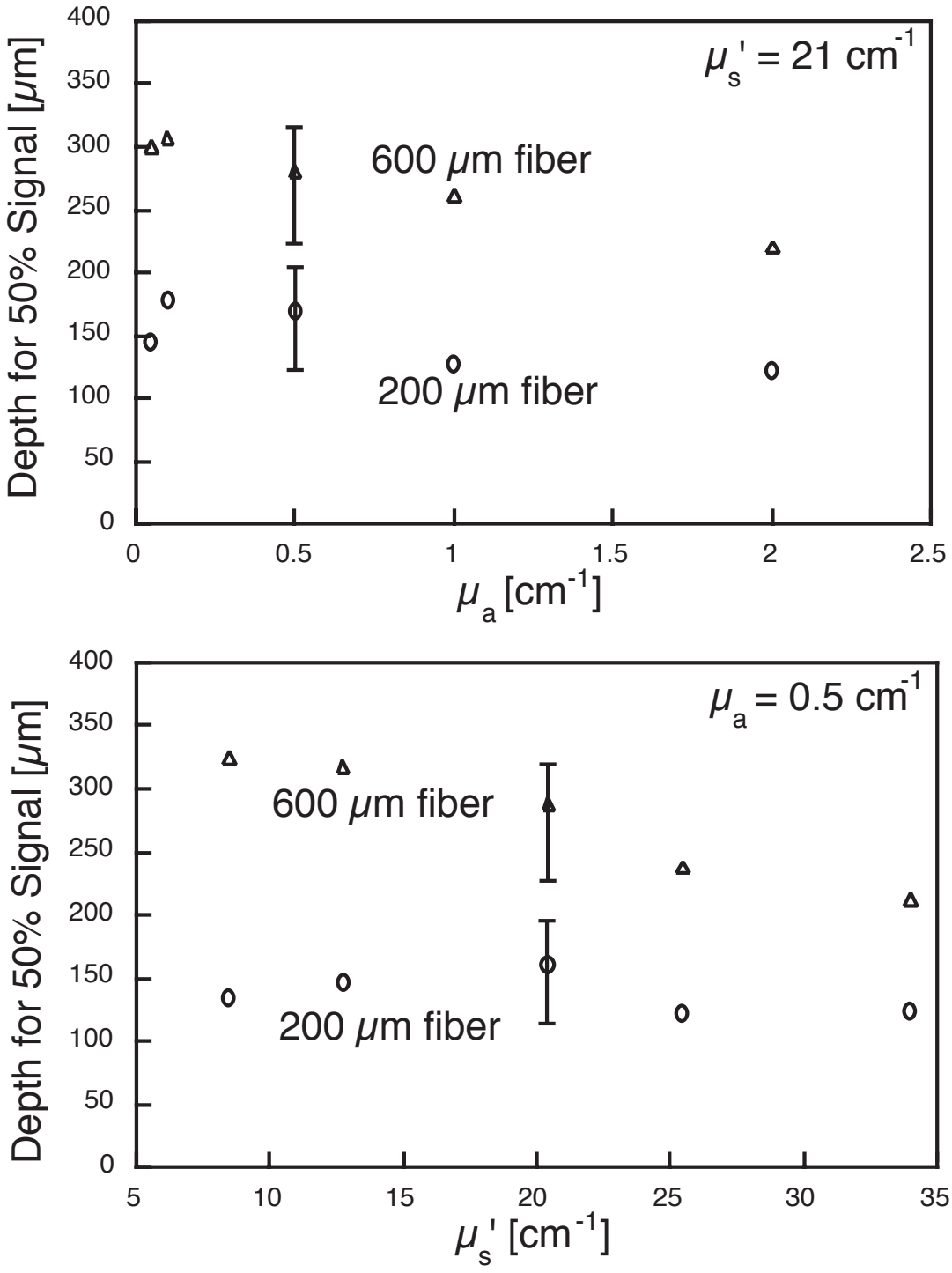

Figure 4.7: Monte Carlo simulations show the separation between a fiber and an absorbing plane where a 50% drop in signal occurs for variations in the absorption and scattering properties. The anisotropy is set to 0.83 to simulate Intralipid.

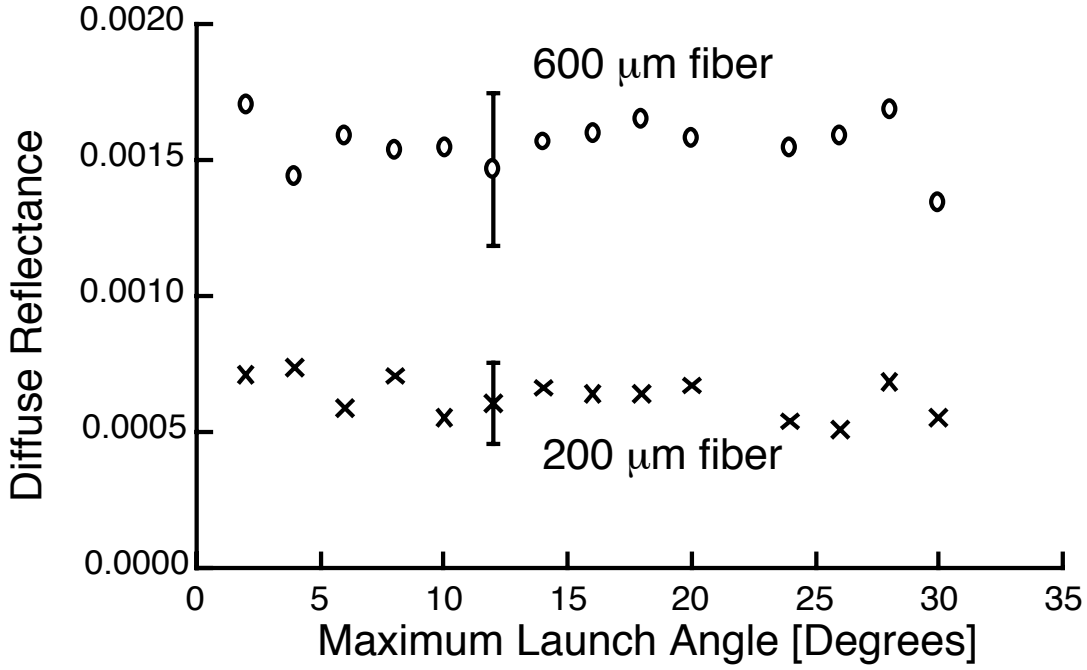

Figure 4.8: For a fixed acceptance angle of the fiber, the maximum angle of launch from a gaussian distribution does not influence the diffuse reflectance collected. This suggests that complete mode filling of the fibers is unnecessary to obtain a consistent result; and by extension, modal variation of the emission does not have any effect upon the measurement. The optical properties used are $\mu_s' = 10.4\,\mathrm{cm}^{-1}$, $\mu_a = 0.5\,\mathrm{cm}^{-1}$, and g = 0.83.

4.3.2 Monte Carlo Simulations

The effect of attenuation near an absorbing plane is shown experimentally in Fig. 4.6. Monte Carlo simulations are also shown which are confirmed by the experimental results. All reflectances are normalized by dividing the perturbed signal by the reflectance that would be measured in the same turbid medium when the fibers are far from any boundaries. Fig. 4.7 shows Monte Carlo results of the 200 and 600 μm fibers indicating at what distance the diffuse reflection drops in half due to a perfectly absorbing plane with respect to independent variation of the absorption and scattering properties.

Monte Carlo simulations also show that the photon launch angle has no effect upon the reflectance collected by the fiber as shown in Fig. 4.8. Thus, the photon launching distribution is inconsequential to the amount of backscattered light collected by the fiber.

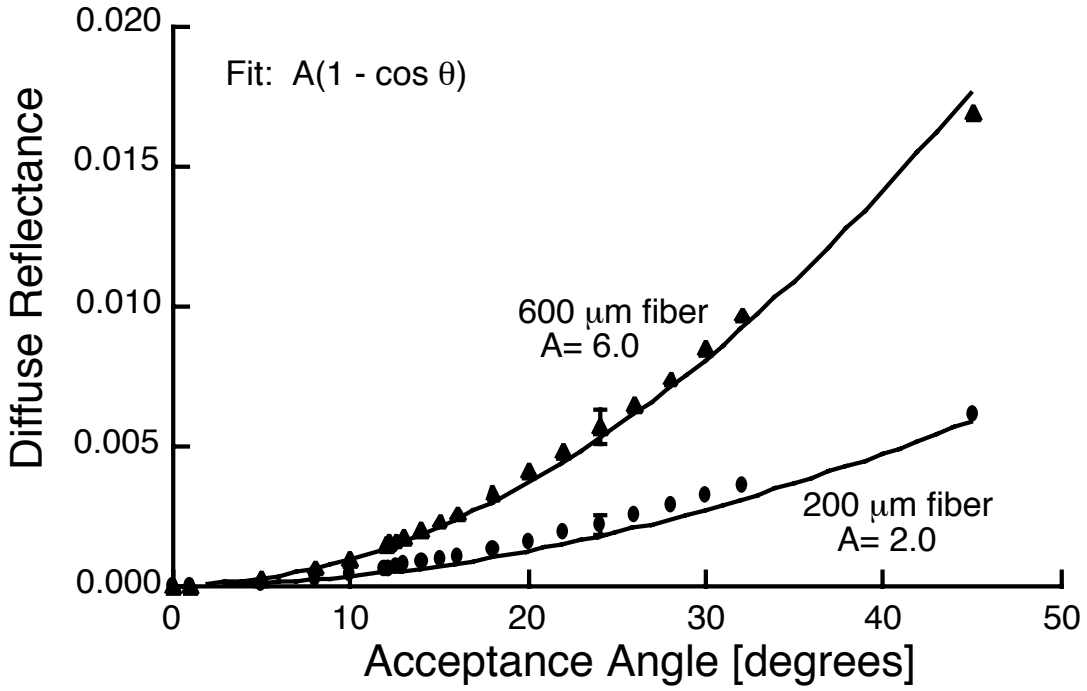

Figure 4.9: The fraction of diffuse light collected by each fiber is dependent on the acceptance angle of the fiber θ in air, increasing with a $1-\cos\theta$ dependence which follows from a geometrical result if light returns to the fibers uniformly from all directions. A is a scaling parameter to fit the relation. The photon launch angle distribution is held constant and only the acceptance angle of the fiber is varied. The optical properties used are $\mu_s' = 10.4\,\mathrm{cm}^{-1}$, $\mu_a = 0.5\,\mathrm{cm}^{-1}$, and $g = 0.83$.

On the other hand, the numerical aperture of the fiber affects the amount of light collected from the tissue. Figure 4.9 shows Monte carlo simulations which demonstrate how the collected diffuse reflectance varies with the maximum acceptance angle dictated by the fiber numerical aperture. The change in maximum half-angle of acceptance has a $1-\cos\theta$ relation to the amount of light collected where θ is the half-angle of the maximum cone of light propagated by the fiber.

4.4 Discussion

Monte Carlo simulations give information about the photons backscattered into the illumination fiber; in particular, the fraction of light collected by the fiber increases with

the maximum angle of acceptance for the fiber following $1-\cos\theta$. The $1-\cos\theta$ dependence is the expected geometric result if the light returning to the fiber is uniform in all directions at the fiber face. The fraction of light collected for this case is the ratio of the area of a spherical cap bounded by the numerical aperture cone, divided by the area of a hemisphere, $\frac{2\pi r^2(1-\cos\theta)}{2\pi r^2} = (1-\cos\theta)$. Furthermore, the angular distribution for which photons are emitted from the fiber is independent of the fraction of light collected by the fibers as shown in Fig. 4.8. This is a significant detail which indicates that complete mode filling of a fiber is unnecessary to obtain consistent results, and implies that modal variation in emission does not have any effect upon the measurement. Finally, the angular dependence of both the emission and the collection of photons indicate that light returning to the fiber is uniformly distributed over all directions.

Smaller fibers collect less light and are less sensitive to optical property changes. The relationship between fiber size and sensitivity can be explained by crudely approximating the light returning to the fiber by an isotropic point source, positioned one reduced mean free path from the fiber face. If $\rho_{\text{fiber}} = (\mu_a + \mu_s')\text{R}_{\text{fiber}}$ is the radius of the fiber in reduced mean free paths, then the half-angle of the cone formed by the point source and the face of the fiber is $\theta_c = \tan^{-1}\rho_{\text{fiber}}$. The fraction of light returning to the fiber can be estimated by the solid angle subtended the face of the fiber relative to the point source divided by 4π steradians (all directions). This fraction reduces to the form,

$$\frac{2\pi\text{mfp}'^2(1-\cos\theta_c)}{4\pi\text{mfp}'^2} = \frac{1}{2}\left(1-\frac{1}{\sqrt{\rho_{\text{fiber}}^2+1}}\right) \approx \frac{\rho_{\text{fiber}}}{4}$$

where $\text{mfp}' = \frac{1}{\mu_a+\mu_s'}$ is the reduced mean free path. For this crude approximation when $\frac{\rho_{\text{fiber}}}{4}$ drops below 1/12 then our system cannot resolve absorption changes less than $2\,\text{cm}^{-1}$. A diffuse point source [17] cannot be used to estimate the amount of the returning light to the fiber because the diffusion approximation is invalid at this distance. In general, as the reduced mean free path increases, the signal collected decreases such that, for reduced mean free paths greater than $500\,\mu$m, the $200\,\mu$m fiber can no longer resolve changes in absorption smaller than a factor of two (e.g., absorption coefficients of 0.5 and $2.0\,\text{cm}^{-1}$ are clearly distinct from $1.0\,\text{cm}^{-1}$). The $600\,\mu$m fiber can resolve changes in absorption by a factor of two for reduced mean free paths up to $1900\,\mu$m.

We found that the 200 and 600 μm fiber system gives optimal resolution when the reduced scattering coefficient is in the range 20–52 cm^{-1}, corresponding to a reduced mean free path range of 190–500 μm. In this range, absorption coefficients of 0.1, 0.2, 0.5, 1.0 and 2.0 cm^{-1} are distinct and changes of 5 cm^{-1} in the reduced scattering coefficient are resolved by this system. Tissues within this range at visible wavelengths include but are not limited to aorta, brain, liver, lung and skin [44]. Differentiation and characterization of tissue is ideally suited for UV/visible wavelengths rather than NIR/IR due to shorter scattering pathlengths in the UV/visible range. When the reduced mean free path for scattering is 500–1900 μm, only absorption coefficients of 0.1, 0.5, and 2.0 cm^{-1} are distinct. For reduced scattering mean free paths above 1900 μm, the absorption coefficient resolution becomes larger than 2 cm^{-1}.

Additionally, we determined that larger fibers collect light from deeper in tissue than smaller fibers. Fig. 4.6 shows that more than half the signal is from photons traveling 1.2 mean free paths into the medium for a 200 μm fiber and 1.9 mean free paths for a 600 μm fiber. The depth for which half of returning photons travel is fairly insensitive to changes in the absorption and the scattering coefficient as shown in Fig. 4.7. Pogue and Burke [27] suggest that light being collected by a 200 μm fiber has an average of 1.2 scattering events while the 600 μm fiber has 1.5 scattering events for $\mu_s' = 10\,\mathrm{cm}^{-1}$ and $\mu_a = 0.1\,\mathrm{cm}^{-1}$, which agrees well with our results, though our results are for an absorption coefficient of 0.5 cm^{-1}. Fig. 4.7 shows that the mean depth of photon travel does not change significantly for absorption in the range of 0.05–2.0 cm^{-1}. Also, nearly 90% of all the collected photons travel less than 800 μm (approximately 1 reduced mean free path) into the medium for both fiber sizes. Effectively, both fibers are sampling the same depth of tissue; however, a greater fraction of photons undergo a single scattering event before returning to the 200 μm fiber than for the 600 μm fiber. In other words, larger fiber diameters collect a greater proportion of multiply scattered photons than smaller fibers.

This study demonstrates feasibility of a sized-fiber device using 200 and 600 μm fibers. We have shown that measurements taken with this device on a Intralipid tissue model agree with our Monte Carlo simulations over a range of absorption 0.1–2.0 cm^{-1}, and reduced scattering, 5.2–52 cm^{-1}. However, further studies are needed. An inversion technique

relating optical properties to fiber reflectance has yet to be implemented. An empirical relation between reflectance and optical properties would be preferable, yet the 200 μm fiber signal is nearly independent of the absorption properties in the range of this study and may be directly related to the reduced scattering coefficient. The 600 μm signal could then be corrected for scattering to extract the absorption coefficient. With an inversion technique, an *in vivo* study measuring optical properties with the sized-fiber device can be performed. Furthermore, studies on anisotropy need to be addressed to determine if the system can resolve tissues with the same reduced scattering coefficient but differ in anisotropy and scattering coefficients.

Sized-fiber measurements have several advantages. The device is compact and measurements can be taken through a needle or endoscope. Real-time monitoring can be performed with the device using a broad spectral source which is best suited in the UV/visible. System calibration only requires measurement of the Fresnel reflectance of air and water. Finally, the device acquires localized information from a volume less than a cubic millimeter extending no more than a millimeter from the fiber face when absorption is resolved.

Chapter 5

Specular Reflection Problem with a Single Fiber for Emission and Collection

5.1 Introduction

A single fiber may be employed to emit and collect light from an optically diffusing medium such as a biological tissue. However, the light returned by the fiber consists of three components: Illumination light, specularly reflected light from the surface, and diffusely scattered light from within the tissue. The first component can be eliminated by using a bifurcated fiber design. Of the remaining signal, only the diffuse reflection contains the desired information regarding the optical absorption and scattering properties of the tissue. Unfortunately, the specular component is comparable in magnitude to the diffuse reflection for visible light. The refractive index mismatch between the fiber and tissue account for a portion of the specular reflection. However, imperfect contact of the fiber with the surface of tissue creates additional boundaries and thus additional specular reflections. In this chapter, the effects of surface contact of the fiber face to the medium are examined to reduce inter-measurement variation.

Sized-fiber reflectometry is founded upon the idea of using the same fiber for emission and collection of light. The collected light is related to the absorption and reduced scattering of tissue. A sized-fiber reflectometer consists of two fibers with diameters of 200 and 1000 microns. Each fiber emits and collects its own backscattered light but the larger

Portions of this chapter were originally published under the title "The specular reflection problem with a single fiber for emission and collection." by T. P. Moffitt and S. A. Prahl in *SPIE Proceedings of Saratov Fall Meeting: Optical Technologies in Biophysics and Medicine*, Vol. 5068, 2002.

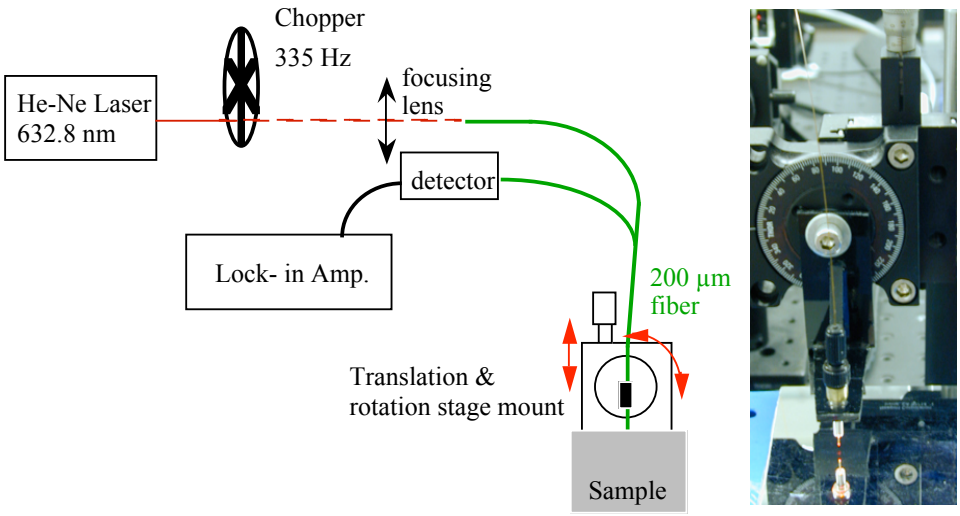

Figure 5.1: The experimental set-up consists of two 100 micron fibers that are end-coupled to a 200 micron fiber to separate illumination from collection light. The photo on the right shows the fiber mounted in the positioning stages over a first surface mirror.

fiber collects light that on average travels deeper into the tissue [130]. The absorption and reduced scattering properties can be determined using a lookup table based on Monte Carlo simulations of the diffuse reflectance collected by these fiber sizes.

The goal of this study was to determine the contribution of the specular reflection to variation between measurements. We examine the effect of contact by a fiber with the surface of a sample to elucidate its influence on the specular reflectance collected by the fiber. Measurements of pure specular reflection are measured by independently varying the angle of contact a fiber makes with a front-surface mirror. Next, the fiber was positioned normal to the surface of the mirror to measure the effect of displacement between fiber face and the surface. These two experiments were then repeated on a epoxy resin block with diffuse scattering properties. Finally, a comparison is shown for the effects of specular reflection collected using perpendicular polished fiber and a fiber with a beveled tip.

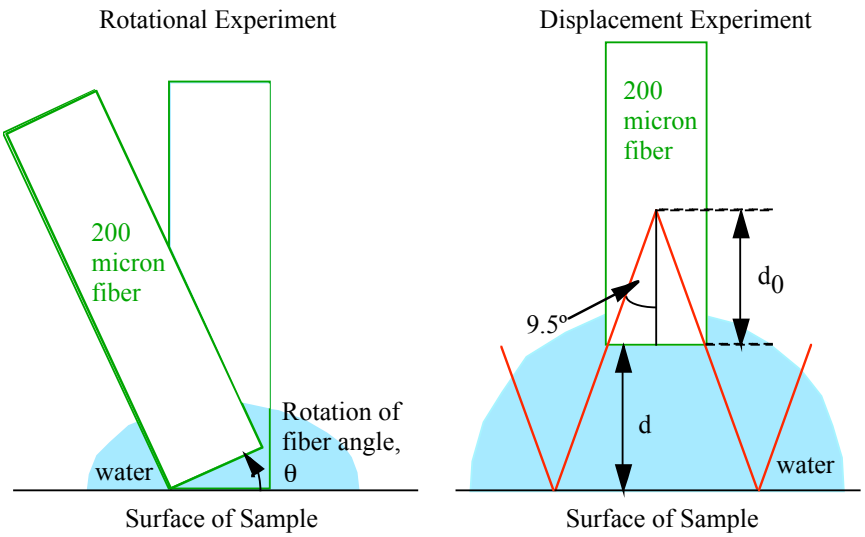

Figure 5.2: Diagrams of the geometry used for the angular rotation of the fiber (left) and the displacement of a fiber form the surface (right).

5.2 Materials and Methods

A single fiber was bifurcated to separate the illumination light from the back-scattered light [130]. A 200 micron fiber was used for emission and collection by being end-coupled to a pair of 100 micron fibers mounted together in an SMA connector. The light source consisted of a 632.8 nm He-Ne laser that was chopped (MC1000, Thorlabs Inc., Newton, NJ) at 335 Hz then focused into one 100 micron fiber. The back-scattered light was channeled through the other 100 micron fiber to a UDT silicon photodiode. A lock-in amplifier (SR830, Stanford Research Systems, Sunyvale, CA) was used to display the voltage produced by the photodiode. All fibers were fused silica glass/glass from Polymicro Technologies LLC, Phoenix, AZ. The manufacturer cited a numerical aperture of 0.22 that corresponds to a maximum exit angle of 12.7 degrees in air. The maximum acceptance angle in air was measured to be 13 ± 1 degrees for the 200 micron fiber. All fibers were encased in Teflon tubing and polished flush in SMA connectors.

Fiber positioning relative to the sample surface is achieved by mounting the 200 micron fiber simultaneously to both a rotation and a translation stage. The sample is set onto

a lab-jack to allow coarse movement of the sample relative to the fiber. To test angular effects, the angle is set with the rotation stage, then the fiber is lowered until the fiber just touches the sample surface using a vernier translator (figure 5.2 left). To test displacement, the fiber angle is aligned perpendicular to the sample and the fiber is brought into contact with the surface using the vernier translator (figure 5.2 right). In all measurements, a drop of water is placed on the sample to act as a coupling agent between the fiber and the surface of the sample.

Two different samples were used for all measurements: a first surface mirror and an epoxy resin block. The mirror returns only specularly reflected light. The resin block is a solid sample with added absorber (India ink) and a scattering agent (Titanium dioxide). The resin block has a large flat surface area that is smoothed with 400 grit sandpaper. Thus the block has some specular reflection in addition to diffusely reflected light. The optical properties of the block are similar to those found in tissue: $\mu_s' \approx 10/\text{cm}$ and $\mu_a \approx 1.0/\text{cm}$ at 632.8 nm.

Data points are normalized using Fresnel reflection from the fiber face in air and water. The voltage returned from the photodiode is converted by

$$\text{Total Reflectance} = \frac{V_{sample} - V_{water}}{V_{air} - V_{water}}[R_{air} - R_{water}] + R_{water}$$

where $R_{air} = 0.03465$ is the Fresnel reflectance for the fiber core/air junction, $R_{water} = 0.00204$ is the Fresnel reflectance for the fiber core/water junction at normal incidence. V_{sample}, V_{water}, and V_{air} are the measured voltages for the fiber incident upon the sample, water, and air respectively. The fiber core has an index of refraction of 1.457 at the 632.8 nm wavelength. Measurements of the air and water Fresnel reflectance are taken periodically throughout the experiments to correct for any variations in light output.

Comparison measurements are made with fibers that are polished at a 65 degree angle tip. The beveled fiber face reduces specular reflections therefore normalization is given by

$$\text{Reflectance} = \frac{(V_{sample} - V_{water})}{(V_{standard} - V_{water})} * (\%\text{ reflection of standard})$$

where V_{sample}, $V_{standard}$, and V_{water} are the detector voltages returned from the tissue sample, a resin block standard, and the specular reflection for the fiber in water. Repeated

measurements were recorded for both probe designs on a resin block tissue phantom and a single spot of skin on the dorsal side of the forearm. Water was used to couple light between the fiber and the samples, though for measurements on the resin block no measurable difference was observed with or without water. The fibers were held by hand in the support mount during each measurement and the fiber was completely removed from the surface of the sample and replaced between all measurements. The skin was marked with a ball point pen by outlining the plastic fiber support to ensure proper alignment. A maximum of five measurements were recorded in succession on the forearm to prevent pressure induced erythema. Measurements were recorded for specular reflections from the fiber face in air and in water. Specular reflection measurements were also made with the fiber faces in contact to a first surface mirror using translation and rotation stages to position the fibers.

5.3 Results

Measurement to measurement variation is demonstrated in figure 5.3 showing the distribution of the total reflectance measured on an epoxy resin standard when the fiber was held by hand and when the fiber was mounted (stationary). Typical measurement variation for the forearm is shown in figure 5.4. The fiber was mounted in an SMA connector to achieve measurement consistency. Direct pressure from a bare fiber caused the signal to increase steadily in excess of 200 percent of the initial value over a period 30 seconds.

Figure 5.5 shows the contribution due to specular reflection when the central-axis of the 200 micron fiber is not normal to a first surface mirror but remains in contact with the mirror. Figure 5.6 shows the deviation in total reflectance when the central-axis of a 200 micron fiber is not normal to a surface on an epoxy resin block, but the fiber still maintains contact with the surface of the block.

Figure 5.7 shows contributions due to the specular reflection when the fiber is displaced from the surface while remaining normal to the surface. Figure 5.8 shows the effect of the specular reflection change due to a displacement of the fiber from the surface of an

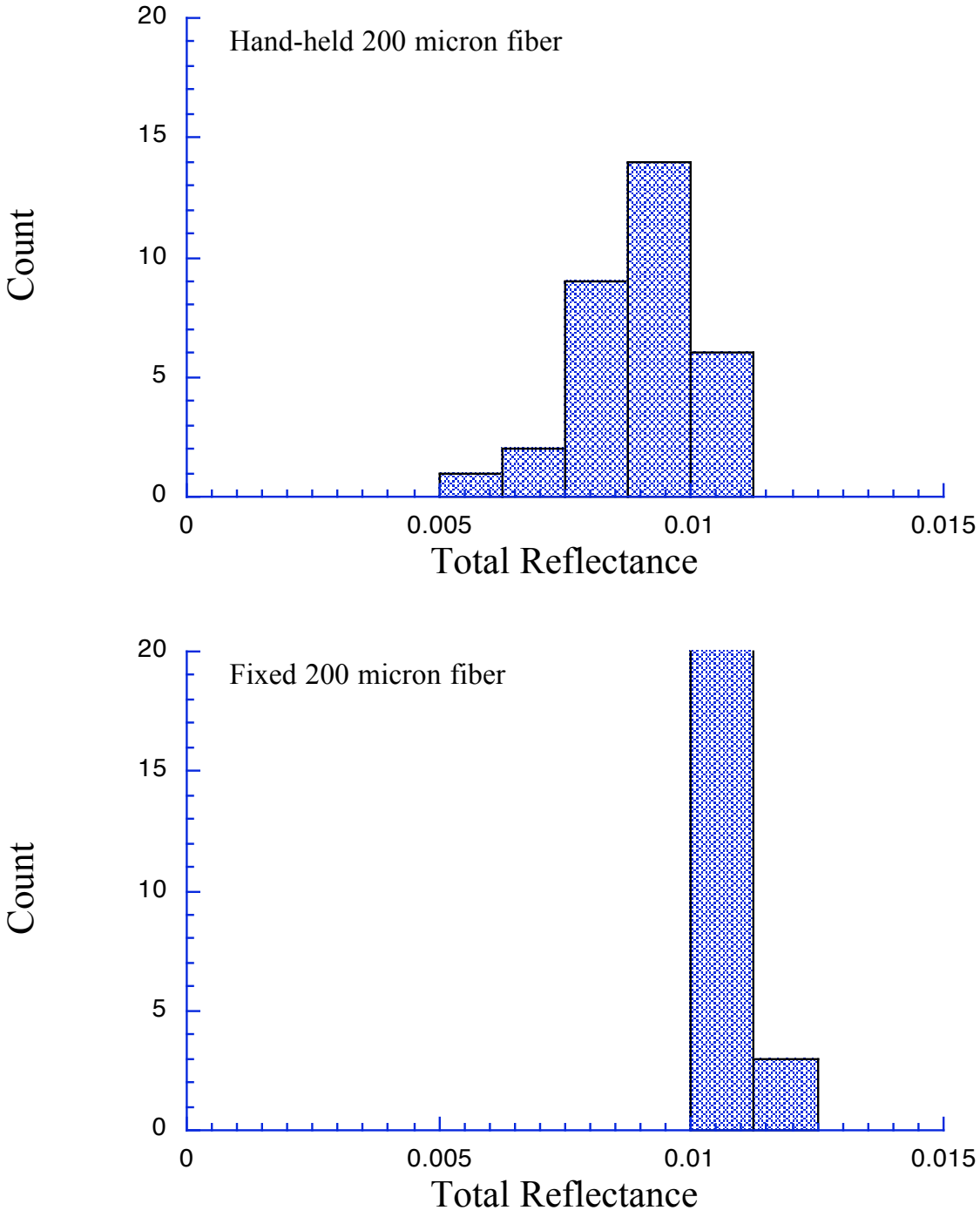

Figure 5.3: Distribution of 32 measurement of a diffusely scattering epoxy resin block with a 200 micron fiber when the fiber is held by hand (Top) and when the fiber is mounted to a translation stage and positioned in contact with the block (Bottom). The fiber is lifted from the surface of the block between every measurement.

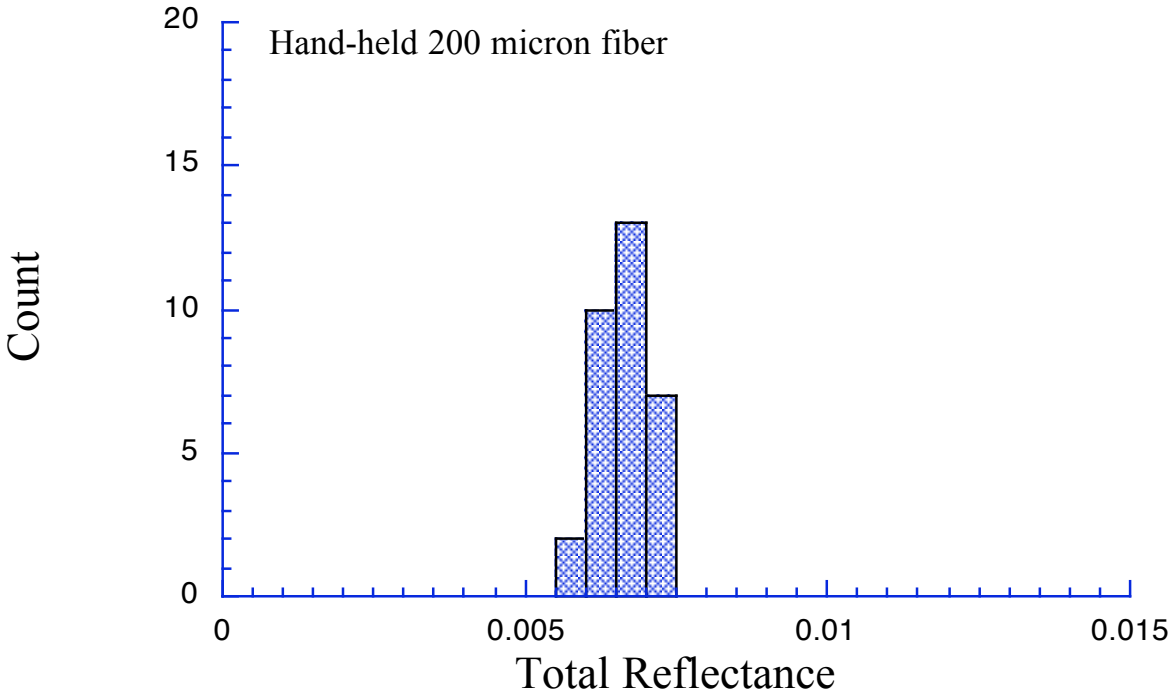

Figure 5.4: Distribution of 32 measurement on a forearm with a 200 micron fiber that is held by hand. The fiber is lifted from the arm between every measurement.

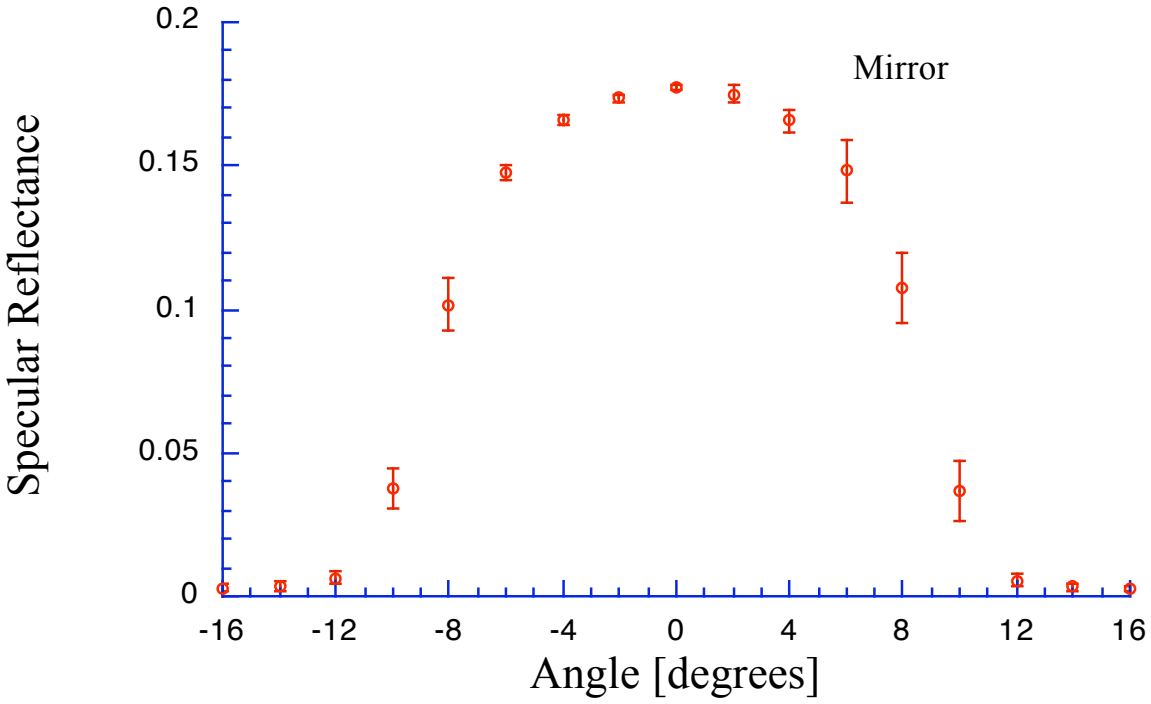

Figure 5.5: The specular reflectance collected from a 200 micron fiber in contact with a first surface mirror. The fiber's optical axis is normal to the mirror at zero degrees.

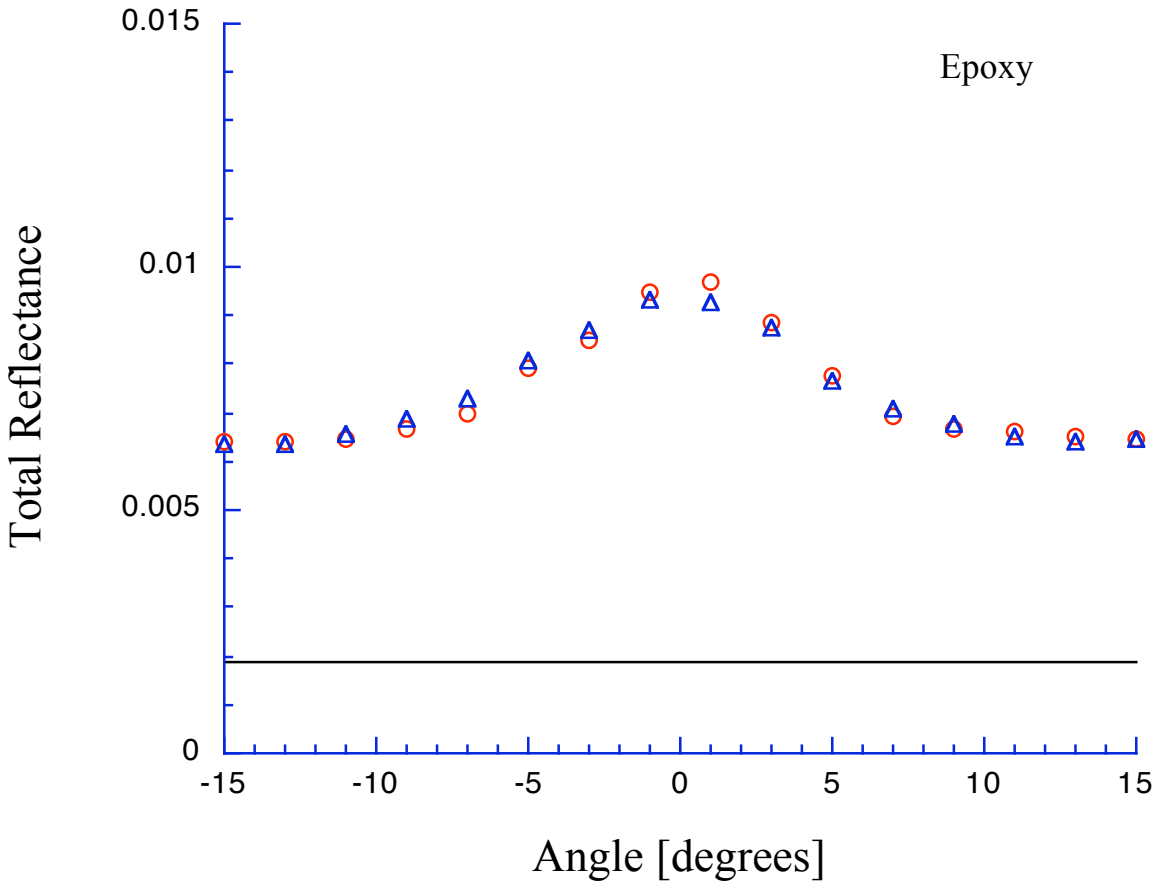

Figure 5.6: The reflectance (specular and diffuse) collected by a 200 micron fiber in contact with an optically diffusing epoxy block.

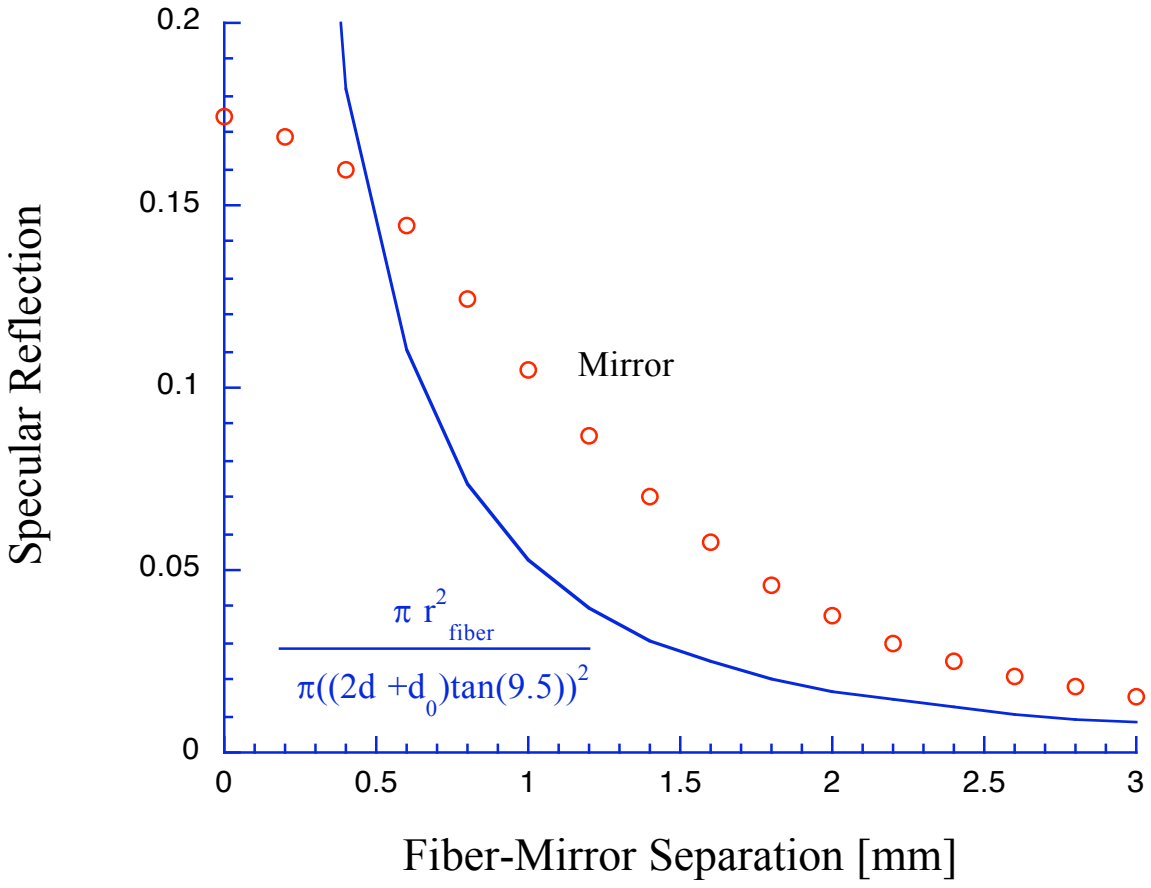

Figure 5.7: The specular reflectance collected with a 200 micron fiber displaced from the surface of a first surface mirror(points) and the expected geometric result (curve).

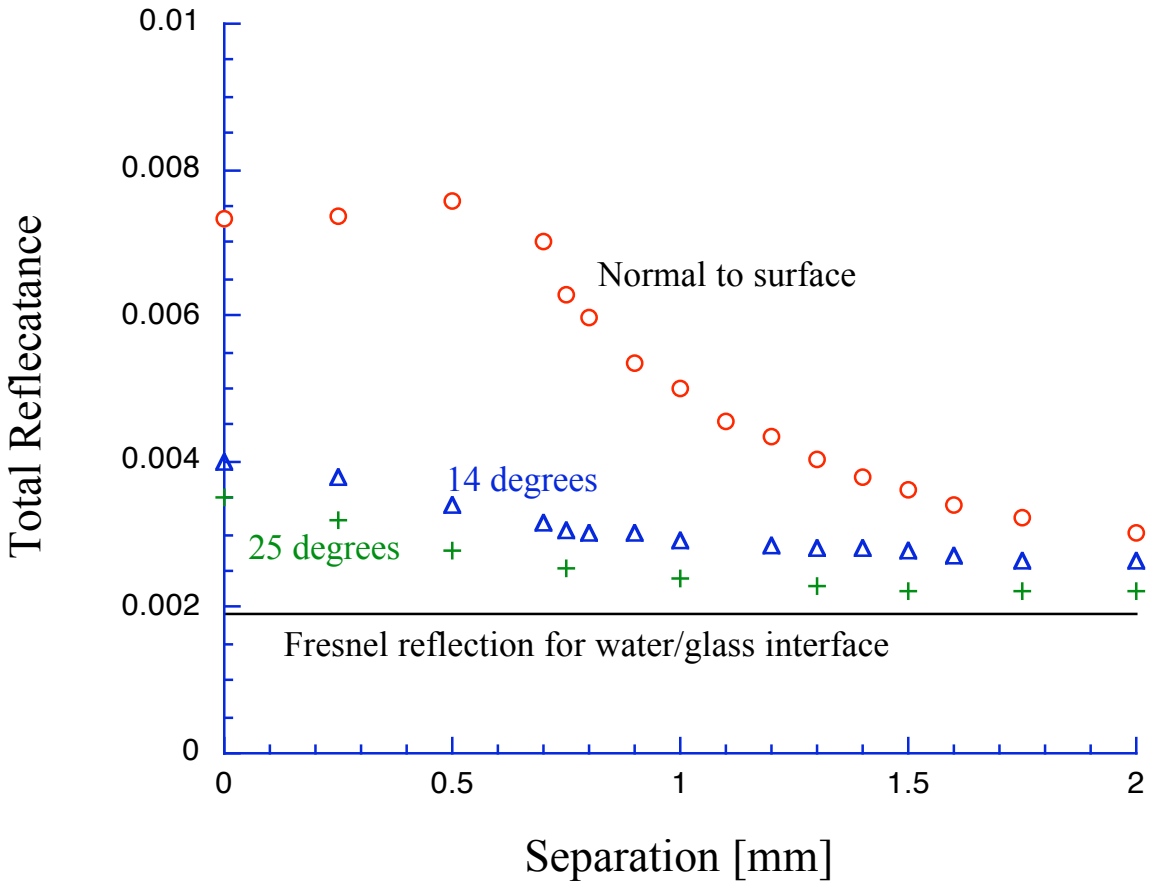

Figure 5.8: The reflectance (specular and diffuse) collected with a 200 micron fiber displaced from the surface of a first surface mirror.

epoxy resin block while the fiber is normal to the surface, and at 65 and 76 degrees to the surface.

5.4 Discussion

When making any type of measurement, the resulting measurement must be reproducible. Single fiber reflectance measurements are prone to significant variability if fiber placement on the material is not carefully controlled. Figure 5.3 exemplifies this point. When a fiber is carefully and precisely aligned (figure 5.3 bottom), the standard deviation is less than 1.8 percent (mean = 0.011); less precise hand-held measurements (figure 5.3 top) have a standard deviation of 12 percent and an average value that is 17 percent lower. The solid block is more sensitive to fiber holding than soft tissue (comparing figure 5.3(upper) to figure 5.4), because the soft tissue deforms and make better contact with the fiber.

Tissue deformation is also a hindrance. Pressure induced by the contact of the optical fiber causes skin to visibly blanch by driving the blood out of the immediate tissue. I am unable to achieve a steady signal with a bare 200 micron fiber on skin. The fiber must be mounted so that a larger area ($\approx 7\,\mathrm{mm}^2$) of support is given around the face of the fiber.

Ideally, a fiber may be positioned such that the fiber face will be in perfect contact with negligible pressure and any pressure fluctuations would have minimal effect. In less than ideal circumstances, two problems affect measurements: displacement of the fiber from the surface and a non-normal fiber angle to the surface. By using a first surface mirror, these two effects can be described for the extreme case of pure specular reflection. First, a small change in the angle less than 2 degrees from the normal causes a 2 percent or less drop in collected light. At 4 degrees, the signal drops by 6.5 percent and at 6 degrees, the signal drops to 83 percent of the value at normal incidence. Beyond 10 degrees, the reflected light incident upon the fiber is outside the numerical aperture (0.22) of the fiber and the collected signal is nearly equal to the Fresnel reflection due to the index mismatch at the fiber face.

Displacement between the fiber and the surface of the sample has a similar effect. A

200 micron displacement causes a 3 percent loss in signal, 400 micron an 8 percent loss, and 600 micron a 17 percent loss of signal. However, the signal does not drop off as rapidly as a pure geometric solution would suggest. In a first approximation that assumes that all modes are evenly filled (the modes were not perfectly even), the collected specular reflection can be described by the ratio of the area of the fiber face relative to the spot size reflected back in the plane of the fiber face (figure 5.2 right) giving the equation

$$\text{Specular Reflection} = \frac{C\pi r_{\text{fiber}}^2}{\pi((2\text{d} + \text{d}_0)\tan 9.5)^2}$$

where C is the maximal reflection from the mirror ($C = 1$), r_{fiber} is the radius of the fiber, d is the distance between the fiber face and the surface of the sample, and d_0 is the height of the triangle (600 micron) that forms the cone of light emitted from the fiber (figure 5.2 right). In water, the maximum half angle of emission of the fiber would be 9.5 degrees. The discrepancy may be due to additional reflections off the meniscus of water back onto the mirror being captured by the fiber. Uneven annular modes of propagation through the fiber may also attribute to the discrepancy especially if the central modes carries substantially less light than outer annular modes. Under-filling of modes will change the fiber exit angle (to less than 9.5 degrees) and not change the general shape of the curve and so this cannot be the sole explanation of the difference between the experiment and the geometric model.

On measurements of the epoxy resin block, the results are similar to the mirror though the deviations were not as pronounced. This was the expected result since the block produces much less specular reflection than a mirror. The collected reflectance did not drop to the surface Fresnel reflection value due to the presence of diffuse reflection. Figure 5.6 shows that the influence of the specular reflection is about the same magnitude as the diffuse reflection. In figure 5.8, the change in specular reflection at normal incidence almost equally offsets any changes in the collected diffuse reflection for separations less than 400 microns. At large fiber angles ($\geq$ 14 degrees), the specular reflection is not collected and the diffuse reflection collected slowly decreases with increasing separation between the fiber and the surface of the epoxy block.

In this study, we examined the effect of fiber contact on the collection of specular

reflection. When fiber contact between the face of the fiber and the surface of the sample is imperfect, the collected specular reflection decreases. Changes in angle greater than 4 degrees or a separation between the fiber and the surface in excess of 400 micron causes at least a 7 percent attenuation of the collected specular reflection. On diffusely scattering media, the change in the specular reflection is nearly identical to the change in diffusely collected light for fiber separations less than 400 micron. Any change in the fiber's optical axis from normal to the surface caused signals to decrease. Imperfect contact of any sort between a fiber and the material caused the light collected to decrease. Therefore, reproducible measurements using a fiber in this manner requires precise control of fiber placement to avoid artificially low signals that may be falsely attributed to increased absorption or a decrease in scattering.

5.5 Beveled optical fibers

The tip of an optical fiber may be angled to prevent the propagation of specular reflectance back through the fiber. A set of experiments is presented to compare the degree of specular reflection collected between fibers with a right-angle tip and a tip polished to a 65 degree angle for both 200 and 1000 micron diameter fibers. In the first experiment, the specular reflectance of each fiber is measured in air, water, and flush against a first-surface silvered mirror. The specular reflectance is normalized by dividing by the reflectance collected from the epoxy block as described above. In another experiment, the measurement variation was evaluated on the epoxy phantom and on skin from the dorsal side of the forearm using hand placement of all fibers.

5.5.1 Results

The relative specular reflectance collected by the 200 and 1000 micron fibers for a perpendicular polished and beveled fiber polish is shown in figure 5.9. To make for a better comparison, the specular reflectance signal from each material is divided by the signal collected by the same fiber on a resin block standard that is roughly the same for both fibers.

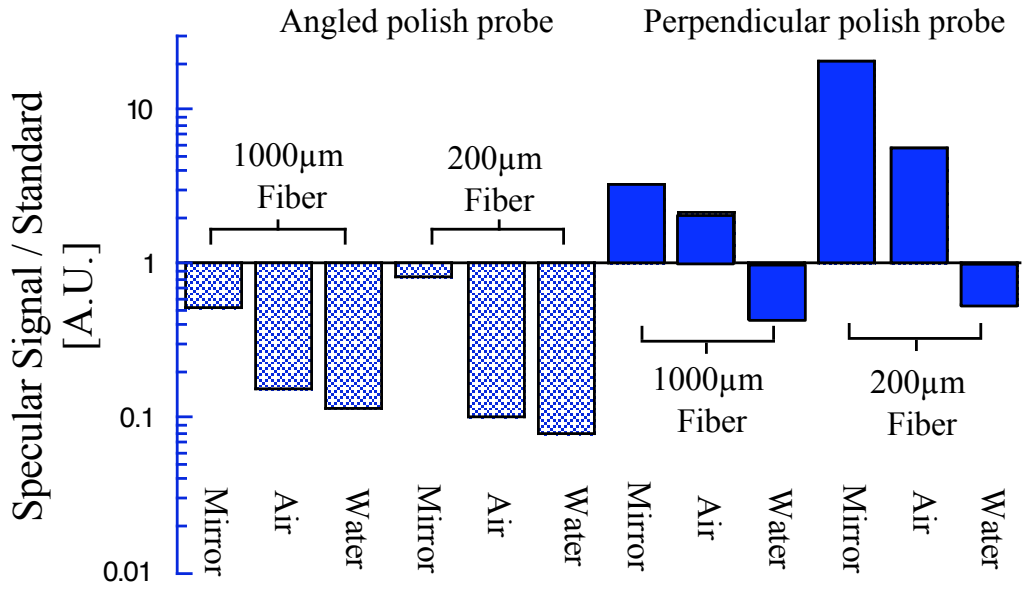

Figure 5.9: Transmitted specular reflectance from the fiber face boundary is reduced for the fibers polished at a 65 degree angle as shown by the ratio of the specular reflection for each media divided by the signal from a epoxy resin block standard.

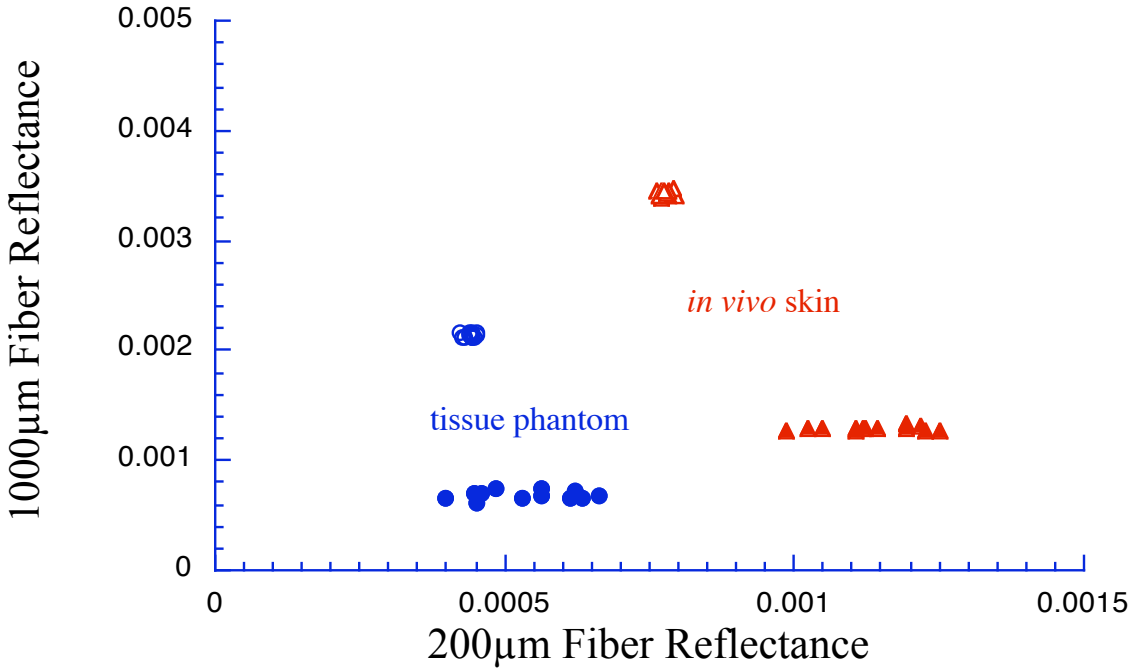

Figure 5.10: Repeated measurements of a resin block tissue phantom (N= 12) and skin (N=13) from the dorsal side of the forearm. Open points represent the angled polish probe and filled points are for the perpendicular polished probe.

Typical distributions of repeated measurements of reflectance collected by the 200 micron diameter plotted against the reflectance collected by the 1000 micron diameter fiber are shown in figure 5.10 on an epoxy resin block tissue phantom and for *in vivo* skin. Though the signal correction does not correct for the specular reflection offset, the relationship between measurements in a cluster does not change since the specular reflection is a constant for each cluster. Clearly the cluster of 12 measurements for the angled polish probe pack tighter than for the perpendicularly polished probe. The mean and standard deviations are presented in table 5.1.

5.5.2 Discussion

Specularly reflected light behaves as a noise source since it does not contain any information about the absorption or scattering properties of the tissue sample being measured.

Fiber diameter	Angled polish probe		Perpedicular polish probe	
	Tissue phantom N = 12	Skin N = 13	Tissue phantom N = 12	Skin N = 13
200 micron	0.00044 ±2.2%	0.00078 ±1.2%	0.00054 ±16%	0.00113 ±7.2%
1000 micron	0.00214 ±0.9%	0.00343 ±0.6%	0.00068 ±5.4%	0.00129 ±1.4%

Table 5.1: The mean and standard deviation (listed as a percentage of the mean) of the distribution of repeated measurements. A value of 1.00 in the mean implies 100% of the emitted light is collected.

Elimination of the specular light from the fiber face removes a portion of the signal variation. The specular reflectance is related to the contact between a fiber and the surface. It was shown in figure 5.5 that the specular reflection signal from a perpendicular polished fiber changes by 6.5% with only a 4 degree rotation of the fiber relative to the normal of the surface being measured. The perpendicularly polished fiber probe collects a Fresnel reflection signal in air of approximately 3.5%, 0.24% in water, and 92% from the first surface mirror. This specular component is reduced 5 times with the beveled fiber-tip in water and by an order of magnitude in air or on the mirror.

Inter-measurement variation with fibers polished at a 65 degree angle is also reduced in comparison to perpendicularly polished fibers. We find that measurement variability decreases 6 fold on *in vivo* skin and nearly 8 fold on a resin tissue phantom with the 200 micron fiber. On a solid resin tissue phantom, the difference between the highest and lowest of 12 measurements is 6.5 and 2.4 percent for the 200 and 1000 micron fiber respectively. On *in vivo* skin where the surface is compliant, the difference between the highest and lowest of 13 measurements drops to 4.5 percent difference with a 200 micron fiber while the 1000 micron fiber is 2.2 percent difference. The greatest contributing factor for the decrease in variation is the elimination of specularly reflected light in the collected signal.

Chapter 6

Interpretation of Two Fiber Reflectometer Measurements

6.1 Introduction

Though measurements using a single emission and collection fiber minimize sampling volume, the collected light also includes a specular reflection component due to a refractive index mismatch between the fiber and the tissue. The specular reflections act as a noise source that are similar in magnitude to the collected diffusely reflected light. Imperfect contact between the fiber and tissue causes measurement variability, in part owing to the specularly reflected light component leading to an inability to predict the optical properties [131]. In this chapter, two dual-fiber probe designs are presented and evaluated taking into consideration the results of the previous chapters. Though specular reflections provide a simple and reliable way to calibrate the measured reflectance, the unpredictable contact of the fiber to tissue leads to imprecise determination of the specular light collected for each fiber. The designs of both probes remove the specular component by beveling the face of the fiber. Given a sufficiently large bevel angle, light reflected internally at the fiber face reflects to a new angular distribution that exceeds the numerical aperture of the fiber. The specular light is then lost through the fiber cladding and is therefore not propagated back to the detector.

Two dual fiber probe designs are presented that optimally collect diffusely scattered light while rejecting specularly reflected light. Monte Carlo models for both probe designs are described that are used to create grids of the collected diffuse reflectance for a range

of optical properties typical for tissues (absorption between 0.1–5 cm^{-1} and reduced scattering between 10–100 cm^{-1}). The Monte Carlo models are used to evaluate the mean optical path-length sample for each fiber in the two designs. Lastly, the effects of changes in anisotropy with constant reduced scattering is evaluated using the models.

The first probe is a modified sized-fiber probe as described in chapter 4. The difference in diameter of the two optical fibers is increased to improve contrast between the reflectance of each fiber. In addition, the original design used the specular reflectance of water/glass and air/glass interface of the fiber to normalize the reflectance. This design requires signal normalization using a diffuse reflection standard since specular Fresnel reflections are greatly reduced. The diffuse reflectance from a 4 by 4 array of tissue phantom array is measured with the device to check the validity of a Monte Carlo model. Finally, the absolute relative error distributions are calculated for the absorption and scattering coefficients presented as a function of the absorption and scattering coefficients using a linear differential approximation of the diffuse reflection collected by the 200 and 1000 μm fibers.

The second probe consists of two 400 μm diameter fibers, one of which emits light while both fiber collect diffusely reflected light. In contrast to the Sized -fiber device, empirically determined relationships between the absorption and reduced scattering coefficients and the collected light for the probe is presented based on the the results of the Monte Carlo model. The accuracy of the empirical method is evaluated using measurements with the probe on a polyurethane phantom characterized using the inverse adding-doubling method from integrating sphere measurements.

6.2 Device Design

6.2.1 Monte Carlo Model

Description

A Monte Carlo program was adapted to simulate the light collected by a fiber irradiating a semi-infinite homogeneous scattering and absorbing medium. The geometry of the fiber includes a beveled fiber face that affects the emission profile of light originating

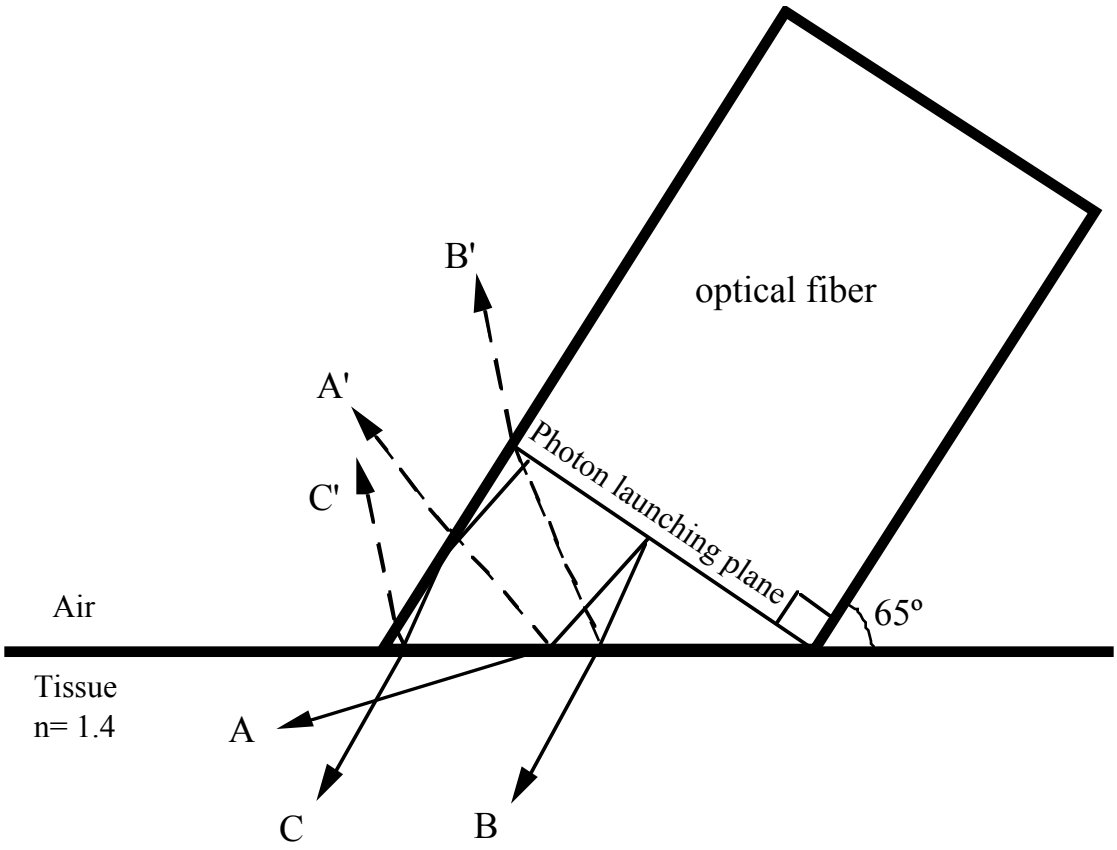

Figure 6.1: In the Monte Carlo model, photon bundles are launched from the last complete plane within the fiber perpendicular to the optical axis of the fiber. Photon bundles are launched with a truncated gaussian angular distribution with a cut-off at the angle with an e^{-2} likely-hood to the central angle. The cut-off angle corresponds to the fiber numerical aperture, which is 0.22 in this model. Photons are tracked to the face of the fiber and the refracted into the tissue as shown for paths A and B. In the case of photon bundle C, the path intersects the fiber wall before reaching the fiber face and is therefore undergoes total internal reflection at the intersection. Paths A′, B′ and C′ (dashed rays) show the specular reflection path from the fiber face which leaks out the side of the fiber.

from the fiber and the collection of reflected photons back into the fiber. The face of the fiber is beveled to a 65 degree angle. The face of the fiber is modeled in perfect contact at the boundary of the medium with air surrounding the fiber as shown in figure 6.1.

To account for the asymmetry of the beveled fiber, photon packets are launched inside the optical fiber at the last plane that is a complete cross-section of the fiber due to the beveling of the fiber tip begins (see figure 6.1). In this plane, the launching of photons uses the same spatial and angular launching distributions as for a perpendicularly polished fiber. The launching position was spatially uniform across the cross-section of the fiber-optic of the initial launching plane. Each photon bundle is assigned a propagation vector with a gaussian angular distribution centered about the fiber's optic axis with the extreme angle cut-off at the e^{-2} level of the gaussian. The width of the gaussian distribution is defined using the maximum propagation angle within the fiber as dictated by the numerical aperture ($\theta_{max} = \sin^{-1}(\text{N.A.}/n_{\text{fiber}})$) such that θ_{max} corresponds to the e^{-2} level. The initial angular distribution of trajectories for photon bundles in the x and z axes is shown in figure 6.2. The photon packets travel along the remainder of the fiber tip until reaching the fiber face and reflecting of the fiber wall whenever the path intercepts the fiber wall. At the fiber face, the propagation vector is refracted into the semi-infinite medium (n = 1.4 for tissue and n_{fiber}= 1.457). Each photon bundle is initialized with a weight of unity that corresponds to the energy in each bundle. The weight of each photon packet is decreased by an amount equal to a Fresnel reflection at normal incidence as it crosses from the fiber into the medium, introducing error that is less than 0.1%.

The tracking of discrete photon packets follows the sequence: photon packets are initiated inside the fiber, undergo refraction as they enter the medium, then propagate through the medium until either scattering back into the fiber, lost through emission through the free space boundary of the medium, or are absorbed by the medium. Photon bundles returning to the fiber face are refracted by the fiber giving the propagation vector inside the fiber. The propagation vector is described by the cosine of the vector along the x, y and z axes (direction cosines). The axis are defined so that the fiber face lies is centered in the x-y plane at z=0 and z is positive going into the medium from the fiber. The dot product of the photon's propagation vector and a vector corresponding to

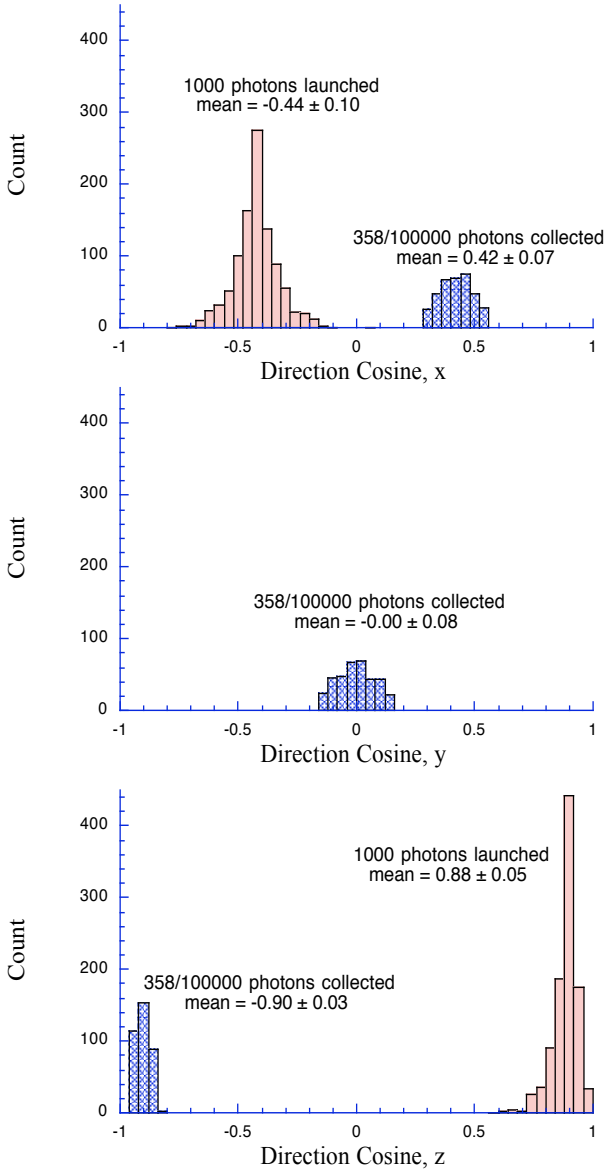

Figure 6.2: Bundles of photons are propagated using a propagational vector given by the direction cosines defined as the cosine of the propagation vector with respect to the x, y and z axes. The initial propagation vector is described a gaussian distribution with a e^{-2} width set by the numerical aperture of the fiber and centered on the optical axis of the fiber. For a 65 degree beveled fiber, the optical axis has direction cosine vector of (0.423, 0, 0.906). The top figure shows the distribution of angle for launch photons and collected photons by the direction cosine along the x-axis. The middle figure shows the collected distribution direction cosine for the y-axis with the launched photons omitted as the overlay the collected photons and has a similar angular spread as for the x-axis. The bottom figure gives the launched and collected photon bundle distributions along the z-axis which is perpendicular to the semi-infinite medium boundary.

the fiber's central axis are compared to the cosine of θ_{max} within the fiber to determine whether the photon path was inside the numerical aperture and is transmitted through the fiber. The angular distribution of trajectories for photon bundles collected by the fiber in the x, y and z axes is shown in figure 6.2. Photons with trajectories outside the numerical aperture count as light lost through the cladding of the fiber. Light incident upon the boundary of the semi-infinite medium but outside the area of the fiber face is lost to free space emission and no longer tracked, excepting for the fraction of energy specularly reflected back into the medium due to refractive index mismatch at the boundary and the air.

In each simulation of the Monte Carlo model, two million photons are launched for each combination of optical properties giving adequate balance of accuracy and computation time. Mean diffuse reflections and the standard deviations were calculated from five runs of the model using different starting seeds for each combination of optical properties. The absorption coefficient was varied from 0.1 to 5.0 cm^{-1} and the scattering coefficient varied from 100 to 1000 cm^{-1} with an anisotropy of 0.9 using a Henyey-Greenstien phase function. Additional details regarding the collected light are examined using the Monte Carlo model. First, the weighted average path-length of the collected diffuse light by

$$\frac{\Sigma(\text{photon weight} * \text{pathlength})}{\Sigma\text{photon weight}}$$

is recorded for each pair of absorption and scattering coefficients. Second, several simulations examine the change in collected diffuse reflectance by varying the anisotropy while keeping the reduced scattering and absorption coefficients constant ($\mu_s' = 30\,\mathrm{cm}^{-1}$ and $\mu_a = 0.2\,\mathrm{cm}^{-1}$).

Results

Monte Carlo simulation results for the angled polish probe design are shown in figure 6.3 for an array of optical properties with absorption coefficient values of 0.1, 0.2, 0.5, 1.0, 2.0, and 5.0 cm^{-1} and reduced scattering coefficient values of 10, 20, 30, 50, 75, and 100 cm^{-1} for 200 and 1000 micron diameter fibers. Each cluster represents a single reduced scattering coefficient and reflectance decreases within each cluster as absorption increases.

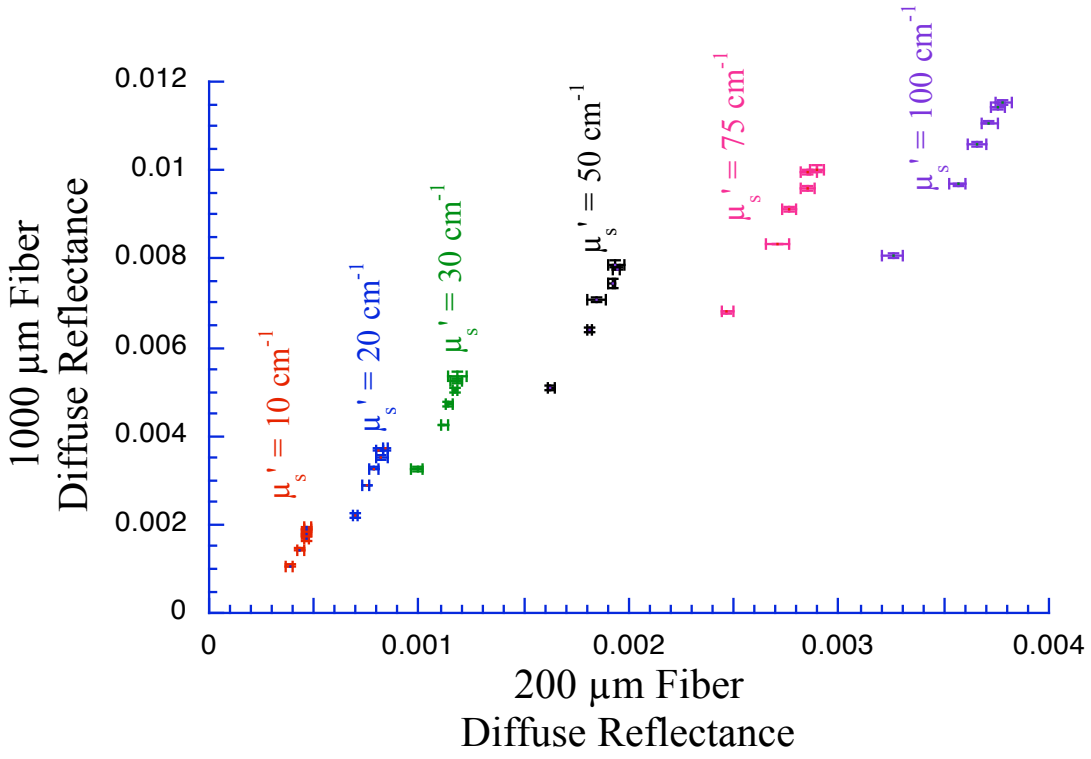

Figure 6.3: A reflectance map of optical properties in the range of tissues. Each cluster of points represent a single reduced scattering coefficient where scattering increases for each cluster as the reflectance increases. The error bars represent the standard deviation of five runs of the Monte Carlo with a different starting seeds. Within each cluster absorption in creases as the reflectance decreases.

An estimation of the optical properties using the Monte Carlo results of the *in vivo* skin from figure 5.10 for the angled polish probe result in an absorption coefficient of about $0.2\,\mathrm{cm}^{-1}$ and a reduced scattering coefficient of $18\,\mathrm{cm}^{-1}$ at 633 nm which agrees with values listed by Cheong [44].

Although I assume that in tissue the anisotropy is constant, figure 6.4 shows that the collected reflectance changes with the anisotropy, g, when the reduced scattering coefficient and absorption remain constant. The volume of the tissue (or other turbid medium) being sampled is influenced by the optical properties. The weighted mean path-length for which

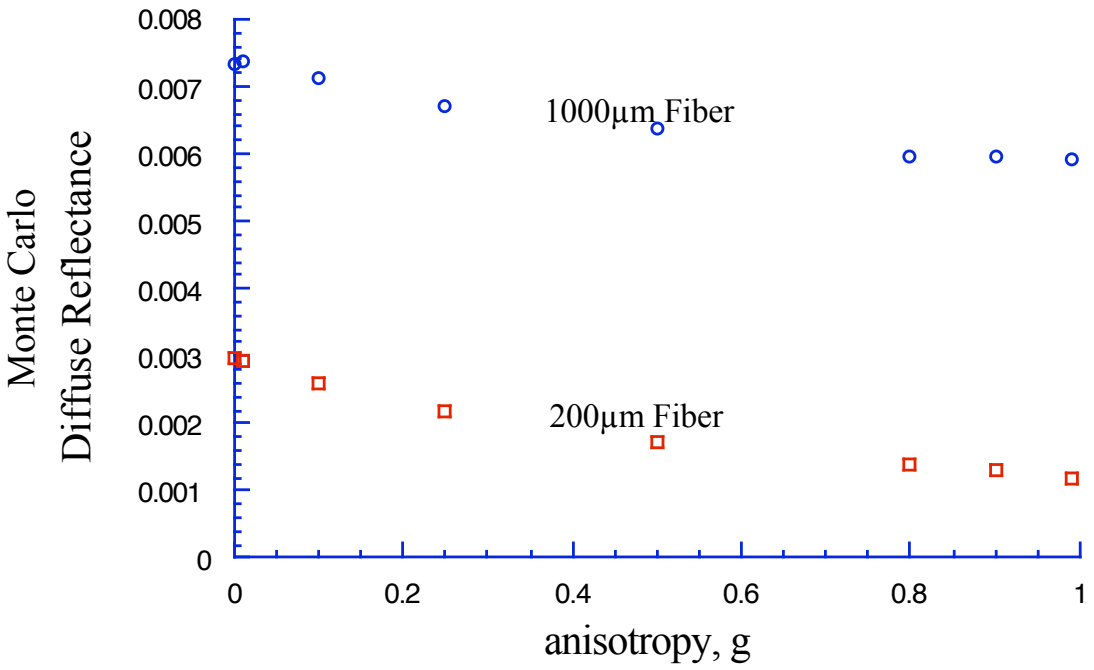

Figure 6.4: The diffuse reflectance collected by the 200 and 1000 micron fibers decreases as the light becomes more forwardly scattered (higher g). Anisotropy values range from g= 0–0.99. The reduced scattering coefficient is held constant at $30\,\mathrm{cm}^{-1}$ and the absorption constant at $0.2\,\mathrm{cm}^{-1}$.

collected light travels is shown in figure 6.5.

Fitting Technique

To evaluate the absorption and reduced scattering coefficients a linear interpolation is made using the grid of optical properties as shown in figure 6.3 for the diffuse reflectance collected by 200 and 1000 micron diameter fibers. The change in absorption coefficient (μ_a) are related to a change in the reflectance measured by a 200 micron diameter fiber (R_{200}) and 1000 micron diameter fiber (R_{1000}) given by

$$(\Delta\mu_a)^2 = \left(\frac{\partial\mu_a}{\partial R_{200}}\Delta R_{200}\right)^2 + \left(\frac{\partial\mu_a}{\partial R_{1000}}\Delta R_{1000}\right)^2.$$

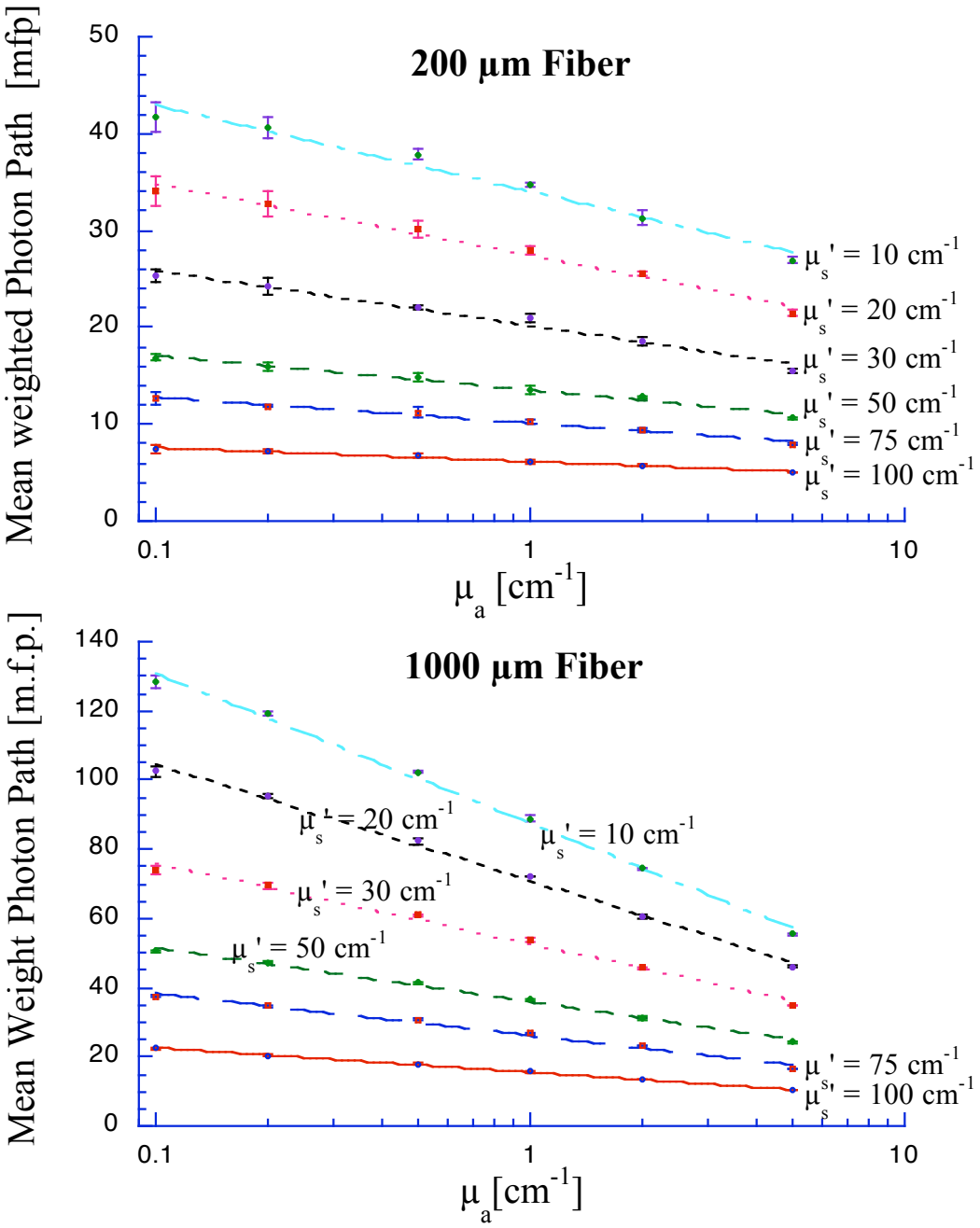

Figure 6.5: The mean optical path through which collected light travels is presented as a function of optical properties in terms of the number of mean free paths traveled (mfp = $1/(\mu_a + \mu_s)$. At any particular absorption coefficient, the scattering coefficient increases with the mean number of mean free paths traveled by collected photons for values of 100, 200, 300, 500, 750, 1000 cm^{-1}. For all simulations the anisotropy was fixed to g = 0.90.

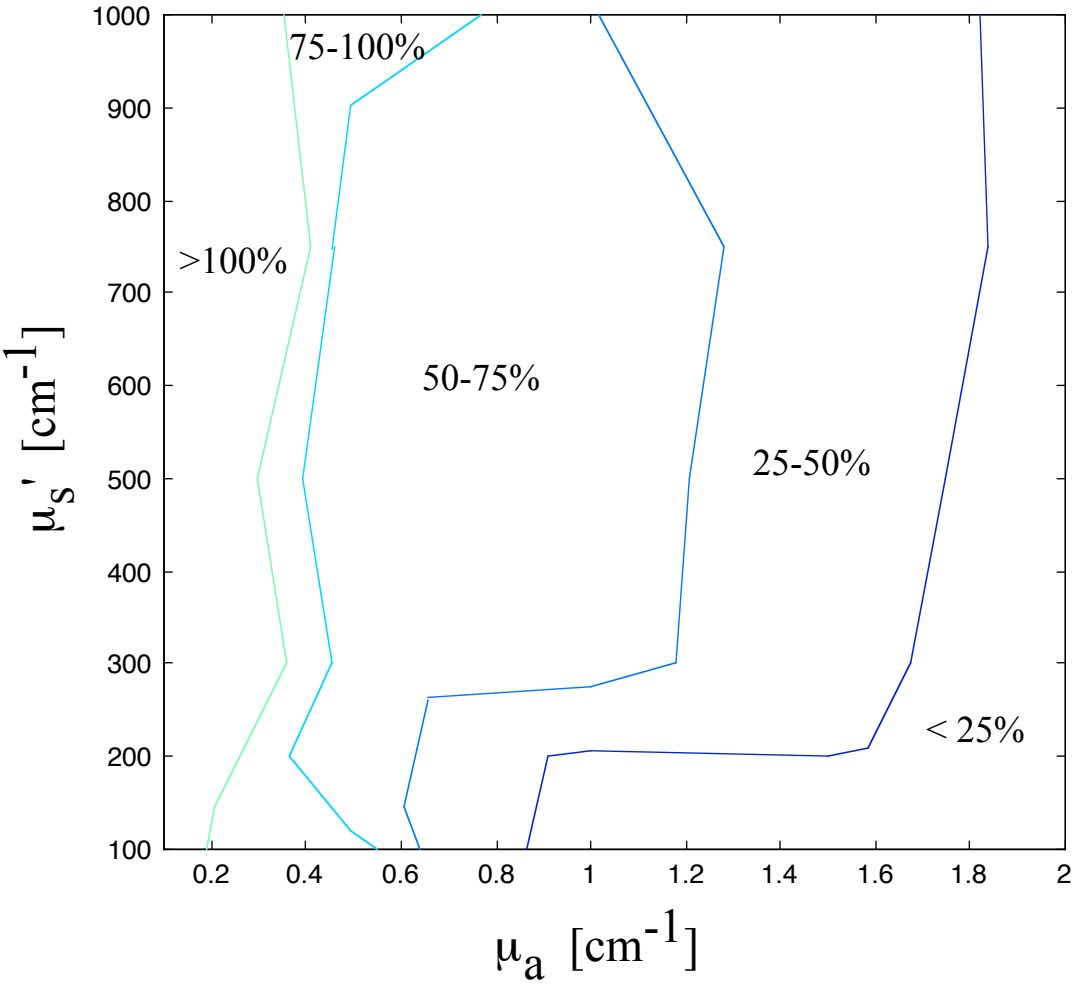

Figure 6.6: A contour plot of the absolute relative error in the absorption coefficient is evaluated with a linear approximation of the Monte Carlo simulations in conjunction with experimentally determined variation.

The partial of the absorption coefficient with respect to the reflectance for each fiber is linearly approximated by dividing the difference of two adjacent absorption coefficients in the Monte Carlo grid ($\mu_{a,1}-\mu_{a,2}$) by the difference in by the respective reflectance collected for each absorption coefficient by that fiber (e. g. $R_{200,1}-R_{200,2}$ for the 200 micron fiber). An absolute relative error map of absorption is presented in figures 6.6. The percent relative error for absorption is calculated by

$$\begin{aligned}\left(\frac{\Delta\mu_a}{\mu_a}\right)^2 &= \left(\frac{\mu_{a,1}-\mu_{a,2}}{R_{200,1}-R_{200,2}}\right)^2\left(\frac{\Delta R_{200}}{R_{200}}\right)^2\left(\frac{R_{200}}{\mu_a}\right)^2 \\ &+ \left(\frac{\mu_{a,1}-\mu_{a,2}}{R_{1000,1}-R_{1000,2}}\right)^2\left(\frac{\Delta R_{1000}}{R_{1000}}\right)^2\left(\frac{R_{1000}}{\mu_a}\right)^2\end{aligned}$$

where the standard deviations of measurements on skin in table 5.1 as our relative error in the 200 and 1000 μm fiber reflectance for the respective terms of $\left(\frac{\Delta R_{200}}{R_{200}}\right)$ and $\left(\frac{\Delta R_{1000}}{R_{1000}}\right)$. Finally, the terms $\left(\frac{R_{200}}{\mu_a}\right)$ and $\left(\frac{R_{1000}}{\mu_a}\right)$ scales the error into relative error. Similarly, the percent relative error for scattering is calculated by

$$\begin{aligned}\left(\frac{\Delta\mu_s}{\mu_s}\right)^2 &= \left(\frac{\mu_{s,1}-\mu_{s,2}}{R_{200,1}-R_{200,2}}\right)^2\left(\frac{\Delta R_{200}}{R_{200}}\right)^2\left(\frac{R_{200}}{\mu_s}\right)^2 \\ &+ \left(\frac{\mu_{s,1}-\mu_{s,2}}{R_{1000,1}-R_{1000,2}}\right)^2\left(\frac{\Delta R_{1000}}{R_{1000}}\right)^2\left(\frac{R_{1000}}{\mu_s}\right)^2\end{aligned}$$

with the analogous terms as for absorption but relating to scattering (not reduced scattering). The error contours are generated using MatLab (Mathworks, Inc., Natick, MA) with a base 10 logarithmic contour spacing. The absolute relative error for the scattering coefficient was $1.5 \pm 0.2\%$ over the entire range of absorption and scattering.

6.3 Measurements

6.3.1 Materials and Methods

The basic probe design (shown in figure 6.7) has previously been described [130] but, a few key modifications are now introduced. The sized-fiber devices consist of 200 and 1000 micron diameter fibers bundled together. Emission and collection light is bifurcated from the 200 and 1000 micron diameter fibers by end-coupling two 100 μm diameter fibers onto the face of a 200 micron diameter fiber and 400 μm diameter fibers onto the face

of a 1000 micron diameter fiber using SMA connectors. The new probe has the 200 and 1000 micron diameter fibers polished at an angle of 65 degrees relative to the fiber's central axis (herein referred to as angled polish) rather than a 90 degree angle used by the previous design (herein referred to as perpendicular polish). The 200 micron fiber with its core, cladding and jacket intact is sleeved with the 1000 micron fiber with the jacket removed but cladding intact into a snug fitting brass tube housing for protective strength. The sleeved fibers are mounted into an SMA type fiber connector made from black Delrin plastic. The fibers are polished within the SMA so that the SMA connector and the fibers are polished to a 65 degree angle. A fiber support fabricated from Delrin plastic that is 1.25 cm in diameter concentrically fastens to the probe end of the two fibers via the SMA connector. A diagram of the fiber tip and the fiber support is shown in figure 6.8 and a picture of the two fibers mounted in the support is shown in figure 6.9). All fibers have a 0.22 a numerical aperture and are fused silica glass/glass from CeramOptec industries, Inc., San Jose, CA.

A He-Ne laser beam (632.8 nm) is split and focused into a 100 and 400 micron fiber that respectively feed to 200 and 1000 micron fibers. Each beam is chopped (MC1000, Thorlabs Inc., Newton, NJ) at differing frequencies (335 and 500 Hz) before entering the fibers. The return leg of the bifurcation fibers are coupled to UDT silicon photodiodes (unbiased, 100 mm^2 area). Lock-in amplifiers (SR830, Stanford Research Systems, Sunyvale, CA) are used to record the signals using a 100 ms time constant.

Signal normalization is performed using measurements of a dark signal subtraction and reference signal. The dark signal is a measure of the specular reflectance in water obtained by placing the fibers into a beaker of water with walls painted flat-black. The reference measurement is taken on a block or resin. Measurements are converted to percent reflectance and corrected for a small degree of specular reflection by the equation

$$\text{Reflectance} = \frac{(V_{sample} - V_{water})}{(V_{standard} - V_{water})} * (\%\ \text{reflection of standard})$$

where V_{sample}, $V_{standard}$, and V_{water} are the detector voltages returned from the tissue sample, a resin block standard, and for the specular reflection for the respective fibers in water. The absorption and reduced scattering properties of the resin block standard

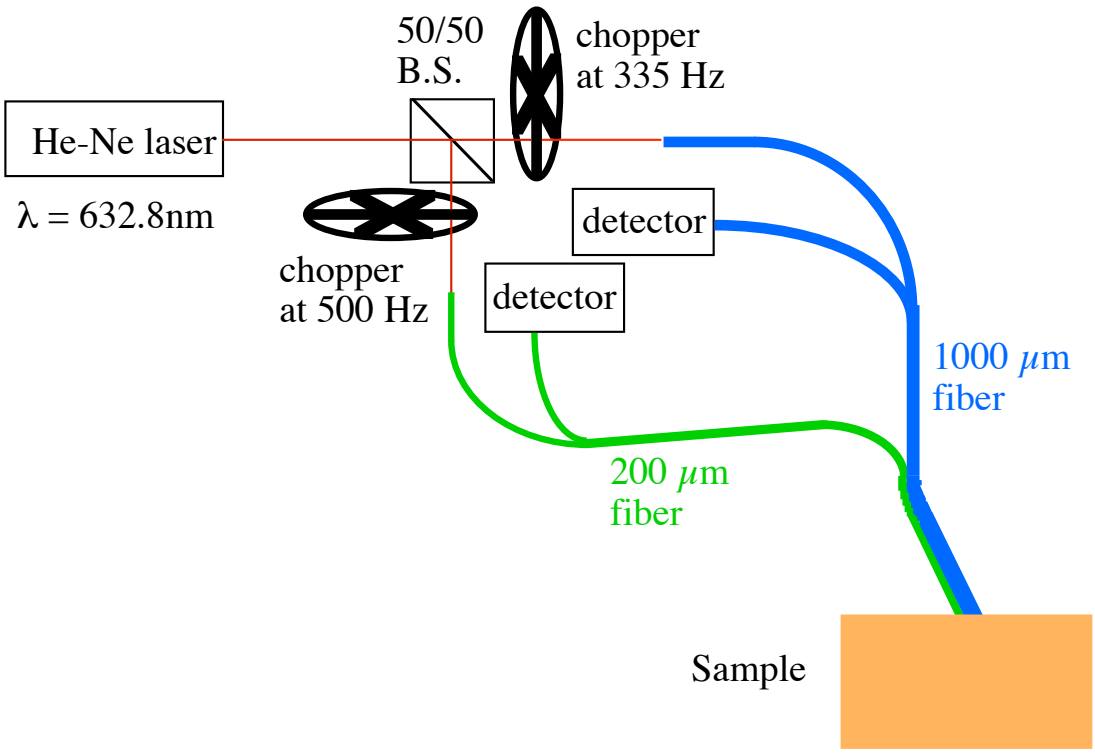

Figure 6.7: This is a diagram of the sized-fiber device. A pair of bifurcated fibers emit and collect light simultaneously by chopping at two distinct frequencies. The fibers are mounted in tubing and have SMA connectors to connects the fibers.

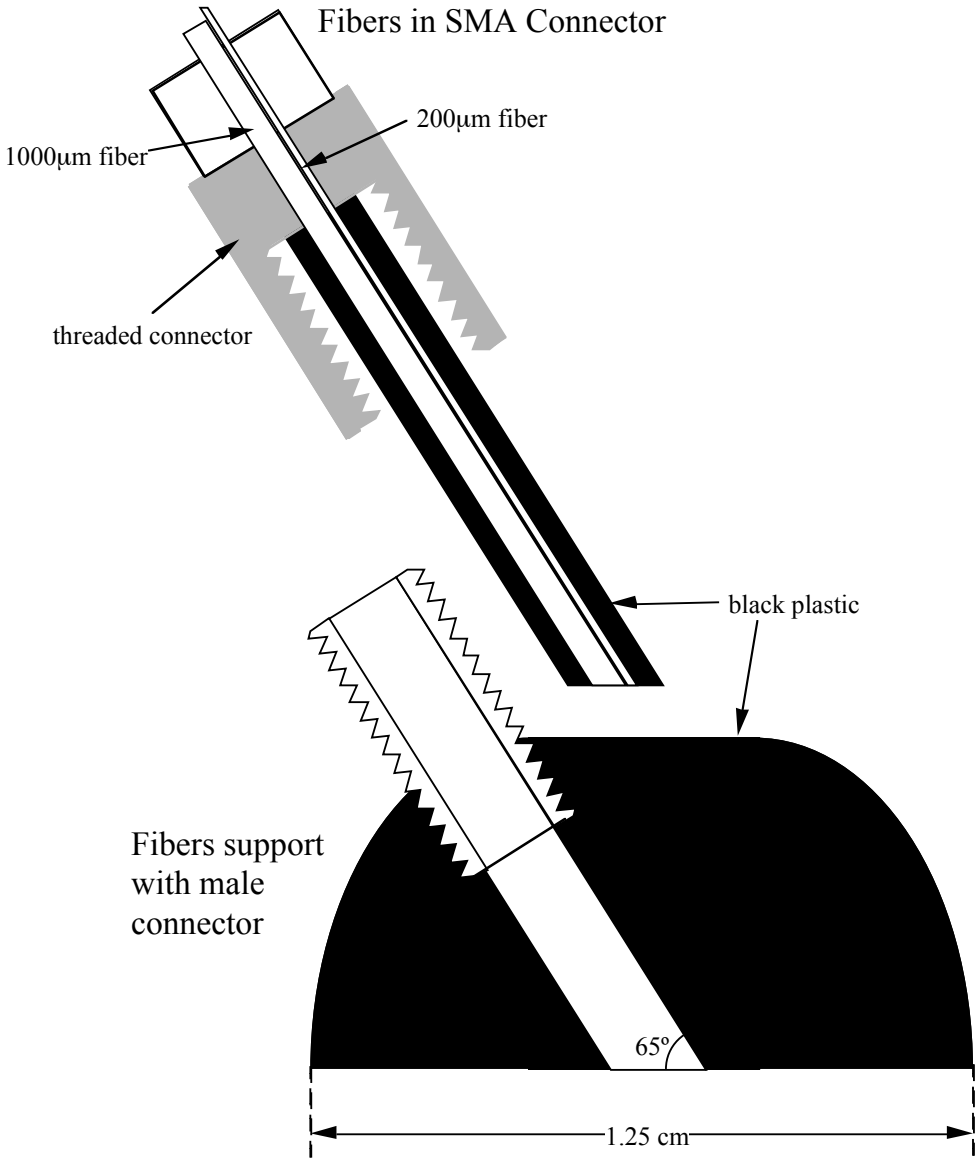

Figure 6.8: This diagram shows a bisecting view of the 200 and 1000 μm fibers mounted together in a black plastic SMA connector. A fiber support 1.25 cm in diameter connects to the fibers via the SMA keeping the fiber concentrically positioned flush within the support.

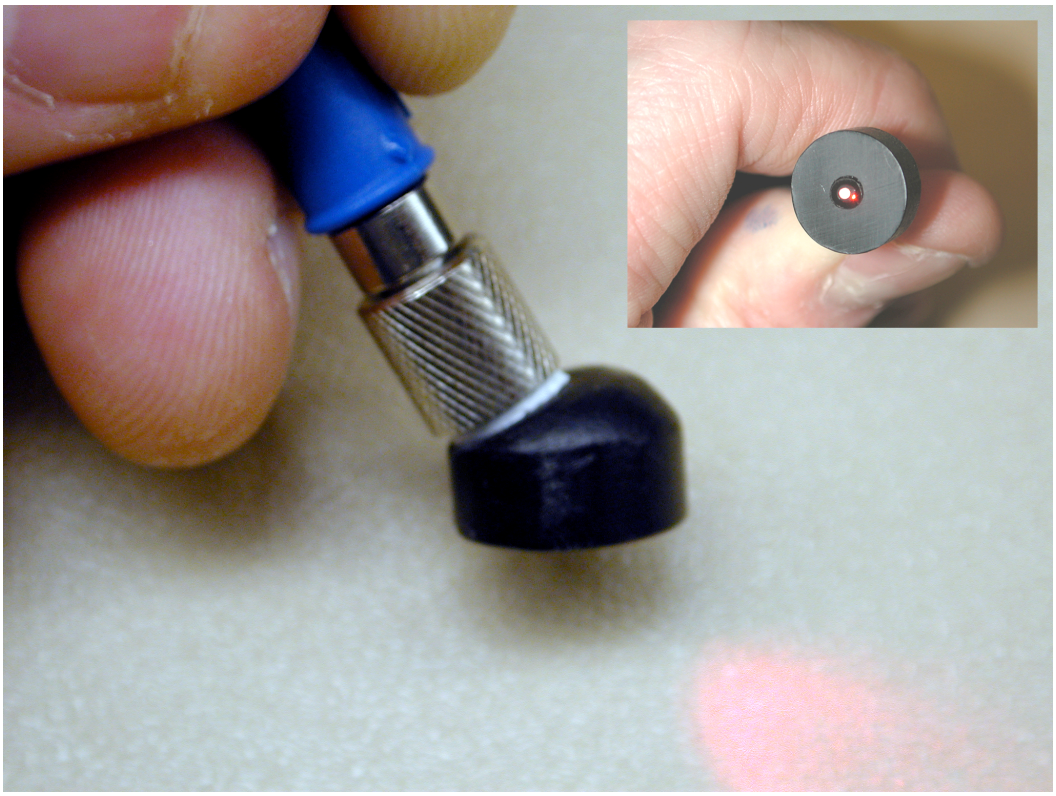

Figure 6.9: This is a picture of the the 200 and 1000 μm fibers attached to the fiber support that aids in placement of the fibers. An end-view of the fibers is pictured in the inset looking down the axis of the fibers to show the emitted light from the two fibers.

were determined by two methods, semi-infinite $R(r)$ measurements as described by Farrell *et al.* [17] and by total diffuse transmittance and reflectance integrating sphere measurements [83]. Both techniques resulted in an absorption coefficient of $0.1\,\mathrm{cm}^{-1}$ and a reduced scattering coefficient of $10\,\mathrm{cm}^{-1}$at 632.8 nm. The Monte Carlo model was used to determine the percent reflectance collected with the 200 and 1000 micron fibers for the optical properties of the standard which are 0.00048 ± 0.00002 and 0.00192 ± 0.00002 respectively ($1.0 = 100\%$)

An array of tissue phantoms were measured with the angled fiber probe design to check the validity of Monte Carlo simulations. The phantoms were constructed using 20% (20 g/100 ml) Intralipid (Liposyn II, Abbott Laboratories, North Chicago, IL) as a scatterer and India ink (No. 4415, Higgs, Lewisburg, TN) as an absorber gelled in a 18% (g/100 ml) acrylamide gelatin. The array was prepared using stock solutions of Intralipid, ink and acrylamide with added water to make each phantom with a final volume of 100 ml and dimensions approximately 4 cm deep and 5 cm in diameter. Aliquots of Intralipid were used to make concentrations of 7, 5, 3.5 and 2.5%. The absorption coefficient of the India ink stock solution was measured by a spectrophotometer (8452A, Hewlett-Packard, Palo Alto, CA) and added to the Intralipid to give final absorption coefficients of 0.1, 0.4, 0.9 and $1.6\,\mathrm{cm}^{-1}$ at 632 nm. The acrylamide stock composed of 1.4 kg of acrylamide acid (99%, electrophoresis grade, Fisher) and 35 g of bis-acrylamide (1:40 ratio, Fisher) in water to create a final volume of 3.5 liters (40% concentration). The gelatin was set by adding 0.4 g of ammonium persulfate (Fisher) and 100 μl of TEMED (Fisher) to each 100 ml sample within the array. Scattering properties were determined after all gelatin samples had set using total diffuse reflectance measurements with an 8 inch integrating sphere(IS-080, Labsphere Inc., North Sutton, NH). The experimental and calculation details to determine the optical properties of the phantom array were elaborated by Bargo [50]. Unlike the absorption coefficient, the scattering properties were found not to be linear with respect to the Intralipid concentration with final reduced scattering coefficients of 13, 18, 23 and $27\,\mathrm{cm}^{-1}$ at 632 nm in order of lowest to highest Intralipid concentration.

6.3.2 Results and Discussion

Measurements of an array of Intralipid and India ink gelatin phantoms are shown in comparison to Monte Carlo simulations in figure 6.10 for the expected optical properties of the array. The absorption coefficient of the array had the values of 0.1, 0.4, 0.9, and $1.6\,\mathrm{cm}^{-1}$ and the reduced scattering coefficient had the range of 13, 18, 23, $27\,\mathrm{cm}^{-1}$ at 632 nm where the anisotropy was modeled with $g = 0.83$ according to van Staveren *et al.* [128].

The typical absolute relative error for predicting the absorption coefficient is roughly 50% ($0.5\,\mathrm{cm}^{-1}$) for absorption coefficients of $1\,\mathrm{cm}^{-1}$ for reduced scattering exceeding $20\,\mathrm{cm}^{-1}$. Below $20\,\mathrm{cm}^{-1}$ of reduced scattering the absorption error decreases since the optical path-lengths increase, increasing the effect of absorption. Since the error is fractionally related to the absorption coefficient, the expected result is for the relative error to increase dramatically especially as absorption coefficient drops below $1\,\mathrm{cm}^{-1}$. The resolution of small changes in absorption is poor but major absorption changes will be resolvable such as the presence of a blood vessel near to the face of the probe.

The precision of predicting small changes of absorption is not surprising when considering the mean path-length that the collected diffuse light travels. The longer mean path-lengths occur with smaller scattering coefficients giving absorption a greater chance to attenuate the collected signal. For absorption at $1\,\mathrm{cm}^{-1}$ and below the collected diffuse reflection can be simplified using a Beer's law approach where

$$R_{\text{collected}} = R_0 e^{-\mu_a \mathrm{d}}.$$

In this absorption range, R_0 varies less than 3% for reduced scattering coefficients between 10–$100\,\mathrm{cm}^{-1}$ for the 1000 μm fiber. The longest mean pathlength of 2.24 mm occurs with $\mu_a = 0.1\,\mathrm{cm}^{-1}$ and $\mu_s' = 10\,\mathrm{cm}^{-1}$ which leads to a 2.2% attenuation of R_0. In contrast for the optical properties with greatest absorption impact, $\mu_a = 1.0\,\mathrm{cm}^{-1}$ and $\mu_s' = 10\,\mathrm{cm}^{-1}$ the absorption attenuation is 14% of R_0 with a 1.55 mm path-length. The change in the optical path-length is inversely related to the absorption coefficient making the effect of absorption less pronounced in the collected signal.

The collected diffuse light is mostly influenced by scattering. Scattering coefficients

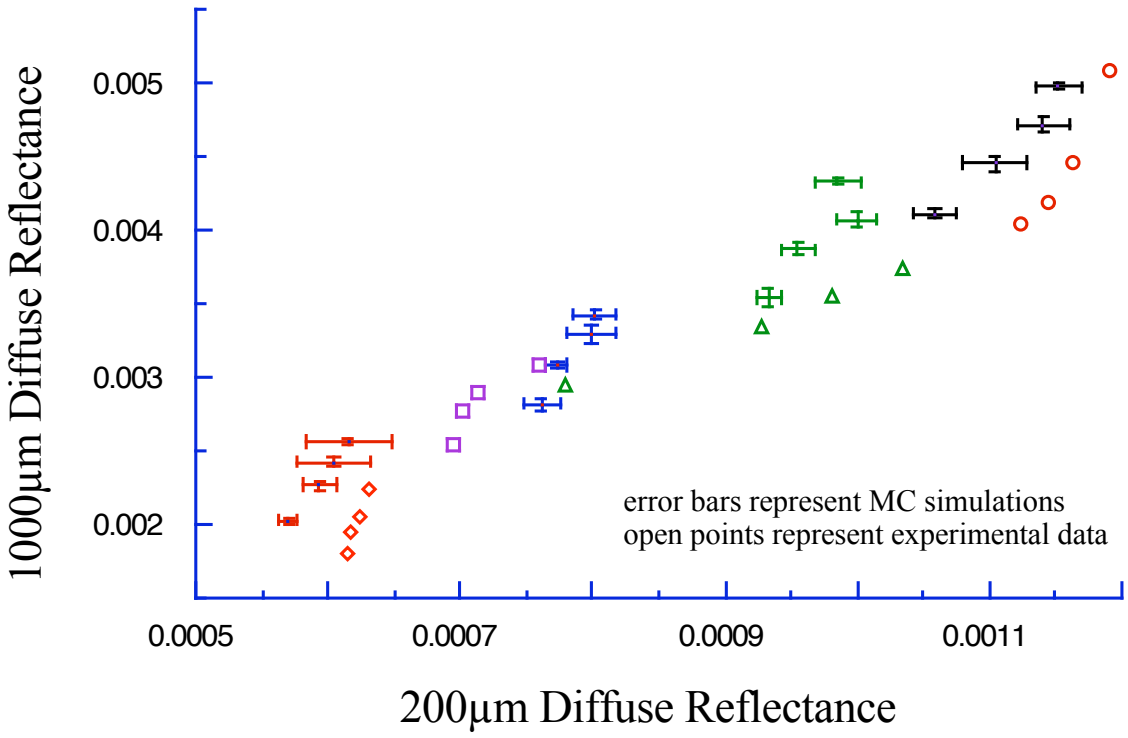

Figure 6.10: Measurements of an array of semi-infinite tissue phantoms are compared to Monte Carlo simulations with absorption coefficients of 0.1, 0.4, 0.9 and 1.6 cm^{-1}. The error bars represent the standard deviations of five Monte Carlo simulations with different starting seeds. Significant changes in the tissue phantoms scattering coefficient occur with changes in hydration of the gelatin. Stability of the phantoms scattering coefficient was compromised due to condensation on the phantoms while stored under refrigeration resulting in the observed difference between the phantoms and the Monte Carlo model.

may be resolved with less than 2% error for reduced scattering coefficients between 10 and $75\,\mathrm{cm}^{-1}$ assuming that anisotropy is constant and known *a priori*. Distinctions between two media with identical reduced scattering coefficients but differing anisotropy will be observed. Without knowledge of the anisotropy error will be introduced to predicted reduced scattering coefficient. Therefore, the sized-fiber device is sensitive to scattering mean free path, and not the approximation of the reduced scattering coefficient but since only two measurements are made the reduced scattering coefficient is utilized.

Sized-fiber reflectometry is not possible without controlling for specularly reflected light at the probe's fiber faces. The specular light was reduced by 50 and 15 times for the 200 and 1000 μm fibers respectively using angled fiber tip at 65 degrees. The experimental variation of measurements on skin of 2.2% is obtained as shown in the previous chapter. The improved signal reproduction gives the ability to determine scattering coefficients with a relative error less than 2% assuming that the anisotropy is known for reduced scattering coefficients between 10 and $75\,\mathrm{cm}^{-1}$. The system resolves absorption with a 50% error for absorption above $1\,\mathrm{cm}^{-1}$. Generally, the device is best suited for detecting gross changes in absorption and ideally suited for the determination of highly localized changes in scattering properties.

6.4 Dual-fiber probe with single emission fiber

In chapter 4, it was shown that single fiber emission and collection of its own back-scattered light is predominated by singly scattered photons. Another dual fiber probe design is now considered that uses a single fiber that emits and collects its back-scattered light (emission fiber) and a second fiber (collection fiber) which is in contact with the first fiber and collects light emitted by the first fiber. The collection fiber is expected to collect light that travels over a longer average path-length than the 1000 micron diameter fiber since light must travel laterally to get collected by the emitting fiber as confirmed in figure 6.12. A longer path-length for collected light gives an increase in sensitivity and resolution of absorption without increasing the diameter of the probe relative to the dual sized-fiber design. The probe consists of a 400 micron diameter fiber to emit and collect

its back-scattered light. The second fiber only collects light emitted by the first fiber and is also 400 microns in diameter. Since the fibers are polished at a 65 degree angle, the arrangement of the fibers influences the light collection behavior by the collection only fiber, but only one arrangement is investigated. The fibers are fixed in contact along the short axis of the elliptical faces of both fibers. The geometry of the fiber faces is shown in figure 6.11.

The design of the probe takes into account the findings in the previous sections of this chapter. The two optical fibers are mounted in a clear acrylic rod for support, robustness and reproducibility of signals. The relatively large area of the acrylic rod (6 by 7 mm for the polished face) to the optical fiber faces reduces measurement variability due to pressure effects during placement on tissues. The rod (6 by 6 mm) has two 430 micron holes into the center of the face of the rod so that two holes barely overlap and are about 4 mm deep. From the other side, a single channel 1 mm in diameter is drilled down to the two smaller holes. A counter bore hole is drilled for the teflon tubing that encases the fibers between the probe tip and the SMA connectors at the other end of the fibers. The fiber holes in the acrylic rod are filled with a light-cured medical grade epoxy (3211, Dymax Corp., Torrington, CT). The polyimide jacket is burned off the ends of the fiber with on open flame. The fibers are inserted through the uncured epoxy filled channels until they extend out through each of the 430 micron holes. The fibers are then fixed by curing the epoxy for 30 s with a fluid core light guide UV curing lamp (Dymax Corp., Torrington, CT) with the protective Teflon tubing set in the counter bore hole. Epoxy is placed on the outside of the tubing and on the top of the rod and cured as before for added strength. The acrylic rod and fibers are then polished together to a 65 degree angle starting with 400 grit wet sand paper to remove the bulk material followed by 9 micron and 0.3 micron wet lap paper to finish.

6.4.1 Monte Carlo simulations

The above Monte Carlo model is adapted to reflect this fiber probe. The changes reflect the fact that only one fiber emits light, while the second fiber collects light originating from the emission fiber. The launching of photons is therefore unchanged. A second boundary

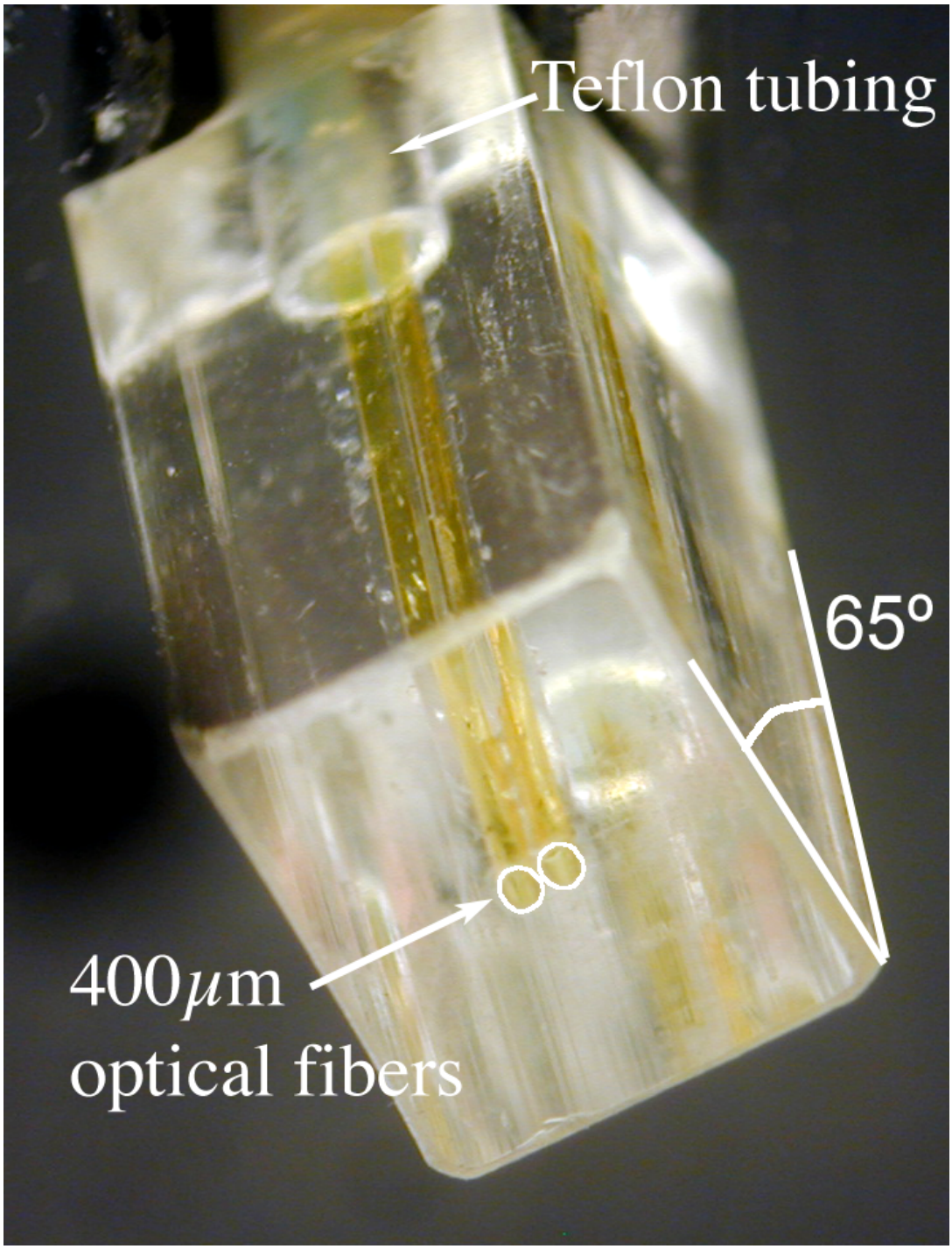

Figure 6.11: Two 400 micron diameter fibers are mounted in contact and stripped of the jackets down to the cladding. The fibers are polished at a 65 degree angle making the the fiber faces elliptical. The fibers are aligned along the minor-elliptical axis of their faces. In this probe design, only one fiber emits light while both fiber collect back-scattered light.

condition is added for photons incident upon the face of the second (collection) fiber. The fibers are modeled to be in contact along the short axis of the elliptical face of the two fibers with the fiber center to center spacing 430 microns apart to reflect the 15 micron thickness of the cladding on each fiber. Collection of photons was unaltered except for the addition of the second fiber. One million photons are launched for each combination of optical properties. The absorption coefficients were 0.05, 0.1, 0.2, 0.5, 1.0, 2.0 and 5.0 cm^{-1} and scattering coefficients of 100, 200, 500 and 1000 cm^{-1} with anisotropy of 0.9 using a Henyey-Greenstien phase function. Mean diffuse reflectance and the standard deviations were calculated from five runs of the model using different starting seeds for each combination of optical properties. Finally, the weighted average path-length of the collected diffuse light by emission and collection fibers was calculated.

6.4.2 Results and Disucssion

A common approach to derive the optical properties from measurements is to use interpolate values from maps generated by simulations (such as Fig. 6.13) or from maps of measurements on phantoms with known optical properties [5]. However, here a different empirical model is presented that relates the collected diffuse reflectance for the emission and collection fibers to the absorption and reduced scattering coefficient where the anisotropy is 0.9. The reflectance for a 400 micron diameter emission fiber may be approximated

$$-\log_{10}(R_{\text{emission}}) = \mu_a F(\mu_s)/100 + F(\mu_s) \tag{6.1}$$

where

$$F(\mu_s) = 4.91 - 0.96\log_{10}(\mu_s).$$

The base ten logarithm of the diffuse reflectance is shown for the emission fiber in figure 6.14 and the collection fiber in figure 6.15. The relative residual for this approximation is shown in figure 6.16. A relationship of this form for the reflectance by collection fiber was not satisfactory, producing residuals well in excess of 10% and continued to exhibit dependence upon either the absorption or scattering coefficient. This relation was determined by noticing that for a single scattering coefficient, the data points could be collapsed onto

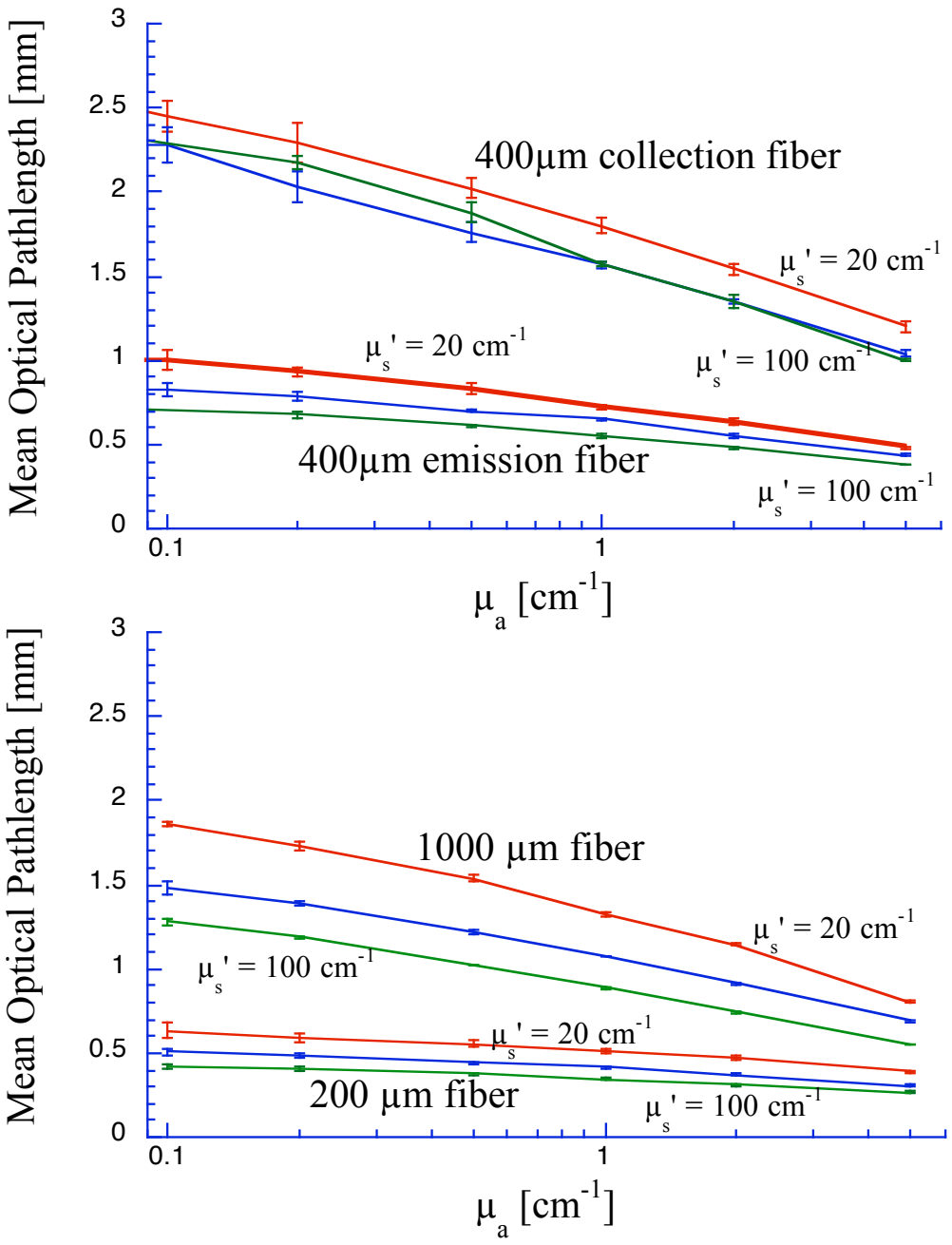

Figure 6.12: The mean path traveled for light collected by two side by side 400 micron diameter fibers is shown (top) in comparison to the mean path travel for the independent emission and collection of 200 and 1000 micron diameter fibers (bottom) as determined through Monte Carlo simulations. Three reduced scattering coefficients are shown 20, 50 and 100 cm^{-1} with the anisotropy fixed at 0.9. Error bars show the standard deviation of the mean for five runs at each combination of optical properties. The collection fiber has a 0.5 mm greater mean path-length for collected light than a 1000 micron fiber collecting its own emitted light.

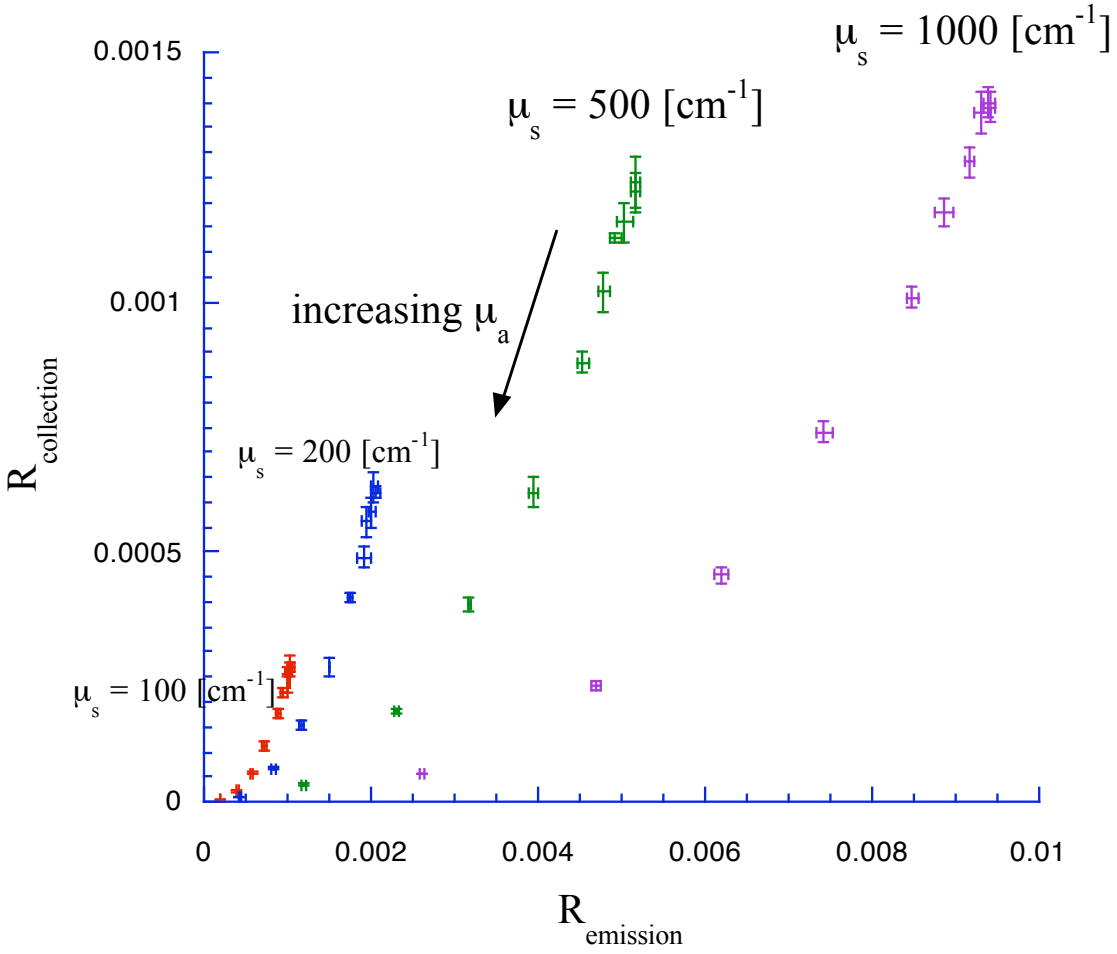

Figure 6.13: A mapping of the reflectance for two 400 micron fibers where one fiber emits and collects lights ($R_{emission}$) and the other fiber ($R_{collection}$) only collects light emitted by the first fiber. Each cluster represents a single scattering coefficient and absorption increases as the reflectance decreases within each cluster. Error bars are given by the standard deviation of five runs of the Monte Carlo model for each pair of optical coefficients. The anisotropy is 0.9 for all simulations.

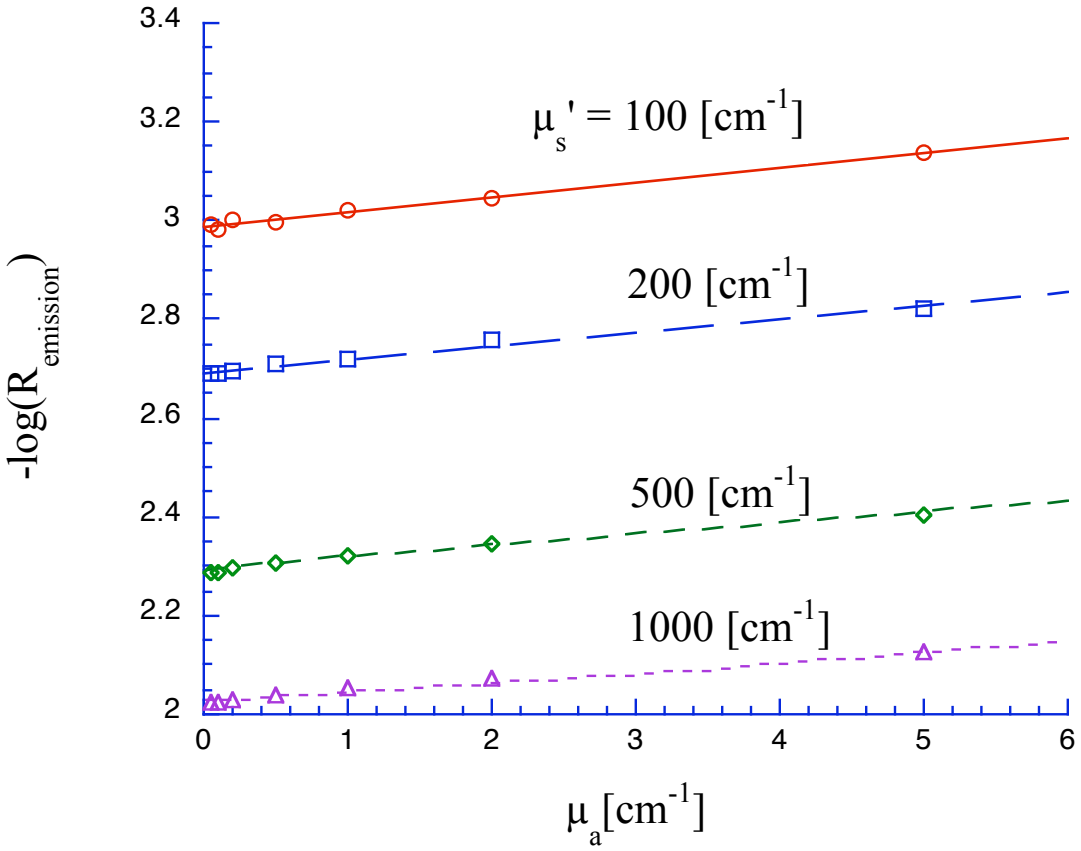

Figure 6.14: The base ten logarithm of the diffuse reflectance for the emission fiber as determined by a Monte Carlo model is modeled by equation 6.1 (lines).

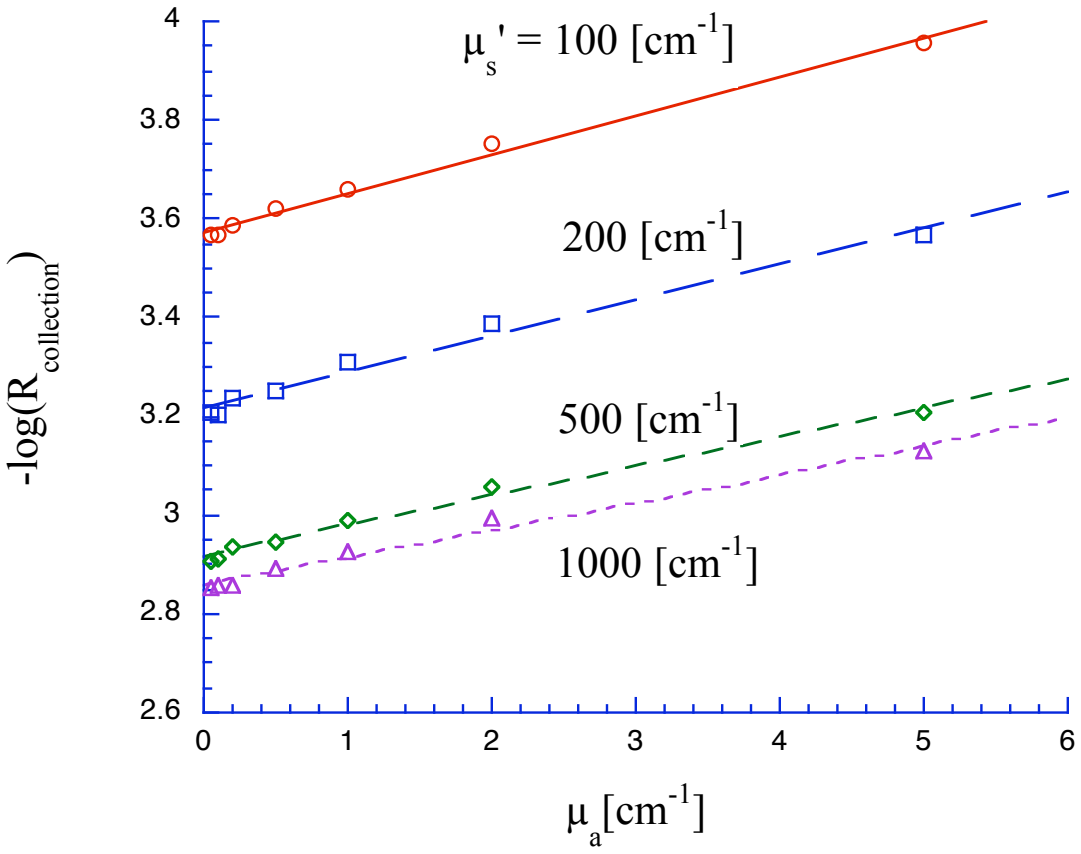

Figure 6.15: The base ten logarithm of the diffuse reflectance for the collection fiber as determined by a Monte Carlo model. The lines represent a linear fitting lines similar to equation 6.1 for the emission fiber, however the slope and offset do not have a simple functional relationship to the scattering coefficient as does the emission fiber.

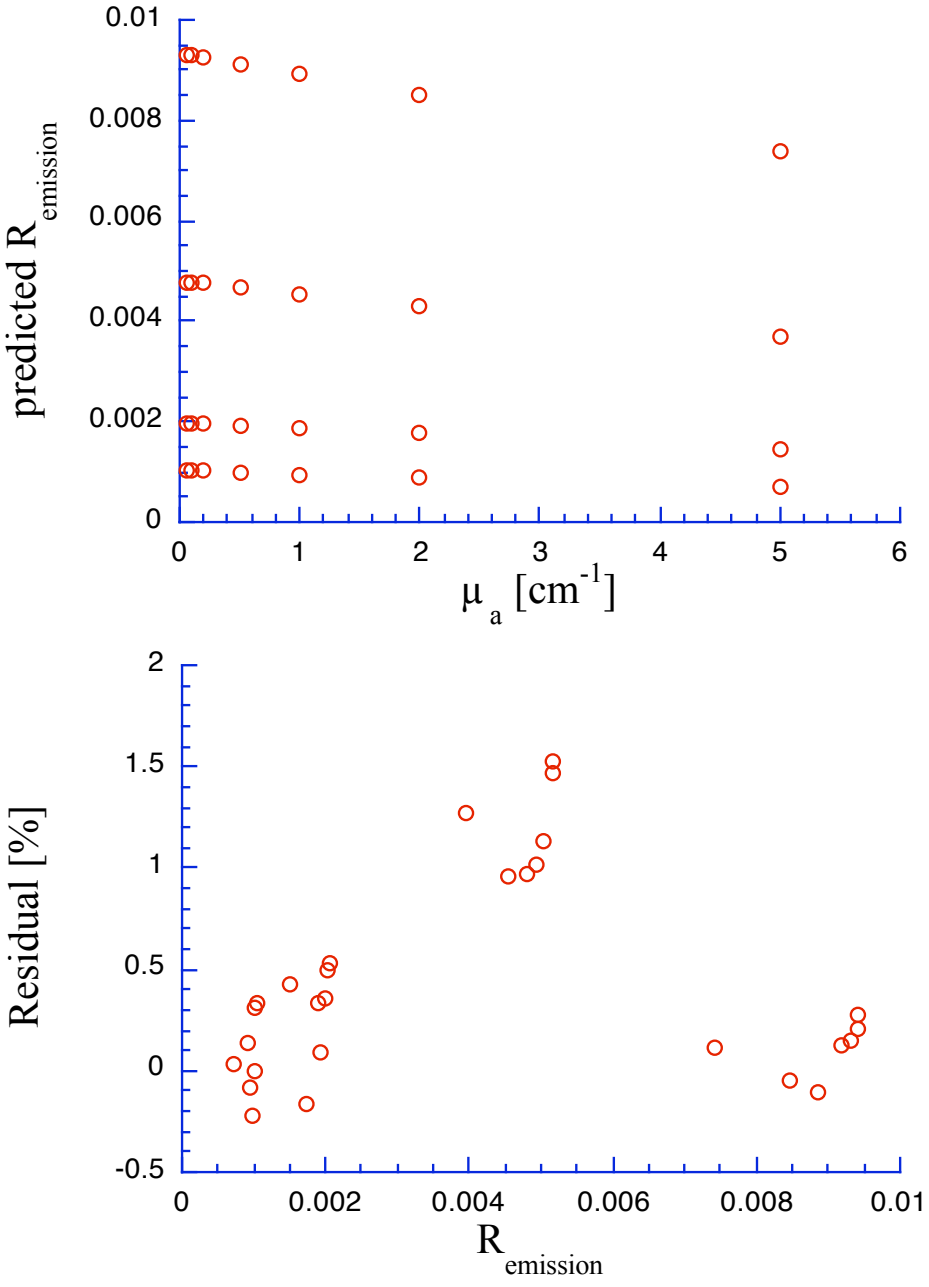

Figure 6.16: The relative residual error of the predicted reflectance to the reflectance established by the Monte Carlo model is given by $(R_{\text{predicted}} - R_{\text{true}})/R_{\text{true}}$. The predicted reflectance for the emission fiber is given by equation 6.1.

each other by the log-linear relation in eq. 6.1. $F(\mu_s)$ was determined by fitting for the slope and intercept coefficients of eq. 6.1 for each scattering coefficient. It was purely coincidental that the slope and intercept were proportional. The predictive nature eq. 6.1 is limited at this point, in the sense that it has not been tested for other scattering anisotropies (other than 0.9) or for other fiber diameters. This factor might be explored as a logical next step.

A closed-form relationship for single fiber measurements to the absorption and scattering properties would provide a similar tool as the diffusion approximation does for large fiber separations [17]. Equation 6.1 is used to determine the absorption coefficient given the scattering coefficient and the emission fiber reflectance. The scattering coefficient was determined from the mapping shown in figure 6.13 where the slope of a linear fit is related to the scattering by

$$R_{collection} = \frac{(R_{emission} + 0.006)}{0.0012(\mu_s + 1000))} - 0.005 \tag{6.2}$$

where $R_{collection}$ and $R_{emission}$ are the diffuse reflectance collected by the collection and emission fibers respectively for absorption coefficients less than $5\,\mathrm{cm}^{-1}$. Figure 6.17 shows the predicted versus true scattering coefficient as determined by eq. 6.2 and the residual error. FIgure 6.18 shows the predicted absorption versus the true absorption for the case where the scattering is known *a priori* and when predicted using eq.6.2.

The accuracy of equations 6.1 and 6.2 were further evaluated experimentally using a polyurethane phantom created as described in chapter 2 and characterized using the single sphere integrating sphere method described in chapter 3. Reflectance measurements were normalized using a teflon block as a reference and a dark measurement subtraction given by

$$R_{phantom} = R_{reference}\frac{M_{\mathrm{phantom}} - M_{dark}}{M_{\mathrm{reference}} - M_{dark}}$$

where M_{phantom} is the measured signal for the phantom, M_{dark} is the measured signal for the probe in a black box and $M_{\mathrm{reference}}$ is the measured signal for the teflon block. The teflon block's absorption and scattering were also characterized using the same integrating sphere method as the phantom. Monte Carlo simulations were then used to determine the reflectance of the teflon block ($R_{\mathrm{reference}}$) for the emission and collections fibers based

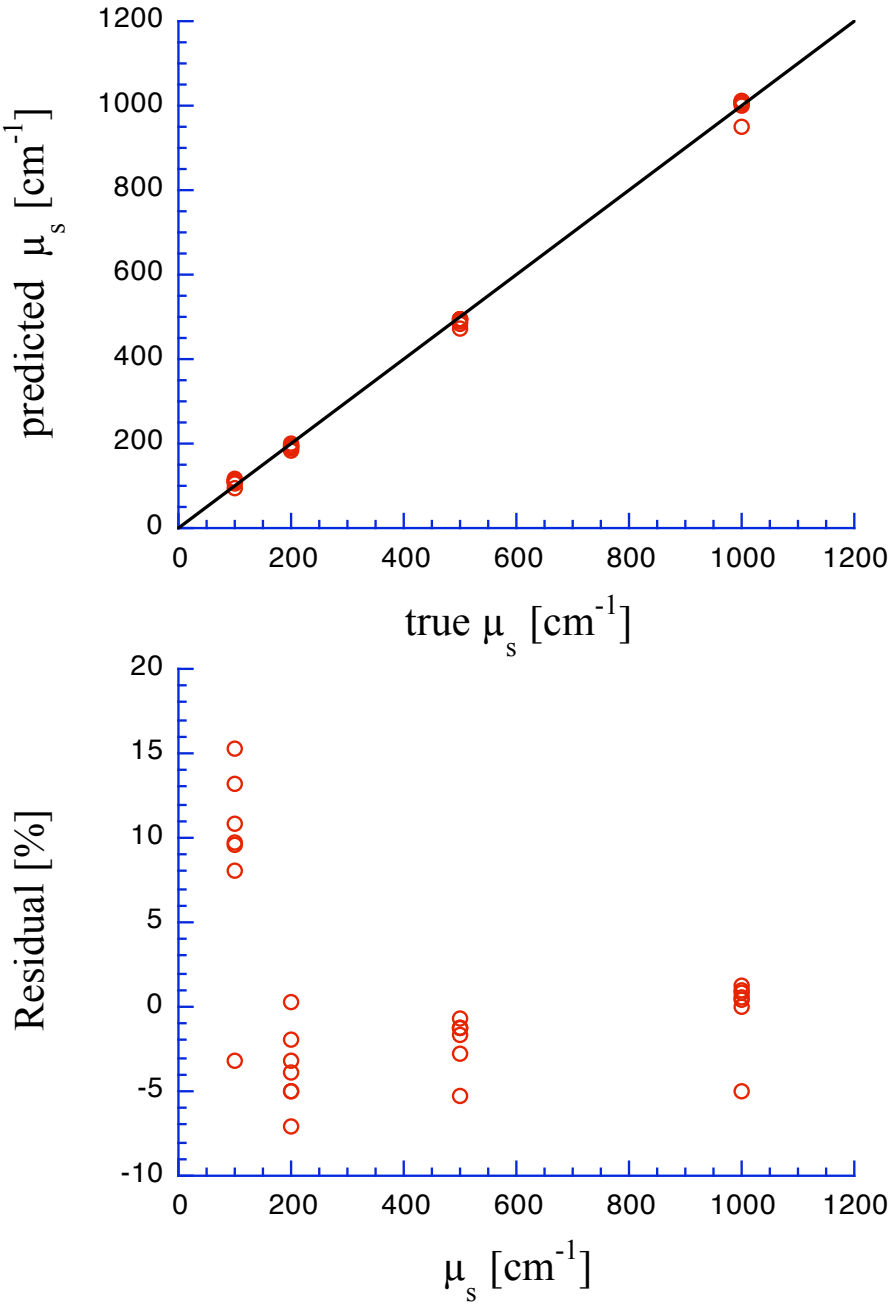

Figure 6.17: The predicted scattering coefficient plotted against the true scattering coefficient (top) for the reflectance generated from Monte Carlo model using equation 6.2. The relative residual error (bottom) of the predicted scattering coefficient is given by $(\mu_s'^{\text{predicted}} - \mu_s'^{\text{true}})/\mu_s'^{\text{true}}$.

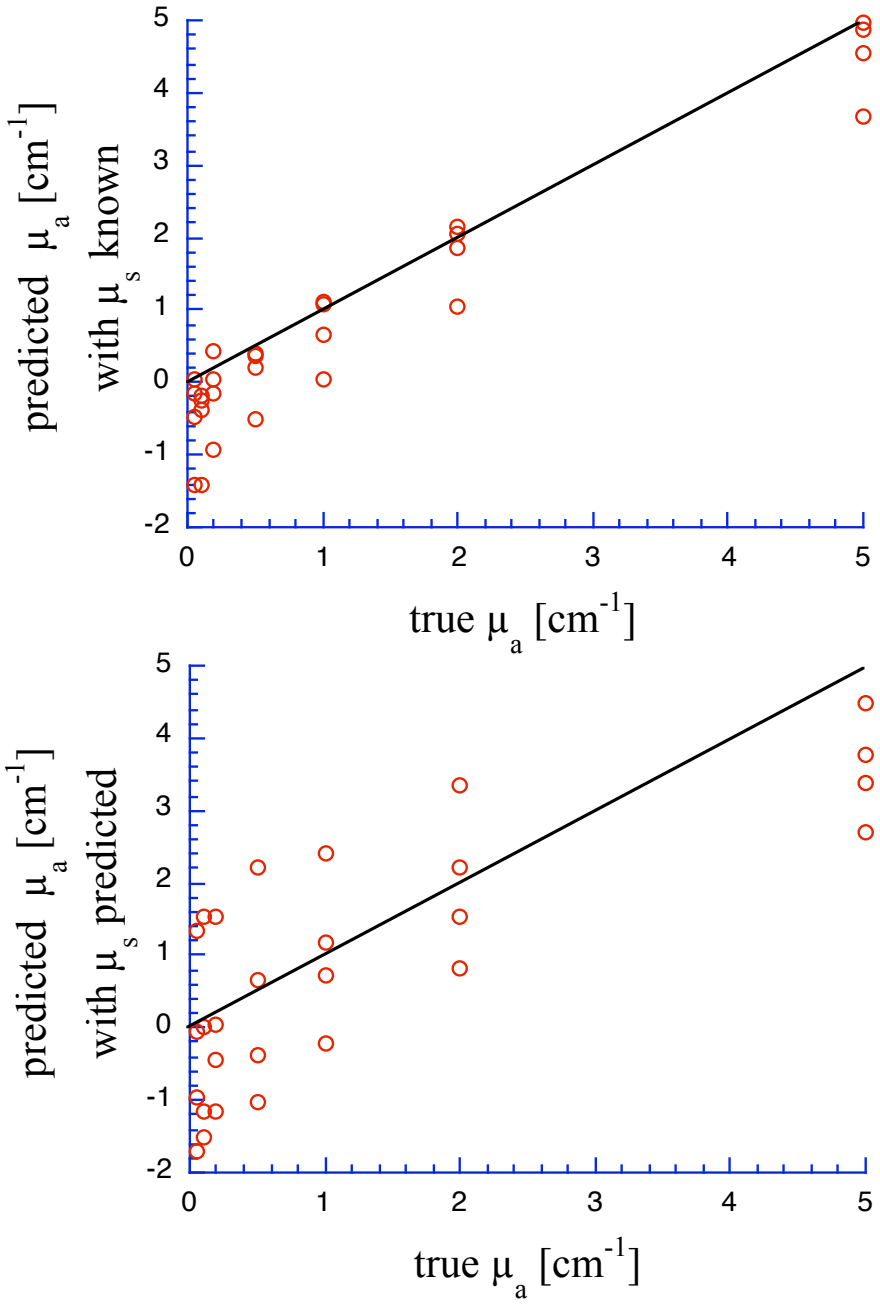

Figure 6.18: The predicted absorption coefficient plotted against the true absorption coefficient (top) for the reflectance generated from Monte Carlo model using equation 6.1 where the scattering coefficient is known exactly. The bottom plot is similar, except that the scattering coefficient is predicted as shown in figure 6.17.

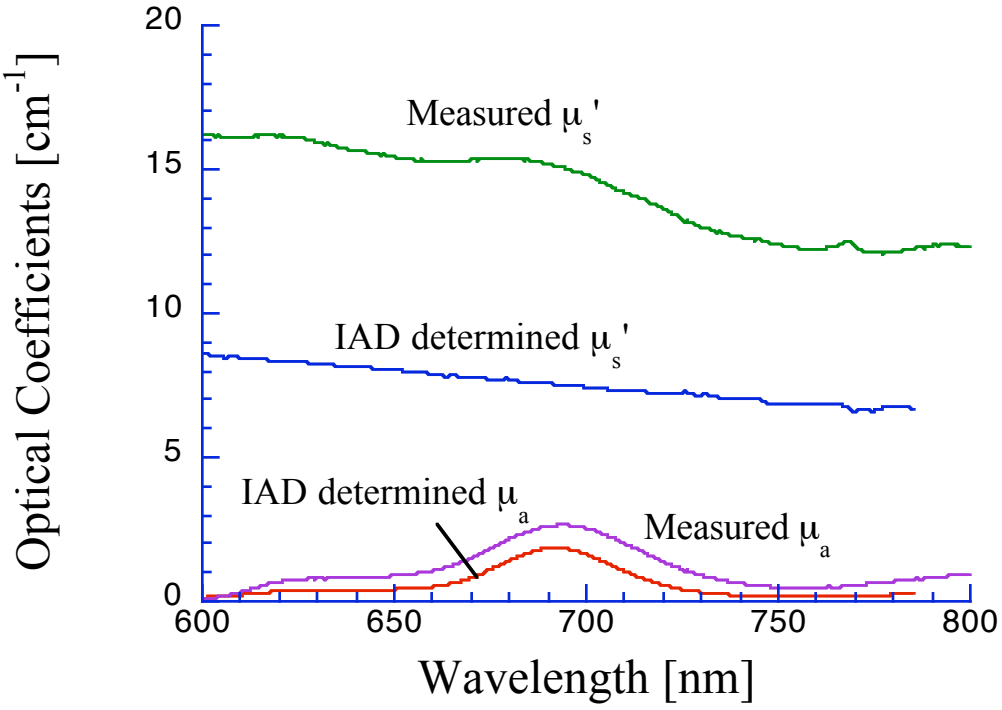

Figure 6.19: The measured optical properties of a polyurethane phantom using the dual 400 micron diameter fiber probe and eqs. 6.1 and 6.2 is shown in relation to the measured optical properties using inverse adding-doubling (IAD) with the single integrating sphere method presented in chapter 3.

on those optical properties. A comparison of the predicted optical properties in relation to the optical properties measured using the integrating sphere method is shown in figure 6.19. This method gives considerable cross-talk between absorption and scattering. In addition, the error in the predicted scattering leads to a doubling of the error in the predicted absorption as shown in figure 6.18. The error in the predicted absorption from the measurements of the optical phantom is consistent with figure 6.18. Moreover, the performance in absorption resolution is on par with the sized-fiber method that was shown to optically sample roughly a 25% shorter optical path.

6.5 Conclusions

Two dual-fiber devices were presented with corresponding methods to invert optical properties from diffuse reflection measurements, a sized-fiber probe that uses a 200 and 1000 micron diameter fibers both emitting and collecting light independently and a dual 400 micron diameter fiber probe with one emitting fiber and both fibers collecting reflected light. Only minor differences exists in performance between the probes. The single emission fiber probe has more compact physical dimensions and has a slightly longer optical sampling path-length (a 25-30% increase) relative to the sized-fiber probe. In the expected range of tissue optical properties for the visible spectrum, the greatest mean optical path-lengths measured are 2.5 mm or less, restricting the resolution of absorption where 100% error is possible. Absolute determination of absorption with either probe is poor for such short path-lengths, yet the relative absorption spectral shape was demonstrated on a measurement of an optical phantom, even with cross-talk between the measured absorption and scattering properties. The dual 400 micron fiber probe is a better design than the sized-fiber probe for two reasons. First, it is a less complex design with a single source fiber that is bifurcated for simultaneous emission and collection of light. Second, it has a slightly larger optical sampling path and a more narrow overall diameter. However for the inversion of optical properties, the linear interpolation of optical properties from a Monte Carlo generated grid gives the ability to determine scattering coefficients with a relative error less than 2% when the anisotropy is known *a priori*.

Chapter 7

Non-invasive Discrimination of Amalgam and Melanin in Pigmented Oral Lesions using a Dual Optical-fiber Probe

7.1 Introduction

Oral malignant melanoma has an estimated lifetime risk of 1/2,000,000 [132], but has a 5–year survival rate in the range 10–25% with a median survival of less than 2 years [133]. The poor survival of cases involving oral melanoma is complicated by several factors. Oral melanoma generally exhibits few symptoms; pain, ulceration, or bleeding are rare until late in the disease [134]. Though oral melanoma is rare, common benign pigmented lesions can easily be confused with melanoma [135]. Pigmented lesions not recognized as a specific entity such as an amalgam tattoo should be diagnosed by biopsy [136]. Buchner and Hansen stressed that histologic diagnosis is required for most pigmented oral lesions [137].

One of the more common oral benign pigmented lesions is the dental amalgam tattoo. A mass screening study of 23,616 predominantly white adults over 35 found melanotic macules and oral nevi (moles) with incidences of 0.38 and 0.47 lesions respectively per 1000 persons [138]. Amalgam tattooing occurs when small grains of amalgam are embedded into the mucosa. This is possible during restorative work when previous fillings are drilled out or even when flossing between teeth with amalgam fillings. These tattoos may exhibit a similar clinical coloration to melanin pigmentation and may also exhibit an uneven border characteristic of melanomas. X-ray images are the primary method to confirm the presence of amalgam in suspected tattoos. However, approximately only one quarter of

amalgam tattoos are visible by radiograph [135] and so the remainder require a biopsy to confirm their identity and rule out melanoma. Amalgam tattoos are 2-10 times more common than melanotic macules or oral nevi [139] but the true incidence is unknown [140]. The standard of care is to biopsy suspicious pigmented lesions due to the low survival rates for oral melanoma. Since the number of amalgam pigmented lesions is comparable to the number of melanin pigmented lesions, a method to non-invasively discriminate between these categories of pigmented lesions could greatly reduce the number of biopsies required, saving patients from additional pain and cost of the biopsy.

Techniques based on diffuse reflectance spectroscopy have shown promise to detect tissue morphological changes and distinguish between cancerous and normal tissues [10–13, 141–144]. In skin, diffuse reflectance spectroscopy has been used to measure chromophore concentrations using absorption profiles [145]. Diffuse reflectance spectroscopy can be performed non-invasively and requires minimal equipment. Other methods could be adapted to differentiate amalgam and melanin pigmentation in the oral cavity such as confocal microscopy [146] and energy dispersive X-ray microanalysis [147]. However, such equipment is considerably more costly than diffuse reflectance spectroscopy.

Dental amalgams vary widely in their exact mixture but they are composed of primarily silver (40–70% by weight), tin (15–30%), copper (12–30%) that is then mixed with roughly an equal weight of mercury. Modern conventional amalgams are considered high copper amalgams while some of the older amalgams used a low copper content amalgam of less than 6%. Other metals have been observed in trace quantities including indium, cadmium, lead, and antimony in various amalgams [148] while zinc may be present in quantity less than 1%. Corrosion of amalgam in the oral environment leads to a large host of possible products. Silver and mercury are least likely to electrochemically dissolve but may form nearly insoluble sulfide layers [149]. Tin forms mostly soluble ionic compounds while zinc is thermodynamically the most active component of amalgam followed by copper in dissolution [149]. However, amalgam tattoos react differently embedded in tissue than amalgam in the oral environment. Large particles are encapsulated and little breakdown occurs to the amalgam [150], while fine particles are digested by macrophages

and giant cells resulting in the progressive loss of tin and mercury leaving behind fine particles containing silver and sulphur [150, 151]. The age of the amalgam tattoo affects the materials in a tattoo; younger tattoos will contain degradation products and the oldest tattoos contains only particles of fine silver and sulphur and possibly large particles of almost unaltered amalgam.

The goal of this study was to evaluate the functionality of a dual-fiber diffuse reflectance probe to differentiate oral pigmented lesions caused by amalgam particles or by melanin. The results of a pilot study are reported using reflectance spectroscopy to differentiate measurements obtained from pigmented oral lesions and nearby non-pigmented sites from 30 patients. An example of an amalgam tattoo is shown in figure 7.1 along with the corresponding radiographic evidence for the presence of amalgam for one subject enrolled in the study. In contrast, figure 7.2 shows a typical subject with natural racial pigmentation. For all subjects, clearly defined borders between pigmented areas and the non-pigmented areas were observed. Melanin pigmentation exhibited a wide range of coloring in the oral cavity similar to the range observed in skin pigmentation.

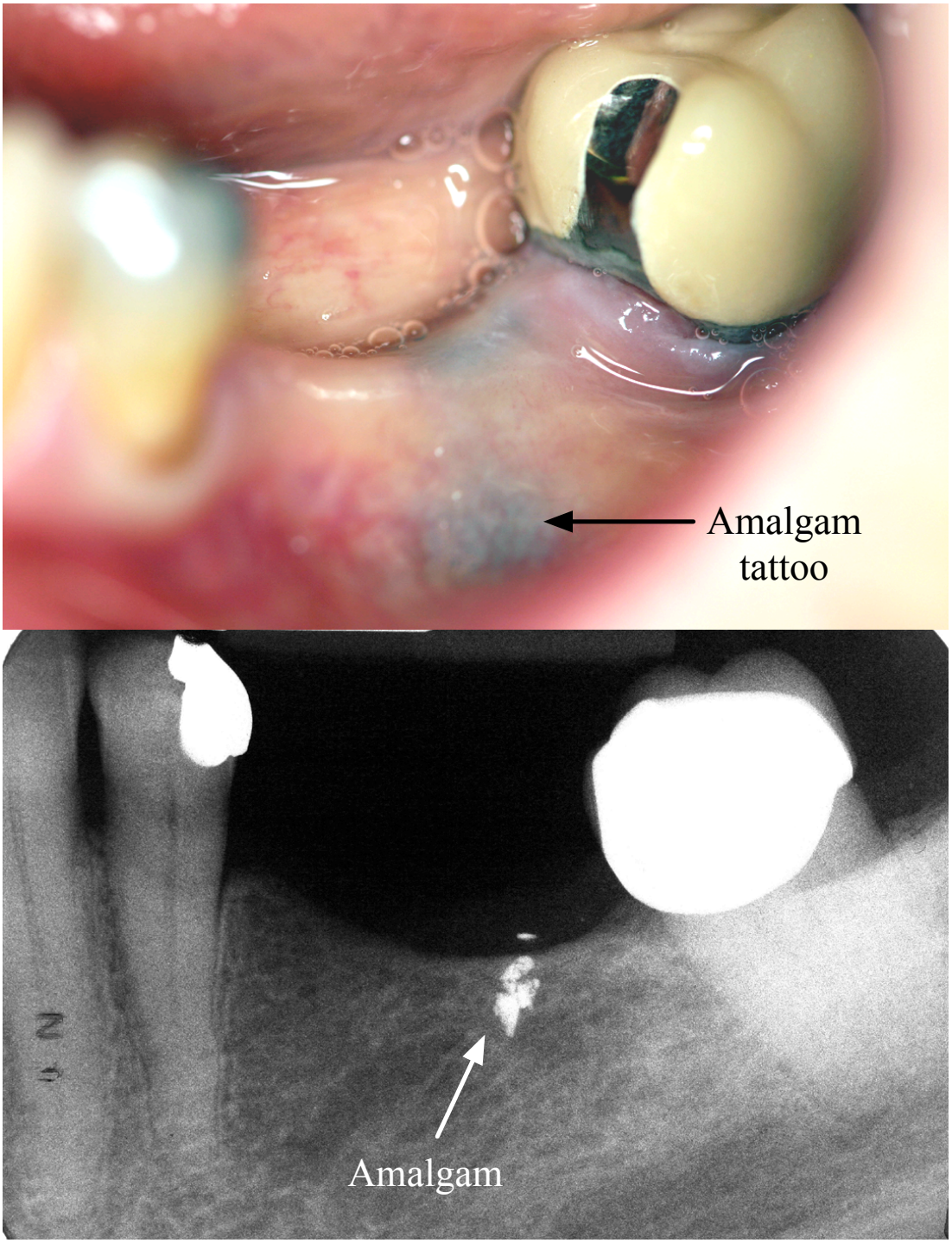

Figure 7.1: **Above:** An amalgam tattoo on the alveolar ridge in one subject is found where a tooth has been extracted leaving a bluish-black lesion as indicated by the arrow. **Below:** The radiograph of the above subject clearly showing a large cluster of amalgam particles emedded in the soft tissue. Large amalgam particles may be seen in radiographs whereas fine particles are not always observable, therefore the dimensions of the tattoo in the picture do not match the radiograph image.

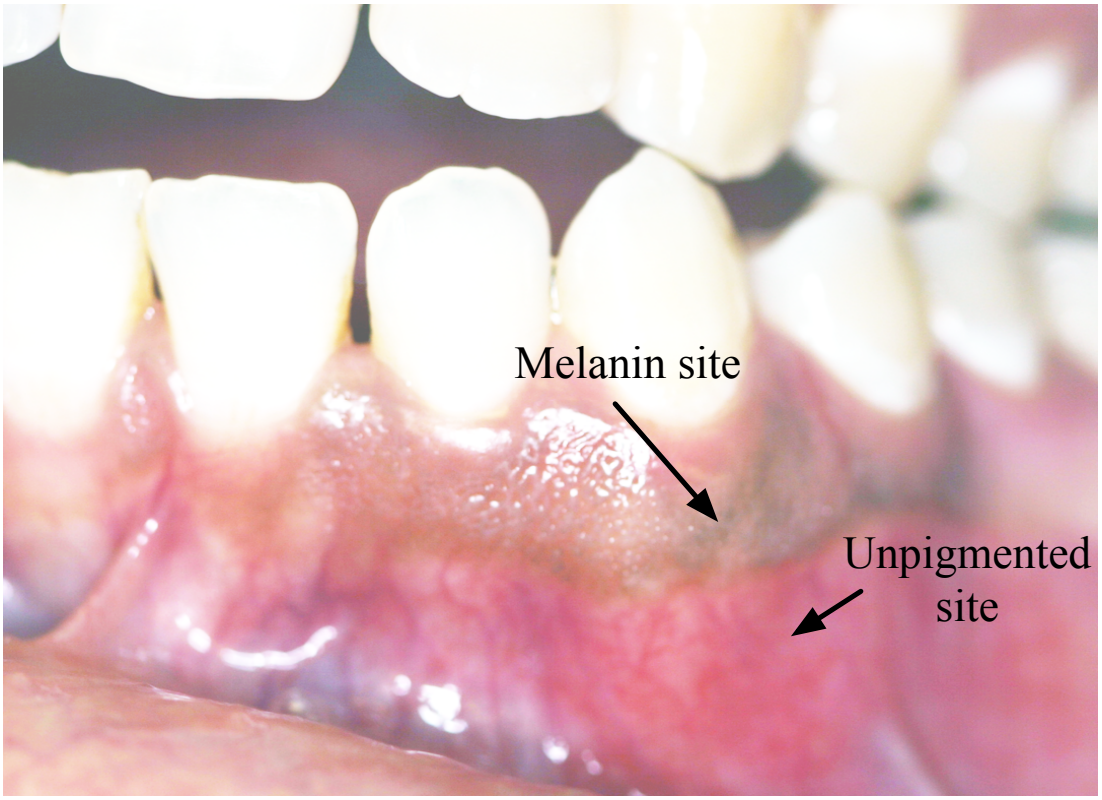

Figure 7.2: Measurements of melanin sites were performed on subjects with obvious racial pigmentation. This typical subject had melanin along the gum line and highly delineated non-pigmented area nearby which is measured as a control site. The darkness of the melanin pigmentation varied widely among subjects as well as the intra-subject variation shown here. The melanin is visibly more concentrated at the point of the arrow for the melanin site than to the left of the arrow.

7.2 Materials and methods

7.2.1 Study population

Thirty volunteers participated in the study that were recruited from the patients receiving dental care through the Oregon Health & Science University (OHSU) Dental School. The study was approved by the Institutional Review Board at OHSU. Potential subjects were approached if they exhibited natural melanin pigmentation of the gums (which is sometimes present in individuals with darker skin color) or had radiographic evidence of an amalgam tattoo that corresponded with a pigmented oral lesion. All volunteers were informed of the details of the experiment and their consent was obtained prior to the experiments. Half of the subjects had an amalgam tattoo, while sixteen subjects had obvious melanin pigmentation. One subject had both racial pigmentation and an amalgam tattoo, and was included in both groups of measurements. Volunteers were then taken to a dental examination chair in the clinic with the spectroscopy cart. An oral pathologist placed the fiber-optic probe onto the surface of the oral lesion and on nearby non-pigmented site. Three measurements were recorded at each site. After recording data from the subject, an additional measurement of a teflon block was made for use as a normalization reference.

7.2.2 Device

A spectroscopic system (fig. 7.3) was used to collect diffuse reflectance spectra from the oral mucosa *in vivo*. The system included a xenon arc lamp (6251, Oriel Instruments, Stratford, CT), with a water filter to reduce longer IR wavelengths while providing a broadband light source, a fiber optic probe that directs light to the tissue and collects diffusely reflected light at two positions, and a silicon-diode array grating spectrometer (1451 photodetector and 1471 controller, EG &G Corp., Fremont, CA) for light detection. The detector was purged with dry nitrogen gas to prevent water condensation on the detector. A fiber optic probe similar to the differential-path-length fiber probe of Amelink et al. [41] consisted of two optical fibers at the probe-face. One fiber both emits and collects light while the second fiber collects light emitted by the first fiber. All fibers (CeramOptec industries, Inc., East Longmeadow, MA) were 400 microns in diameter with a numerical

aperture of 0.22. The emission fiber was bifurcated fiber by end-coupling two fibers to a single fiber to allow for simultaneous emission and collection of light as described in section 6.4. Light was intentionally lost while coupling between fibers at the bifurcation by using fibers of the same diameter. The loss of light kept the magnitude of the collected light by the emitting fiber comparable to the collection-only fiber for measurements on the block of Teflon used as a reflectance standard. This allowed both the emission and collection fibers to use a comparable dynamic range while being switched into a single detector. The fibers were encased in Teflon tubing for robustness and the distal end of the fibers were fixed into a clear square-cylinder of acrylic then polished together to a 65 degree angle to the fiber-axis to prevent collection of specular reflected light. The probe tip was placed in contact with the tissue after the surface was patted dry with sterile gauze.

The diffuse reflectance of oral pigmented lesions and adjacent non-pigmented (normal) sites were collected with this system from 415–800 nm every 0.5 nm. The spectral resolution was 7 nm FWHM. The detector integration time was 0.6 s for all measurements. For most subjects, three measurements are recorded for both fibers on each site. The probe was placed by an oral pathologist on a pigmented oral lesion six times (for three consecutive measurements with each fiber) and then on a nearby non-pigmented site (6x). After each patient was measured, measurements on standards were recorded. These include a measurement on a white Teflon block 2.4 cm thick and 2.5 cm in diameter (M_{standard}) and a dark measurement by placing the probe tip in a black box (M_{dark}). The reflectance, $R(\lambda)$ was normalized by

$$R(\lambda)[\text{a.u.}] = \frac{M_{\text{tissue}}(\lambda) - M_{\text{dark}}(\lambda)}{M_{\text{standard}}(\lambda) - M_{\text{dark}}(\lambda)}$$

where M_{tissue} is the measured reflectance of the tissue. The probe was disinfected between patients by soaking in Cidex OPA(Johnson & Johnson) disinfectant followed by a spray rinsing of ethanol.

7.2.3 Amalgam characterization

The dominant chromophores in skin in the visible spectrum are hemoglobin (both oxygenated and deoxygenated) and melanin [152]. The absorption properties of hemoglobin

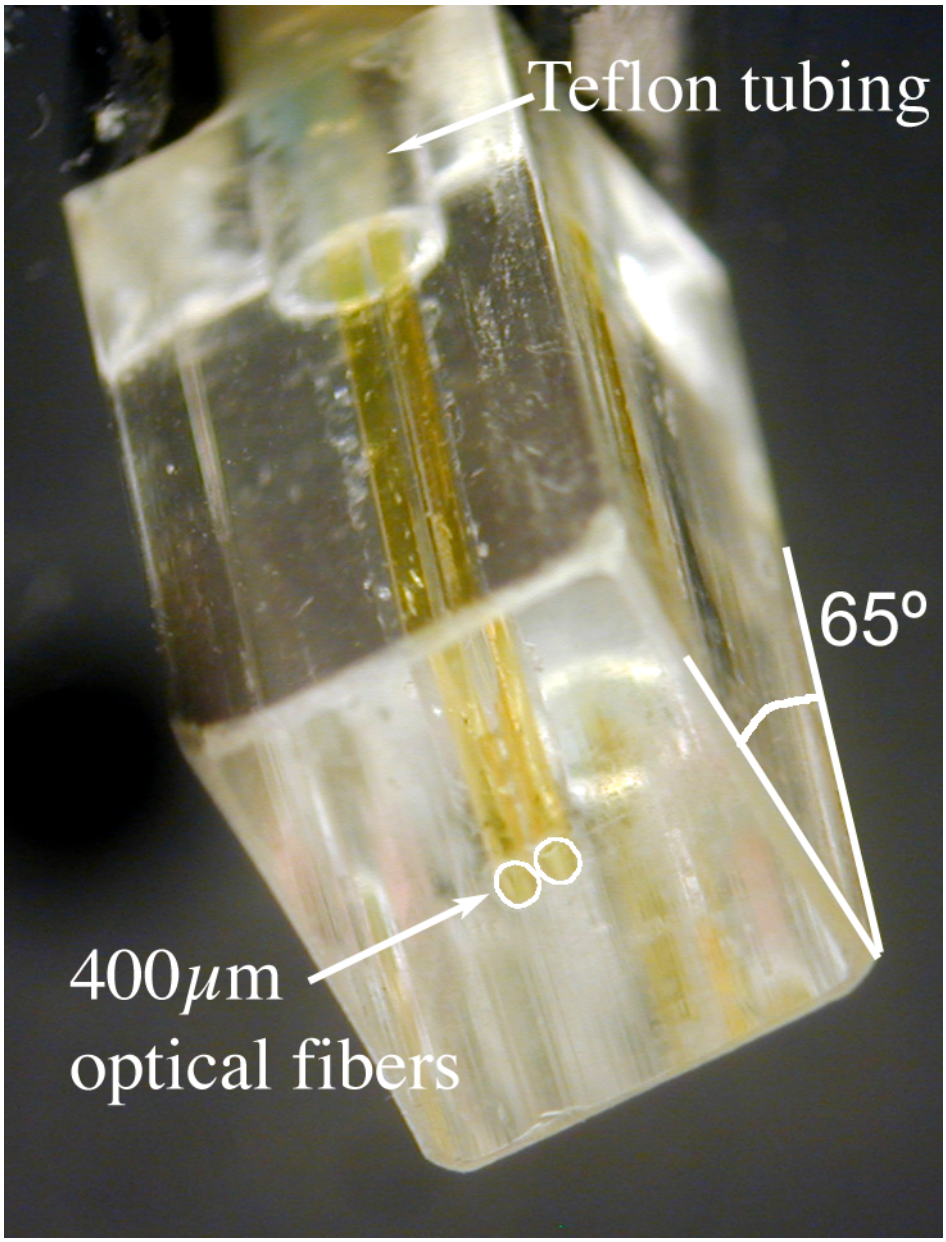

Figure 7.3: The device consists of two 400 micron fibers that are held together in an acrylic housing. One of the the fibers is bifurcated by end-coupling two 400 micron diameter fibers to a single 400 micron diameter for illumination and collection (the emission fiber) while the second fiber (collection fiber) collects light emitted by the emission. The fibers are switched into a spectrometer to record diffuse reflection for both fibers sequentially with a 0.6 s integration time. All optical fibers are encased in teflon tubing for robustness.

[153, 154] and melanin [155, 156] are well-documented. Dental amalgam is the exogenous chromophore causing the tattoos of interest in this study, but whose absorption properties are undocumented. Absorption by amalgam particles was characterized for three common alloys of amalgam: New True Dentalloy, Tytin and Dispersalloy. Each ot the three amalgam have differing ratios of metals. The three alloys were mixed and pressed into pellets. After 1 week, filings of each alloy were taken from the pellets allowing sufficient time for all chemical interactions in the amalgam. The fillings were placed between glass microscope slides with 0.15 mm cover-slips used as spacers. A reference blank slide was prepared without particles for signal normalization. All slides were cleaned with ethanol prior to use to remove any extraneous dust. Total diffuse reflection and transmission measurements were made with a double integrating sphere experiment since the particles both scatter and absorb light.

A pair of 203.2 mm diameter integrating spheres (IS-080-SF, Labsphere, Inc., North Sutton, NH) with a spectraflect coating were used for all measurements. The reflectance sphere had three open ports: a 6.3 mm port for the entrance, 19.1 mm sample port and a 12.7 mm detector port. A 1 mm diameter fiber (PWF1000T, CeramOptec Industries, East Longmeadow, MA) guided light from the detector port to a scanning grating photomultiplier tube detector in a spectrofluorometer (Fluorolog-3, Instruments S. A.,Inc., Edison, NJ); this fiber was used for collection from both spheres in sequential measurements of reflection and transmission. Spectra were recorded for visible wavelengths 400–800 nm in 1 nm increments with a 5 nm band-pass. A 600 micron optical fiber delivered white light from a tungsten lamp (LS-1, Ocean Optics Inc., Dunedin, FL) with a 5 mm diameter spot size. The fiber was held by a 4 mm steel tube painted with flat white spray paint inserted through the entrance port. The transmission sphere used identical port dimensions as the reflection sphere for the sample and detector ports, but no open entrance port. The relative absorption with respect to wavelength was determined using the combined inverse adding-doubling and Monte Carlo model. Results were considered to be relative since the concentration of amalgam particles was not precisely determined in the optical path of the beam nor was the particle distribution uniform across the sample port.

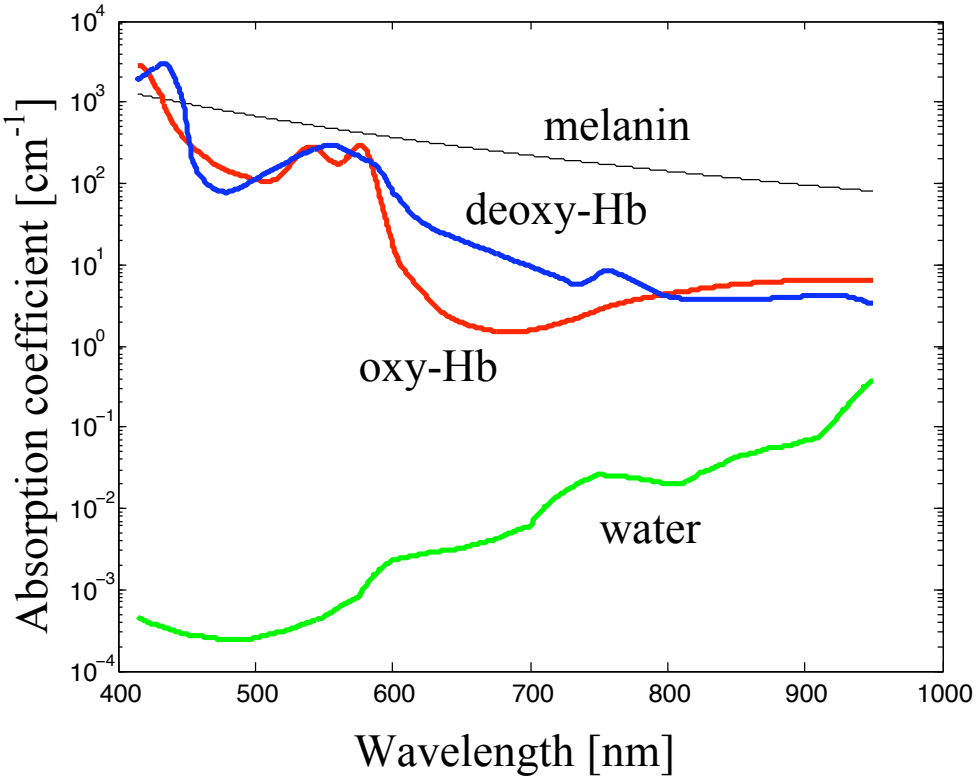

Figure 7.4: The absorption coefficients for the chromophores in tissue are used to fit to the spectral shape of the fiber measurements made with the collection fiber to determine if other optical characteristics of the measured spectra beyond melanin absorption can discriminate among sites.

7.2.4 Data Analysis

Spectral analysis was applied to the collection fiber data to determine the fraction of blood and melanin, the oxygen saturation using the absorption spectra of these components and evaluate the scattering properties from the shape of the measured reflectance. These parameters would then be examined to see which may be used as indicators to discriminate between sites. The absorption spectra for each component is shown in figure 7.4. A wavelength independent instrument scalar and a baseline offset were included into the fit to allow for variations due to contact variation of the fiber to the tissue but do not

alter the spectral shape of the fitting in of themselves. The reflectance measurements of the oral sites varied widely even within a single subject and compensation is necessary for a better fitting of the measurements. Kollias and Baqer [155, 157] showed that melanin concentration in skin may be estimated by the spectral region of 620–720 nm. The concentration of melanin was shown to be proportional to the slope (m) of a linear fit of the negative logarithm of the reflectance spectra in between 650-750 nm given by

$$-\log_{10} R(\lambda) = m\lambda + b.$$

This linear relationship is then applied to obtain the melanin fraction as was shown by Jacques [158]. The melanin concentration M was then

$$M = (m - m_{\text{ave, nonmelanin}}) * 100$$

where $m_{\text{ave, nonmelanin}} = 0.00033\,\text{OD/nm}$ was the average slope for all the sites without melanin which indicates the slope in the absence of melanin pigmentation. Typical values for m in melanin pigmented sites were $0.0015\,\text{OD/nm}$. The proportionality constant of 100 was not established experimentally but rather a value was chosen arbitrarily which set the melanin fraction to values that are published values of the melanin fraction in darker skinned individuals [158]. A 20% change to the proportionality constant did not affect the other fitting parameters other than the scattering.

A minimization routine was used to reduced the absolute error between the measurement and a predicted measurement based on the diffusion approximation in the wavelength range 450–725 nm. The predicted measurement was evaluated using the diffusion equation to get a reflectance between points spaced 200 microns apart with a melanin term separated out given by

$$\text{predicted Measurement} = Ke^{-M\mu_{a,\text{melanin}}D} R_{\text{diffusion}}(\mu_{a,\text{net}}, a\mu_s') + b$$

where fit values were K the instrument scaling factor, a a scattering coefficient scaling factor, and b a baseline offset. The melanin concentration M was determined as described above to prevent cross-talk between scattering scaling factor and the melanin concentration. The absorption spectrum of melanin was given by

$$\mu_{a,\text{melanin}} = 6.6 * 10^{11} \lambda^{-3.33}$$

and a constant path-length factor $D = 0.0060\,\mathrm{cm}$ was used. $R_{\mathrm{diffusion}}$ is the diffusion model equation with an extrapolated boundary given by Farrell [17] using an absorption coefficient given by

$$\mu_{a,\mathrm{net}} = B(S\mu_{a,\mathrm{oxy-Hb}} + (1-S)\mu_{a,\mathrm{deoxy-Hb}}) + 0.7\mu_{a,\mathrm{water}}$$

with fit parameters B the fraction of blood and S the oxygen saturation used in conjunction with the absorption coefficient for oxygenated hemoglobin ($\mu_{a,\mathrm{oxy-Hb}}$)and de-oxygenated hemoglobin ($\mu_{a,\mathrm{deoxy-Hb}}$). The absorption spectrum of water assumed a constant concentration at 70% in tissue. The scattering coefficient μ_s' was a linear combination of Rayleigh and Mie scattering terms given by

$$\mu_s' = 1.4 * 10^{12}\lambda^{-4} + 4.59 * 10^{3}\lambda^{-0.913}$$

where λ in the wavelength in units of nm. The measured reflectance was scaled as a function of wavelength by the reflectance that would be collected by the collection fiber on the teflon standard R_{teflon}. This value was determined by calculating the absorption and reduced scattering properties of the teflon by integrating sphere measurements and then calculating the expected reflection by the collection fiber using the Monte carlo model using a refractive index of 1.35 for the teflon at all wavelengths.

Two approaches were employed to analyze the reflectance spectra, each to answer separate questions regarding the pigmentation rely upon melanin absorption as a means to distinguish sites.. The first approach focused on the quantity of melanin as observed in the reflectance spectrum. As previously stated, Kollias and Baqer [155, 157] showed that melanin concentration in skin may be estimated by the spectral region of 620–720 nm. The concentration of melanin was shown to be proportional to the slope (m) of a linear fit of the negative logarithm of the reflectance spectra in that wavelength range given by

$$-\log_{10} R(\lambda) = m\lambda + b.$$

I found that absorption by oxy-hemoglobin affected the reflectance spectra in our probe measurements below 640 nm. Therefore, a linear fit was used to establish the value of m for each measurement (both emission and collection fibers) between 640 and 720 nm.

The values of m were then separated into 4 groups: melanin sites, non-pigmented sites on melanin subjects (melanin controls), amalgam sites and non-pigmented sites on amalgam subjects (amalgam controls) as seen in table 7.1. Sites that contain melanin pigmentation were determined by using a threshold value of the slope. A Receiver Operator Characteristic (ROC) [159] was determined for measurements with the emission and collection fibers independently for different threshold values. Measurements from all 4 groups were included giving an N= 48 for melanin sites and N= 132 for non-melanin sites. The sensitivity at each threshold was calculated by

$$\text{Sensitivity} = \frac{\Sigma\text{True positive}}{\Sigma\text{True positive} + \Sigma\text{False negative}}$$

and the specificity by

$$\text{Specificity} = \frac{\Sigma\text{True negative}}{\Sigma\text{True negative} + \Sigma\text{False positive}}.$$

True positives are defined as melanin sites identified as containing melanin, false negatives are melanin sites identified as containing no melanin pigmentation, true negatives are amalgam and unpigmented sites identified as containing no melanin pigmentation, and false positives are amalgam and unpigmented sites identified as containing melanin.

Discriminant analysis was used as a second alternative analysis to classify measurements into one of three groups: melanin pigmentation, amalgam pigmentation, or non-pigmented. For the discriminant analysis, the reflectance spectra were modified to simulate the reflectance measurements that would be produced using several spectral filters, white light, and a broadband absorbing detector (e. g. silicon). The spectral filters were centered every 25 nm starting at 450 nm and extending to 700 nm for 11 simulated measurements (Fig. 7.5). Each filter was modeled as a normalized gaussian function (area under the gaussian equal to one) with full width at half max (FWHM) of 12 nm given by

$$T(\lambda) = Ce^{-\left(\frac{(\lambda_0-\lambda)^2}{2\sigma^2}\right)}$$

where C is a normalization constant, λ_0 is the centroid wavelength, and $\sigma = 5$ nm. The filter functions were multiplied by each of the reflectance spectra recorded from the subjects. This effectively generated a set of 22 measurements at each site, 11 different wavelength bands and collection by both fibers.

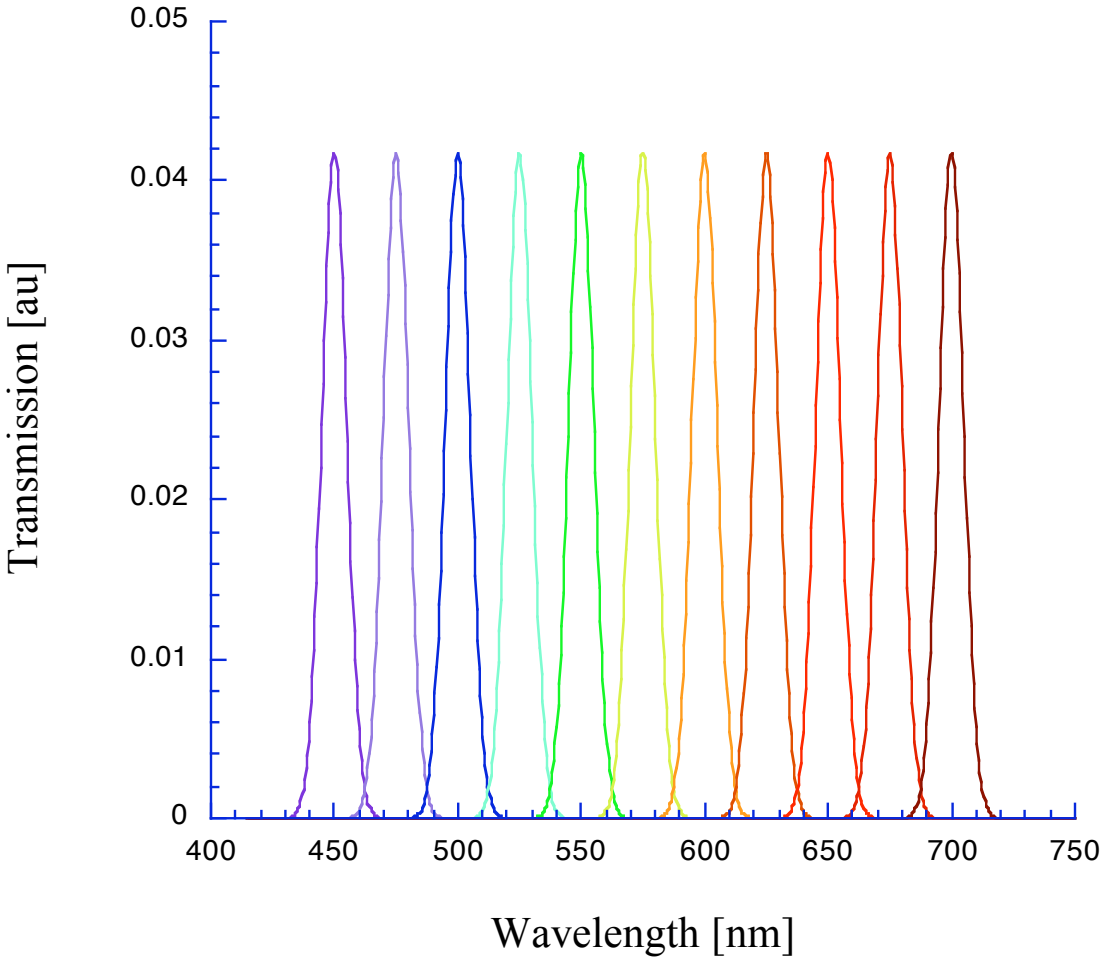

Figure 7.5: Each fiber measurements was multiplied by the 11 gaussians shown here to simulate the collection of light using spectral filters. Each filter is a gaussian with a 12 nm at FWHM and normalized to have an area under the curve of one.

The simulated spectral filter data was split into a classification group (roughly 2/3 of all data) and a test group (the remaining 1/3). All measurements for a single subject were included together in a single group. To prevent bias in selection, the test group consisted of every third subject for the cases with melanin pigmentation and every third with amalgam pigmentation. The number of melanin subjects was not divisible by three and so the one extra subject was included in the test group. In total, the classification group consisted of 10 subjects with an amalgam tattoo, 10 subjects with natural melanin pigmentation and 20 non-pigmented sites on those subjects. The test group consisted of 5 subjects with an amalgam tattoo, 6 subjects with melanin pigmentation and the corresponding non-pigmented sites for those subjects. The classification group was used to determine the discriminant functions and which variables (spectral filters) to include or exclude.

It is expected that some of the wavelength measurements will be dependently related to each other and therefore will not improve the discriminant model. The reduction of redundant data was performed using only data in the classification group. All statistical tests were performed using SPSS software. The reflectance populations at each wavelength band were tested for normality, an assumption of discriminant analysis. Discriminant functions were calculated with the software giving weights to each input variable (wavelength bands) and showing the classification table for those functions (eg. table 7.1). An organized trial and error approach was employed to determine the best discriminant functions. The first discriminant functions used only the wavelength bands where the reflectance was normally distributed. A second set of discriminant functions were calculated using a subset of inputs where the lowest weighted ($\leq 5\%$) inputs were excluded. The process was repeated to find the minimum number of wavelength bands that provided the best classification of only the melanin sites (amalgam and non-pigmented sites were not yet considered). Separation of the melanin sites from the other sites required just two reflectance measurements by the collection fiber.

Next, the process was repeated to evaluate the wavelength bands that best differentiate the amalgam sites from the non-pigmented sites using a two-group discriminant analysis omitting melanin site data. The first discriminant function used all normally distributed

wavelength bands. New discriminant functions were determined eliminating the least contributing inputs ($\leq$ 5% weight). This step was repeated while correct classification of the two groups did not drop. This led to the identification of six measurements that provided the best discrimination between amalgam and non-pigmented sites.

Of a possible 22 inputs measurements, eight measurements were identified as key to discriminating the three groups. Classification using those eight measurements was compared to classification with discriminant functions that included a ninth input measurement. Each of the omitted measurements was individually included with the eight key measurements and classified with discriminant analysis. Finally, classification was performed using all combinations with 1 of the 8 measurements removed. The correct classification rate of the three groups was reduced whenever a measurement was removed. Classification was unimproved with a ninth measurement.

Classification in one of the three groups is decided by using two discriminant functions to score each site. The first discriminant function (F_1) separates the melanin sites from the non-pigmented sites and amalgam sites,

$$\begin{aligned} F_1 &= -1.72 - 35.61R_{\text{em, 475}} + 65.34R_{\text{em, 500}} - 27.35R_{\text{em, 550}} + 6.539R_{\text{coll, 475}} \\ &+ 19.02R_{\text{coll, 500}} - 24.57R_{\text{coll, 525}} + 80.75R_{\text{coll, 650}} - 76.86R_{\text{coll, 675}} \end{aligned}$$

where R_{em} is an emission fiber reflectance, R_{coll} is a collection fiber reflectance and the number in the subscript denotes the centroid wavelength.

The second discriminant function then divides the non-pigmented sites from the amalgam sites and is given by

$$\begin{aligned} F_2 &= -2.16 - 3.605R_{\text{em, 475}} + 29.03R_{\text{em, 500}} - 23.52R_{\text{em, 550}} + 0.1358R_{\text{coll, 475}} \\ &- 3.906R_{\text{coll, 500}} - 6.306R_{\text{coll, 525}} - 35.55R_{\text{coll, 650}} + 45.32R_{\text{coll, 675}} \end{aligned}$$

A scatter plot of all measurements in the classification group is shown in figure 7.6. The measurements in the test group are evaluated by the discriminant function scores. Measurements are then classified by the nearest group centroid from the classification group set. The centroids of the melanin sites, amalgam sites and non-pigmented sites are respectively: $(F_1, F_2) = (-2.667, 0.236)$, $(0.315, -1.049)$, and $(1.222, 0.402)$.

7.3 Results

The optical properties of dental amalgam must be different from those of melanin in order to differentiate lesions. The absorption properties of three formulations of dental amalgam are shown in figure 7.7. Absolute absorption coefficients could not be established from our measurements but all three amalgams exhibited a spectrally uniform absorption from 400–800 nm.

All the measurements for both fibers are shown in figure 7.8 separated by the site pigment type. The mean reflectance spectra obtained from all subjects is shown for the emission fiber in figure 7.9 and the collection fiber in figure 7.10. The reflectance for any individual measurement is similar to the mean reflectance for its site type. Though the standard deviation for each site type is large relative to the difference between the means, some observations were consistent within an individual subject. The non-pigmented sites produce the highest measured reflectance in measurements with both fibers. The absorption of light by hemoglobin (producing valleys at 550 and 570 nm) is obvious in the reflectance by the non-pigmented sites and by the amalgam sites though to a lesser degree. In contrast, the absorption by hemoglobin is almost completely obscured in measurements at melanin sites with the emission fiber. The most distinguishing feature between reflectance collected on amalgam and melanin sites is the change in the reflectance slope with respect to wavelength.

Component spectral fitting was performed on the data for the collection fiber to ascertain which known variables might be useful for discrimination. Typical fit spectra are shown with the measurement being fit in figure 7.11. Five parameters were allowed to vary in the fitting, the fraction of blood, the blood oxygen saturation, a total reflectance scalar, a scattering scalar, and the baseline offset. A handful of measurements did not fit well; these measurements exhibited much less blood absorption or reflected blue light and red light nearly equally well. Histograms of the the spectral components parameters are shown in figures 7.12, 7.14, 7.15, and 7.16. The oxygen saturation tended to have lower values with drop in the fraction of blood and was likely due to inability to resolve with a small hemoglobin signature in the reflectance measurement. The method for establishing

	Group	Predicted non-pigmented	Predicted melanin	Predicted amalgam	Total
Actual count	non-pigmented	27	0	3	30
	melanin	0	17	1	18
	amalgam	7	0	8	15
Actual percentage	non-pigmented	90	0	10	100
	melanin	0	94.4	5.6	100
	amalgam	46.7	0	53.3	100

Table 7.1: Classification table of measurements from the test group as predicted using discriminant function analysis on an independent classification group of measurements. Overall, 82.5% of measurements are correctly classified.

the fraction of melanin scaled the melanin sites within expectations but allowed the non-melanin sites to have a small negative melanin content if the slope was less than the mean for non-melanin pigmented sites. The melanin concentrations are shown in figure 7.13. Histograms of the scaler to the scattering coefficient is shown in figure 7.14. Melanin sites that show an elevated scattering properties were due to outliers in cause by poor fitting. The values for blood concentration, oxygen saturation, scattering, instrument scaling and baseline offset all show little is if any difference between site types. Therefore, melanin is the only factor that consistently differentiates the spectral shape of the measurements for the collection fiber as is shown in figure 7.17 in comparison to the blood fraction..

Figure 7.18 shows box plot distributions of the melanin slope m for the emission and collection fibers. Using a simple threshold value to determine sites that are predominantly influenced by melanin absorption, the sensitivity and specificity are shown in figures 7.19 and 7.20 as ROC curves of the threshold value.

Figure 7.21 shows a scatter-plot of the two discriminant function scores of the measurements in the test group. The discriminant functions are described by equations 7.1 and 7.1. Measurements are classified into the group of the nearest group centroid of the classification data set. A summary of the classification results are shown in table 7.1.

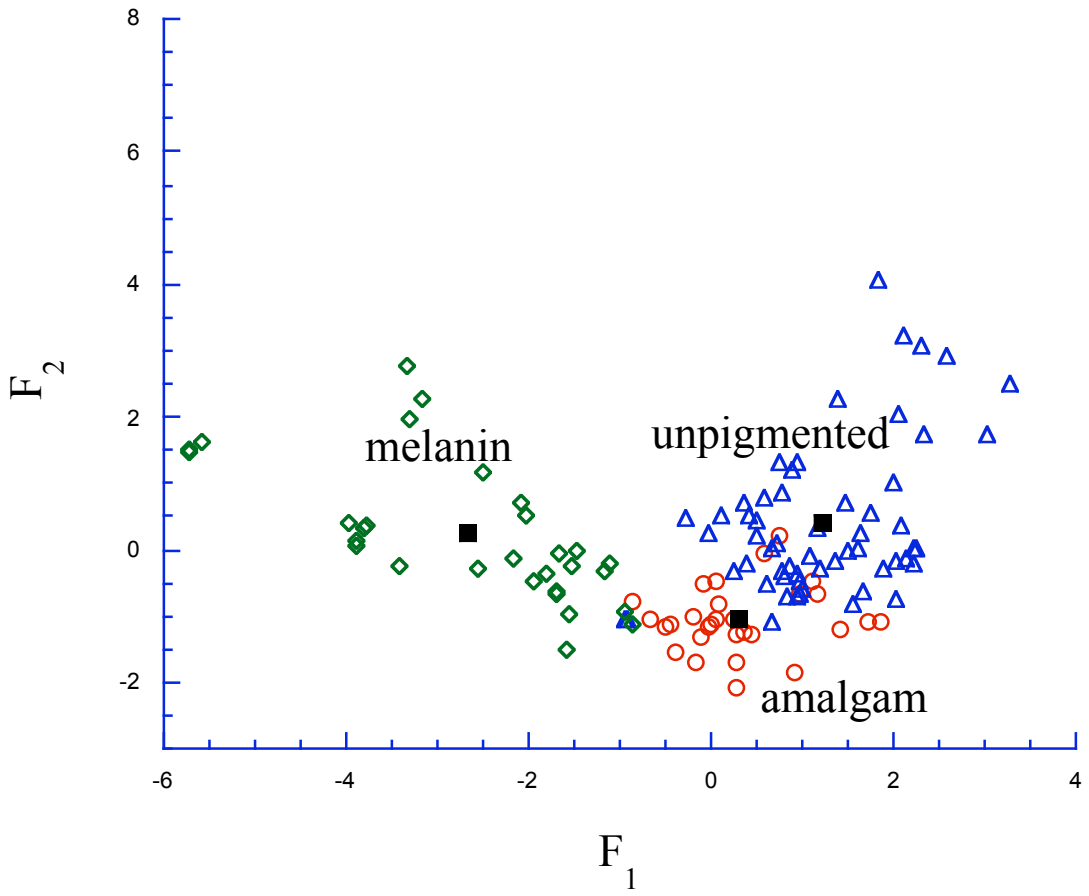

Figure 7.6: A scatterplot of the measurements in the classification group in the discriminant function space. Points indicated by diamonds represent measurements from melanin sites, circles indicate amalgam sites, and triangles indicate the non-pigmented sites. The centroids of each group is shown as a filled square. Future cases are determined by the nearest group centroid.

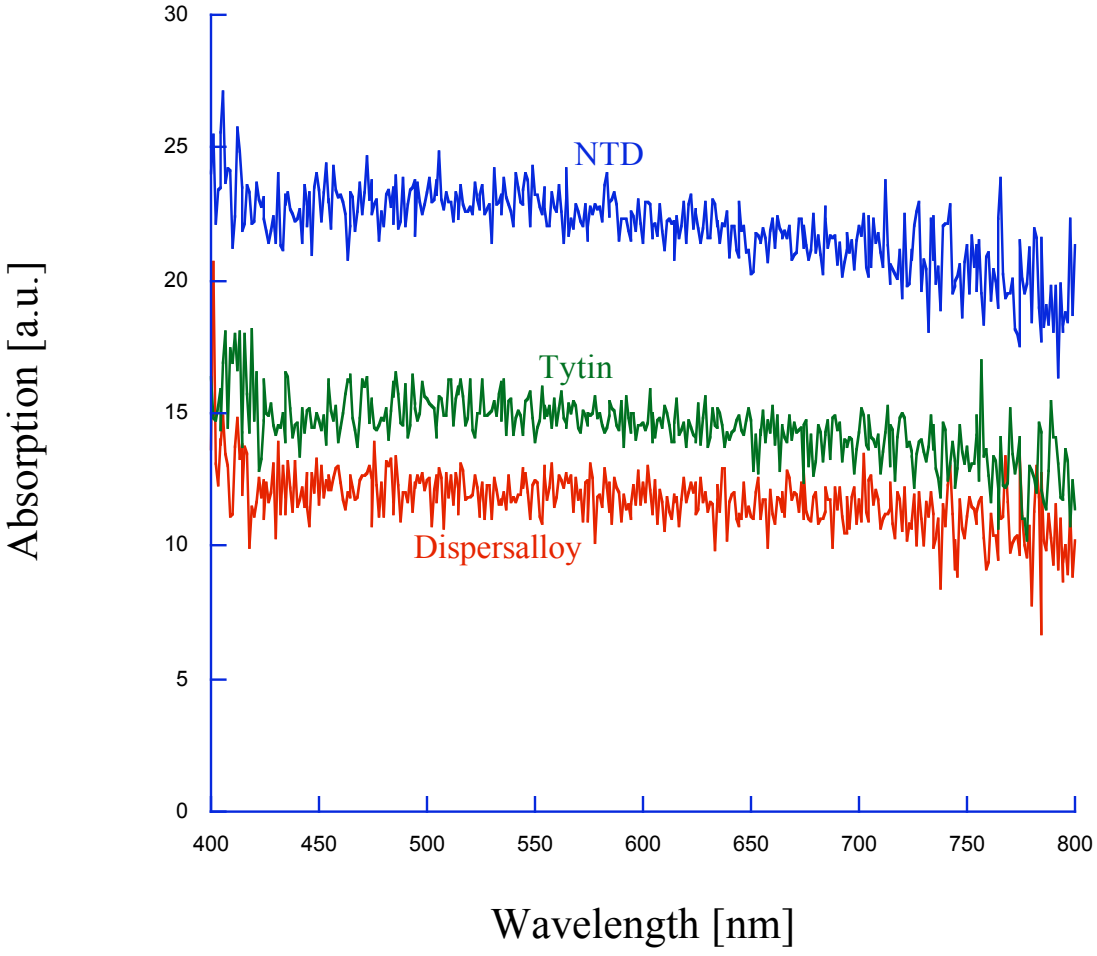

Figure 7.7: The fraction of light absorbed of three commercial alloys of dental amalgams determined from single integrating sphere measurements. In the visible spectrum amalgam absorbs light uniformly acting like a neutral density filter. The absorption coefficient was not determinable due to the unknown concentration of particles in the light-path for each alloy. In this regard, it is not determinable whether one ally absorbs more strongly than any other.

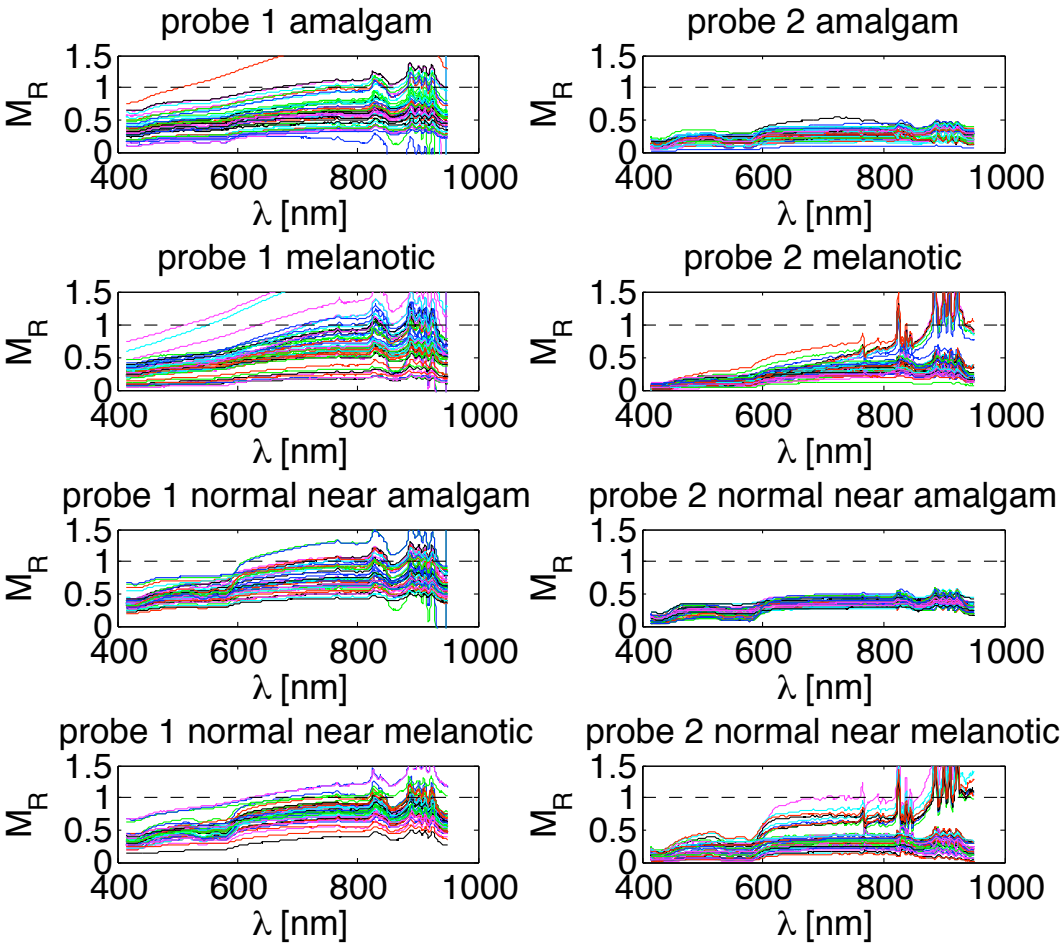

Figure 7.8: The normalized measured reflectance spectra for all sites is shown with the emission fiber indicated as probe 1 and the collection fiber as probe 2. Measurement variation necessitates the use of a baseline adjustment and instrument scaling factor in order to fit the measurements using the spectral shape of the known components.

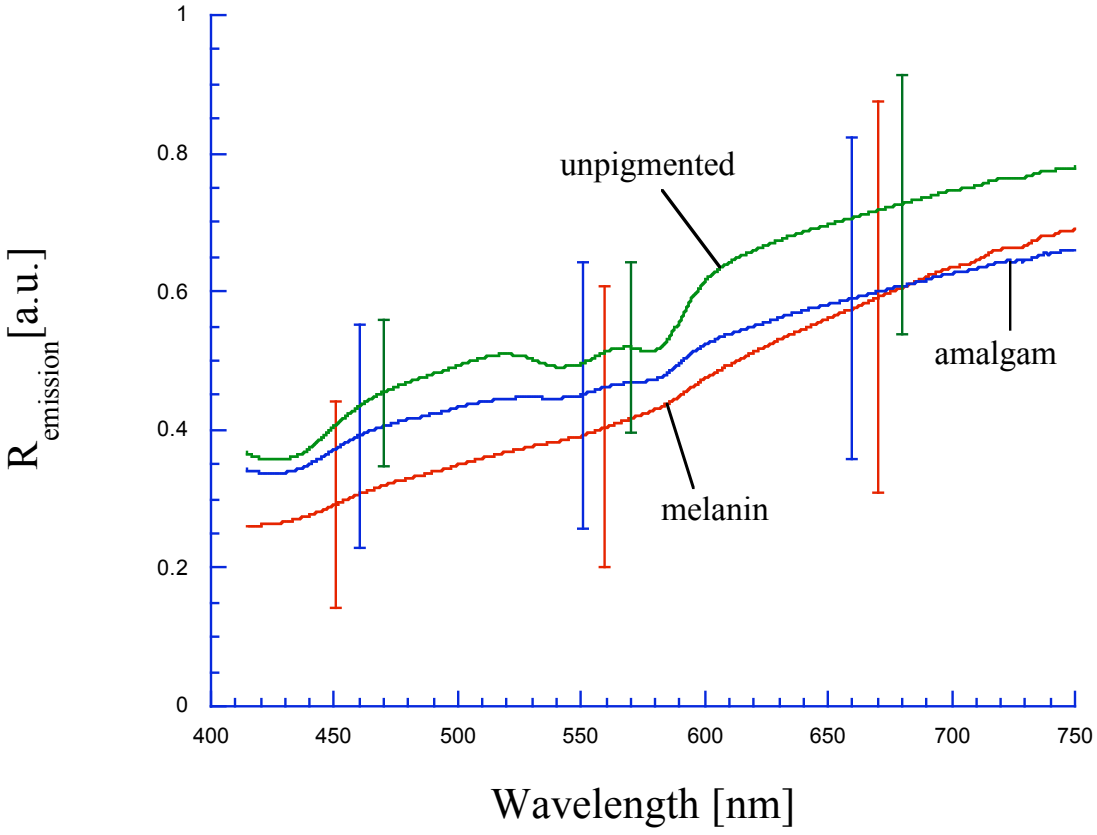

Figure 7.9: The mean reflectance collected by the emission fiber for all amalgam, melanin and non-pigmented sites is shown. The error bars represent the standard deviation.

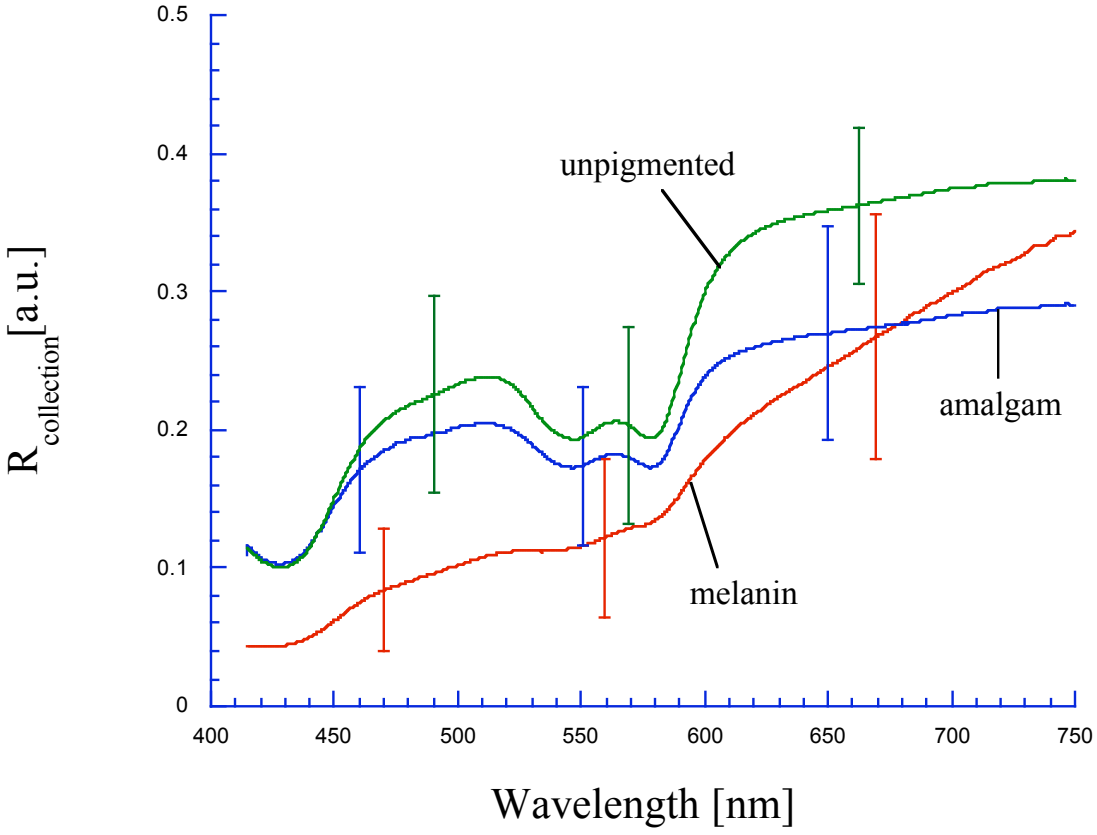

Figure 7.10: The mean reflectance collected by the collection fiber for all amalgam, melanin and non-pigmented sites is shown. The error bars represent the standard deviation.

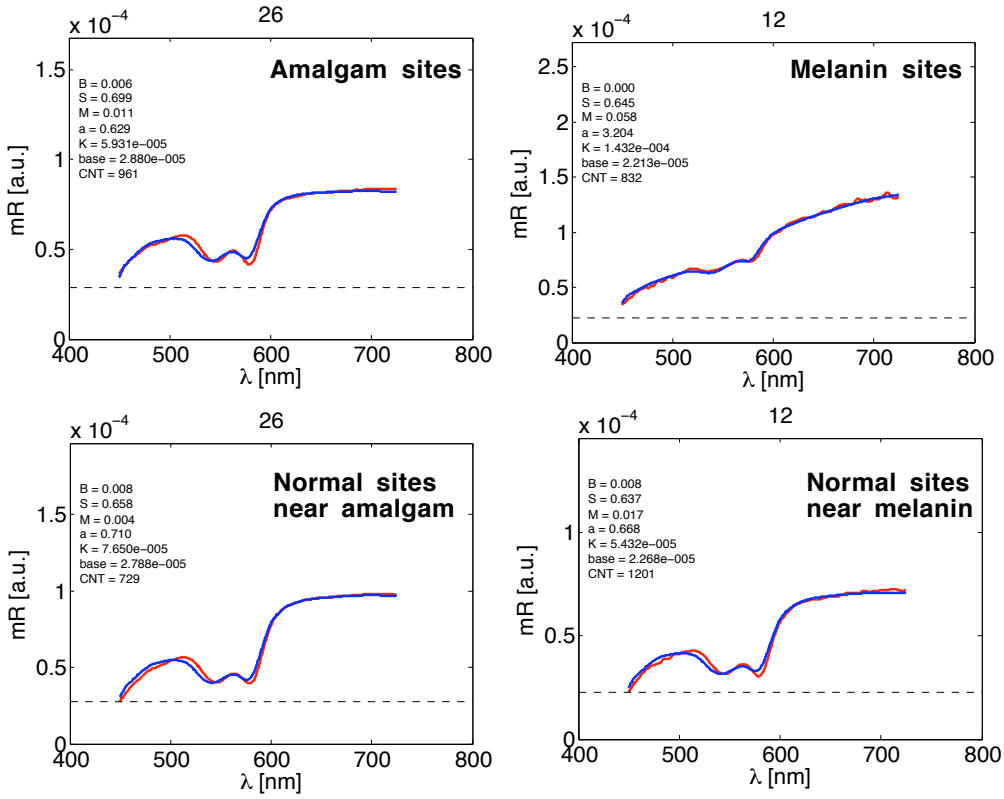

Figure 7.11: The measured reflectance spectra with the collection fiber are fit using the known absorption spectra for blood, water and melanin, to evaluate concentrations and scattering properties. Typical fits are shown over-layed on the measured reflectance for an amalgam site (upper left) and a nearby non-pigmented site on the same patient (lower left) and a melanin site (upper right) and its nearby non-pigment site (lower right). Five parameters were varied in the fitting: the blood fraction, the oxygen saturation, a reflectance scaling factor, a scattering scaling factor, and a wavelength invariant baseline.

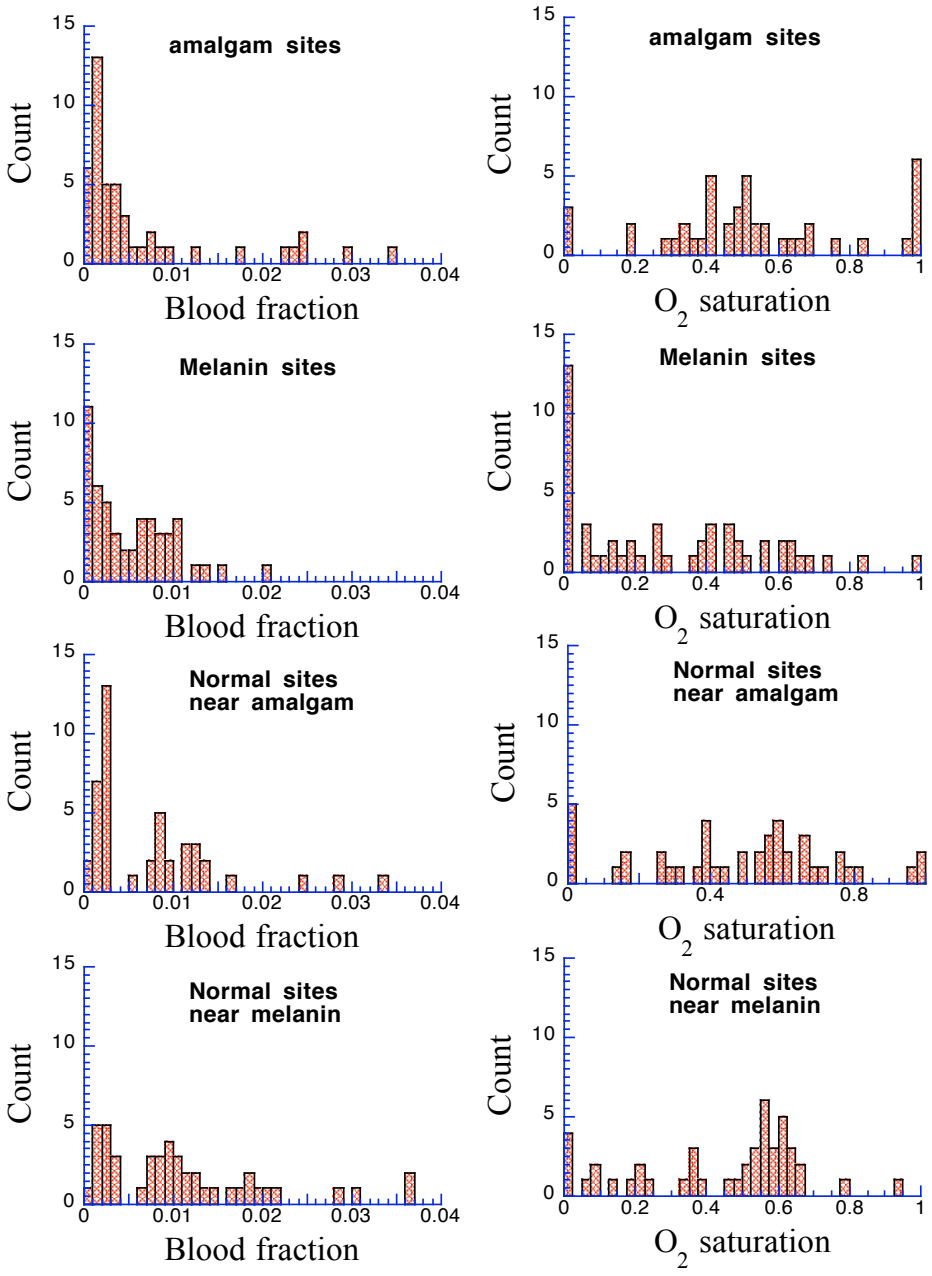

Figure 7.12: Histograms of the fraction of blood in the tissue and oxygen saturation for all measurements with the collection fiber are shown separated by type of site. The blood content is similar for all measurements but the oxygen saturation is given a low value when the blood content is relatively low.

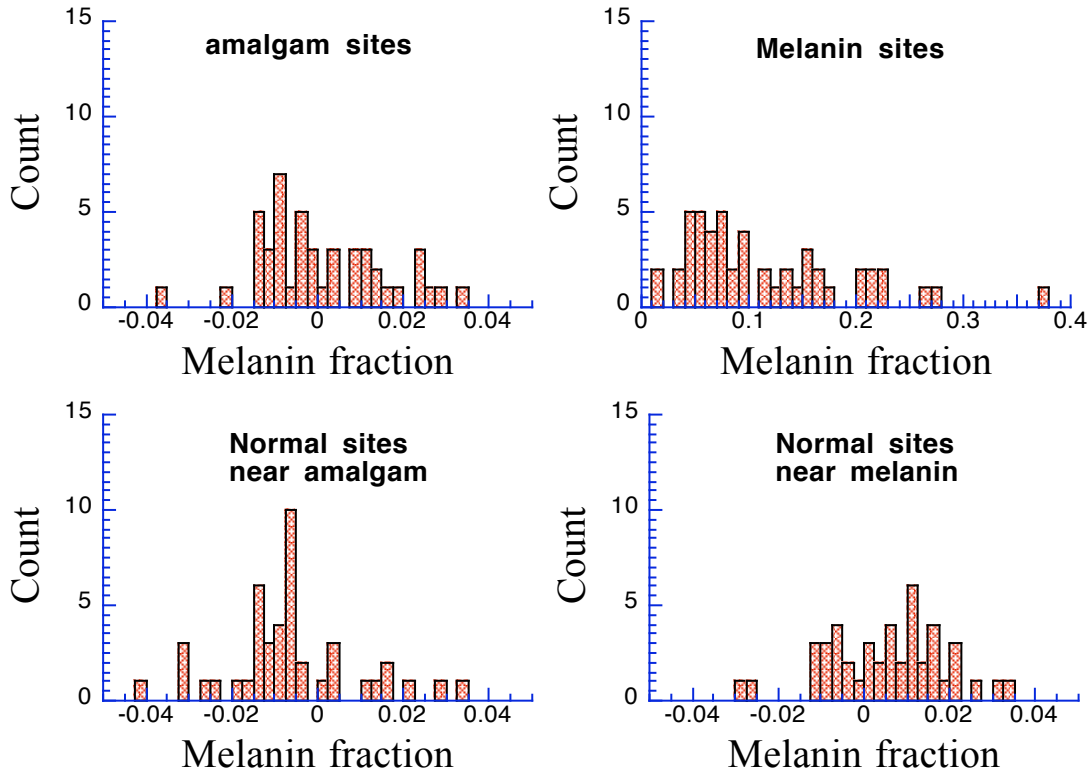

Figure 7.13: The melanin concentration was proportionally fixed to the negative slope to the logarithm of the reflectance between 650-750nm for the collection fiber measurements. This prevented cross-talk between melanin concentration and the scattering scalar. An increase in melanin has a similar overall effect to the reflectance measurement as does a decrease in scattering in the fitting model. In establishing the melanin concentration linearly to the slope, an offset slope equal to the mean of sites without melanin is used to account for the slope with the fiber without melanin absorption. However, this approach forces the non -pigmented sites to register a small negative melanin content.

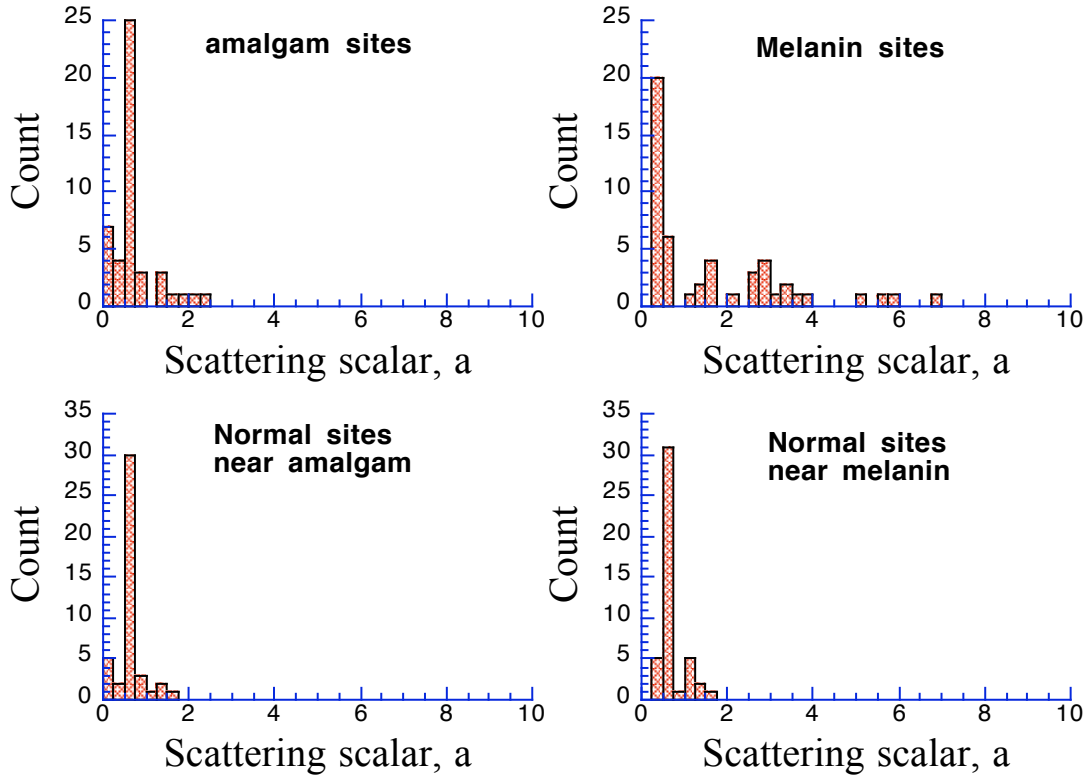

Figure 7.14: Histograms of the scaler to the scattering coefficient that has a wavelength dependence the follows a linear combination of Rayleigh and Mie scattering terms. Melanin sites show a wider variability in scattering but the values above 4 were poorly fits with the model.

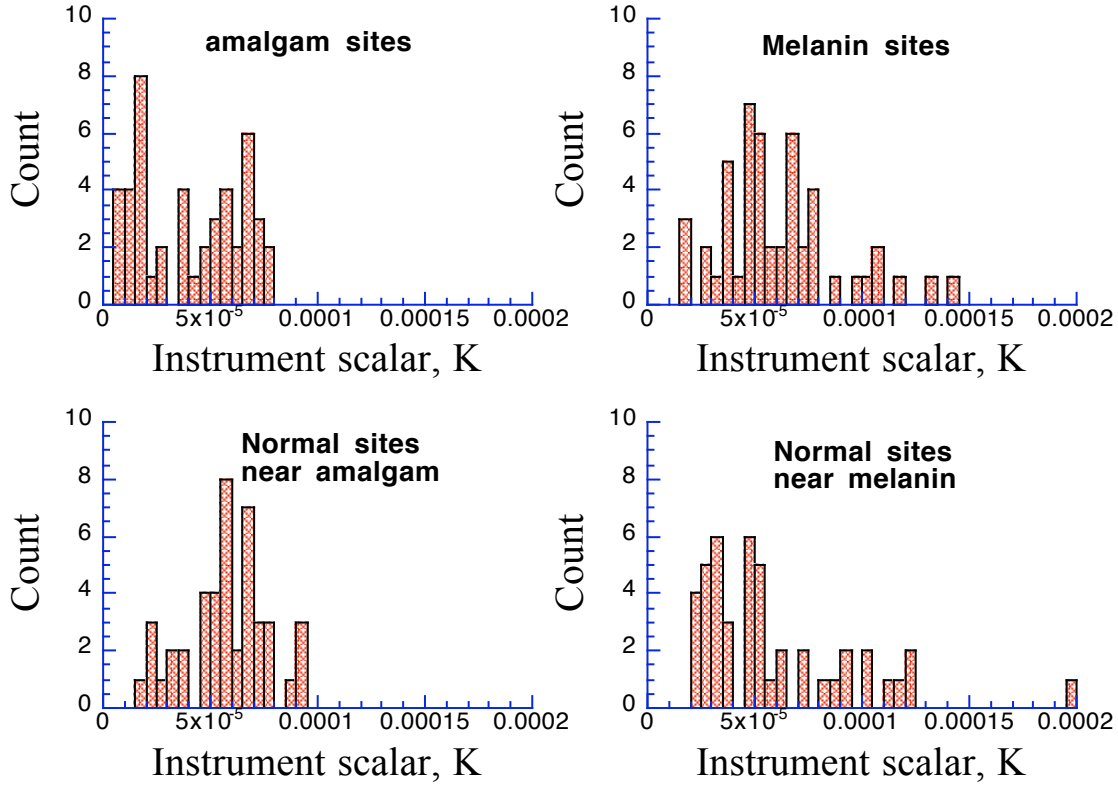

Figure 7.15: The overall predicted measurement is scaled by a wavelength independent constant to correct for differences in fiber contact to the tissue among measurements.

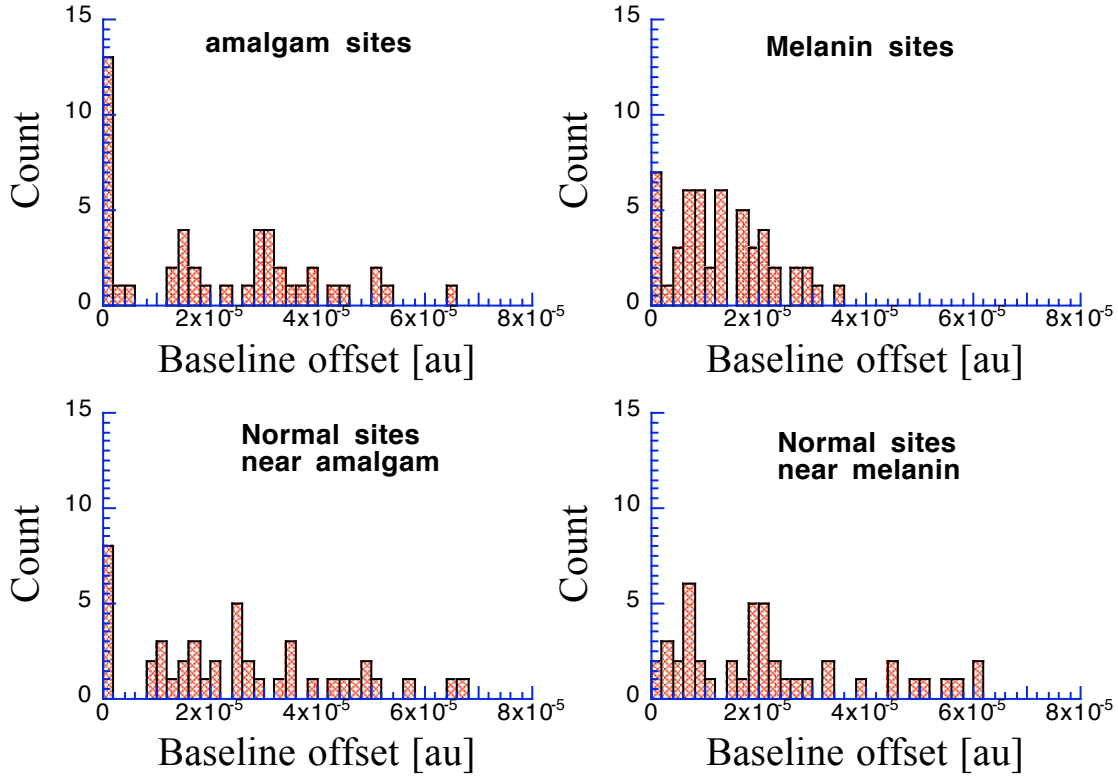

Figure 7.16: The baseline for each measured site was allowed to differ to account for contact variability. It is expected that the offset would be similar for all measurements with the exception of the amalgam sites due to absorption by the amalgam which is spectrally flat. however, no discernible difference is seen.

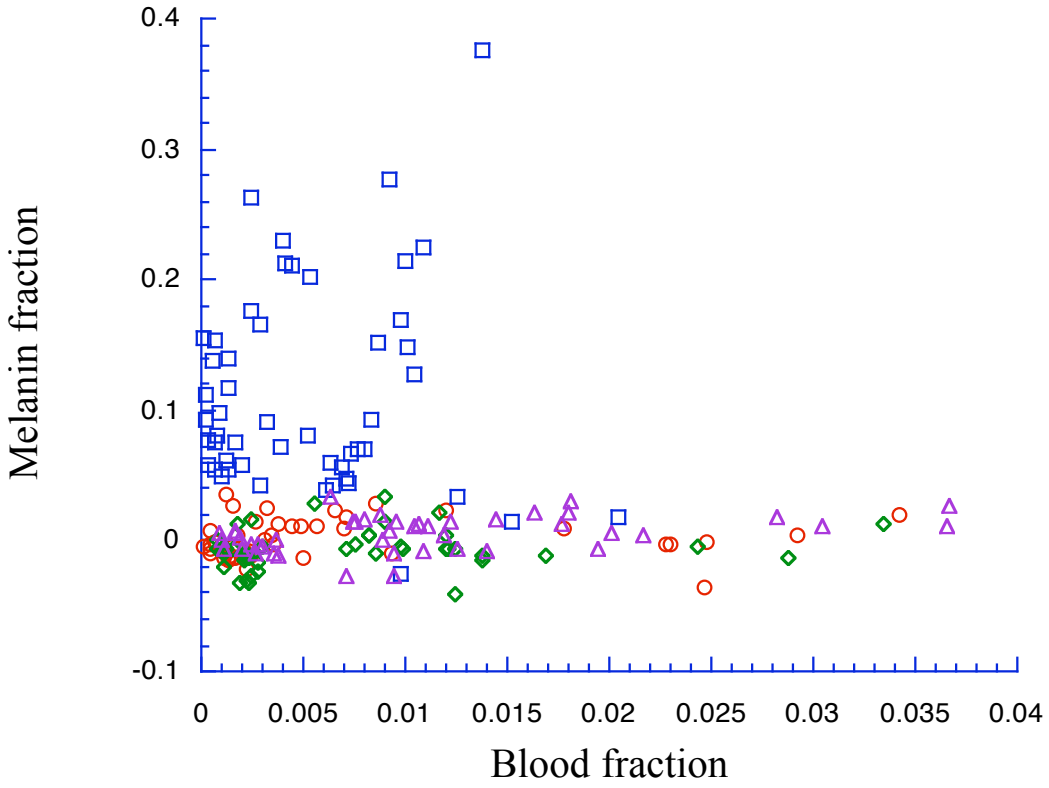

Figure 7.17: TThe fraction of blood versus the fraction of melanin is shown for all measurements with the collection fiber. Melanin sites are shown as squares, amalgam sites by circles, and non-pigmented sites nearby amalgam and melanin sites are respectively diamonds and triangles. The blood fraction does not distinguish among site types as expected, while the melanin sites are clearly differentiated.

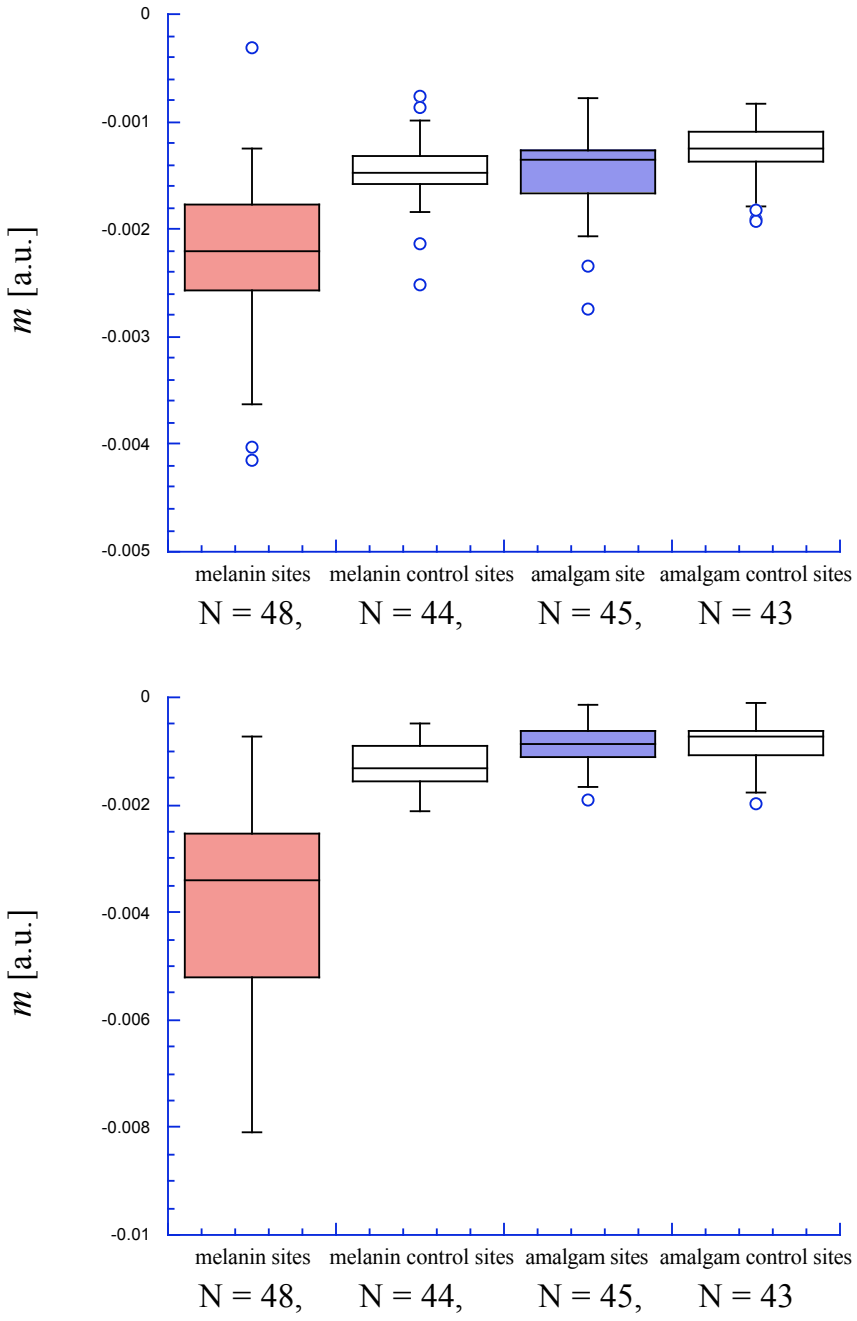

Figure 7.18: This is a box plot of the melanin slope m with the emission fiber (top) and collection fiber (bottom). The control sites refer to the non-pigmented sites adjacent to a type of pigmented site. The control sites and amalgam sites show similar distributions while the melanin sites generally have a greater magnitude of slope which has a wide distribution that mirrors the skin color range of the subjects.

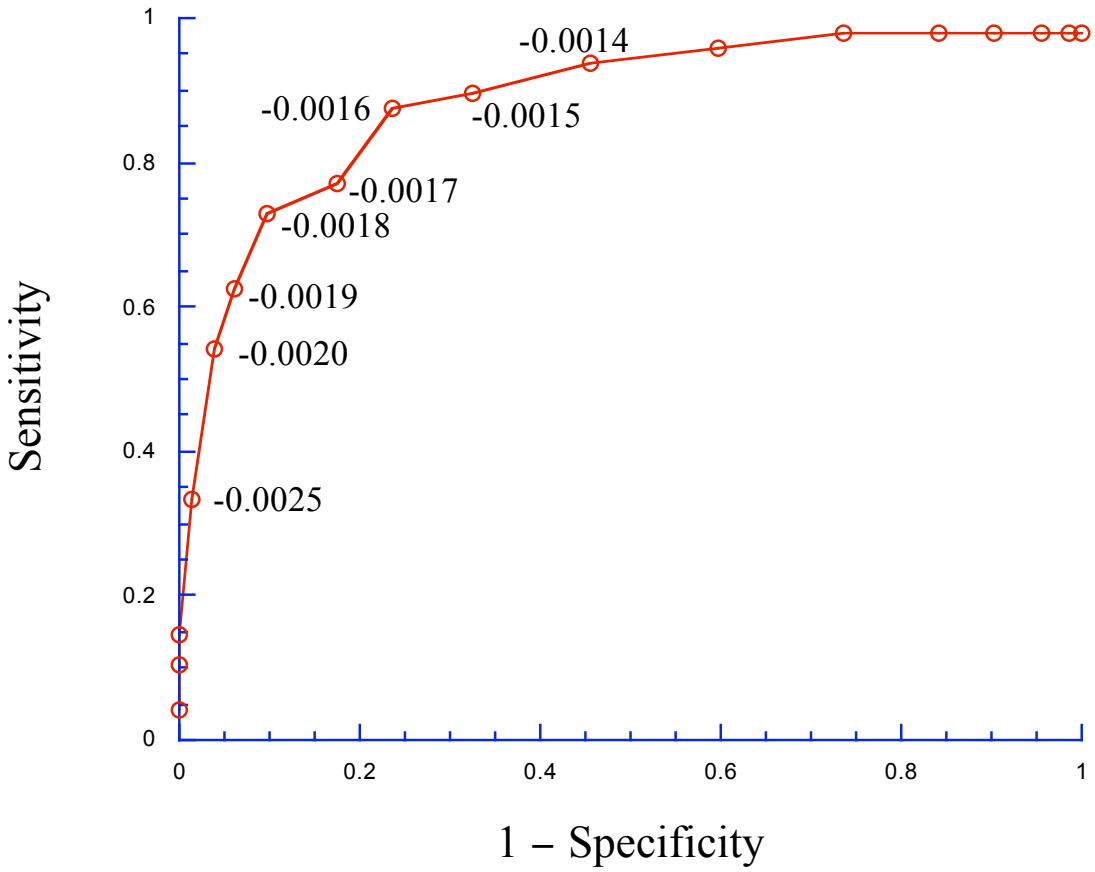

Figure 7.19: ROC curve for sites containing melanin as determined by a threshold value for the melanin slope m by the emission fiber. As the threshold value increases (values labeled), the sensitivity increases at the sacrifice of a decrease in specificity (shown as $1 -$ specificity).

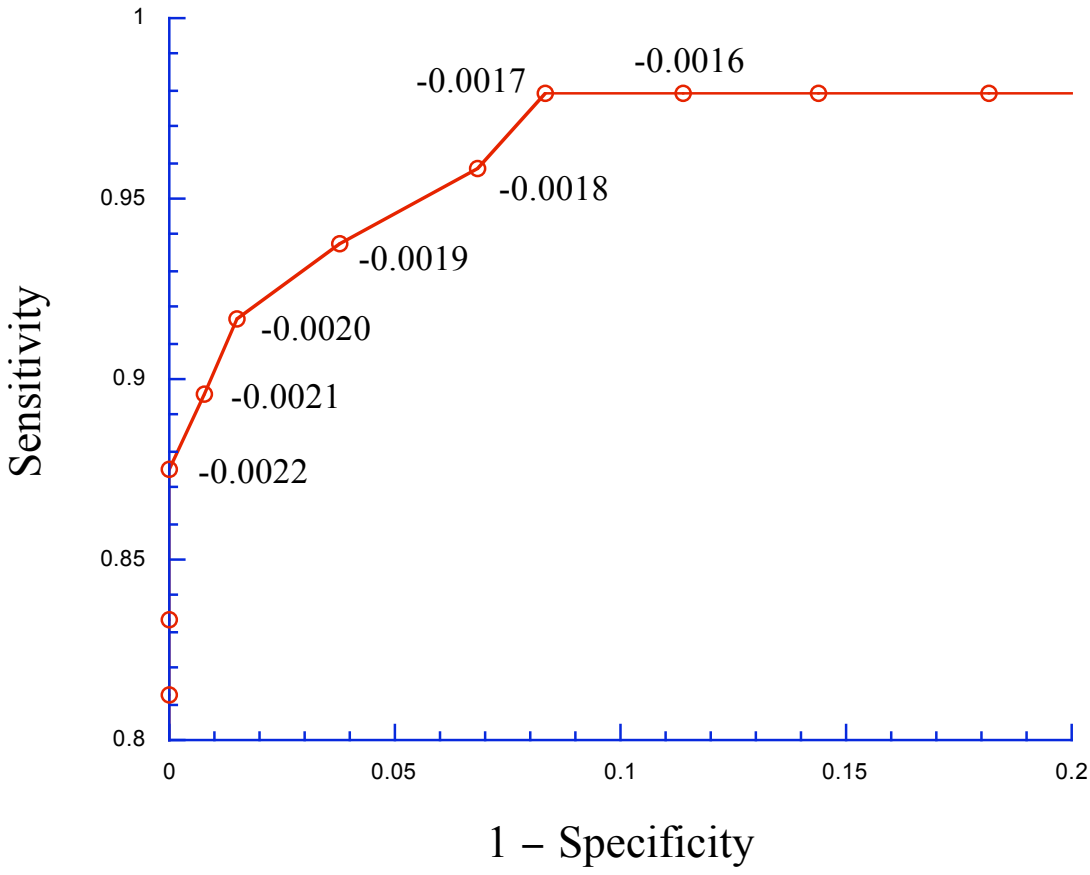

Figure 7.20: ROC curve for sites containing melanin as determined by a threshold value for the melanin slope m by the collection fiber. For clarity, the domain and range are truncated to show detail. As the threshold value increases (values labeled), the sensitivity increases at the sacrifice of a decrease in specificity (shown as $1 -$ specificity).

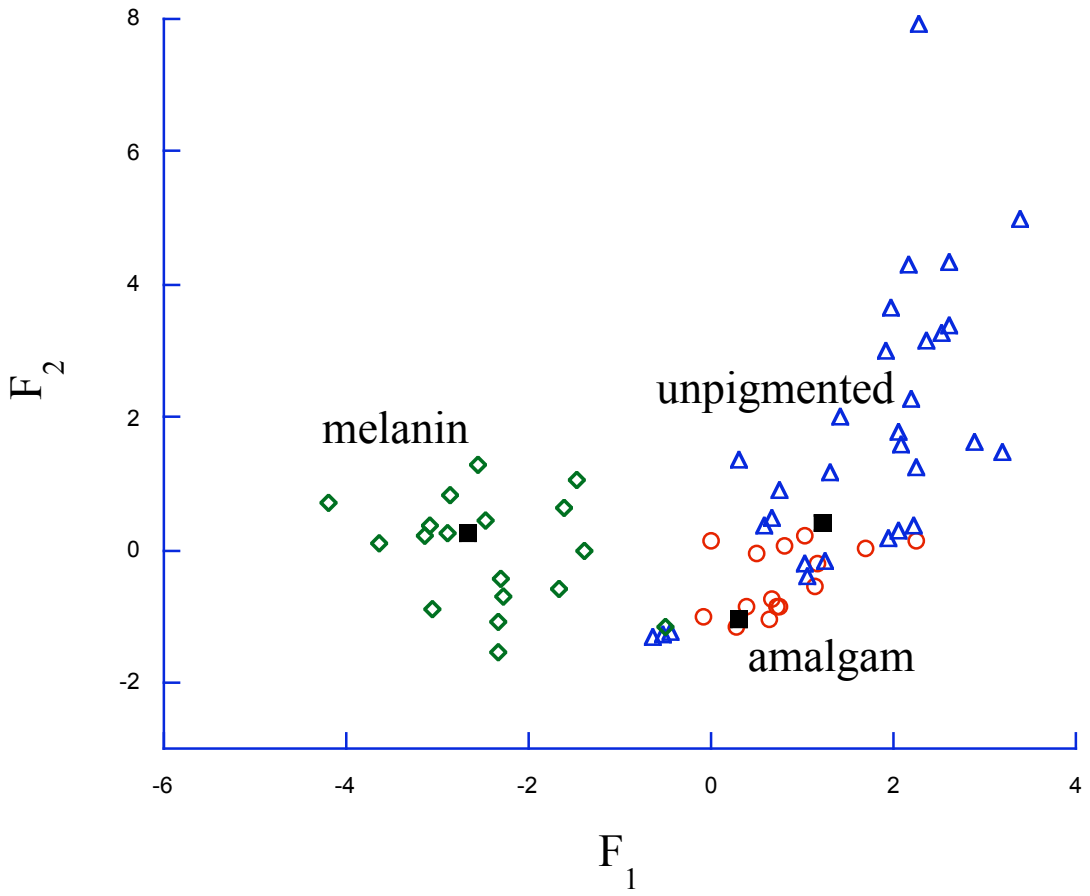

Figure 7.21: The discriminant functions scores of measurements in the test case group are shown in a scatterplot. Measurements are classified according to the shortest distance to one of the group centroids (shown as filled squares) established from the the classification group measurements. Points indicated by diamonds represent measurements from melanin sites, circles indicate amalgam sites, and triangles indicate the non-pigmented sites.

7.4 Discussion

Diffuse reflectance spectroscopy provides an information rich signal regarding the chemical content of tissues [6]. The primary endogenous absorbers in the visible and near-infrared wavelengths are oxy- and deoxy-hemoglobin, melanin, and water. In this study, dental amalgam is the lone exogenous chromophore. The problem addressed in this study is whether sites that contain melanin can be differentiated from the sites that contain amalgam. Spectral fitting of the shape of the measured sites to the known absorbers confirmed that melanin absorption is the only consistently distinguishing characteristic. Yet, a secondary goal of this study is to provide a basis for the design of a second generation probe that would effectively test pigmented oral lesions but require less expensive instrumentation. It is this goal that informed the remainder of the method of analysis.

Melanin could be distinguished from normal and amalgam sites using diffuse reflectance over the wavelength range 640–720 nm (figs. 7.19 and 7.20). Though the reflectance spectrum is processed in the same manner, both the sensitivity and specificity of identifying melanin pigmented lesions is approximately 10% greater with the collection fiber than for reflectance collected with the emission fiber. The difference may be attributed to volume of tissue being sampled and the location of melanin within the oral mucosa. Like in skin, oral melanin pigmentation arises from melanocytes at the epitheleal-conective tissue junction [132] and is found in the epithelium as shown in figure 7.22. The light reflected into the collection fiber travels a longer distance than light collected by the emission fiber (as shown in chapter 6), and thus a greater attenuation of light due to melanin occurs with the collection fiber. A probe that discriminates based on a threshold due to melanin absorption could be reduced to a pair of side-by-side fibers, one for illumination and the other for light collection.

Though a threshold for melanin absorption discrimination approach still requires a spectrometer, the main limitation is that the discrimination between pigmented and non-pigmented sites without melanin is needed to ensure accurate placement of the probe. The diffuse reflectance spectra was used to simulate narrow spectral bandwidth reflectance measurements that would be obtained using an array of lamp filters or LEDs as a light

source and the same probe geometry. Discriminant function analysis was used to evaluate these pseudo-measurements for classification of sites as pigmented by melanin, amalgam or non-pigmented. Discriminant analysis is comparable to multiple logistic regression, but that the predictor variables are continuous. Separation of sites containing melanin pigmentation was determined by reflectance at the wavelength bands at 650 and 675 nm. The wavelength bands at 550 and 575 nm also correlated with separation of melanin sites, but were relatively weak predictors in comparison to the 650 and 675 nm wavelength bands as given by the weights when used together in the discriminant analysis. The 550 and 575 nm wavelength bands correspond with absorption by hemoglobin, which had a less pronounced dip in reflectance in that spectral band for sites with melanin pigmentation than either non-pigmented or amalgam sites.

The amalgam and non-pigmented sites had a smaller separation between group centroids than with melanin sites as shown in table 7.1 and therefore accuracy suffered in discriminating between these two groups. Discrimination of the amalgam and non-pigmented sites was best established by the reflectance at 475, 500 and 550 nm with the emission fiber and 475, 500, and 525 nm with the collection fiber as predictors. The overall reflectance was lower for amalgam sites than non-pigmented sites with intra-subject measurements; but, the reflectance distribution of the amalgam sites and non-pigmented sites overlap considerably leading to a large overlapping of the two groups. It is for this reason that only 53% of amalgam sites in the test group were classified correctly while all incorrectly classified amalgam tattoos were attributed as non-pigmented sites and all mis-classified cases of non-pigmented sites were attributed as amalgam sites.

A possible pitfall to the grouping overlap between amalgam and non-pigmented sites is the misplacement of the probe in cases of amalgam tattoo. Misclassification of amalgam sites in this manner could lead to misplaced measurements where the probe is positioned proximal to the pigmented site but misses the actual pigmented site. To avoid this problem, site identification may be achieved by a real-time indicator of the reflectance for nearly any visible wavelength, though wavelengths longer than 640 nm are preferable since they are less affected by hemoglobin absorption artifacts. Moving the probe over the pigmented site would then drop the reflectance relative to the surrounding non-pigmented mucosa

localizing the pigmented site for assessment.

Other investigators have explored solutions of similar problems regarding the discrimination of melanin pigmented lesions. Marchesini *et al.* [142] used discriminant function analysis to differentiate nevi from melanoma of the skin but differed in their analysis. Rather than using absolute reflectance, spectral features such as the second derivative with respect to wavelength in specific wavelength bands were shown to be capable classifiers in the discriminant functions. Another difference in their analysis was the use of leave-one-out classification. I chose to use separate sets of measurements for classification and testing of future cases since a more conservative and realistic representation of classification is determined.

7.5 Conclusions

The design of the fiber probe was constrained by practical limitations. The dimensions of surface contact of the probe with the tissue is restricted by two conflicting factors. Small areas of contact lead to large variations in the measured reflectance due to changes in blood perfusion caused by contact pressure instability (as demonstrated in chapter 5). On the other hand, larger areas of contact implicitly increase the physical size of the probe thereby restricting the placement of the probe, such as in close proximity to a tooth on the alveolar ridge. One potential subject was rejected for this study by the dental pathologist performing the measurements, since it was felt that the probe could not be placed on the amalgam tattoo due to its proximity to a molar.

In addition, poor probe design can lead to discomfort during measurements. Natural racial oral pigmentation in subjects generally occurs along the gum-line as shown in fig. 7.2. Non-pigmented sites typically occur further away from the teeth on the gums. On two occasions, a subject felt a short pinching sensation with placement of the probe on this non-pigmented location of the gums. Pressure imparted by the probe placement onto one of the shallow nerves in this area was considered to be the cause. In no other instances did any subject feel discomfort during measurements. It is possible that the beveled fiber tip of the probe aided in placement over a probe with a perpendicular viewing angle. The beveled

tip reduced the necessary bend in the optical fibers to place the probe on the surface of the inner gums. A side-looking fiber probe design is a promising potential solution for future probe designs to provide ease of placement in wide variety of tight compartments found in the oral cavity while minimizing the pressure of the probe pressing into the mucosa.

Amalgam tattoo and melanin oral pigmented lesions can be distinguished using diffuse reflectance from a dual optical-fiber probe. Two methods of discrimination were investigated. The first method used the spectral features of melanin in the 640–720 nm wavelength band. The pigmented lesions containing melanin exhibited a higher change in reflectance with respect to wavelength over this band in comparison to amalgam tattoos or non-pigmented sites. The sensitivity and specificity for identifying melanotic lesions from amalgam tattoo was 90% and 99% respectively when the threshold was -0.0021 using the collection fiber reflectance measurement. A better threshold was -0.0017 giving a sensitivity of 98% and a specificity of 92% due to preference that melanin pigmented sites be correctly identified for further screening by biopsy.

A second method of discriminating amalgam tattoo, melanin pigment and non-pigmented sites uses discriminant function analysis on uniformly spaced wavelength bands of reflectance to simulate spectrally filtered reflected light. The discriminant functions are created using two-thirds of the measurements to determine the classification functions and the remaining one-third of the measurements to be used for testing. The sensitivity and specificity was 94% and 100% respectively for classifying melanin pigmented sites. A single melanin pigmented site (6%) was falsely classified as being amalgam.

The discriminant function performed poorly in classifying amalgam tattoos. The sensitivity was 53% with a specificity of 92%. All cases of misclassified amalgam tattoo were classified as non-pigmented sites. The poor classification of amalgam is attributed to the large inter-subject variability for reflectance measurements on amalgam tattoos and non-pigmented sites. However, intra-subject measurements produce higher reflectance on non-pigmented sites relative to the amalgam tattoo. It is suggested that a device show real-time reflectance to assist in localization of the probe on the pigmented lesion.

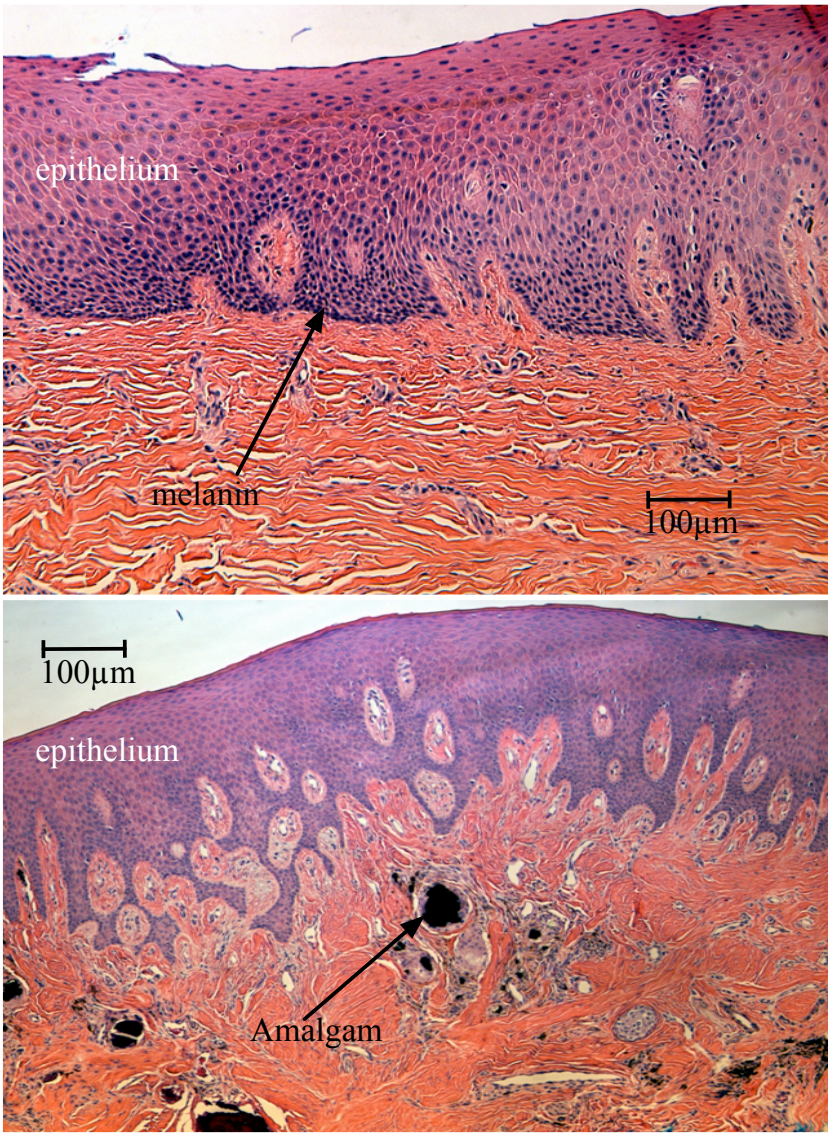

Figure 7.22: The top image shows normal oral buccal mucosa with melanin pigmentation. The melanin is formed along the epithelium border to the underlying connective tissue. The bottom image is from a biopsy of an amalgam tattoo showing both large and fine amalgam particles. The fine particles are digested by macrophages and giant cells resulting in the progressive loss of tin and mercury leaving behind fine particles containing silver and sulphur [150, 151]. Amalgam is not found in the epithelium as it is typically shed every 5-6 days.

Chapter 8

General Discussion and Conclusions

This thesis has presented methods of reflectance spectroscopy with fiber-optics using the shortest source-detector separation possible with the source fiber also acting as the collection fiber. Two probe configurations were presented that incorporate the use of a single fiber to emit and collect its own back-scattered light. A Monte Carlo was developed and tested against measurements on phantoms. The model was used to relate two separate diffuse reflectance measurements to the absorption and reduced scattering coefficients of the medium for both probe designs. The model was used to establish that the device behavior for both probes was not independent of the scattering anisotropy. The optical sampling path-length for 200, 400, 600, and 1000 micron diameter fiber measurements was evaluated with the Monte Carlo model in cases of perpendicularly polished fibers and for bevel-tipped fibers. In addition, analysis was presented for the ability to resolve the absorption and reduced scattering optical properties in the range commonly found in tissue. Finally, a clinical study was presented using a fiber-optic probe to distinguish two kinds of pigmented oral lesions, naturally occurring melanin and amalgam tattoos.

Complimentary work to the optical fiber probe characterization was presented in chapters 2 and 3. Experimental measurements on phantoms with known optical properties was used to validate the Monte Carlo model. A method for fabricating optically-stable phantoms was developed for use at multiple wavelengths. The stability of phantoms make them useful as a diffuse reflectance standard. In order to independently assess the optical properties of the phantom, an experimental method using integrating spheres was presented with a model to interpret both single and double sphere experiments. A term for the sphere gain was introduced showing the influence of the sphere on total diffuse reflectance

and transmittance in terms of the sphere's dimensions (eg. wall area, port areas, and wall reflectance). A combined inverse adding-double and Monte Carlo model was developed to characterize the optical properties of phantoms with a slab geometry using integrating sphere reflectance and transmittance measurements.

8.1 Fabrication of optically stable phantoms

A method to fabricate tissue phantoms that simulate the optical properties of living tissue at the 690 and 830 nm wavelengths was presented. The optical properties of the phantoms has been consistent over a period of 14 months from the date of casting. The two molecular dyes provided independent absorption between our chosen wavelengths for absorption coefficients up to 5 and $3\,\mathrm{cm}^{-1}$ at 690 and 830 nm respectively. These dyes exhibited stable absorption through the curing process of polyurethane. In addition, the high molecular extinction coefficient of each dye allowed us to keep the addition of dye stock to less than 0.1 percent of the volume of the polyurethane. The polyurethane itself was the only component that changed optical properties after casting. The absorption due to the polyurethane decreased approximately by a factor of 2 over the visible spectrum. This change is assumed to occur gradually though evidence was not obtained to support this belief. Though polyurethane slowly changes absorption properties, the effect is to make the material more colorless that helps to make any added dyes the more dominant absorber. Four linear relationships (eqs. 1–4) that describe the absorption coefficient as a function of dye concentration and the reduced scattering coefficient as a function of the titanium dioxide concentration were determined. These relationships predicted the measured absorbing and scattering properties with less than 4% error. Degassing of the polyurethane was a time-consuming yet necessary step to obtain uniformity across a batch of phantoms. The optical properties of the phantoms have shown to be stable over a period of 14 months making the phantoms suitable for use as reference standards.

8.2 Combined Monte Carlo and inverse adding-doubling model for use with integrating sphere measurements.

The combined IAD/MC model was demonstrated to accurately determine optical properties of homogenous optically turbid samples with a reasonable precision using multiple sample thicknesses and sample port sizes for both single and double sphere experiments. The nomenclature for integrating sphere measurements was simplified and rationalized using the concept of sphere gain to express the results. Explicit directions for determining sphere parameters were shown. Formulas were given that work for diffuse incidence or collimated incidence or any combination thereof. Inversion of optical properties from integrating sphere measurements requires a theoretically compatible inversion model and experimental methods otherwise gross error occurs. With substitution method sphere measurements, the inversion model must correct for the sphere gain which increases the measured reflectance and decreases transmittance. A 3D model such as Monte Carlo is essential to correct for light lost through sample edges which improves the resolution and accuracy of samples with small absorption coefficients. With these two corrections, experimental error becomes comparable in magnitude to the error in the predicted optical properties for the presented IAD/MC model.

8.3 Sized-fiber reflectometry

Sized-fiber reflectance spectroscopy was the first method for measuring absorption and reduced scattering of tissue using 200 and 600 μm diameter optical fibers. Backscattered light measurements for solutions with absorption coefficients of 0.1–2.0 cm^{-1} and reduced scattering coefficients of 5–50 cm^{-1} demonstrate that the device is most sensitive for the highest scattering materials. Monte Carlo simulations suggest the device is insensitive to the fiber illumination distribution and that the light returning to the fiber is nearly uniform over all directions. Finally, experiments and Monte Carlo simulations of the sized-fiber device indicate that 50% of the signal arises from roughly 1.2 and 1.9 reduced mean free paths for the 200 and 600 μm fibers respectively and that in general larger fibers sample deeper optically.

8.4 Specular reflectance noise with single fiber measurements

Specularly reflected light behaves as a noise source since it does not contain any information about the absorption or scattering properties of the tissue sample being measured. Additionally, the amount of specular light was shown to be highly correlated to fiber contact. It was shown 5.5 that the specular reflection signal from a perpendicular polished fiber changes by 6.5% with only a 4 degree rotation of the fiber relative to the normal of the surface being measured. Elimination of the specular light from the fiber face was tested for a reduction in signal variation using a beveled-tip fiber. The measurement variability decreases 6 fold on *in vivo* skin and nearly 8 fold on a resin tissue phantom with the 200 micron fiber with the beveled-tip fiber. On a solid resin tissue phantom, the difference between the highest and lowest of 12 measurements is 6.5 and 2.4 percent for the 200 and 1000 micron fiber respectively. On *in vivo* skin where the surface is compliant, the difference between the highest and lowest of 13 measurements drops to 4.5 percent difference with a 200 micron fiber while the 1000 micron fiber is 2.2 percent difference.

8.5 Two dual fiber reflectance probe designs

Two dual-fiber devices with beveled-tips were presented with corresponding methods to invert optical properties from diffuse reflection measurements, a sized-fiber probe that uses a 200 and 1000 micron diameter fibers both emitting and collecting light independently and a dual 400 micron diameter fiber probe with one emitting fiber and both fibers collecting reflected light. Only minor differences exists in performance between the probes. The single emission fiber probe has more compact physical dimensions and a slightly longer optical sampling path-length (a 25-30% increase) relative to the sized-fiber probe. In the visible spectrum for typically expected range of tissue optical properties, the greatest mean optical path-lengths measured are 2.5 mm or less, restricting the resolution of absorption where 100% error is possible. Absolute determination of absorption with either probe will be poor for such short path-lengths which appears as cross-talk between the measured absorption and scattering properties. Yet the relative absorption spectral

shape was demonstrated on measurements of an optical phantom. The dual 400 micron fiber probe is a better design than the sized-fiber probe for two reasons. First, it is a less complex design with a single source fiber that is bifurcated for simultaneous emission and collection of light. Second, dual 400 micron fiber probe has a slightly larger optical sampling path and a more narrow overall diameter. However for the inversion of optical properties, the linear interpolation of optical properties from a Monte Carlo generated grid demonstrated better performance than the empirically derived relations for the single emitting fiber probe, despite its greater mean sampling optical path-length.

8.6 Clinical discrimination of amalgam tattoos from melanin pigmented oral lesions

A clinical study was presented using the dual 400 micron fiber probe to discriminate between pigmented oral lesions due to melanin or amalgam tattoo. Amalgam tattoos, though benign, are often biopsied to rule out melanoma which have a similar appearance. Two methods of analysis were performed with the clinical data. The first method analysis relied on the correlation of slope of the reflected spectrum to the concentration of melanin from 640–720 nm. A sensitivity of 98% was obtained with a specificity of 92% with a slope threshold of -0.0017 for the collection fiber to identify melanin sites.

The second method of analysis used the reflctance spectra obtained in the clinic to simulate data collected using either spectral filters or LED sources centered at 11 wavelengths from 450-700 nm. Discriminant function analysis was used to create two discriminant functions with two-thirds of the measurements. The classification of the discriminant functions were evaluated using the other remaining third as an independent data set. Melanin sites were identified with a sensitivity and specificity of 94% and 100% respectively. A single melanin pigmented site (6%) was falsely classified as being amalgam. The discriminant function performed poorly in classifying amalgam tattoos. The sensitivity was 53% with a specificity of 92%. All cases of misclassified amalgam tattoo were classified as non-pigmented sites. The poor classification of amalgam is attributed to the large inter-subject variability for reflectance measurements on amalgam tattoos and non-pigmented

sites. However, intra-subject measurements produce higher reflectance on non-pigmented sites relative to the amalgam tattoo. We suggest that a device show real-time reflectance to assist in localization of the probe on the pigmented lesion.

Appendix A

Angled-Fiber Monte Carlo Program

This program will calculate the diffuse reflectance emitted by a bevel-tipped fiber into a semi-infinite medium that is collected by the emitting fiber and a second collection fiber in contact to the side (perpendicular to the direction of the bevel). The angle of the fiber tip is specified for a bevel in the x-z plane. For each fiber, the mean path of travel for collected photons is calculated. The results are calculated for absorption and scattering coefficients which are input as arrays as well as the fiber radius, so that multiple combinations are run sequentially.

Important assumptions in this program are that the face of the beveled-tip is parallel to the medium boundary. Both the emission and collection fibers have identical properties (eg. diameter, numerical aperture, bevel angle etc.). The fibers are assumed to be stripped to the cladding and in contact with each other in the y-axis with a center to center spacing of two fiber radius plus twice the cladding thickness.

A sample output for a 400 micron diameter fiber is given for 1,000,000 photons with the fibers at the surface of the medium.

```
Fiber MC Reflectance by Scott Prahl (http://omlc.ogi.edu)
1 W Uniform Fiber Illumination of Semi-Infinite Medium
modified by Ted Moffitt for beveled-tip fibers

   0.9000       Scattering Anisotropy
   1.3500       Medium Refractive Index
   1.4570       Fiber Refractive Index
        0       Fiber Depth                    (microns)
  1000000       Number of photons

 diameter         g         mu_a         mu_s         Em_core         Em_Path         Col_core         Col_Path         time         @Y
  microns         ---         1/cm         1/cm          ---          cm          ---          cm          sec          @Y
      400     12.00   10.0000  200.0000    0.9000  0.001148  0.0373378  0.0001471  0.1000460     106.38
      400     12.00   10.0000  200.0000    0.9000  0.0012247  0.0362642  0.0001593  0.0991180     106.27
      400     12.00   10.0000  200.0000    0.9000  0.0011750  0.0372791  0.0001425  0.0972004     106.42
      400     12.00   10.0000  200.0000    0.9000  0.0011279  0.0379130  0.0001618  0.0984582     106.25
      400     12.00   10.0000  200.0000    0.9000  0.0011574  0.0371960  0.0001542  0.0985450     106.38

 total elapsed time =      84.62
```

Figure A.1: Sample output of five runs with the same optical parameters using a 65 degree beveled fiber 400 micron in diameter.

```
char  t1[80] = "Fiber MC Reflectance by Scott Prahl (http://omlc.ogi.edu)";
char  t2[80] = "1 W Uniform Fiber Illumination of Semi-Infinite Medium";
char  t3[80] = "modified by Ted Moffit for beveled-tip fibers";
#include <stdio.h>
#include <stdlib.h>
#include <math.h>
#include <time.h>
#define RND ((rand()+1.0)/(RAND_MAX+1.0))
#define PI 3.141592653589

long  iphoton, photon_kind, photons = 100000;
double mu_a = 1.0;              /* background excitation absorption in 1/cm */
double mu_s = 200;              /* Scattering Coefficient in 1/cm */
double g = 0.9;                 /* Scattering Anisotropy -1<=g<=1 */
double n_medium = 1.40;         /* Index of refraction of medium */
double n_fiber = 1.457;         /* Index of refraction of fiber */
double fiber_depth = 0.0;       /* Depth fiber is immersed in cm */
double numerical_aperture = 0.22; /* acceptance in air */
double fiber_radius = 0.03;     /* Number of elements run from radius_array */
double clad_thickness = 0.0015; /* the thickness of the fiber cladding */
double clad_rd, fiber1_rd, fiber2_rd, fiber_accept_angle, fiber_crit_angle,fiber_radius;
double mu_a,mu_s,x,y,z,u,v,w,weight, rs, air_rd, bit, air_crit_angle,mu_t, heat, pathsum;
fiber1_path, fiber2_path, clock_t first_time, start_time, finish_time;


double bevel_angle = 25;        /* angle of bevel on fiber from perpendicular in degrees */
#define COS_bevel_angle cos(bevel_angle*PI/180.0)
#define TAN_bevel_angle tan(bevel_angle*PI/180.0)
#define SIN_bevel_angle TAN_bevel_angle*COS_bevel_angle

static void launch(void) /* Start the photon */
{
double phi,theta,nx,ny,nz,nu,mu,xx,yy,zz;
        /* launch uniformly over fiber face - modified for an elliptical face*/
        do {x=2.0*RND - 1.0; y=2.0*RND - 1.0;} while (x*x+y*y>1);
        x *= fiber_radius;
        y *=fiber_radius;
        z = fiber_depth;

        /* This section gives translates light with a gaussian launch distribution from the last */
        /* whole plane  perpendicular to the fiber axis and propagates out remaining fiber */
        /* to the angled fiber face then refracts the light as it enters the medium */

        phi = rand_pi_pi();
```

```
/* random gaussian launch angles in spherical coordinates */
do {theta = gaussian_rand(numerical_aperture/n_fiber);} while (theta<0);
u = sin(theta)*cos(phi);                    /* convert spherical to cartesian coordinates*/
v = sin(theta)*sin(phi);
w = cos(theta);
                                                                                    50
/* find intercept of photon with the plane of the fiber face, (xx,yy,zz) */
xx = (fiber_radius*TAN_bevel_angle + x*w/u − z)/(w/u +TAN_bevel_angle);
yy = v*(xx−x)/u + y;
zz = w*(xx−x)/u + z;

/*Condition for reflecting photons off the interior wall of the fiber*/
while (xx*xx+yy*yy>fiber_radius*fiber_radius)
{
/*determine fiber wall intercept coordinates (nx,ny,nz)*/
        if (u==0) {                                                                 60
                if(v>0)
                        ny = sqrt(fiber_radius*fiber_radius − x*x);
                else
                        ny = −sqrt(fiber_radius*fiber_radius − x*x);
                nx = x;
                nz = w*(ny−y)/v +z;
        }
        else if (u>0) {
                nx = (v*v*x − u*v*y + sqrt(u*u*(fiber_radius*fiber_radius*(u*u + v*v)
                        −(v*x − u*y)*(v*x − u*y))))/(u*u + v*v);                     70
                ny = (nx−x)*v/u + y;
                nz = w*(nx−x)/u +z;
        }
        else if (u<0) {
                nx = (v*v*x − u*v*y − sqrt(u*u*(fiber_radius*fiber_radius*(u*u + v*v)
                        −(v*x − u*y)*(v*x − u*y))))/(u*u + v*v);
                ny = (nx−x)*v/u + y;
                nz = w*(nx−x)/u +z;
        }
                                                                                    80
        x = nx; /* photon reflection point position (x,y,z) */
        y = ny;
        z = nz;

        /* reflect photon off fiber wall */
        nx /= fiber_radius;
        ny /= fiber_radius;
        nz = 0;
        nu = nx*u + ny*v + nz*w; /* cosine of incoming angle with normal to fiber wall */
        mu = −2*nu;                                                                 90
```

```
            u = u + mu*nx; /* reflection photon direction cosine vector (u,v,w) after reflection*/
            v = v + mu*ny;
            w = w + mu*nz;

            /* find new intercept of photon with the plane of the fiber face, (xx,yy,zz) */
            xx = (fiber_radius*TAN_bevel_angle + x*w/u − z)/(w/u +TAN_bevel_angle);
            yy = v*(xx−x)/u + y;
            zz = w*(xx−x)/u + z;
        }                                                                          100

        /* map coordinaes so that (xx,yy,zz) is rotated about the y-axis */
        /* such that the fiber face is in the z = 0 plane */
        x = fiber_radius/COS_bevel_angle + (xx−fiber_radius)/(2*COS_bevel_angle)
                − zz/(2*SIN_bevel_angle);
        y = yy;
        z = (xx−fiber_radius)*SIN_bevel_angle + zz*COS_bevel_angle;

        /* rotate the u and w direction coines accordingly */
        u = −u*COS_bevel_angle − w*SIN_bevel_angle;                                110
        w = u*SIN_bevel_angle + w*COS_bevel_angle;

        /* refract the cosines due to index mismatch */
        u = n_fiber*u/n_medium;
        v = n_fiber*v/n_medium;
        w = sqrt(1 − u*u − v*v);
        /* end of angled fiber launching code */



                                                                                   120
        weight = 1.0 − rs;                                  /* fiber surface reflection */
        mu_t = mu_s + mu_a;
        pathsum = 0;
}

static double transmitted_weight(double n_index) /* weight out of medium*/
{

        double t     = sqrt(1.0−n_index*n_index*(1.0−w*w)); /* cos of exit angle*/
        double r_par = (w − n_index*t)/(w + n_index*t);                            130
        double r_per = (t − n_index*w)/(t + n_index*w);       /* refl = 0.5*(temp1**2+temp**2) */
        return (1.0 − 0.5*(r_par*r_par+r_per*r_per)) * weight;
}

static void bounce (void) /* Interact with top surface (at z=0) */
{
```

```
        double exit_weight;
        w = −w; z = −z;
        if (w <= air_crit_angle) return;            /* total internal reflection */
        exit_weight = transmitted_weight(n_medium);                                  140
        air_rd += exit_weight;
        weight −= exit_weight;
}

static void fiber_bounce (void) /* Interact with fiber surface at z=surface */
{
        double exit_weight, dot_product;
        double delta = (z−fiber_depth) / w;
        double xx = x − delta * u;
        double yy = y − delta * v;                                                   150
        /* x-direction cosine for refracted angle of fiber axis */
        double exit_vector_u = n_fiber*sin(bevel_angle)/n_medium;
Tab8/* z-direction cosine for refracted angle of fiber axis */
        double exit_vector_w = sqrt(1 − exit_vector_u*exit_vector_u);]

        if (xx*xx*COS_bevel_angle*COS_bevel_angle + yy*yy > fiber_radius*fiber_radius
            && xx*xx*COS_bevel_angle*COS_bevel_angle + (yy−2*fiber_radius−2*clad_thickness)
            *(yy−2*fiber_radius−2*clad_thickness)
            > fiber_radius*fiber_radius) return;     /* missed fiber faces */
        w = −w; z = 2*fiber_depth−z;                                                 160

        /* product of direction cosine and refracted axis of fiber */
        dot_product = u*exit_vector_u + w*exit_vector_w;
        fiber_accept_angle = numerical_aperture/n_medium;
        fiber_accept_angle = sqrt(1−fiber_accept_angle*fiber_accept_angle); /* cos in medium */

        if (dot_product>fiber_accept_angle) /* condition for transmission through fiber */
        {
        exit_weight = transmitted_weight(n_medium/n_fiber);
                                                                                     170
                pathsum += delta/mu_t;
                if (xx*xx*COS_bevel_angle*COS_bevel_angle + yy*yy <= fiber_radius*fiber_radius)
                        {fiber1_rd += exit_weight;
                        fiber1_path += pathsum*exit_weight;
                        }
                else {
                        fiber2_rd += exit_weight;
                        fiber2_path += pathsum*exit_weight;
                        }
        }                                                                            180
        else
                clad_rd += exit_weight;
```

```
        weight −= exit_weight;
}

static void move() /* move to next scattering or absorption event */
{
double z_old = z;
double d   = −log(RND);
        x += d * u / mu_t;                                                    190
        y += d * v / mu_t;
        z += d * w / mu_t;
        if ( z_old>fiber_depth && z<fiber_depth) fiber_bounce();
        if ( z<0 ) bounce();
        pathsum += d/mu_t;          /* tracks the pathlength travled for a packet of photons */
}

static void roulette() /* play roulette to terminate photon */
{
        if (weight > 0.001) return;                                           200
        bit −= weight;
        if (RND > 0.1) weight = 0; else weight /= 0.1;
        bit += weight;
}

static void absorb () /* absorb or convert to a fluorescent photon */
{

        heat     += weight * mu_a/mu_t;    /* bkgrnd absorption */
        weight   *= mu_s / mu_t;                    /* new weight for photon */  210
        roulette();                                              /* try to kill photon   */

}

static void scatter() /* Scatter photon and establish new direction */
{
double x1, x2, x3, t, mu;

        do {
                x1=2.0*RND − 1.0;                                             220
                x2=2.0*RND − 1.0;
                } while ((x3=x1*x1+x2*x2)>1);

        if (g==0) { /* isotropic */
                u = 2.0 * x3 −1.0;
                v = x1 * sqrt((1−u*u)/x3);
                w = x2 * sqrt((1−u*u)/x3);
                return;
```

```
        }
        mu = (1−g*g)/(1−g+2.0*g*RND);
        mu = (1 + g*g−mu*mu)/2.0/g;
        if ( fabs(w) < 0.9 ) {
                t = mu * u + sqrt((1−mu*mu)/(1−w*w)/x3) * (x1*u*w−x2*v);
                v = mu * v + sqrt((1−mu*mu)/(1−w*w)/x3) * (x1*v*w+x2*u);
                w = mu * w − sqrt((1−mu*mu)*(1−w*w)/x3) * x1;
        } else {
                t = mu * u + sqrt((1−mu*mu)/(1−v*v)/x3) * (x1*u*v + x2*w);
                w = mu * w + sqrt((1−mu*mu)/(1−v*v)/x3) * (x1*v*w − x2*u);
                v = mu * v − sqrt((1−mu*mu)*(1−v*v)/x3) * x1;
        }
        u = t;
}

static void print_header(void)
{
        printf("%s\n%s\n\n",t1,t2);
        printf("%9.4f \tScattering Anisotropy\n",g);
        printf("%9.4f \tMedium Refractive Index\n",n_medium);
        printf("%9.4f \tFiber Refractive Index\n",n_fiber);
        printf("%9.0f \tFiber Depth         \t(microns)\n",fiber_depth*10000);
        printf( "%9ld \tNumber of photons\n\n",photons);

        printf("%9s\t %9s \t %9s\t %9s\t %9s\t %10s\t %10s\t %10s\t %10s\t %9s\n",
              "diameter","g","mu_a","mu_s","Em_core","Em_Path","Col_core","Col_Path","time");
        printf("%9s\t %9s \t %9s\t %9s\t %9s\t %10s\t %10s\t %10s\t %10s\t %9s\n",
              "microns","---","1/cm","1/cm","---","cm","---","cm","sec");
        fflush(NULL);
}

static void print_results(void)
{
printf("%9.0f\t%9.2f\t%9.4f\t%9.4f\t%10.7f\t%10.7f\t%10.7f\t%10.7f\t%10.2f\n",
           fiber_radius*2*10000, g, mu_a, mu_s,
           fiber1_rd/(photons+bit), fiber1_path/fiber1_rd, fiber2_rd/(photons+bit), fiber2_path/fiber2_rd,
           (double)(finish_time−start_time)/CLOCKS_PER_SEC);
fflush(NULL);
}

int main ()
{
int iradius, iabs, isca, mua_cnt, mus_cnt, radius_cnt;
double mu_a_array[20] = {.1,.2,.5,1,2,5};
double mu_s_array[20] = {100,100,100,200,200,200,500,500,500,1000,1000,1000};
double radius_array[3] = {0.02,0.015,0.03};
```

```
        mua_cnt = 2;
        mus_cnt = 1;
        radius_cnt = 1;

        srand (15);                                                                    280
        rs = (n_medium−n_fiber)/(n_medium+n_fiber); /* specular reflection */
        rs = rs * rs;
        air_crit_angle = sqrt(1.0−1.0/n_medium/n_medium);       /* cos of critical angle */
        fiber_crit_angle = (n_medium<n_fiber) ? 0.0 : sqrt(1−n_fiber*n_fiber/n_medium/n_medium);

        first_time = clock();
        print_header();
        for (iradius = 0; iradius < radius_cnt; iradius++) {
                for (iabs = 0; iabs < mua_cnt; iabs++) {
                        for (isca = 0; isca < mus_cnt; isca++) {                       290
                                mu_a = mu_a_array[iabs];
                                mu_s = mu_s_array[isca];
                                fiber_radius = radius_array[iradius];
                                air_rd = 0; clad_rd = 0; fiber1_rd = 0; fiber2_rd = 0; heat = 0; bit = 0;
                                fiber1_path = 0; fiber2_path = 0;

                                start_time = clock();
                                for (iphoton = 1; iphoton <= photons; iphoton++){
                                        launch ();
                                        while (weight > 0) {                           300
                                                move ();
                                                absorb ();
                                                scatter();
                                        }

                                }
                                finish_time = clock();
                                print_results();
                                fflush(NULL);
                        }                                                              310
                }
        }
        printf("total elapsed time = %10.2f\n",(double)(finish_time−first_time)/CLOCKS_PER_SEC);
        return 0;
}
```

Bibliography

[1] S. A. Prahl and S. L. Jacques, "Sized-fiber spectroscopy," in *SPIE Proceedings of Laser Tissue Interaction IX* (S. L. Jacques, ed.), vol. 3254, pp. 348–352, 1998.

[2] N. Kollias, A. Baqer, and K. R. Naqvi, "Fiber optic spectrophotometer for noninvasive transmission and diffuse reflection studies," *Spectroscopy Lett.*, vol. 19, pp. 149–165, 1986.

[3] U. Utzinger and R. Richards-Kortum, "Fiber optic probes for biomedical optical spectroscopy," *J. Biomed. Optics*, vol. 8, pp. 121–147, 2003.

[4] R. Bays, G. Wagnieres, D. Robert, D. Braichotte, J. F. Savary, P. Monnier, and H. van den Bergh, "Clinical determination of tissue optical properties by endoscopic spatially resolved reflectometry," *Appl. Opt.*, vol. 35, pp. 1756–1766, 1996.

[5] P. R. Bargo, S. A. Prahl, T. Goodell, R. A. Sleven, G. Koval, G. Blair, and S. L. Jacques, "*In vivo* determination of optical properties of normal and tumor tissue with white light reflectance and an empirical light transport model during endoscopy," *J. Biomed. Optics*, vol. 10, p. 034018, 2005.

[6] R. Richards-Kortum and E. Sevick-Muraca, "Quantitative optical spectroscopy for tissue diagnosis," *Annu. Rev. Phys. Chem.*, vol. 47, pp. 555–606, 1996.

[7] N. Ramanujam, "Fluorescence spectroscopy of neoplastic and nonneoplastic tissues," *Neoplasia*, vol. 2, pp. 89–117, 2000.

[8] M. B. Wallace, L. T. Perelman, V. Backman, J. M. Crawford, M. Fitzmaurice, M. Seiler, K. Badizadegan, S. J. Shields, I. Itzkan, R. R. Dasari, J. V. Dam, and M. S. Feld, "Endoscopic detection of dysplasia in patients with barrett's esophagus using light-scattering spectroscopy," *Gastroenterology*, vol. 119, pp. 677–682, 2000.

[9] I. Georgakoudi and M. S. Feld, "The combined use of fluorescence, reflectance, and light scattering spectroscopy for evaluating dysplasia in barrett's esophagus," *Gastrointest. Endosc. Clin. N. Am.*, vol. 14, pp. 519–537, 2004.

[10] M. G. Muller, T. A. Valdez, I. Georgakoudi, V. Backman, C. Fuentes, S. Kabani, N. Laver, Z. Wang, C. W. B. amd R. R. Dasari, S. M. Shapshay, and M. S. Feld, "Spectroscopic detection and evaluation of morphologic and biochemical changes in early human oral carcinoma," *Cancer*, vol. 97, pp. 1681–1691, 2003.

[11] F. Koenig, R. Larne, H. Enquist, F. J. McGovern, K. T. Schomacker, N. Kollias, and T. F. Deutsch, "Spectroscopic measurement of diffuse reflectance for enhanced detection of bladder carcinoma," *Urology*, vol. 51, pp. 342–345, 1998.

[12] U. Utzinger, M. Brewer, E. Silva, D. Gershenson, R. C. Blast, M. Follen, and R. Richards-Kortum, "Reflectance spectroscopy for *in vivo* characterization of ovarian tissue," *Laser Surg. Med.*, vol. 28, pp. 56–66, 2001.

[13] G. Zonios, L. T. Perelman, V. Backman, R. Manoharan, M. Fitzmaurice, J. V. Dam, and M. S. Feld, "Diffuse reflectance spectroscopy of human adenomatous colon polyps *in vivo*," *Appl. Opt.*, vol. 38, pp. 6828–6837, 1999.

[14] T. M. Breslin, F. Xu, G. M. Palmer, C. Zhu, K. W. Gilchrist, and N. Ramanujam, "Autofluorescence and diffuse reflectance properties of malignant and benign breast tissues," *Ann. Surg. Oncol.*, vol. 11, pp. 65–70, 2004.

[15] B. W. Murphy, R. J. Webster, B. A. Turlach, C. J. Quirk, C. D. Clay, P. J. Heenan, and D. D. Sampson, "Toward the discrimination of early melanoma from common and dysplastic nevus using fiber optic diffuse reflectance spectroscopy," *J. Biomed. Optics*, vol. 10, p. 064020, 2005.

[16] M. G. Nichols, E. L. Hull, and T. H. Foster, "Design and testing of a white-light, steady-state diffuse reflectance spectrometer for determination of optical properties in highly scattering systems," *Appl. Opt.*, vol. 36, pp. 93–104, 1997.

[17] T. J. Farrell, M. S. Patterson, and B. Wilson, "A diffusion theory model of spatially resolved, steady-state reflectance for the noninvasive determination of tissue optical properties *in vivo*," *Med. Phys.*, vol. 19, pp. 879–888, 1992.

[18] S. L. Jacques, "Time-resolved reflectance spectroscopy in turbid tissues," *BME*, vol. A5365, pp. 65–74, 1989.

[19] S. J. Madsen, B. C. Wilson, M. S. Patterson, Y. D. Pard, S. L. Jacques, and Y. Hefetz, "Experimental tests of a simple diffusion model for the estimation of scattering and absorption coefficients of turbid media from time-resolved diffuse reflectance measurements," *Appl. Opt.*, vol. 31, pp. 3509–3517, 1992.

[20] A. Kienle and M. S. Patterson, "Improved solutions of the steady-state and the time-resovled diffusion equations for reflectance from a semi-infinite turbid medium," *J. Opt. Soc. Am. A*, vol. 14, pp. 246–254, 1997.

[21] M. S. Patterson, J. D. Moulton, B. C. Wilson, K. W. Berndt, and J. R. Lakowicz, "Frequency-domain reflectance for the determination of the scattering and absoprtion properties of tissue," *Appl. Opt.*, vol. 28, pp. 2331–2336, 1991.

[22] B. W. Pogue and M. S. Patterson, "Frequency-domain optical absorption spectroscopy of finite tissue volumes using diffusion theory," *Phys. Med. Biol.*, vol. 39, pp. 1157–1180, 1994.

[23] J. B. Fishkin, O. Coquoz, E. R. Anderson, M. Brenner, and B. J. Tromberg, "Frequency-domain photon migration measurements of normal and malignant tissue optical properties in a human subject," *Appl. Opt.*, vol. 36, pp. 10–20, 1997.

[24] T. Johnson and J. Mourant, "Polarized wavelength-dependent measurements of turbid media," *Opt. Exp.*, vol. 4, pp. 200–216, 1999.

[25] V. Backman, R. Gujar, K. Badizadegan, I. Itzkan, R. Dasari, L. Perelman, and M. Feld, "Polarized light scattering spectroscopy for quantitative measurement of epithelial cellular structures *in situ*," *IEEE J. Sel. Top. Quant. Elec.*, vol. 5, pp. 1019–1026, 1999.

[26] A. Myakov, L. Nieman, L. Wicky, U. Utzinger, R. Richards-Kortum, and K. Sokolov, "Fiber optic probe for polarized reflectance spectroscopy *in vivo*: design and performance," *J. Biomed. Optics*, vol. 7, pp. 388–397, 2002.

[27] B. W. Pogue and G. Burke, "Fiber-optic bundle design for quantitative fluorescence measurement from tissue," *Appl. Opt.*, vol. 37, pp. 7429–7436, 1998.

[28] C., Q. Liu, and N. Ramanujam, "Effect of fiber optic probe geometry on depth-resolved fluoroscence measurements from epithelial tissues: a monte carlo simulation," *J. Biomed. Optics*, vol. 8, pp. 237–247, 2003.

[29] T. F. Cooney, H. T. Skinner, and S. M. Angel, "Comparative study of some fiber-optic remote raman probe designs. i. model for liquids and transparent solids," *Appl. Spectros.*, vol. 50, pp. 836–848, 1996.

[30] T. F. Cooney, H. T. Skinner, and S. M. Angel, "Comparative study of some fiber-optic remote raman probe designs. ii. tests of single-fiber, lensed, and flat- and bevel-tip multi-fiber probes," *Appl. Spectros.*, vol. 50, pp. 849–860, 1996.

[31] M. S. Patterson, B. Chance, and B. C. Wilson, "Time resolved reflectance and transmittance for the non-invasive measurement of tissue optical properties," *Appl. Opt.*, vol. 28, pp. 2331–2336, 1989.

[32] D. T. Delpy, M. Cope, P. van der Zee, S. Arridge, S. Wray, and J. Wyatt, "Estimation of optical pathlength through tissue from direct time of flight measurement," *Phys. Med. Biol.*, vol. 33, pp. 1433–1442, 1988.

[33] J. R. Lakowicz, K. W. Berndt, and M. L. Johnson, "Photon migration in scattering media and tissue," in *Proc. SPIE*, vol. 1204, pp. 468–480, 1990.

[34] B. C. Wilson, M. S. Patterson, and B. W. Pogue, "Instrumentation for *in vivo* tissue spectroscopy and imaging," in *SPIE Proceedings of Medical Lasers and Systmes II*, vol. 1892, pp. 132–147, 1993.

[35] R. A. J. Groenhuis, H. A. Perverda, and J. J. ten Bosch, "Scattering and absorption of turbid materials determined form reflection measurements 1: Theory," *Appl. Opt.*, vol. 22, pp. 2456–2462, 1983.

[36] R. A. J. Groenhuis, J. J. ten Bosch, and H. A. P. and, "Scattering and absorption of turbid materials determined form reflection measurements 2: Measuring method and calibration," *Appl. Opt.*, vol. 22, pp. 2463–2467, 1983.

[37] A. Kienle, L. Lilge, M. S. Patterson, R. Hibst, R. Steiner, and B. C. Wilson, "Spatially resolved absolute diffuse reflectance measurements for noninvasive determination of the optical scattering and absorption coefficients of biological tissue," *Appl. Opt.*, vol. 35, pp. 2304–2314, 1996.

[38] J. R. Mourant, T. Fuselier, J. Boyer, T. M. Johnson, and I. J. Bigio, "Predictions and measurements of scattering and absorption over broad wavelength ranges in tissue phantoms," *Appl. Opt.*, vol. 36, pp. 949–957, 1997.

[39] J. R. Mourant, I. J. Bigio, D. A. Jack, T. M. Johnson, and H. D. Miller, "Measuring absorption coefficients in small volumes of highly scattering media: source-detector separations that do not depend on scattering properties," *Appl. Opt.*, vol. 36, pp. 5655–5661, 1997.

[40] J. C. Finlay and T. H. Foster, "Hemoglobin oxygen saturations in phantoms and *in vivo* measurements of steady-state diffuse reflectance at a single short source-detector separation," *Am. Assoc. Phys. Med.*, vol. 31, pp. 1949–1959, 2004.

[41] A. Amelink and H. J. Sterenborg, "Measurement of the local optical properties of turbid media by differential path-length spectroscopy," *Appl. Opt.*, vol. 43, pp. 3048–3054, 2004.

[42] A. Amelink, H. J. Sterenborg, M. P. L. Bard, and S. A. Burgers, "*In vivo* measurement of the local optical properties of tissue by use of differential path-length spectroscopy," *Opt. Letters*, vol. 29, pp. 1087–1089, 2004.

[43] F. P. Bolin, L. E. Preuss, R. C. Taylor, and R. J. Ference, "Refractive index of some mammalian tissue using a fiber optic cladding method," *Appl. Opt.*, vol. 28, pp. 2297–2303, 1989.

[44] W. F. Cheong, S. A. Prahl, and A. J. Welch, "A review of the optical properties of biological tissues," *IEEE J. Quantum Electron.*, vol. 26, pp. 2166–2185, 1990.

[45] J. M. Conway, K. H. Norris, and C. E. Bodwell, "A new approach for the estimation of body composition: infrared interactance," *Am. J. Clin. Nutr.*, vol. 40, pp. 1123–1130, 1984.

[46] H. W. Lim and N. A. Soter, *Clinical Photomedicine*. New York: Marcel Dekker, 1993.

[47] B. C. Wilson and S. L. Jacques, "Optical reflectance and transmittance of tissues: Principles and applications," *IEEE J. Quantum Electron.*, vol. 26, pp. 2186–2199, 1990.

[48] B. C. Wilson, P. J. Muller, and J. C. Yanche, "Instrumentation and light dosimetry for intra-operative photodynamic therapy (PDT) of malignant brain tumors," *Phys. Med. Biol.*, vol. 31, pp. 125–133, 1986.

[49] B. C. Wilson, M. S. Patterson, and D. M. Burns, "Effect of photosensitizer concentration in tissue on the penetration depth of photoactivating light," *Lasers Med. Sci.*, vol. 1, pp. 235–244, 1986.

[50] P. R. Bargo, *Optical Measurements for Quality Control in Photodynamic Therapy*. PhD thesis, Oregon Health & Science University, 2003.

[51] J. R. Mourant, J. P. Freyer, A. H. Hielscher, A. A. Eick, D. Shen, and T. M. Johnson, "Mechanisms of light scattering from biological cells relevant to noninvasive optical tissue diagnostics," *Appl. Opt.*, vol. 37, pp. 3586–3593, 1998.

[52] M. Canpolat and J. R. Mourant, "Particle size analysis of turbid media with a single optical fiber in contact with the medium to deliver and detect white light," *Appl. Opt.*, vol. 40, pp. 3792–3799, 2001.

[53] S. Nickell, M. Hermann, M. Essenpreis, T. J. Farrell, U. Kramer, and M. S. Patterson, "Anisotropy of light propagation in human skin," *Phys. Med. Biol.*, vol. 45, pp. 2873–2886, 2000.

[54] R. Bays, G. Wagnieres, D. Robert, J. Theumann, A. Vitkin, J. Savary, P. Monnier, and H. van den Berg, "Three-dimensional optical phantom and its application in photodynamic therapy," *Lasers Surg. Med.*, vol. 21, pp. 227–234, 1997.

[55] P. R. Bargo, S. A. Prahl, and S. L. Jacques, "Optical properties effects upon the collection efficiency of optical fibers in different probe configurations," *IEEE J. Sel. Top. Quant. Elec.*, vol. 9, pp. 314–321, 2003.

[56] P. R. Bargo, S. A. Prahl, and S. L. Jacques, "Collection efficiency of a single optical fiber in turbid media," *Appl. Opt.*, vol. 42, pp. 3187–3197, 2003.

[57] B. C. Wilson, Y. D. Park, Y. Hefetz, M. Patterson, S. Madsen, and S. Jacques, "Potential of time-resolved reflectance measurements for the noninvasive determination of tissue optical properties," in *SPIE Proceedings of Thermal and Optical Interactions with Biological and Related Composite Materials* (M. J. Berry and G. M. Harpole, eds.), vol. 1064, pp. 97–106, 1989.

[58] J. Linford, S. Shalev, and J. Bews, "Development of a tissue equivalent phantom for diaphanography," *Med. Phys.*, vol. 13, pp. 869–875, 1986.

[59] B. C. Wilson, T. J. Farrell, and M. S. Patterson, "An optical fiber-based diffuse reflectance spectrometer for non-invasive investigation of photodynamic sensitizers *in vivo*," in *SPIE Proceedings of Future Directions and Applications in Photodynamic Therapy* (C. J. Gomer, ed.), vol. IS 6, pp. 219–232, 1990.

[60] B. Chance, J. Haselgrove, N.-G. Wang, M. Maris, and E. Sevick, "Photon dynamics in tissue imaging," in *Proc. SPIE*, vol. 1525, pp. 68–82, 1991.

[61] S. T. Flock, S. L. Jacques, B. C. Wilson, W. M. Star, and M. J. C. van Gemert, "Optical properties of intralipid: A phantom medium for light propagation studies," *Lasers Surg. Med.*, vol. 12, pp. 510–519, 1992.

[62] S. J. Madesn, M. S. Patterson, and B. C. Wilson, "The use of india ink as an optical absorber in tissue-simulating phantoms," *Phys. Med. Biol.*, vol. 37, pp. 985–993, 1992.

[63] R. Cubeddu, A. Pifferi, P. Taroni, A. Torricelli, and G. Valentini, "A solid tissue phantom for photon migration studies," *Phys. Med. Biol.*, vol. 42, pp. 1971–1979, 1997.

[64] G. Wagnieres, S. Cheng, M. Zellweger, N. Utke, D. Braichotte, J. Ballinni, and H. van den Bergh, "An optical phantom with tissue-like properties in the visible for use in pdt and fluoescence spectrosopy," *Phys. Med. Biol.*, vol. 42, pp. 1415–1426, 1997.

[65] M. N. Lizuka, M. D. Sherar, and I. A. Vitkin, "Optical phantom materials for near infrared laser photocoagulation studies," *Lasers Surg. Med.*, vol. 25, pp. 159–169, 1999.

[66] M. Lauldi, A. Colombo, B. Farina, S. Tomatis, and R. Marchesini, "A phantom with tissue-like optical properties in the visible and near-infrared for use in photomedicine," *Lasers Surg. Med.*, vol. 28, pp. 237–243, 2001.

[67] M. Firbank and D. T. Delpy, "A design for a stable and reproducible phantom for use in near infra-red imaging and spectroscopy," *Phys. Med. Biol.*, vol. 38, pp. 847–853, 1993.

[68] U. Sukowski, F. Shubert, D. Grosenick, and H. Rinneberg, "Preparation of solid tissue phantoms with defined scattering and absorption properties for optical tomography," *Phys. Med. Biol.*, vol. 41, pp. 1823–1844, 1996.

[69] M. L. Vernon, J. Frechette, Y. Painchaud, S. Caron, and P. Beaudry, "Fabrication and characterization of a solid polyurethane phantom for optical imaging through scattering media," *Appl. Opt.*, vol. 38, pp. 4247–4251, 1999.

[70] M. Firbank, O. Motaki, and D. T. Delpy, "An improved design for a stable and reproducible phantom for use in near infra-red spectroscopy and imaging," *Phys. Med. Biol.*, vol. 40, pp. 995–961, 1995.

[71] S. R. Arridge, P. van der Zee, D. T. Delpy, and M. Cope, "Particle sizing in the mie scattering region: singular value analysis," *Inverse Problems*, vol. 5, pp. 671–689, 1989.

[72] A. Duncan, J. H. Meek, M. Clemence, C. E. Elwell, P. Fallon, L. Tyszczuk, M. Cope, and D. T. Delpy, "Measurement of cranial optical path length as a function of age using phase resolved near infrared spectroscopy," *Pediatr. Res.*, vol. 39, pp. 889–894, 1996.

[73] N. Okui and E. Okada, "Wavelength dependence of crosstalk in dual-wavlength measurement of oxy- and deoxy-hemoglobin," *J. Biomed. Optics*, vol. 10, p. 011015, 2005.

[74] B. J. Tromberg, O. Coquoz, J. B. Fishkin, T. Pham, E. R. Anderson, J. Butler, M. Cahn, J. D. Gross, V. Venugopalan, and D. Pham, "Noninvasive measurements of breast tissue optical properties using frequency-domain photon migration," *Philos. Trans. R. Soc. London B: Biol. Sci.*, vol. 352, pp. 661–668, 1997.

[75] G. Mitic, J. Kölzer, J. Otto, E. Plies, G. Sölkner, and W. Zinth, "Time-gated transillumination of biological tissues and tissuelike phantoms," *Appl. Opt.*, vol. 33, pp. 6699–6710, 1994.

[76] M. Firbank, M. Hiraoka, M. Essenpreis, and D. T. Delpy, "Measurement of the optical properties of the skull in the wavelength range 650–950 nm," *Phys. Med. Biol.*, vol. 38, pp. 503–510, 1993.

[77] C. R. Simpson, M. Kohl, M. Essenpreis, and M. Cope, "Near-infrared optical properties of *ex vivo* human skin and subcutaneous tissues measured using the monte carlo inversion technique," *Phys. Med. Biol.*, vol. 43, pp. 2465–2478, 1998.

[78] D. K. Sardar, M. L. Mayo, and R. D. Glickman, "Optical characterization of melanin," *J. Biomed. Optics*, vol. 6, pp. 404–411, 2001.

[79] N. Ugryumova, S. J. Matcher, and D. P. Attenburrow, "Measurement of bone mineral density via light scattering," *Phys. Med. Biol.*, vol. 49, pp. 469–483, 2004.

[80] A. N. Bashkatov, E. A. Genina, V. I. Kochubey, and V. V. Tuchin, "Optical properties of human skin, subcutaneous and mucous tissues in the wavelength range from 400 to 2000 nm," *J. Phys. D: Appl. Phys.*, vol. 38, pp. 2543–2555, 2005.

[81] S. C. Gebhart, W. C. LIn, and A. Mahadevan-Janseb, "*In vitro* determination of normal and neoplastic human brain tissue optical properties using inverse adding-doubling," *Phys. Med. Biol.*, vol. 51, pp. 2011–2027, 2006.

[82] R. Ulibricht, "Photometer for mean spherical candle-power," *Electrotech. Zeit.*, vol. 21, pp. 595–597, 1900.

[83] S. A. Prahl, M. J. C. van Gemert, and A. J. Welch, "Determining the optical properties of turbid media by using the adding-doubling method," *Appl. Opt.*, vol. 32, pp. 559–568, 1993.

[84] I. V. Yaroslavsky, A. N. Yaroslavsky, T. Goldbach, and H. J. Schwartzmaier, "Inverse hybrid technique for determining the optical properties of turbid media from integrating-sphere measurements," *Appl. Opt.*, vol. 35, pp. 6797–6809, 11996.

[85] J. Swartling, J. S. Dam, and S. Anderson-Engels, "Comparison of spatially and temporally resolved diffuse-reflectance measurement systems for determination of biomedical optical properties," *Appl. Opt.*, vol. 42, pp. 4612–4620, 2003.

[86] C. Chen, J. Q. Lu, H. Ding, P. Blokland, K. M. Jacobs, Y. Du, and X. H. Du, "A primary method for determination of optical parameters of turbid samples and application to intralipid between 550 and 1630 nm," *Opt. Exp.*, vol. 14, pp. 7420–7435, 2006.

[87] A. H. Taylor, "Measurement of diffuse reflection factors and a new absolute reflectometer," *Sci. Papers Bur. Std.*, vol. S16, pp. 421–436, 1920.

[88] J. A. Jacquez and H. F. Kuppenheim, "Theory of the integrating sphere," *J. Opt. Soc. Am.*, vol. 45, pp. 460–470, 1955.

[89] D. K. Edwards, J. T. Gier, K. E. Nelson, and R. D. Roddick, "Integrating sphere for imperfectly diffuse samples," *J. Opt. Soc. Am.*, vol. 51, pp. 1279–1288, 1961.

[90] B. J. Hisdal, "Reflectance of perfect diffuse and specular samples in the integrating sphere," *J. Opt. Soc. Am.*, vol. 55, pp. 1122–1128, 1965.

[91] B. J. Hisdal, "Reflectance of nonperfect surfaces in the integrating sphere," *J. Opt. Soc. Am.*, vol. 45, pp. 1255–1260, 1965.

[92] D. G. Goebel, "Generalized integrating sphere theory," *Appl. Opt.*, vol. 6, pp. 125–128, 1967.

[93] L. M. Hanssen, "Effects of restricting the detector field of view when using integrating spheres," *Appl. Opt.*, vol. 28, pp. 2097–2103, 1989.

[94] J. W. Pickering, C. J. M. Moes, H. J. C. M. Sterenborg, S. A. Prahl, and M. J. C. van Gemert, "Two integrating sphere with an intervening scattering sample," *J. Opt. Soc. Am. A*, vol. 9, pp. 621–631, 1992.

[95] J. W. Pickering, S. A. Prahl, N. van Wieringen, J. F. Beek, H. J. C. M. Sterenborg, and M. J. C. van Gemert, "Double-integrating-sphere system for measuring the optical properties of tissue," *Appl. Opt.*, vol. 32, pp. 399–410, 1993.

[96] J. W. Pickering, S. Bosman, P. Posthumus, P. Blokland, J. F. Beek, and M. J. C. van Gemert, "Changes in the optical properties (at 632.8 nm) of slowly heated myocardium," *Appl. Opt.*, vol. 32, pp. 367–371, 1993.

[97] J. P. Ritz, A. Roggan, C. T. Germer, C. Isbert, G. Muller, and H. J. Buhr, "Continuous changes in the optical properties of liver tissue during laser-induced interstitial therapy," *Lasers Surg. Med.*, vol. 28, pp. 307–312, 2001.

[98] D. Zhu, Q. Luo, and J. Cen, "Effects of dehydration on the optical properties of *in vitro* porcine liver," *Lasers Surg. Med.*, vol. 33, pp. 226–231, 2003.

[99] J. F. Beek, P. Blokland, P. Posthumus, M. Aalders, J. W. Pickering, H. J. C. M. Steronberg, and M. J. C. van Gemert, "*In vitro* double-integrating-sphere optical properties of tissues between 630 and 1064 nm," *Phys. Med. Biol.*, vol. 42, pp. 2255–2261, 1997.

[100] T. L. Troy and S. N. Thennadil, "Optical properties of human skin in the near infrared wavelength range of 1000 to 2200 nm," *J. Biomed. Optics*, vol. 116, pp. 167–176, 2001.

[101] H. J. Wei, D. Xing, J. J. Lu, H. M. Gu, G. Y. Wu, and Y. Jin, "Determination of optical properties of normal and adenomatous human colon tissues *in vitro* using integrating sphere techniques," *World J. Gastroenterol.*, vol. 11, pp. 2413–2419, 2005.

[102] G. de Vries, J. F. Beek, G. W. Lucassen, and M. J. C. van Gemert, "The effect of light losses in double integrating spheres on optical properties estimation," *IEEE J. Sel. Top. Quant. Elec.*, vol. 5, pp. 944–947, 1999.

[103] T. P. Moffitt, Y. Chen, and S. A. Prahl, "Preparation and characterization of polyurethane optical phantoms," *J. Biomed. Optics*, vol. 11, p. 041103, 2006.

[104] D. J. Segelstein, "The complex refractive index of water," Master's thesis, U. of Missouri-Kansas City, 1981.

[105] M. I. Cabrera, O. M. Alfano, and A. E. Cassano, "Absorption and scattering coefficients of titanium dioxide particulate suspensions in water," *J. Phys. Chem.*, vol. 100, pp. 20043–20050, 1996.

[106] H. T. Torres, A. J. Welch, I. Cilesiz, and M. Motamedi, "Tissue optical property measurements: overestimation of absorption coefficient with spectrophotometric techniques," *Lasers Surg. Med.*, vol. 14, pp. 249–257, 1994.

[107] A. Roos, "Interpretation of integrating sphere signal output for nonideal transmitting samples," *Appl. Opt.*, vol. 30, pp. 468–474, 1991.

[108] K. M. Meek, S. Dennis, and S. Khan, "Changes in the refractive index of the stroma and its extrafibrillar matrix when the cornea swells," *Biophys. J.*, vol. 85, pp. 2205–2212, 2003.

[109] J. Welzel, C. Reinhardt, E. Lankenau, C. Winter, and H. H. Wolff, "Changes in function and morphology of normal human skin: evaluation using optical coherence tomography," *Br. J. Derm.*, vol. 150, pp. 220–225, 2004.

[110] S. L. Jacques, "The arf excimer laser in dermatology," in *Lasers in Dermatology* (R. Steiner, R. Kaufmann, M. Landthaler, and O. Braun-Falco, eds.), pp. 116–129, Springer-Verlag, 1991.

[111] E. K. Chan, B. Sorg, D. Protsenko, M. O'Neil, M. Motamedi, and A. J. Welch, "Effects of compression on soft tissue optical properties," *IEEE J. Sel. Top. Quant. Elec.*, vol. 2, pp. 943–950, 1996.

[112] B. J. Tromberg, L. O. Svaasand, M. K. Fehr, S. J. Madsen, P. Wyss, B. Sasone, and Y. Tadir, "A mathematical model for light dosimetry in photodynamic destruction of human endometrium," *Phys. Med. Biol.*, vol. 41, pp. 233–237, 1996.

[113] M. S. Patterson, B. C. Wilson, J. W. Feather, D. M. Burns, and W. Pushka, "The measurement of dihematoporphyrin ether concentration in tissue by reflectance spectrophotometry," *Photochem. Photobiol.*, vol. 46, pp. 337–343, 1987.

[114] M. A. O'Leary, D. A. Boas, B. Chance, and A. G. Yodh, "Reradiation and imaging of diffuse photon density waves using fluorescent inhomogeneities," *J. Lumin.*, vol. 60–61, pp. 281–286, 1994.

[115] F. F. Jobsis, J. H. Keizer, J. C. LaManna, and M. Rosenthal, "Reflectance spectroscopy of cytochrome aa3 *in vivo*," *J. Appl. Physiol.*, vol. 43, pp. 858–872, 1977.

[116] B. Chance, J. S. Leigh, H. Miyake, D. S. Smith, S. Nioka, R. Greenfield, M. Finander, K. Kaufmann, W. Levy, M. Young, P. Cohen, H. Yoshioka, and R. Boretsky, "Comparison of time-resolved and -unresolved measurements of deoxyhemoglobin in brain," *Proceedings of National Academy of Science*, vol. 85, pp. 255–259, 1988.

[117] M. Cope and D. T. Delpy, "System for long-term measurement of cerebral blood and tissue oxygenation on newborn infants by near infrared transillumination," *Med. Biol. Eng. Comput.*, vol. 26, pp. 289–294, 1988.

[118] R. Cubeddu, A. Pifferi, P. Torricelli, and G. Valentini, "Experimental test of theoretical models for time-resolved reflectance," *Med. Phys.*, vol. 23, pp. 1625–1633, 1996.

[119] W. M. Star, "Diffusion approximation," in *Optical-Thermal Response of Laser Irradiated Tissue* (A. J. Welch and M. J. C. van Gemert, eds.), ch. 5, pp. 131–206, Plenum Press, 1995.

[120] S. L. Jacques and L. Wang, "Monte carlo modeling of light transport in tissue," in *Optical-Thermal Response of Laser Irradiated Tissue* (A. J. Welch and M. J. C. van Gemert, eds.), pp. 101–129, Plenum Press, 1995.

[121] T. J. Farrell, B. Wilson, and M. S. Patterson, "The use of neural network to determine tissue optical properties from spatially resolved diffuse reflectance measurements," *Phys. Med. Biol.*, vol. 37, pp. 2281–2286, 1992.

[122] J. S. Dam, T. Dalgaard, P. E. Fabricius, and S. Andersson-Engels, "Multiple polynomial regression method for determination of biomedical optical properties from integrating sphere measurements," *Appl. Opt.*, vol. 39, 2000.

[123] G. H. Weiss, R. Nossal, and R. F. Bonner, "Statistics of penetration depth of photons re-emitted from irradiated tissue," *J. Modern Optics*, vol. 36, pp. 349–359, 1989.

[124] M. S. Patterson, S. Andersson-Engels, B. C. Wilson, and E. K. Osei, "Absorption spectroscopy in tissue-simulating materials: a theoretical and experimental study of photon paths," *Appl. Opt.*, vol. 34, pp. 22–30, 1995.

[125] F. Bevilacqua, D. Piquet, P. Marquet, J. D. Gross, B. J. Tromberg, and C. Depeursinge, "*In vivo* local determination of tissue optical properties: applications to the human brain," *Appl. Opt.*, vol. 38, pp. 4939–4950, 1999.

[126] T. P. Moffitt and S. A. Prahl, "In vivo sized-fiber spectroscopy," in *SPIE Proceedings of Optical Biopsy III* (R. R. Alfano, ed.), vol. 3917, pp. 225–231, 2000.

[127] S. A. Prahl, "The adding-doubling method," in *Optical-Thermal Response of Laser Irradiated Tissue* (A. J. Welch and M. J. C. van Gemert, eds.), ch. 5, pp. 101–129, Plenum Press, 1995.

[128] H. J. van Staveren, C. J. M. Moes, J. van Marle, S. A. Prahl, and M. J. C. van Gemert, "Light scattering in Intralipid-10% in the wavelength range of 400–1100 nm," *Appl. Opt.*, vol. 31, pp. 4507–4514, 1991.

[129] J. P. A. Marijnissen, W. M. Star, J. L. van Delft, and N. A. P. Franken, "Light intensity measurements in optical phantoms and *in vivo* during HpD photoradiation treatment using a miniature light detector with isotropic response," in *Photodynamic Therapy of Tumors and other Diseases* (G. Jori and C. Perria, eds.), pp. 387–390, Padova, Italy: Libreria Progetto, 1985.

[130] T. P. Moffitt and S. A. Prahl, "Sized-fiber reflectometry for measuring local optical properties," *IEEE J. Sel. Top. Quant. Elec.*, vol. 7, pp. 952–958, 2001.

[131] T. P. Moffitt and S. A. Prahl, "The specular reflectance problem with a single fiber for emission and collection," in *SPIE Proceedings of Saratov Fall Meeting: Optical Technologies in Biophysics and Medicine*, vol. 5068, pp. 264–272, 2002.

[132] G. W. Mirowski and J. S. Waibel, "Pigmented lesions of the oral cavity," *Dermatologic Therapy*, vol. 15, pp. 218–228, 2002.

[133] B. Collins, J. Abernethy, and L. Barnes, "Oral malignant melonoma," *eMedicine*, p. http://www.emedicine.com/derm/topic669.htm, 2002.

[134] G. Anneroth, G. O. Carlson, C. M. Eneroth, and G. Moberger, "Primary melanoma in the oral mucous membrane," *Swed. Dent. J.*, vol. 66, pp. 27–37, 1973.

[135] A. Buchner and L. S. Hansen, "Amalgam pigmentation (amalgam tattoo) of the oral mucosa," *Oral Surg.*, vol. 2, pp. 139–147, 1980.

[136] M. Gorsky and J. B. Epstein, "Melanoma arising from the mucosal surfaces of the head and neck," *Oral Surg. Oral Med. Oral Pathol. Oral Radiol. Endod.*, vol. 86, pp. 715–719, 1998.

[137] A. Buchner and L. S. Hansen, "Pigmented nevi of the oral mucosa: a clinicopathologic study of 36 new cases and review of 155 cases from the literature, 2: analysis of 191 cases," *Oral Surg. Oral Med. Oral Pathol.*, vol. 63, pp. 676–82, 1987.

[138] J. E. Bouquot, "Common oral lesions found during a mass screening examination," *J. Amer. Dent. Assoc*, vol. 112, pp. 50–57, 1986.

[139] M. J. Hicks and C. M. Flaitz, "Oral mucosal melanomas: epidemology and pathobiology," *Oral Oncology*, vol. 36, pp. 152–169, 2000.

[140] L. C. Hartman, J. R. Natiella, and M. A. Meenaghan, "The use of elemental microanalysis in verification of the compostition of presumptive amalgam tattoo," *J. Oral Maxillofac. Surg.*, vol. 44, pp. 628–633, 1986.

[141] R. Marchesini, M. Brambilla, C. Clemente, M. Maniezzo, A. E. Sichirillo, A. Testori, D. R. Venturoli, and N. Cascinelli, "*In vivo*, spectrophotometric evaluation of neoplastic and nonneoplasctic skin pigmented lesions-i, reflectance measurments," *Photochem. Photobiol.*, vol. 53, pp. 77–84, 1991.

[142] R. Marchesini, N. Cascinelli, M. Brambilla, C. Clemente, L. Mascheroni, E. Pignoli, A. Testori, and D. R. Venturoli, "*In vivo*, spectrophotometric evaluation of neoplastic and nonneoplasctic skin pigmented lesions-ii, discriminant analysis between nevus and melanoma," *Photochem. Photobiol.*, vol. 55, pp. 515–522, 1992.

[143] J. R. Mourant, I. J. Bijio, J. Boyer, R. L. Conn, T. Johnson, and T. Shimada, "Spectroscopic diagnosis of bladder cancer with elastic light scattering," *Lasers Surg. Med.*, vol. 17, pp. 350–357, 1995.

[144] D. C. G. de Veld, M. Skurichina, M. J. H. Witjes, R. P. W. Duin, H. J. C. M. Sterenborg, and J. L. N. Roodenburg, "Autofluorescence and diffuse reflectance spectroscopy for oral oncology," *Laser Surg. Med.*, vol. 36, pp. 356–364, 2005.

[145] G. N. Stamatas, B. Z. Zmudzka, N. Kollias, and J. Z. Beer, "Non-invasive measurements of skin pigmentation *in situ*," *Pigment Cell Res*, vol. 17, pp. 618–626, 2004.

[146] A. L. Clark, A. M. Gillenwater, T. G. Collier, R. Alizadeh-Naderia, A. El-Naggar, and R. R. Richards-Kortum, "Confocal microscopy for real-time detection of oral cavity neoplasia," *Clinical Cancer Research*, vol. 9, pp. 4714–4721, 2003.

[147] X. Zhang, H. R. Gelderblom, K. Zierold, and P. A. Reichart, "Morphological findings and energy dispersive x-ray microanalysis of oral amalgam tattoos," *Micron*, vol. 38, pp. 543–548, 2007.

[148] J. F. de Freitas, "A survey of the elemental composition of alloy for dental amalgam," *Aust. Dent. J.*, vol. 24, pp. 17–25, 1979.

[149] D. Brune, "Corrosion of amalgams," *Scand. J. Dent. Res.*, vol. 89, pp. 506–514, 1981.

[150] B. M. Eley, "Tissue reactions to implanted dental amalgam, including assessment by energy dispersive x-ray micro-analysis," *J. Pathol.*, vol. 138, pp. 251–272, 1982.

[151] B. M. Eley and J. R. Garrett, "Tissue reactions to the separate implantation of individual constituent of dental amalgam, including assessment by energy dispersive x-ray microanalysis," *Biomaterials*, vol. 4, pp. 73–80, 1983.

[152] R. R. Anderson and J. A. Parrish, "The optics of human skin," *J. Invest. Dermatol.*, vol. 77, pp. 13–19, 1981.

[153] B. L. Horecker, "The absorption spectra of hemoglobin and its derivatives in the visible and near infra-red regions," *J. Biol. Chem.*, vol. 148, pp. 173–183, 1943.

[154] L. Cordone, A. Cupane, M. Leone, and E. Vitrano, "Optical absorption spectra of deoxy- and oxyhemoglobin in the temperature range 300–20 K," *Biophys. Chem.*, vol. 24, pp. 259–275, 1986.

[155] N. Kollias and A. Baqer, "Spectroscopic characteristics of human melanin *in vivo*," *J. Invest. Dermatol.*, vol. 85, pp. 38–42, 1985.

[156] I. A. Vitkin, J. Woolsey, B. C. Wilson, and R. R. Anderson, "Optical and thermal characterization of natural (*Sepia officinalis*) melanin," *Photochem. Photobiol.*, vol. 59, pp. 455–462, 1994.

[157] N. Kollias and A. Baqer, "On the assessment of melanin in human skin *in vivo*," *Photochem. Photobiol.*, vol. 43, pp. 49–54, 1986.

[158] S. L. Jacques, "Biomedical optical instrumentation and laser-assisted biotechnology," in *Reflectance spectroscopy with optical fiber devices and transcutaneous bilirubinometers*, pp. 83–94, Kluwer Academic Publishers, Netherlands, 1996.

[159] M. Pagano and K. Gauvreau in *Principles of Biostatistics*, Pacific Grove, CA: Duxbury, 2 ed., 2000.